Atomistic simulation of thermal transport in oxide nanomaterials

Yeandel, Stephen

Award date:
2015

Awarding institution:
University of Bath

Atomistic Simulation of Thermal Transport in Oxide Nanomaterials

Stephen Robert Yeandel

A thesis submitted for the degree of Doctor of Philosophy

University of Bath

Department of Chemistry

October 2015

Table of Contents

Acknowledgements

I would first like to thank my supervisor Professor Steve Parker, who has given his constant support and enthusiasm since my very first day at university. Without his help I would not be where I am today.

I also wish to thank the many people I have met and who have helped me over the course of my PhD. The full list of names is much too extensive to cover here, however particular thanks must go to Dr Marco Molinari for all his help and advice over the course of my PhD and Dr James Grant for the many hours of discussion about theory and programming.

Special thanks go to my parents and family, who have encouraged and supported me throughout my entire education. Thanks also to my friends, for giving me much needed respite from work and reminding me to go outside occasionally.

I would like to acknowledge the EPSRC and the University of Bath for funding my DTA studentship. A number of the calculations in this work were performed using the ARCHER UK National Supercomputing Service (http://www.archer.ac.uk), provided via our membership of the UK's HEC Materials Chemistry Consortium, which is funded by EPSRC (**EP/L000202**).

Many of the images in this work were generated using the visualisation program VMD[1].

Abstract

The aim of this work has been to use atomistic computer simulation methods to calculate the thermal conductivity and investigate factors that will modify the behaviour when applied to three different oxide materials: MgO, SiO_2 and $SrTiO_3$. These were chosen as they represent distinct classes of materials and are substrates for thermoelectric devices, where one of the primary goals is to tailor the system to reduce the thermal conductivity.

Chapter 1 introduces thermoelectric concepts, gives a background of the theory and a review of various important thermoelectric materials.

In Chapter 2 an overview of the interatomic interactions is presented along with details on the implementation of these interactions in a simulation of a 3D periodic crystal.

Chapter 3 outlines the importance of phonon processes in crystals and several approaches to the calculation of thermal conductivity are presented.

MgO results are given in Chapter 4. Both the Green-Kubo and Boltzmann transport equation (BTE) methods of calculating thermal conductivity were used. The effect on thermal conductivity of two different grain boundary systems are then compared and finally extended to MgO nanostructures, thus identifying the role of surfaces and complex nanostructure architectures on thermal conductivity.

In Chapter 5 two different materials with the formula unit SiO_2 are considered. The two materials are quartz and silicalite which show interesting negative thermal expansion behaviour which may impact upon the thermal transport within the material.

Chapter 6 presents results on the promising thermoelectric material STO. Once again the results from both Green-Kubo and BTE calculations are compared. Grain boundaries are also studied and the effect of inter-boundary distance and boundary type on the thermal conductivity is explored. Finally, a nanostructured STO system (assembled nanocubes) with promising thermoelectric applications is studied.

Chapter 7 outlines the conclusions made from this work and suggests areas for future study.

1. Introduction

Many electricity generating systems are inefficient, losing much of their energy to their surroundings in the form of heat. A simple strategy to boost efficiency in these systems is to recover the lost heat to generate electricity. One approach for recovering the lost heat and converting it into useful electricity is to use thermoelectric (TE) devices. Thermoelectric devices use a temperature difference to generate electricity directly, without the need for any mechanical parts.

The potential applications of thermoelectric devices are widespread and diverse [2, 3], being applicable in many high temperature industrial processes, vehicles [4], low-power electronic devices as well as electricity generation [5]. Reduction of wasted energy in these areas means less greenhouse gases are emitted at the power generation facility as well as a reduction in the resources consumed.

Thermoelectric power generation offers many advantages over other power generation techniques as thermoelectric devices are solid state and have no moving parts, significantly reducing the need for periodic maintenance [6] and giving a potentially long lifespan. Furthermore, thermoelectric devices produce no toxic waste/greenhouse gases emissions during their operation which allows safe application in many areas [7-9].

The range of applications for thermoelectric devices spans many orders of magnitude of power usage, as shown in Figure 1.1.

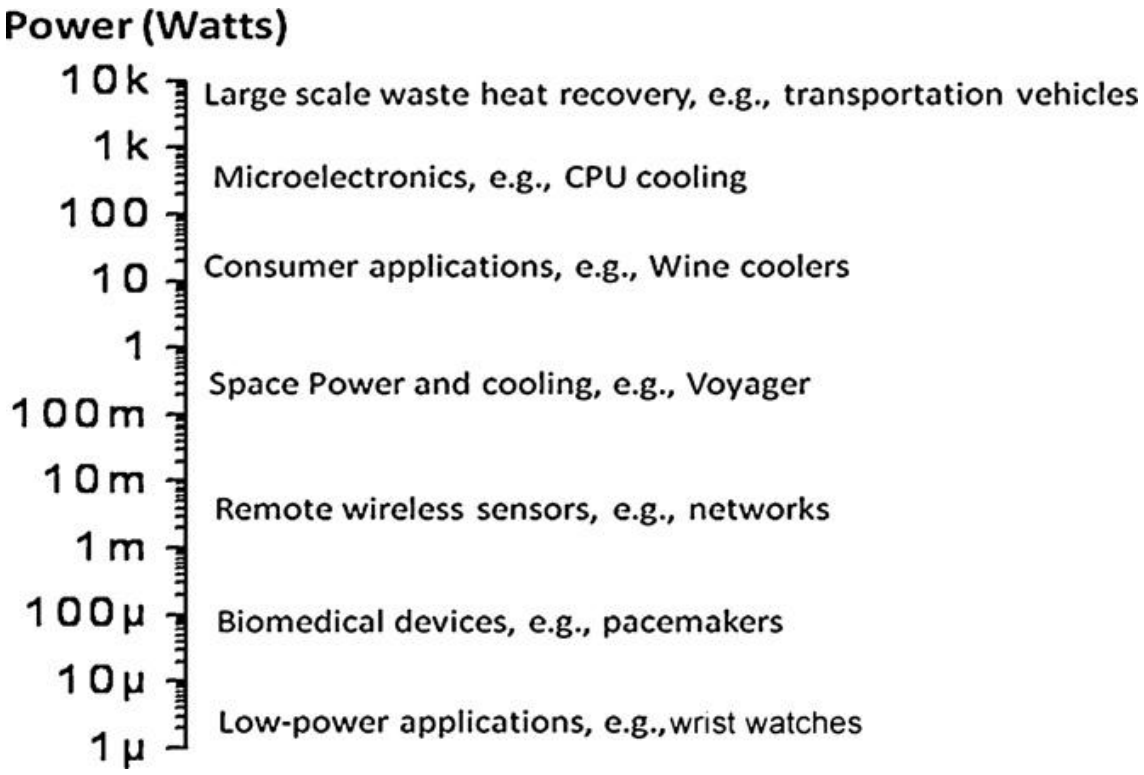

Figure 1.1 The range of applications for thermoelectric materials [10].

The major drawbacks preventing the widespread use of thermoelectric materials is that their efficiencies remain low compared to other power generation systems [11], and the materials currently used to make the best performing thermoelectric materials are often toxic, expensive, unstable at high temperatures and prone to oxidation [12-14]. Despite these limitations, thermoelectric devices are still used in niche applications such as space exploration, where the advantages of simple operation and long lifetimes significantly outweigh the drawbacks (such as the use of plutonium as a heat source) [15].

The potential benefits of improved thermoelectric materials are so large that there is an extensive literature covering the subject [12, 16-28]. The important applications, theory and materials of thermoelectric will now be summarised.

1.1. Thermoelectric Devices and Applications

The construction of a working thermoelectric generator (TEG) requires both n-type and p-type thermoelectric materials. In n-type materials the charge carriers are electrons and in p-type materials they are electron-holes. These materials are combined thermally in

parallel but electrically in series. Charge carriers are driven to one side of the device and a voltage difference is generated across the terminals. A schematic representation of a TEG module is given in Figure 1.2.

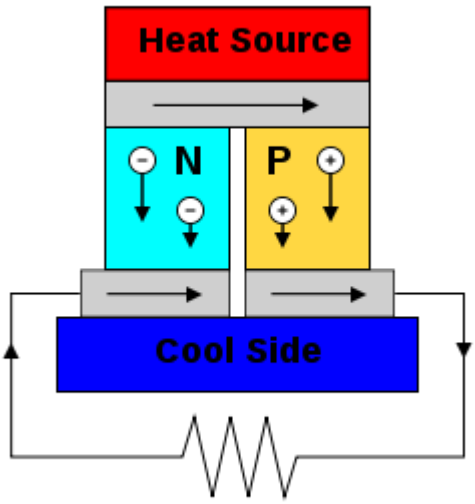

Figure 1.2 Schematic of a TEG [29].

TEGs may be applied in a number of different areas. Recovery of waste heat is of significant interest due to the inefficiencies present in power generation systems. Power generation systems are types of thermodynamic heat engines which convert thermal energy into mechanical motion, and then on to electrical energy via an electric generator. Thermoelectric devices are also heat engines and use electrons as their working fluid [12].

Heat engines have a maximum theoretical efficiency imposed by the temperature difference, known as the Carnot efficiency (or Carnot limit) [30], given by:

$$\eta_{\max} = \frac{T_{\mathrm{H}} - T_{\mathrm{C}}}{T_{\mathrm{H}}} = 1 - \frac{T_{\mathrm{C}}}{T_{\mathrm{H}}}$$

Equation 1.1

where η_{max} is the Carnot efficiency, T_{H} is the high temperature part of the cycle and T_{C} is the cold temperature part of the cycle. It must be noted that the Carnot efficiency is for idealised systems only, but does establish an upper bound for all thermodynamic heat engines.

Traditional fossil-fuel power facilities offer relatively high efficiencies in the region of 30-60% [31] and are close to the theoretical maximum of approximately 80%. These efficiencies are based on modern power plants which use gas (either natural gas or generated from coal) as a fuel and run by the use of gas turbines in combination with steam turbines in a technique known as combined cycling.

Internal combustion engines made from steel usually have a theoretical maximum efficiency of approximately 37%; however the real world average efficiency is usually only approximately 18-20% [32]. Most of the additional inefficiencies stem from heat loss to the exhaust gases. Combined cycling techniques are not applicable for internal combustion engines due to the lower temperatures involved and the bulk of such systems. Applying TEGs to the exhaust system instead would allow recovery of the wasted heat to charge the battery or drive other electronics within the vehicle [33-35]. However the current low efficiencies, oxidative instability and toxicity of the best performing thermoelectric materials mean they are not suitable for widespread application.

Personal devices with very low energy requirements are another area of application. Many portable electronic devices have very modest power requirements and may be driven entirely by body heat [36]. For some time there have been wristwatches available powered by small TEG devices [37]. Extension of this concept to more complex wearable devices such as smart watches or medical sensors would be possible though increased efficiency [38].

Thermoelectric materials may also be utilised as heat pumps. By applying an electrical current to properly tuned thermoelectric materials a temperature difference can be generated. This phenomenon is known as the Peltier effect [39] and a Peltier cooler is schematically represented in Figure 1.3. Exploitation of the Peltier effect means thermoelectric devices can be used in either small scale cooling (computer processors etc.) or in general refrigeration. The advantage of solid state cooling devices is that they may operate continuously for years with minimal need for replacement due to the lack of moving parts [18, 40].

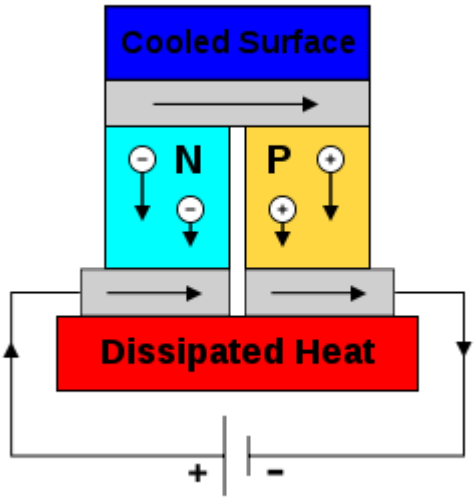

Figure 1.3 Schematic of a Peltier cooler [41].

Developing more efficient thermoelectric systems requires an understanding of the underlying principles of thermoelectric materials. The next section introduces the parameters which must be improved to increase the efficiency of thermoelectric devices.

1.2. Thermoelectric Theory

A measure of how well a material performs as a thermoelectric is given by the thermoelectric figure of merit (ZT):

$$ZT = \frac{\sigma S^2}{\kappa} T$$

Equation 1.2

where σ is the electrical conductivity, S is the Seebeck coefficient, κ is the thermal conductivity and T is the average operating temperature. Thus a good thermoelectric has high electrical conductivity, high Seebeck coefficient and low thermal conductivity. These properties allow a large temperature gradient to be established (due to the low thermal conductivity), a large conversion from thermal to electrical energy (due to the large Seebeck coefficient) and easy transport of charge carriers (due to high electrical conductivity). However, these properties are closely interrelated and cannot be modified independently and so improving the ZT of a material is often difficult [42].

By combining the expression for the thermoelectric figure of merit with the expression for Carnot efficiency, a new expression is derived which directly relates the operating temperatures and the ZT at that temperature to the overall efficiency of the device:

$$\eta_{\max} = \left(\frac{T_{\mathrm{H}} - T_{\mathrm{C}}}{T_{\mathrm{H}}}\right)\left(\frac{\sqrt{1+ZT}-1}{\sqrt{1+ZT}+\frac{T_{\mathrm{C}}}{T_{\mathrm{H}}}}\right)$$

Equation 1.3

Equation 1.3 allows a more direct comparison of thermoelectric devices with other power generation techniques.

1.2.1. Power Factor

The power factor (P. F.) of a thermoelectric material describes the electronic contributions and is defined by:

$$\mathrm{P.F.} = \sigma S^2$$

Equation 1.4

The power factor is difficult to modify for a given bulk material as the electrical conductivity and Seebeck coefficient are both very closely related to the electronic structure of the material. An improvement in power factor thus requires extension beyond bulk systems to more complex nanostructured systems [43] where the electronic properties may be altered.

Additional problems occur for the power factor as many materials have a strong correlation between thermal and electrical conductivity. For example metals have high electrical conductivity and high thermal conductivity; conversely ceramics have low electrical conductivity and low thermal conductivity [18]. TEGs require a high σ, high S but have the additional requirement of low κ and so semiconductors are often the material of choice where the thermal conductivity is low but the electronic properties are tuneable.

Tuning of these parameters is possible via more complex systems and a good understanding of each thermoelectric property.

1.2.2. Seebeck Coefficient

The Seebeck effect [44, 45] occurs due to the disparity in charge carrier transport when a thermal gradient is applied. At the hot terminal, more charge carriers gain enough energy to move to the conduction band than at the cold terminal. This concentration disparity results in a net diffusion of charge carriers from the hot to cold terminals. The unequal distribution of charge carriers creates a potential difference across the material which can be harnessed to create an electrical current. The measure of the strength of the voltage difference generated by the temperature gradient is given by the Seebeck coefficient, S:

$$S = -\frac{\Delta V}{\Delta T}$$

Equation 1.5

where ΔV and ΔT are the voltage and temperature differences respectively. In reality the temperature gradient will drive both electrons and holes to diffuse across the material and so the sign and strength of the Seebeck coefficient depends upon which predominates and by how much. A negative Seebeck coefficient arises when the charge carriers are electrons and a positive Seebeck arises when the charge carriers are electron-holes.

The Seebeck coefficient tends to be highest in semiconductor materials that allow limited movement of charge carriers [46]. In metals the Seebeck coefficient tends to be very low due to the partially filled bands and lack of band gap, thus it is much easier for charge carriers to diffuse against the temperature gradient. Superconductors have a Seebeck coefficient of zero as by definition a superconductor has no electrical resistance at all. However, in some higher temperature superconductors under strong magnetic fields, large Seebeck coefficients have been reported [47].

By placing n-type and p-type thermoelectric materials electrically in series, the voltage generated by a given temperature gradient can be increased. When arranged in this manner it is important that the materials used are sufficiently compatible in order to maximise the efficiency [48].

1.2.3. Electrical Conductivity

The electrical conductivity is closely related to the Seebeck coefficient and also depends upon electronic structure of the material. The electrical conductivity is of the order of ~10^6 S/m in metallic systems and ~10^{-6} S/m in insulators. Semiconductors fall in between this range and their electrical conductivity is highly dependent upon temperature, which affects both carrier concentration and mean free paths.

1.2.4. Thermal Conductivity

Lattice vibrations (phonons) transport thermal energy and thus compete with energy transport via charge carriers. A lower thermal conductivity therefore results in a higher ZT. The thermal conductivity of a material, κ, can be split into two main contributions:

$$\kappa = \kappa_{\text{elec}} + \kappa_{\text{latt}}$$

Equation 1.6

where κ_{elec} is the electrical contribution to the thermal conductivity and κ_{latt} is the lattice contribution. More exotic mechanisms of heat transfer could also be included (for example emission and reabsorption of infrared light at very high temperatures [49]) but are generally negligible.

For semiconductor materials the lattice contribution to the thermal conductivity is much larger than the electronic contribution [50]. In these materials the thermal conductivity is normally related to the average atomic weight. A heavier average atomic weight often leads to a denser material, a lower phonon propagation velocity, and thus a reduction in thermal conductivity [51].

There are five main ways that the lattice thermal conductivity can be reduced in thermoelectric materials [52]:

1. Use materials with complex crystal structures
2. Include heavy elements which are weakly bound
3. Addition of impurities
4. Formation of solid solutions
5. Generate a large numbers of grain boundaries

These techniques generally reduce the thermal conductivity by introducing new scattering mechanisms via an increase in the number of environments. Nanostructuring may be considered a combination of these approaches. An additional advantage of nanostructures is that they allow different regions of the material to present different properties to the electrons and phonons, approaching the idea first put forth by Slack [44] of a Phonon-Glass Electron-Crystal (PGEC).

In a PGEC material the phonons experience the environment like a glass, scattering frequently and so the thermal energy takes a random walk through the material. Conversely the electrons would experience the environment as a crystal, being transported rapidly and thus leading to high electrical conductivity. It is therefore advantageous to develop nanostructured materials which approach this philosophy.

1.2.5. Wiedemann-Franz Law

Improving the figure of merit is further complicated due to a relationship known as the Wiedemann-Franz law:

$$\frac{\kappa_{\text{elec}}}{\sigma} = LT$$

Equation 1.7

where L is a proportionality constant known as the Lorenz number. The relationship outlined in Equation 1.7 implies it is not possible to improve the thermal or electrical conductivity for TEGs without modifying the other in a detrimental manner.

The Wiedemann-Franz law often holds true for metals where the electronic thermal conductivity is the dominating factor. In semiconductor materials the electronic thermal conductivity is much less significant and a large number of other factors can change the Lorenz number [10, 17] and therefore semiconductors are the materials of choice for almost all thermoelectric applications.

1.3. Thermoelectric Materials

The main issue affecting application of thermoelectric devices is the low figure of merit, ZT, of the materials used to construct them. These materials must have certain properties if they are to function well as thermoelectric material.

The concentration of charge carriers is a particularly important property as it influences both the Seebeck coefficient and the electrical conductivity [53]. Tuning the concentration of charge carriers is most easily achieved by doping. However, the optimisation of dopant levels must be done carefully as increasing the carrier concentration increases conductivity, but reduces the Seebeck coefficient [54]. It has been stated that the optimum concentration of charge carriers is between 10^{19} and 10^{21} per cm^3 [18, 55].

While there are many classes of thermoelectric material available, each has its own advantages and disadvantages. Several classes are particularly popular due to their inherent properties, some of which are outlined below. A very good review of many types of thermoelectric material can be found in the review of Sootsman et al. [56].

1.3.1. Bismuth Telluride (Bi_2Te_3)

The most used and studied thermoelectric material to date is bismuth telluride due to its very high ZT values [57]. The high ZT values found in Bi_2Te_3 originate from its high power factor and very low thermal conductivities (~2 W/(m.K)) [58]. These properties result from an unusual bonding arrangement in the bulk structure of bismuth telluride which is comprised of distinct layers. A schematic diagram of the bonding in bismuth telluride is provided in Figure 1.4, showing that the Te(1)-Bi-Te(2)-Bi-Te(1) layers are held together by covalent-ionic type interactions whereas the inter-layer bonding is of the van der Waals type.

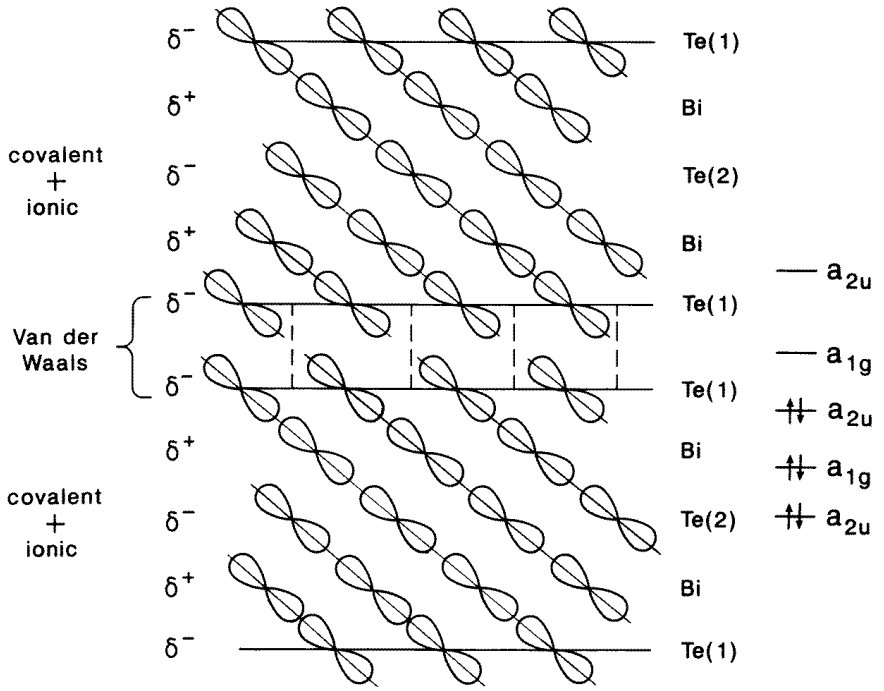

Figure 1.4 Schematic of bonding is bismuth telluride [59].

DFT calculations have also shown that the weakly bonded Te(1) type atoms contribute the most to the electronic density of states near the valence band edge, suggesting it will act as an electron donor, conversely bismuth atoms contribute most on the corresponding edge at the bottom of the conduction band, showing their behaviour as electron acceptors. This interesting effect of the bonding may go some way to reveal the origin of high charge carrier concentrations found in bismuth telluride [60, 61].

Bismuth telluride may also be alloyed with other binary tellurides to optimise the thermoelectric properties further and is an active area of research [62-64]. It has long been known that the dominant effect of these high mass dopants does not result from the electronic properties, but the different masses leading to increased phonon scattering and hence lower thermal conductivity [65].

1.3.2. Bulk Phonon-Glass and Electron-Crystal materials

Some classes of bulk material approach the PGEC (Phonon-Glass and Electron-Crystal) concept of the ideal thermoelectric material by splitting the requirements of PGEC materials into separate parts of the material. The covalent superstructure provides pathways for high electrical conductivity but contain cages holding ionic guest atoms. The ionic guest atoms introduce rattling vibrational modes which act to reduce thermal

conductivity [66]. The reduction in thermal conductivity has only a very small impact on the electrical properties as the superstructure is intact [67].

Clathrates are one such material that fulfils the PGEC requirements. The cages consist of tetrahedral units and in some respects are similar to zeolite structures [68]. Within the cages formed by the tetrahedral units are guest ions, which are usually metals [69]. The use of heavy metals as guests in the structure generates localised low frequency modes that overlap the acoustic branch and facilitate phonon scattering [70]. This arrangement gives very low thermal conductivity while keeping the lattice intact to minimise the charge carrier scattering.

Skutterudites are another PGEC material which innately have good electronic conduction and high Seebeck coefficient, though they do suffer from high thermal conductivity. The high thermal conductivity of skutterudites is mitigated by including guest ions to scatter acoustic phonons in the same way as clathrates [71].

Half-Heuslers are three component systems of the MgAgAs type structure (space group $F\bar{4}3m$) [72]. The system usually contains two elements from the transitions metals and the third a metal or metalloid. Half-Heuslers are promising because their high Seebeck coefficient and extremely varied elemental combinations [73] allows for much improvement via doping.

1.3.3. Oxides Materials

Metal oxides are a promising thermoelectric material as they are normally abundant, cheap, have low toxicity (depending on the metal) [74] and are stable at high temperatures [14]. The oxidative stability of oxides make them ideal for practical applications, however they have poor charge carrier mobility and high thermal conductivities. These drawbacks mean that they were generally not considered a promising thermoelectric material until good thermoelectric performance was demonstrated in the layered cobalt oxide $NaCo_2O_4$ [75].

A further advantage of oxide type materials is the range of possible bulk structures. A large variety of both n-type and p-type semiconductors are available containing oxides, including: ZnO [76], $Ca_3Co_4O_9$ [77] and $NaCo_2O_4$ [78]. One particular class of oxides that have many potential thermoelectric materials are the perovskites, including: $BaSnO_3$ [79], $BaPbO_3$ [80] and $SrTiO_3$ [81]. These materials generally have good

transport properties and with potential for further improvement via doping or nanostructuring.

As a result, oxide based thermoelectric materials are a very active area of research due to their potential benefits [28]. A breakthrough in oxide thermoelectric materials could both reduce the harmful elements currently used to produce thermoelectric materials while simultaneously allowing more widespread application in high temperature, oxidising environments.

The challenge faced by oxide thermoelectric materials is to increase the electrical conductivity whilst simultaneously reducing thermal conductivity. A successful approach to this in the past has been via the use of defective systems.

1.3.4. Defects

There are a wide variety of possible defects for any material [82]. These defects disrupt the periodic structure of the material and impede phonon transmission, lowering thermal conductivity. Since the size of a defect and its dimensionality result in interactions with different wavelength phonons, a wide variety of defect sizes can lead to low thermal conductivities, Figure 1.5 [21].

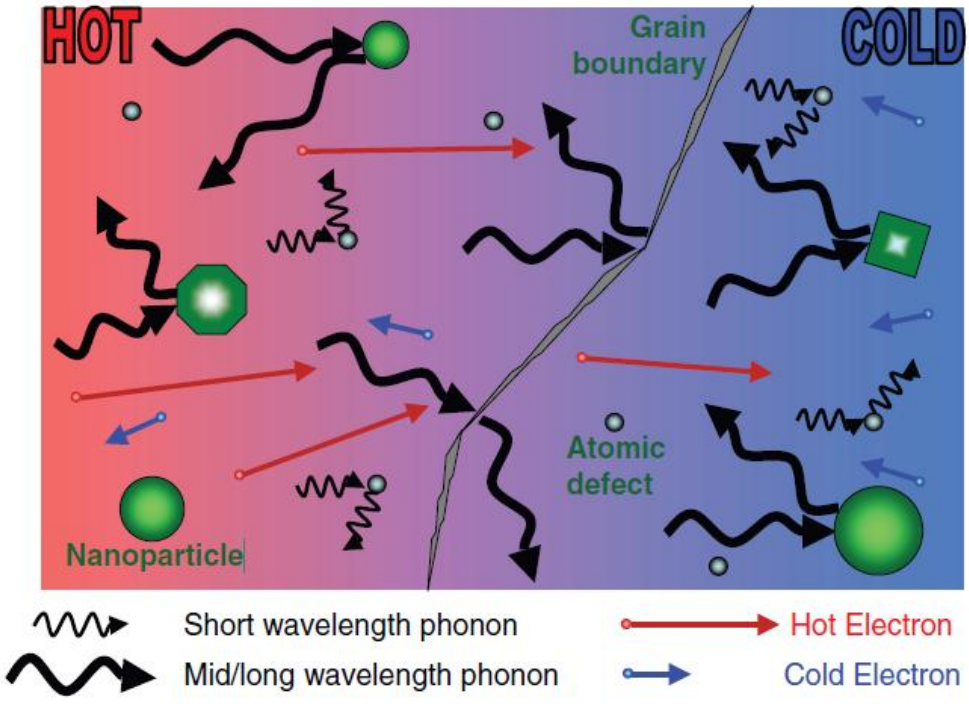

Figure 1.5 Scattering of different wavelength phonons in a thermoelectric material [21].

1.3.4.1. Point defects

Doping a material with different elements is often used to introduce charge carriers or otherwise tune the electronic structure of the material [27]. An additional impact of doping is from the high mass of dopant atoms, which reduces the lattice thermal conductivity in a number of ways [83]. Firstly, the mean phonon velocity is reduced as adding heavy atoms introduces more optical vibrational modes, which have lower group velocities [84]. Secondly, there is an enhancement of phonon scattering, which reduces the amount of energy transported by phonons in a given time period [85].

The thermal conductivity is also impacted by the charge compensating vacancies created by the introduction of dopant atoms. The vacancies also act as phonon scattering sites and will reduce the thermal conductivity in addition to the dopant atoms themselves [18]. The fact that vacancies also scatter phonons means that other materials which can be atom deficient without the addition of dopants, such as the oxygen deficient perovskites, can also be promising thermoelectric materials [86, 87].

1.3.4.2. Surfaces

Surfaces can also have interesting effects on the thermoelectric properties of a material. The surfaces of a material act in a similar way to a grain boundary except that transmittance of phonons across the boundary is impossible and only scattering can occur (except at very short inter-surface distances with very long range interactions). Scattering of phonons from the surface can dramatically reduce thermal conductivity in nanowires, with increased surface roughness reducing the thermal conductivity still further [88]. The exact mechanisms involved are unclear but the presence of surfaces close enough to the bulk in some nanostructured materials means this method could become very important.

1.3.4.3. Grain Boundaries

Grain boundaries are an important type of defect which can have numerous different and complex effects on the thermoelectric properties of a material and may be helpful or detrimental in improving the figure of merit. The simplest way grain boundaries affect the ZT of a material is by scattering phonons, lowering the thermal conductivity [89]. However, depending on the grain boundary and bulk material the presence of grain boundaries can also prevent charge carriers from diffusing and thus lower the ZT.

The importance of the boundary orientation/structure has been highlighted in work on bismuth telluride by Deng et al.[89] which identified different figures of merit depending on which surface is preferentially expressed and hence the packing arrangement and grain boundaries. When bismuth telluride was grown on quartz under different conditions the ratio of the expressed (001) and (015) surfaces changed, this then altered the packing as shown in Figure 1.6. The overall result was that the film with preferential growth on the (015) plane had a ZT of 0.14 and the film with growth on the (001) film had a ZT of 0.54. It is interesting to note that the electrical properties change much more than the thermal conductance between the two samples, revealing how the different grain boundaries present can have different effects on the power factor.

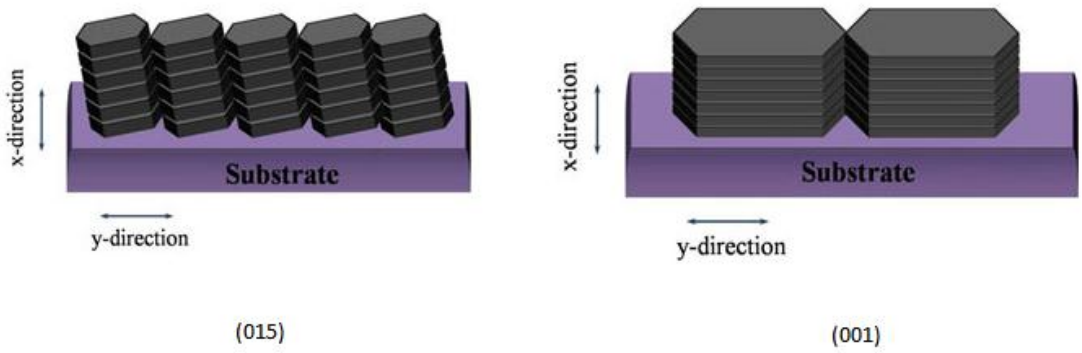

Figure 1.6 Alternative stacking arrangements of bismuth telluride grains [89].

The work by Deng et al.[89] demonstrates the effect of highly ordered grain boundaries which may be considered a type of nanostructuring. A number of other studies have also found that the ZT can be improved with an increase in the number and density of grain boundaries. The studies reveal numerous materials and methods for applying this techniques, including: Gd-doped $CaMnO_3$ [90], lead telluride [91] and skutterudites [92]. The wide selection of material classes within which increasing grain boundaries is an effective technique to improve the figure of merit.

The presence of grain boundaries can also increase the ZT of a material in other ways [93]. An unusual increase in the Seebeck coefficient sometimes occurs at grain boundaries due to energy filtering of the charge carriers by a potential barrier that can also be present [54]. Additionally the presence of randomly orientated grains can improve mechanical properties as cleavage planes do not penetrate through large parts of the material [94]. Caution must be applied when using polycrystalline materials

because a reduction in density of only a few percent below the theoretical maximum can lower the carrier mobility by a few orders of magnitude [95].

1.3.5. Nanostructures

Nanostructured materials use defects in a coherent manner to create larger structures with modified and controllable properties. Much work has focused on the nanostructuring of thermoelectric materials with very promising results [57, 96].

1.3.5.1. Superlattices

Superlattice materials are a promising area of research and have displayed high ZT in recent publications [97]. Superlattice materials are built from arranging grains or layers of one or more materials in a coherent way. The different materials used may impart specific properties to the superlattice; alternatively the boundaries themselves may result impart unusual effects to the overall material.

Boundaries between materials in superlattices can be subtle and result in minimal disruption to the lattice. In these cases the boundary may be considered a domain boundary rather than a grain boundary. Two domains may be of the same material, differing only in the type of atom present at a given site (i.e. the A site of perovskite materials) or the orientation of different groups (tetrahedral tilting in quartz Dauphiné twins). The boundaries between the regions may have unusual electronic properties such as quantum confinement of charge carriers to the boundary plane, resulting in a large increase in the Seebeck coefficient and electrical conductivity [98]. However, superlattices are also capable of increasing the ZT of a material via increased phonon scattering at the boundary, resulting in very high ZTs on the order of ~2 [99].

An example of the power of superlattices is demonstrated by the WSe_2/W layered system. In this structure the thermal conductivity is found to be extremely low at 0.02 W/(m.K) in the direction perpendicular to the layers [100]. An unusual effect was that bombardment by ionic radiation resulted in an increase of thermal conductivity, despite an apparent increase in disorder.

1.3.5.2. Nano-inclusions

Nano-inclusions may be considered an extension of superlattices, differing in that the second material is localised to a smaller area and the way they increase the ZT of the

system. In these systems the electronic properties are slightly reduced but more than compensated for by the enhanced phonon scattering [101]. Indeed, the thermal conductivity is found to be below the alloy limit for many of these materials, indicating the drastic differences that can be achieved compared to simple alloys and solid solutions [101-103].

An early nano-inclusion system was the LAST-m ($AgPb_mSbTe_{m+2}$) material which was first studied in the 1950s. The LAST-m system was originally thought to be a solid-solution type material [21], though later studies revealed the presence of nano-inclusions [104, 105]. Nanoscale inclusions in the LAST-m thermoelectric material display coherent interfaces with the matrix they are imbedded in [104], which has also been observed in other systems [106, 107]. These coherent boundaries act in a similar way to superlattice systems in that they scatter phonons without significantly affecting the electronic properties. The presence of strain around the coherent interfaces seems to be responsible for increased phonon scattering, reducing thermal conductivity well below what is normally achieved by solid solutions alone.

The question of exactly why nano-inclusion materials are so good at scattering phonons was tackled by considering the scattering processes [21, 108, 109]. Phonon scattering around atomic scale defects, chiefly responsible for the reduction of thermal conductivity in alloy systems, follows Rayleigh scattering:

$$\text{scattering} \propto \frac{d^6}{\lambda^4}$$

Equation 1.8

where d is the nano-inclusion diameter and λ is the phonon wavelength. Hence point defects such as dopants and vacancies are effective at scattering small wavelength phonons while the introduction of nano-inclusions with coherent boundaries allows scattering of much longer wavelength phonons. It is thus possible to have a system with a wide range of defect sizes which can induce scattering in phonons of various wavelengths, leading to a drastic reduction of thermal conductivity [110].

1.3.5.3. Nanowires

Nanowires confine the conduction of both electrons and phonons to one dimension. This reduction in dimensionality has a larger effect on the thermal transport properties

than the electrical transport properties [96, 111]. One such system is bismuth telluride one-dimensional heterostructures which display interesting properties dependent on the stoichiometry.

It was shown that the length of a nanowire segment could be carefully controlled based on the ionic concentrations of bismuth and tellurium in the electrolyte solution used during growth [112], opening up routes for finely controlled one-dimensional phonon scattering systems. The coherent boundaries between segments theoretically allow undisrupted electrical conduction while the strain disrupts thermal conduction. Calculations predict exceptional ZT values of up to 14 [113], though currently synthesised materials only achieve a maximum ZT of approximately 1 at low temperatures, possibly due to the polycrystalline nature of the wires synthesised [114].

1.4. Thermoelectric Simulations

Simulations can provide further information when studying thermoelectric materials as well as guide future experimental research. Simulations allow access to the atomic scale processes that generate that macroscale effects seen in experiments and give a deeper understanding of their behaviour/properties [115]. Furthermore, the study of thermoelectric materials in simulations can give indications of which particular features of a material affect the thermoelectric properties and guide experimental design of materials.

1.4.1. Ab Initio Simulations

Ab initio methods derive atomic interactions directly from first principles. There are various levels of ab initio calculations of varying complexity and expense. Ab initio calculations give information on the electronic structure of materials and thus are necessary for calculating the properties pertaining to the power factor, i.e. electrical conductivity and Seebeck coefficient [116].

The predictive power of simulations can be used to quickly and efficiently screen potential thermoelectric materials. DFT calculations on a large range of half-Heusler materials have been used to calculate the electrical properties and optimal doping levels, resulting in candidates for thermoelectric materials [117]. Other DFT work on Mg_2Si looked at the effect of strain on the bulk system and what impact it had on the electrical

properties [118]. In highly doped systems under strain it was found that the maximum in power factor shifted to lower temperature.

The Green-Kubo method is rarely used in ab initio simulations due to the long-time scales required and the difficulty of decomposing the energy into individual atomic contributions, although some progress is being made in this area [119]. However, it is possible to calculate the thermal conductivity via lattice dynamics and the finite displacement method, using the Boltzmann transport equation (BTE). This approach only approximates the anharmonic terms to some low order, whereas dynamic approaches are in principle exact for a given model [120]. Additional problems arise from the small size of the system under study, which makes calculation of thermal conductivity in defective systems challenging. However, more simple systems can be studied.

Work by Molinari et al. studied the oxygen deficient perovskite systems $CaMnO_{(3-\delta)}$ [116]. An interesting feature of this study was that all thermoelectric parameters were calculated. The authors found that the Seebeck coefficient of partially reduced $CaMnO_{2.75}$ increased with increasing temperature, whereas the reverse was found for $CaMnO_3$ and $CaMnO_{2.5}$. The authors also note the importance of differing defect arrangements on the properties. Due to the computational expense the thermal conductivity was only calculated for stoichiometric $CaMnO_3$ (using finite displacements and the BTE equation as implemented in the Phonopy code [121, 122]). Although the ZT did not appear to be improved over the stoichiometric case, this could very well be down to the use of the bulk thermal conductivity in the calculation of the ZT for all stoichiometries.

1.4.2. Classical Simulations

Rather than explicitly calculating electronic behaviour, classical methods approximate interactions between atoms with parameterised equations. The interactions using these potential equations are many orders of magnitude quicker to compute than with ab initio methods, allowing extension to larger time and length scales. The larger scale of classical simulations therefore allows study of thermal transport in the bulk systems as well as systems with large defects and/or low dopant concentrations.

There are several approaches to calculating the thermal conductivity of a system via classical methods [123]. These methods can be broadly classified into static and dynamic approaches. The static approaches generally aim to solve the Boltzmann transport equation (BTE) via a systematic generation of force constants and thus phonon frequencies and then phonon interactions. Dynamic approaches simulate the system at a given temperature using molecular dynamics and measure the resultant thermal conductivity. The dynamic approaches may be further subdivided into equilibrium and non-equilibrium approaches. Equilibrium approaches use fluctuations in the system's heat-flux to calculate thermal conductivity via the Green-Kubo relations [124, 125], whereas the non-equilibrium methods generate a temperature gradient and measure the thermal conductivity directly [126]. A more detailed review of these methods is given in Chapter 3.2.

Shukla et al. performed non-equilibrium molecular dynamics calculations on single crystal and polycrystalline MgO and $Nd_2Zr_2O_7$ [127]. The study aimed to determine the applicability of an MgO and $Nd_2Zr_2O_7$ ceramic in an inert matrix fuel. Although not motivated by thermoelectric applications, the study demonstrates the possibility of grain boundaries and nanostructuring in general in reducing the lattice thermal conductivity. By converting single crystal samples to polycrystalline samples, reductions in lattice thermal conductivity by up to an order of magnitude were achieved for MgO at 300 K, and a reduction of 60% for $Nd_2Zr_2O_7$ at 300 K.

Goh et al. used extensive data to fit interatomic potentials for $SrTiO_3$ [128]. Obtaining good potential parameters for perovskites can be difficult due to the complex nature of the interactions of the transition metals. The thermal expansion of the potential matches closely with experimental data and also has a marked improvement in isothermal compressibility, heat capacity and indeed lattice thermal conductivity. However, the charges used in the model are unusual and are not easily transferrable, making the study of defects challenging. Additionally the RNEMD simulations used may suffer from a small cell cross section [123, 129] and the Green-Kubo calculations may suffer from being averaged over only 2 ns [123]. A further discussion of the importance of these aspects can be found later in Chapter 3.2.

1.4.3. Other Methods

Continuum methods are also available to model the thermoelectric properties of a material. In a continuum model the specific structure of the material is ignored, instead the phonon interactions are computed explicitly based on mathematical models and parameters relating to the material of interest [130, 131]. These models are not particularly suited to defective systems where the character of a point defect or grain boundary is not particularly well captured.

1.5. Aim of this Work

One of the challenges for developing more efficient thermoelectric materials is to identify ways of lowering the thermal conductivity in a reproducible and quantifiable way. Thus there is a need to be able to reliably calculate the thermal conductivity and be able to interpret the data in a way as to offer predictions and give some level of control.

Thus, along with the thermal conductivity, additional information is also sought in order to gain an understanding of the underlying phonon processes. Therefore a dual approach is used whereby thermal conductivity is calculated via both molecular dynamics and lattice dynamics calculations. These approaches may give complementary information about the phonon modes within the system and some indication of the modes most important for thermal conductivity.

Three materials have been chosen which can exhibit various levels of nanostructuring while being structurally distinct. The first system studied is MgO (Chapter 4) which is an ionic material. The bulk thermal conductivity is calculated and compared to experiments before the study is extended to two different grain boundary systems and then finally two different nanostructured systems in order to understand how the increasing complexity of the system impacts the thermal conductivity.

The work is then continued in the covalent silica system (SiO_2) (Chapter 5). Silica may exist in many polymorphs, the most common of which is quartz. The thermal conductivity of quartz is calculated and compared to experiments. The phase change of quartz is likely to impact the thermal conductivity of the material due to change in the structure and therefore the available phonon modes. Further calculations are also

performed for silicalite. Silicalite is a low density zeolite with a large number of environments, which should have a large impact on the thermal conductivity.

Finally the $SrTiO_3$ (STO) system (Chapter 6) is studied which contains a mix of ionic and covalent interactions. The bulk thermal conductivity is once again calculated and then compared to a number of grain boundary systems with varying inter-boundary distances. A series of complex nanostructures of STO are then generated out of ordered arrays of nanocubes and the thermal conductivity is again calculated to determine the effect of different orderings.

With the information obtained from all studies some understanding about the interaction between nanostructure and thermal conductivity may be obtained. This understanding will then allow new materials to be engineered with specific phonon modes which most effectively reduce the thermal conductivity. First the methodologies employed and the underlying theory for these studies will be discussed.

2. Methodology

2.1. Potential Modelling

This work has been conducted using interatomic pair potentials. Pair potentials approximate interatomic forces by using simple parameterised equations rather than solving the full electronic structure of the system. While potential models are less accurate than ab initio methods, larger systems and longer timescales can be simulated. This section outlines the potential methodology that has been used throughout this work.

2.1.1. Born Model of Solids

The Born model of solids considers a crystal lattice to be an infinite array of ions [132]. The lattice energy, U, is the sum of all the interactions between ions:

$$U = \sum_{ij} \frac{q_i q_j}{4\pi\varepsilon_0 r_{ij}} + \sum_{ij} \Phi_{ij}(r_{ij}) + \sum_{ij} \Phi_{ijk}(r_{ijk}) \ldots$$

Equation 2.1

where r_{ij} is the interatomic distance between atoms i and j with charges q_i and q_j; ε_0 is the vacuum permittivity. The first term represents the Coulombic interactions, which remain significant even at large separations. The remaining terms represent the two-body (e.g. van der Waals/bonds) and three-body short-ranged interactions respectively. Higher terms are also possible but are often neglected due to their small contribution, but can be important in molecular systems.

2.1.2. Coulombic Interactions

The Coulombic term in Equation 2.1 represents about 80% of the total interaction energy. The energy of an infinite lattice of point charges, φ, is given by:

$$\varphi = \frac{1}{2} \sum_{|\boldsymbol{n}|=0}^{\infty\ \prime} \sum_{i=1}^{N} \sum_{j=1}^{N} \frac{q_i q_j}{4\pi\varepsilon_0 \left| \boldsymbol{r}_{ij} + \boldsymbol{n\lambda} \right|}$$

Equation 2.2

where $\boldsymbol{\lambda}$ represents the set of lattice vectors corresponding to the periodicity of the lattice and $\boldsymbol{n}$ is a vector of integers used to generate the periodic images of the unit cell. The first summation contains a prime to indicate that $i = j$ is ignored in the summation when $n = 0$.

The r^{-1} nature of Equation 2.2 means that the Coulombic part of the lattice energy is slow to converge and long range. A number of methods have been developed to ensure the calculation is convergent.

2.1.2.1. Ewald Summation

The Ewald summation is the most widely implemented method for calculating the Coulombic contribution to the lattice energy [133, 134]. In the Ewald method the coulomb equation is split into long-range (φ_1), short-range (φ_2) and self-interaction (φ_3) components:

$$\varphi = \varphi_1 + \varphi_2 + \varphi_3$$

Equation 2.3

With this approach each point charge is considered as being surrounded by a diffuse charge of equal magnitude but opposite sign. A Gaussian charge density, $\rho_i(\boldsymbol{r})$, is often used:

$$\rho_i(\boldsymbol{r}) = \frac{q_i \alpha^3}{\pi^{\frac{3}{2}}} \exp(-\alpha^2 \boldsymbol{r}^2)$$

Equation 2.4

where the diffusivity of the Gaussian is determined by the α parameter and $\boldsymbol{r}$ is the point in space relative to the centre of the charge distribution. As the diffuse Gaussian charge is of opposite sign, the interaction tends quickly to zero with increasing distance and so the interaction has become short-ranged and may be calculated easily in real space:

$$\varphi_2 = \frac{1}{2} \sum_{|\boldsymbol{n}|=0}^{\infty\ \prime} \sum_{i=1}^{N} \sum_{j=1}^{N} \frac{q_i q_j}{4\pi\varepsilon_0} \frac{\operatorname{erfc}\left(\alpha \left| \boldsymbol{r}_{ij} + \boldsymbol{n}\boldsymbol{\lambda} \right|\right)}{\left| \boldsymbol{r}_{ij} + \boldsymbol{n}\boldsymbol{\lambda} \right|}$$

Equation 2.5

The interaction of each charge with its own Gaussian counterpart of opposite sign is omitted. The complementary error function is given in Equation 2.6.

$$\mathrm{erfc}(x) = \frac{2}{\sqrt{\pi}} \int_{x}^{\infty} \exp(-t^2)\, dt$$

Equation 2.6

To compensate for the added Gaussian charge distribution of opposite sign, a second Gaussian charge distribution of the same sign is added. In this case the interaction is long-ranged, but the energy tends to a finite value as r_{ij} tends to zero; thus it can be represented as a Fourier series in reciprocal space. The value of φ_1 can then be determined by summing the Fourier components in reciprocal space:

$$\varphi_1 = \frac{1}{2} \sum_{k \neq 0} \sum_{i=1}^{N} \sum_{j=1}^{N} \frac{1}{\pi V} \frac{q_i q_j}{4\pi\varepsilon_0} \frac{4\pi^2}{k^2} \exp\left(-\frac{k^2}{4\alpha^2}\right) \cos\left(\boldsymbol{k} \cdot \boldsymbol{r}_{ij}\right)$$

Equation 2.7

where V is the cell volume and $\boldsymbol{k}$ is a vector in reciprocal space, given by Equation 2.8 and Equation 2.9.

$$\boldsymbol{k} = \frac{2\pi \boldsymbol{n}}{\boldsymbol{\lambda}}$$

Equation 2.8

$$k = |\boldsymbol{k}| = \sqrt{\sum_{i=1}^{n} k_i^2}$$

Equation 2.9

A more complete discussion of the reciprocal lattices may be found elsewhere [135]. A visual representation of the Ewald method is shown in Figure 2.1.

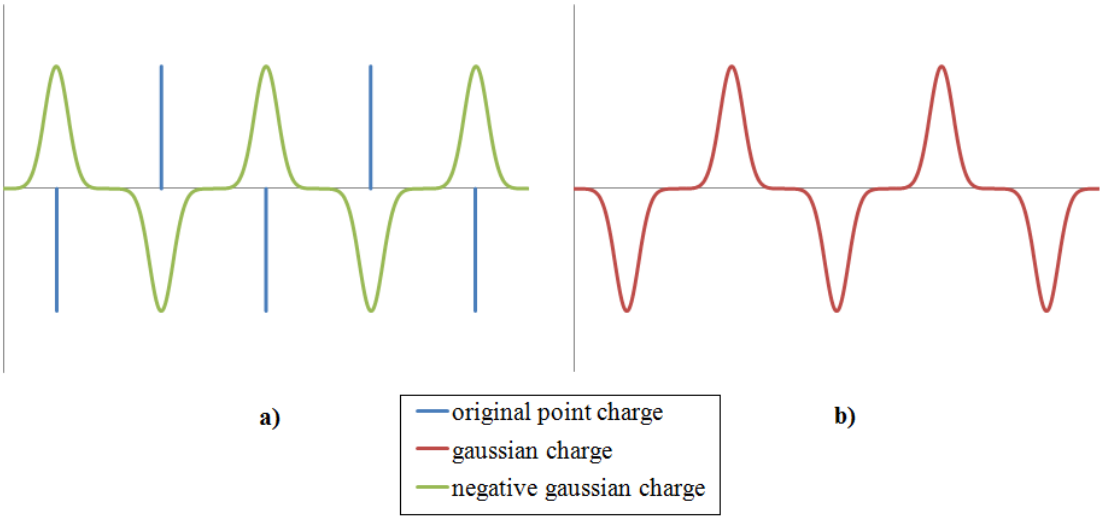

Figure 2.1 a) The real space φ_2 component of the calculation and b) the reciprocal φ_1 component of the calculation.

In Equation 2.7 (the long-ranged φ_1 contribution) the term for $k = 0$ can be neglected if the charge of the simulation cell is zero. Furthermore, it must be noted that the φ_1 long-ranged contribution to the summation includes an interaction of the point charge with its own Gaussian counterpart; therefore a self-interaction correction is required:

$$\varphi_3 = -\frac{\alpha}{\sqrt{\pi}} \sum_{k=1}^{N} \frac{q_k^2}{4\pi\varepsilon_0}$$

Equation 2.10

The net result of the Ewald summation is that the Coulombic interaction is split into a short-range component which is rapidly convergent in real space, and a long-range component which is rapidly convergent in reciprocal space. The splitting of work between real and reciprocal components can be controlled by adjusting the diffusivity of the compensating charge, α. A more diffuse charge screens more of the real space interaction (which therefore converges more rapidly with distance) but requires a larger Fourier series in reciprocal space.

The Ewald method may also be extended to include terms for charged cells, dipoles and multipoles [136].

2.1.2.2. FFT-Based Ewald Summation

The drawback of the Ewald method is the slow calculation of the Fourier transforms [137], to speed calculation a number of methods have been developed: Particle-Particle Particle-Mesh (PPPM/P3M) [138, 139], Particle Mesh Ewald (PME) [140] and Smooth Particle Mesh Ewald (SPME) [141]. These accelerated methods are all based on the premise of reassigning the long range component of the Coulombic interaction from the particles to the nodes of a 3D mesh. The property of equally spaced nodes on the mesh allows use of Fast Fourier Transforms (FFT), which greatly accelerates calculation.

2.1.2.3. Parry Summation

For systems with two-dimensional periodicity it is more common for the Parry summation to be used than the Ewald summation. The Parry summation is a modification of the Ewald summation that considers the crystal to be built from a series of two-dimensional planes. Thus the vectors in the summation are split into in-plane and cross-plane vectors and treated separately. With this approach it can no longer be guaranteed that each plane is charge neutral and so the term involving $k = 0$ must also be considered. A more complete overview of the Parry summation may be found elsewhere [142-144].

2.1.3. Short-Range Interactions

Short-range must also be considered when evaluating the energy and forces. The short-range contribution is dominated by two interactions. The first is Pauli repulsion which arises from the overlap of electron clouds at small interatomic separations. As the electron clouds overlap some are forced into higher energy states as no two electrons can have identical quantum numbers, leading to a large repulsion at very short range. The second dominating contribution is from the London dispersion forces, also known as the instantaneous dipole-induced dipole forces, which tend to be attractive over medium range. Both of these contributions tend quickly to zero with increasing distance.

Often, short-range interactions are only included for anion-anion and anion-cation pairs, with short range cation-cation interactions neglected. The reason for this is that the electrons present on cations are very tightly bound and thus the short-range effects of the anion-anion interaction will dominate [145].

A number of parameterised potential functions have been developed to describe these interactions, usually containing an attractive term and a repulsive term. The differences between the potential forms tends to be related to the curvature of the attraction/repulsion, therefore no one potential form can be said to be better or worse than the others as different functions may be more appropriate for different systems; i.e. "hard" or "soft" repulsion.

The accuracy and reliability of any simulation is heavily dependent on the parameters used in the potential equations. These may be fitted to experimental data or ab initio simulations, which must also be accurate and reliable.

2.1.3.1. Lennard-Jones Potential

One of the earliest equations developed for short-range interatomic interactions was the Lennard-Jones potential [146, 147]. This potential is fairly simple and has gained widespread use due to its effectiveness and ease of computation:

$$U(r_{ij}) = \varepsilon\left[\left(\frac{r_{\mathrm{m}}}{r_{ij}}\right)^{12} - 2\left(\frac{r_{\mathrm{m}}}{r_{ij}}\right)^{6}\right] = 4\varepsilon\left[\left(\frac{\sigma}{r_{ij}}\right)^{12} - \left(\frac{\sigma}{r_{ij}}\right)^{6}\right]$$

Equation 2.11

where r_{ij} is the interatomic distance, ε is the energy at the minimum of the energy well, r_{m} is the position of the energy well minimum and σ is the finite distance where the potential energy is zero. These quantities are visualised on the potential curve in Figure 2.2.

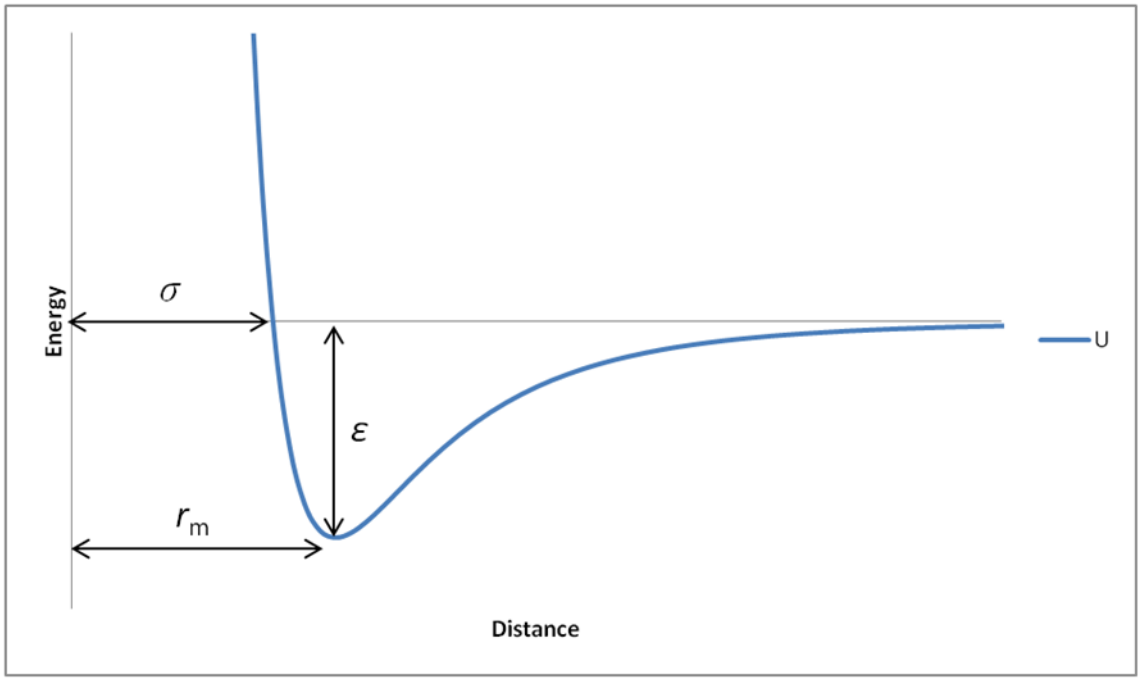

Figure 2.2 Lennard-Jones potential with parameters.

The Lennard-Jones potential may be recast into a repulsive term and an attractive term:

$$U(r_{ij}) = \frac{A_{ij}}{r_{ij}^{12}} - \frac{B_{ij}}{r_{ij}^{6}}$$

Equation 2.12

A_{ij} and B_{ij} are given by:

$$A_{ij} = \varepsilon r_{\mathrm{m}}^{12} = 4\varepsilon\sigma^{12}$$

Equation 2.13

$$B_{ij} = 2\varepsilon r_{\mathrm{m}}^{6} = 4\varepsilon\sigma^{6}$$

Equation 2.14

A_{ij}/r_{ij}^{12} is repulsive and very short range due to the r^{-12} term, whereas the $-B_{ij}/r_{ij}^{6}$ term is attractive and dominates at medium distances due to the r^{-6} term. The r^{-6} nature of the attractive term is justified as it arises out of the dipole-dipole dispersion interaction of electron clouds [148] (higher terms are also possible such as r^{-8} which represents dipole-quadrupole interactions). There is no physical justification for the r^{-12} term and it is simply a mathematically convenient way to model the repulsion as r^{-12} is the square of r^{-6}.

The A_{ij} and B_{ij} parameters are fitted for different systems and are related to features in the potential energy curve and are chosen to best reproduce the physical properties of interest for any given material.

The Lennard-Jones potential has had great success for modelling simple neutral particles such as the noble gases [149-152].

2.1.3.2. Mie Potential

The Lennard-Jones potential is a particular case of a more general class of potentials known as the Mie potential [153]:

$$U(r_{ij}) = \left(\frac{n}{n-m}\right)\left(\frac{n}{m}\right)^{m/(n-m)} \epsilon \left[\left(\frac{\sigma}{r_{ij}}\right)^{n} - \left(\frac{\sigma}{r_{ij}}\right)^{m}\right]$$

Equation 2.15

where ϵ is the well depth and σ is the value of r_{ij} where $U(r_{ij})$ is zero. Thus the Mie potential is equivalent to the conventional Lennard-Jones potential when $n = 12$ and $m = 6$, but is much more flexible.

2.1.3.3. Buckingham Potential

A slightly more complex potential equation which is commonly used is the Buckingham potential [154] which replaces the inverse twelfth power repulsion with an exponential repulsion which can better describe the Pauli repulsion:

$$U(r_{ij}) = A_{ij} e^{\left(-\frac{r_{ij}}{\rho_{ij}}\right)} - \frac{C_{ij}}{r_{ij}^{6}}$$

Equation 2.16

where A_{ij} is now different to the one used in the Lennard-Jones potential and along with ρ_{ij} is related to the ionic size and "hardness" of the interacting species. Once again the r_{ij}^{-6} term is the attractive portion, controlled by the parameter C_{ij}.

As the Buckingham potential has three adjustable parameters, as opposed to the two parameters available to the 12-6 Lennard-Jones equation, it is more flexible and can be applied to a larger range of systems. However, the exponential term is more

computationally demanding to compute than the power term used in the Lennard-Jones potential.

One property of the Buckingham potential to be aware of is that the r_{ij}^{-6} term becomes dominant at extremely short distances, causing the function to turn over and become attractive where it should be purely repulsive. This is particularly problematic in high temperature molecular dynamics simulations where particle collisions may overcome the repulsive barrier resulting in unphysical particle fusion.

2.1.3.4. Morse Potential

The Morse potential [155] introduces a parameter related to the curvature of the energy well:

$$U(r_{ij}) = D_{ij}(1 - e^{[-B_{ij}(r_{ij}-r_0)]})^2 - D_{ij}$$

Equation 2.17

where r_0 is the interatomic separation at the energy well minimum, D_{ij} is the well depth and B_{ij} is related to the curvature of the well. B_{ij} can be calculated from the bond vibrational frequency by:

$$B_{ij} = \omega \sqrt{\frac{\mu}{2D_{ij}}}$$

Equation 2.18

where μ is the reduced mass and ω is the bond vibrational frequency. ω can also be related to the spring constant, k, of the bond:

$$\omega = \sqrt{\frac{k}{\mu}}$$

Equation 2.19

The Morse potential has historically been used to model covalent bonds as the parameters required can be obtained from structural and spectroscopic data. As these parameters contain within them contributions from all the interactions between the two atoms, it is sometimes necessary to subtract some portion of the Coulombic contribution

to retain the physical origin of the potential (which includes all interactions when parameters are obtained from experiment).

2.1.3.5. Pedone Potential

A development of the Morse potential is the Pedone potential [156] which is simply the Morse potential with the addition of Lennard-Jones type repulsion. The addition of the extra repulsive term gives an extra parameter which can allow better tuning of the repulsive properties of the potential at very short distances:

$$U(r_{ij}) = \left(D_{ij}(1 - e^{[-B_{ij}(r_{ij}-r_0)]})^2 - D_{ij}\right) + \frac{A_{ij}}{r_{ij}^{12}}$$

Equation 2.20

2.1.3.6. Tabulated Potentials

All of the above potentials have varying complexity in terms of computation time. However, by using tabulated energies and forces as a function of distance computed beforehand, the computationally demanding exponential and/or power terms are removed and replaced with a simple linear/spline interpolation.

The tabulated energies/forces need not necessarily be generated by the simulation code itself. Externally generated tables can be made with more complex potential equations not originally available within the code, or generated directly from ab initio simulations, avoiding parameterised equations altogether.

While it is possible for tabulated potentials to bring great benefits in terms of computational speed, one must be very careful when implementing this technique. To avoid spurious interpolations (and hence energy/force) a high density of points must be present in the table. However, having too many points will lead to excessive memory usage and may in fact be detrimental.

2.1.3.7. Bonded Interactions

Bonded interactions occur where the interaction is between two specific atoms, and no others. This type of interaction is most often used in molecular species in order to reproduce covalent bonds, but can also appear in a mixed ionic-covalent system. For

example, the CO_3^{2-} anion requires a bonded interaction between the carbon and oxygen atoms, but not between the carbon and other oxygen atoms within the system.

The bonded interaction may take many forms. A simple form would be a harmonic bond specified by:

$$U(r_{ij}) = \frac{1}{2}K(r_{ij} - r_0)^2$$

Equation 2.21

where K is the spring constant and r_0 is the equilibrium bond distance.

2.1.3.8. Many-Body Interactions

In addition to the bonded interactions outlined above, covalently bonded systems may require additional interactions involving three or more bodies to restrict structures to their correct form. For example the carbonate (CO_3^{2-}) ion is planar due to the sp^2 hybridisation.

To keep fragments in the correct conformation, an energy penalty is applied so as to restore the structure to its equilibrium position. Many expressions for the energy penalty are possible; a simple harmonic expression is given by:

$$U(\theta_{ijk}) = \frac{1}{2}K_{ijk}(\theta_{ijk} - \theta_0)^2$$

Equation 2.22

where K_{ijk} is a spring constant related to the stiffness of the angle, $\theta_{ijk}$is the current angle and θ_0 is the equilibrium angle. While a simple harmonic three-body interaction is useful for keeping an equilibrium angle between three atoms, it is not very useful for arrangements of four or more atoms, where a torsional term may be more appropriate. Again there are many forms of torsional equations; one example is given in Equation 2.23.

$$U(\phi_{ijkl}) = K_{ijkl}[1 - \cos(N\phi_{ijkl})]$$

Equation 2.23

where K_{ijkl} is twice the barrier height, ϕ_{ijkl} is the torsion angle and N is the periodicity of the torsion. When N is set to 2 this expression has minima at either 0° or 180°.

Often many-body terms are present in systems with molecular units. However, the interactions can also be represented to some degree by a system of pair potentials.

2.1.4. Ionic Polarisability

The electron cloud of an atom is polarisable and can generate dipoles, which will have a significant effect on the interatomic interactions. Many potential functions include terms for the attractive dispersion forces that arise out of instantaneous dipole-induced dipole interactions. It is also possible for a species to have a permanent dipole created by neighbouring species with a large electronegativity disparity. These interactions may also be treated in a classical framework by either the shell model or via partial charges.

2.1.4.1. Shell Model

Ions are often polarisable, and these effects should also be represented in simulation. One of the most common method is the "shell model" of Dick and Overhauser [157]. In the shell model the charged ion is divided into two components; a core carrying a positive charge and all of the mass, and a massless shell with some negative charge. The core and shell both carry a charge but are Coulombically screened from each other and are instead permanently linked together by a simple spring:

$$U(r_{ij}) = \frac{1}{2!}K_2 r_{core-shell}^2 + \frac{1}{4!}K_4 r_{core-shell}^4$$

Equation 2.24

where the strength of the springs is governed by K_2 and K_4. However the second term can often be ignored except in rare cases where it is required to avoid unphysical core-shell separations. Thus the spring constant is related to the free ion polarisability (α) and the charge on the shell (Y) by:

$$\alpha = \frac{1}{4\pi\varepsilon_0}\frac{Y^2}{K}$$

Equation 2.25

It is most common for the shell model to be used on anions as their valence electrons are less closely bound than in cations. In this case the shell can be thought of as the polarisable electron cloud, with its position being allowed to deviate from that of the core, as shown in Figure 2.3. As the shell represents the electron cloud it is usual to

have all the short-range van der Waals interactions attributed to the shell rather than the core.

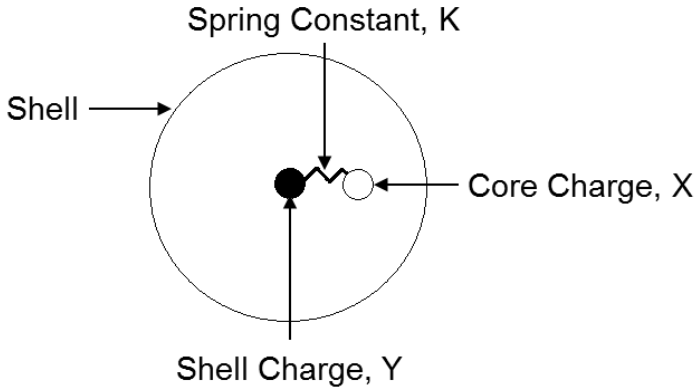

Figure 2.3 The shell model.

When using the shell model in molecular dynamics care must be taken to avoid the shell obtaining unphysical velocities. There are two main approaches to doing this, either by optimising the position of the shells at each step [158], or by assigning a small mass to the shell [159, 160]. By dividing ions into two species the Coulombic calculation becomes much more complex, and the addition of the spring between the core and shell also adds a small calculation penalty.

2.1.4.2. Partial Charge Model

An alternative method to the shell model is to use partial charges on the ions, rather than formal charges. This approach can give a collection of atoms the correct dipole moment without the independent species being polarisable. This approach is popular for organic systems which contain a large permanent dipole in their covalent bonds, but has also been applied to inorganic systems where the bonding is also partially covalent. This method requires no additional computational resource as it only requires a modification to the atomic charges.

2.1.5. Potentials Used in this Work

The magnesium oxide potential used in this work was developed specifically for thermal conductivity calculations [127] and is of the Buckingham form, Table 2.1.

Species	Charge
Mg	1.7
O	-1.7

Interaction	A (eV)	ρ (Å)	C (eV.Å^6)
O-O	35686.18	0.201	32.0
Mg-O	929.69	0.29909	0.0

Table 2.1 MgO potential.

The potential used for silica calculations is the well-known BKS potential [161, 162], also of the Buckingham form, Table 2.2.

Species	Charge
Si	2.4
O	-1.2

Interaction	A (eV)	ρ (Å)	C (eV.Å^6)
O-O	1388.7730	0.3623	175.0
Si-O	18003.7572	0.2052	133.5381

Table 2.2 SiO_2 potential.

The potential used for STO is again of the Buckingham form and is known as the Teter potential [163], Table 2.3.

Species	Charge
Sr	1.2
Ti	2.4
O	-1.2

Interaction	A (eV)	ρ (Å)	C (eV.Å^6)
O-O	1844.7458	0.3436	192.58
Sr-O	14566.637	0.2450	81.773
Ti-O	23707.909	0.1856	14.513

Table 2.3 STO potential.

2.2. General Simulation Methodology

A number of general methodologies are often employed in the study of crystal systems which make the calculations more tractable and/or accurate.

2.2.1. Periodic boundary conditions

Real crystals have finite bounds at surfaces/interfaces, but these are often far apart at the atomic scale and thus a crystal may be considered as an infinite array of ordered atoms. Calculating the properties of such a system is not tractable and thus techniques must be used to simplify the problem.

Periodic Boundary Conditions (PBCs) exploit the translational symmetry found in crystals by connecting the simulation cell to itself via its opposing faces, Figure 2.4. This allows the periodic passage of both particles and interactions, thereby approximating an infinite lattice. While an artificial periodicity is induced, the size of the system inside the boundaries can be chosen to minimise the impact of the artificial periodicity.

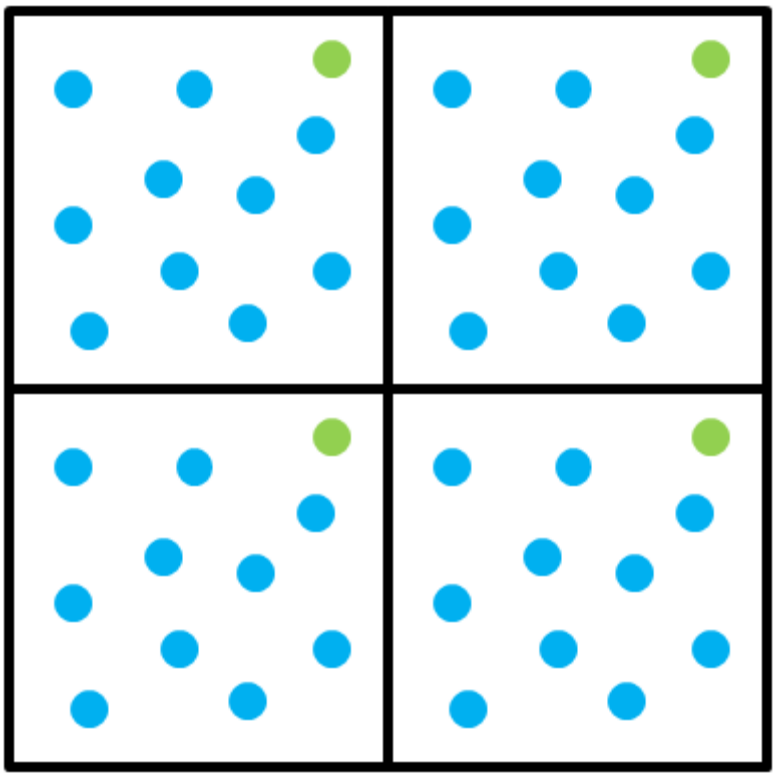

Figure 2.4 Example of a system under 2D PBCs.

PBCs reproduce the environment at the centre of pure crystals where the effect of surfaces and defects is negligible. In molecular dynamics simulations, a simulation cell many times larger than a single unit cell is used to allow the system to explore more disordered states introduced by the kinetic motion of particles. This is vitally important for some properties such as diffusion, where diffusion mechanisms may require several unit cells to operate correctly.

Other dynamical properties such as thermal expansion, heat capacity and thermal conductivity are also better represented by larger simulation cells. The vibrational modes present in a simulated system can be artificially limited by small simulation cells as only the modes with wavelength smaller than the simulation cell are allowed, leading to spurious values for these properties.

2.2.2. Short-Range Cutoffs

The short-range interactions detailed in Chapter 2.1.3 rapidly converge towards zero; therefore it is unnecessary to evaluate the potential at long distances as the contribution to the energy and force is negligible. When a simple cutoff is applied to the potential, all

interactions above the cutoff are set to zero with no compensation for the sharp discontinuity in energy and forces. This approach has been used throughout this work.

While it is usually acceptable to have a simple cutoff with a very small discontinuity, some simulation artefacts may occur as atoms move in and out of the cutoff distance, leading to spurious energy and force values. To compensate a number of methods have been developed to make the discontinuity smooth.

2.2.2.1. Potential Shifting

The most obvious method of removing the discontinuity is to shift the function so that the value at the cutoff is zero. If this is naively performed on just the energy function then the first derivative will not be zero, and so must be performed initially on the first derivative and then on the energy function [164]. An example for the Lennard-Jones potential is given by:

$$U(r_{ij}) = \frac{A_{ij}}{r_{ij}^{12}} - \frac{B_{ij}}{r_{ij}^{6}} + \alpha r_{ij} + \beta$$

Equation 2.26

where α is chosen so that the first derivative at the cutoff is zero and β is chosen so that the energy of the new function at the cutoff is also zero. Force and energy values above the cutoff are then set to zero as before, but with the benefit that both now transition smoothly to zero at the cutoff.

More advanced switching functions are also available, based on any function that can be made to vary smoothly between one and zero over a given range. Potential shifting has not been used in this work.

2.2.2.2. Minimum Image Convention

The minimum image convention states that the cutoff should be no larger than half the shortest cell vector, displayed in Figure 2.5. The minimum image convention thus prevents a particle interacting twice with another particle which may lead to spurious vibrational effects.

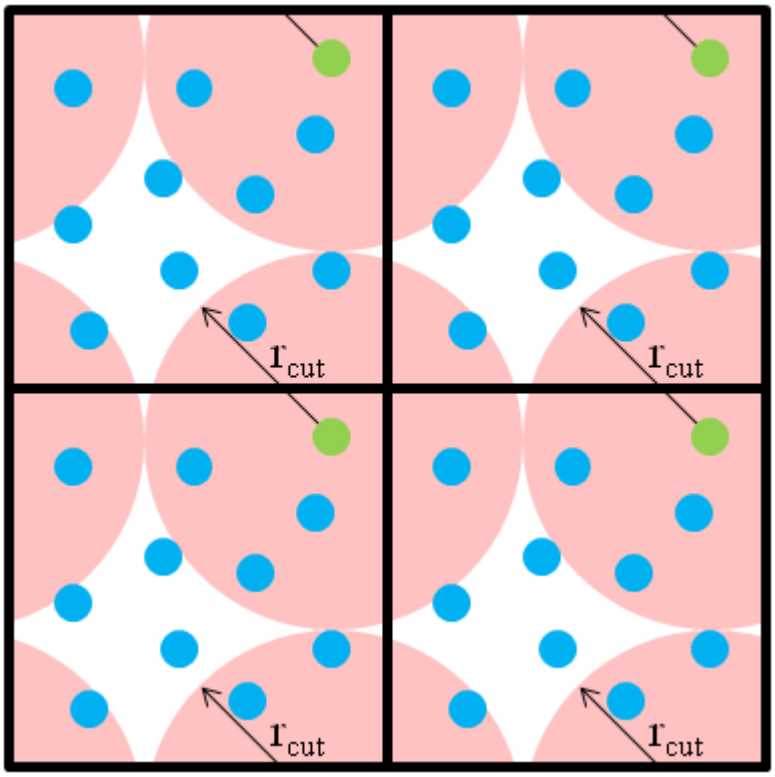

Figure 2.5 The minimum image convention within PBCs.

An additional advantage of the minimum image convention is that an algorithm for generating interatomic distances need only check each pair once as it is guaranteed they can only be within the cutoff in one direction.

2.3. Energy Minimisation

Energy minimisation seeks to find the lowest energy configuration of a system. While energy minimisation is extremely useful, there are a few important points to consider:

1. Initial configuration – a starting configuration is required, preferably near the global energy minimum.
2. Local minima – energy minimisation techniques typically locate the nearest minima, which may not necessarily be the global minimum.
3. Vibrational modes – energy minimised structures can be considered to be at 0 K, neglecting even zero point vibrations. This can cause difficulties when a structure only present at high temperatures is to be studied.

This work has primarily used the METADISE code [165] for energy minimisation, but under some situations the energy minimisation features of the molecular dynamics code

LAMMPS [166] have also been used. The algorithms outlined below are general and may also be applied when the interatomic forces are generated from other methods.

2.3.1. Lattice Energy

All energy minimisation strategies function by moving the atoms until the total force (F) acting on them is zero:

$$F = -\frac{\delta U(\boldsymbol{r})}{\delta \boldsymbol{r}} = 0$$

Equation 2.27

where U is the energy and $\boldsymbol{r}$ is the equilibrium coordinates. Energy minimisation is often an iterative approach and seeks the energy minimum by reducing the energy at each step. The energy of the system can be expressed as a Taylor expansion with respect to atomic coordinates, $\boldsymbol{r}$:

$$U(\boldsymbol{r} + \delta \boldsymbol{r}) = U(\boldsymbol{r}) + \frac{\delta U(\boldsymbol{r})}{\delta \boldsymbol{r}} \delta \boldsymbol{r} + \frac{1}{2!} \frac{\delta^2 U(\boldsymbol{r})}{\delta \boldsymbol{r}^2} \delta \boldsymbol{r}^2 + \mathcal{O}(\delta \boldsymbol{r}^3)$$

Equation 2.28

where the first term is the lattice energy at the minimum, with subsequent terms describing higher derivatives with respect to displacement. It is usual for energy minimisation techniques to use the first and second derivatives. The higher derivatives, denoted by $\mathcal{O}(\delta \boldsymbol{r}^3)$, are often neglected.

In Equation 2.28 and those to follow, $\boldsymbol{r}$ is a $3 \times N$ matrix where N is the number of atoms and the 3 is due to the degrees of freedom. The use of a matrix here allows the minimisation algorithms to act globally, ensuring all degrees of freedom are minimised simultaneously.

2.3.2. Minimisation Algorithms

2.3.2.1. Steepest Descent

The steepest descent [134] (or gradient descent) method is the simplest algorithm to both understand and implement. Steepest descent is based on using the gradient of the energy function, which is related to the force:

$$\boldsymbol{g}_n = \frac{\delta U}{\delta \boldsymbol{r}_n}$$

Equation 2.29

$$\boldsymbol{F}_n = -\boldsymbol{g}_n$$

Equation 2.30

$$|\boldsymbol{F}_n| = \sqrt[2]{\sum_{i=1}^{n} F_i^2}$$

Equation 2.31

$$\widehat{\boldsymbol{F}}_n = \frac{\boldsymbol{F}_n}{|\boldsymbol{F}_n|}$$

Equation 2.32

where $\boldsymbol{F}$ is the force, $\widehat{\boldsymbol{F}}_n$is the force unit vector, $\boldsymbol{g}_n$ is the gradient of the energy and n denotes the iteration. In steepest descent the positions of the atoms are then updated by:

$$\boldsymbol{r}_{n+1} = \boldsymbol{r}_n + \alpha_n \widehat{\boldsymbol{F}}_n$$

Equation 2.33

where a_n is the minimisation step size. The choice of a_n can be either a default scaling; i.e. increase step size by a given factor if the step direction results in a decrease of energy, or reduce the step size by another factor if the energy is found to increase. This method is computationally inexpensive in calculating step size, but may require more steps to find the minimum. An alternative method involves conducting computationally expensive line searches to find the minimum in the given direction, but with the advantage of taking fewer steps to converge.

Steepest descent is very efficient for systems where a few large interatomic forces dominate the interactions, as this dictates the direction of the gradient. However, one significant drawback of this method is that when line searches are used the new direction of minimisation is orthogonal to the previous direction, making minimisation in narrow valleys on the energy landscape highly inefficient.

2.3.2.2. Conjugate Gradient

The conjugate gradient method [167] is a more advanced variant of the steepest descent method, where the step size and direction is modified after the first iteration to include information from previous iterations. In conjugate gradient minimisation, the direction vector is given by:

$$\boldsymbol{F}_n = -\boldsymbol{g}_n + \gamma_n \boldsymbol{F}_{n-1}$$

Equation 2.34

$$\gamma_n = \frac{\boldsymbol{g}_n \cdot \boldsymbol{g}_n}{\boldsymbol{g}_{n-1} \cdot \boldsymbol{g}_{n-1}}$$

Equation 2.35

here γ_n is a scalar coefficient which is related to the proportion of the previous gradient that should be used to correct the next gradient. Several variants exist for computing γ_n which may perform better under different conditions.

Equation 2.33 and Equation 2.34 are used again to update positions, where a_n is computed with a line search. This approach cannot be used for the first iteration, for which standard steepest descent is used instead.

The advantage gained by the conjugate gradient method over steepest descent is that it does not oscillate along narrow valleys. An additional property of the conjugate gradient method is that for a quadratic function of M variables, the minimum value will be found in M steps [167].

2.3.2.3. Newton-Raphson

Both steepest descent and conjugate gradient are considered first-order minimisation algorithms as they only employ information about the gradient of the energy. By also using second derivatives information about the change of gradient can also be included. Such methods are called second-order, of which Newton-Raphson [168] is the simplest.

The Newton-Raphson method requires calculation of the second derivative matrix (called the Hessian), which is then inverted:

$$\boldsymbol{W}_n = \left(\frac{\delta^2 U}{\delta \boldsymbol{r}_n^2}\right)^{-1}$$

Equation 2.36

The positions are then updated by:

$$\boldsymbol{r}_{n+1} = \boldsymbol{r}_n - \boldsymbol{g}_n \boldsymbol{W}_n$$

Equation 2.37

Due to the nature of quadratic equations (where the second derivative is a constant) the Newton-Raphson method can locate the minimum in a single step. This is called the harmonic approximation and holds near the energy minimum, but not far from the minimum, where the Newton-Rapshon method may become unstable.

The Newton-Raphson method requires calculation and inversion of the Hessian matrix at every iteration, which is a very computationally expensive operation. To counteract these issues it is common to use a more robust minimiser to approach the minimum, before Newton-Raphson is used to locate the minimum in one or two iterations.

2.3.2.4. Quasi-Newton Methods

Quasi-Newton methods [169] aim to accelerate the Newton-Raphson minimisation by avoiding calculation of the inverse Hessian matrix at each iteration. Instead, the inverse Hessian matrix is built over successive iterations:

$$\lim_{n\to\infty} \boldsymbol{W}_n = \left(\frac{\delta^2 U}{\delta \boldsymbol{r}_n^2}\right)^{-1}$$

Equation 2.38

There exists a multitude of ways to perform the update including DFP [170] and BFGS [171-174].

2.3.2.5. FIRE minimisation

Energy Minimisation has also been performed by molecular dynamics quenching where the thermostat is set to zero Kelvin to remove all kinetic energy as it is converted from potential energy. An advanced form of this type of minimisation is known as the FIRE minimiser (Fast Inertial Relaxation Engine) [175].

The FIRE minimiser calculates the forces on a per-atom basis and then allows the positions to change based on a simple molecular dynamics time integrator, with a few added conditions. The basic algorithm is outlined below:

1. Calculate $\boldsymbol{r}$, $\boldsymbol{F}$ and $\boldsymbol{v}$ with any MD integrator. Check for convergence,
2. Calculate $P = \boldsymbol{F} \cdot \boldsymbol{v}$
3. Set $\boldsymbol{v} \rightarrow (1-\alpha)\boldsymbol{v} + \alpha\widehat{\boldsymbol{F}}|\boldsymbol{v}|$
4. If $P > 0$ and the number of steps since P was negative is larger than N_{min}, increase the timestep $\Delta t \rightarrow \min(\Delta t f_{inc}, \Delta t_{max})$, and decrease $\alpha \rightarrow \alpha f_{\alpha}$,
5. If $P \leq 0$, decrease the timestep $\Delta t \rightarrow \Delta t f_{dec}$, remove velocities $\boldsymbol{v} \rightarrow 0$ and set $\alpha \rightarrow \alpha_{start}$,

where $\boldsymbol{F}$ is the force, $\widehat{\boldsymbol{F}}$ is the unit vector of the force, $\boldsymbol{v}$ is the velocity and $|\boldsymbol{v}|$ denotes the absolute value of the velocities. α is a scaling factor which balances the contribution from the velocity and from the direction the force is acting in. When P is below zero the minimisation has reached a minimum in that direction. Once this occurs the velocities are reset to zero and a time latency of N_{min} is allowed before the timestep and balancing factor are allowed to be adjusted, ensuring some inertia is allowed to accumulate in the minimising direction.

The recommended parameters for any simulation are $N_{min} = 5$, $f_{inc} = 1.1$, $f_{dec} = 0.5$, $\alpha_{start} = 0.1$ and $f_{\alpha} = 0.99$. The adjustable parameter of $\Delta t_{max}$is usually set at ~10x the usual MD timestep. One issue to be careful of is that the algorithm assumes all degrees of freedom to be comparable and hence the velocities should be on the same scale; this can be approximated by setting all atom masses equal. The mass of the species is unimportant for energy minimisation as it only has an effect on the accelerations and not the forces or potential energy.

The FIRE minimiser gives advantages over steepest descent and conjugate gradient in that it uses more of the previous information to guide the minimisation to the minimum. The advantage over the Newton-Raphson method is a large reduction in storage requirements and reduction in computation time as the inverse Hessian is not required.

In this work the FIRE minimiser has primarily been used to minimise large grain boundary systems in conjunction with a few constant pressure Newton-Raphson iterations.

2.3.3. Constant Pressure Minimisation

As energy minimisation of atomic coordinates occurs it is also possible to minimise the geometry of the simulation cell itself. Such a minimisation is called constant pressure (as opposed to constant volume) as the forces acting on the cell can be considered equivalent to pressure. In many cases a minimisation at constant volume is performed first to allow the cell contents to find their preferred geometry with respect to each other, and then minimise the whole system including the simulation cell geometry.

To perform a constant pressure energy minimisation the cell dimensions are treated as additional variables in the minimisation. The bulk lattice strain according to Hooke's law is given by:

$$\boldsymbol{\varepsilon} = \boldsymbol{C}^{-1}\boldsymbol{\sigma}$$

Equation 2.39

where $\boldsymbol{C}^{-1}$ is the inverse second order derivative of lattice energy with respect to strain (also called the elastic compliance matrix). $\boldsymbol{\sigma}$ is the stress defined as the sum of the static pressure, plus any applied pressure:

$$\boldsymbol{\sigma} = \boldsymbol{P}_{static} + \boldsymbol{P}_{applied}$$

Equation 2.40

$$\boldsymbol{P}_{static} = \left(\frac{1}{V}\right)\left(\frac{\delta U}{\delta \boldsymbol{\varepsilon}}\right)$$

Equation 2.41

where V is the volume, U is the lattice energy and $\boldsymbol{\varepsilon}$ is the lattice strain. A more complete overview of constant pressure minimisation is given in Leach (2001) [134].

The final configuration of a constant pressure energy minimisation often makes a good starting point for molecular dynamics simulations as the atoms are at their equilibrium positions. If an atom is some distance from its equilibrium position then a large velocity may be generated on the first timestep, which could significantly interfere with the structure or dynamics.

2.3.4. Overcoming Local Minima

The configuration located by energy minimisation is not necessarily the global energy minimum. Energy minimisation functions by iteratively seeking lower energy configurations from a starting configuration. Thus it is possible for a configuration to become trapped in a local energy minimum rather than the global minimum. As many real materials exhibit several stable polymorphs (Titania, Silica etc.) the local minima may also be viable structures.

However it is often preferable to locate the global minimum and several techniques can be used to try and locate it. The simplest method is to try multiple starting configurations and energy minimise them, searching for the lowest energy system. Other techniques may search via Monte Carlo methods or molecular dynamics. A remaining issue is that it is hard to be certain a given configuration is the global minimum unless the entirety of the energy landscape has been explored.

2.4. Molecular Dynamics

Molecular dynamics is a technique that iteratively integrates Newton's laws of motions for a given system of particles by assigning velocities and stepping forward in time. Small energy barriers may be overcome with molecular dynamics as the probability (P) of overcoming an energy barrier is proportional to the height of the energy barrier and the temperature of the system:

$$P \propto \exp(-E_a/k_{\mathrm{B}}T)$$

Equation 2.42

where E_a is the height of the energy barrier relative to the current minimum, k_{B} is Boltzmann's constant and T is the temperature. However this is rarely the most efficient approach due to kinetic factors, whereas Monte Carlo techniques operate purely on the thermodynamics of the system. A more detailed discussion of Monte Carlo simulations may be found elsewhere [134].

Molecular dynamics can be employed to calculate properties of a system that are only accurately measurable under the flow of time such as diffusion and thermal conductivity. However, such calculations may require much simulation time to accrue reasonable statistical accuracy.

2.4.1. Calculation of Forces

The approach to force calculation in molecular dynamics is different to that in energy minimisation. Below is an outline of functional, but perhaps not optimal, classical potential molecular dynamics algorithms. First the distance between the atoms is calculated from their Cartesian coordinates:

$$\boldsymbol{r}_{ij} = \boldsymbol{r}_i - \boldsymbol{r}_j$$

Equation 2.43

where $\boldsymbol{r}_i$ and $\boldsymbol{r}_j$ are the Cartesian coordinates of atom i and j respectively. The distance between atoms i and j may also be written:

$$r_{ij} = \left|\boldsymbol{r}_{ij}\right| = \sqrt[2]{x_{ij}^2 + y_{ij}^2 + z_{ij}^2}$$

Equation 2.44

where x_{ij}, y_{ij} and z_{ij} are the difference in Cartesian coordinates in each dimension. It is important to note that the vector $\boldsymbol{r}_{ij}$ gives the distance of atom i with respect to atom j and thus the calculated forces will also be of atom i with respect to atom j.

The distance is then used to calculate the force:

$$F_{ij} = -\frac{dU}{dr_{ij}}$$

Equation 2.45

The force must next be decomposed into contributions from each dimension by using the distance unit vector:

$$\boldsymbol{F}_{ij} = F_{ij}\frac{\boldsymbol{r}_{ij}}{\left|\boldsymbol{r}_{ij}\right|} = -\frac{dU}{d\boldsymbol{r}_{ij}}$$

Equation 2.46

The force acting on atom j with respect to atom i can be obtained from Newton's third law. When one body exerts a force on a second body, the second body exerts a force of equal and opposite magnitude on the first body:

$$\boldsymbol{F}_{ji} = -\boldsymbol{F}_{ij}$$

Equation 2.47

The total force acting upon an atom is the sum of the forces acting upon it from all other atoms:

$$\boldsymbol{F}_i = \sum_{\substack{j=1 \\ j \neq i}}^{N} \boldsymbol{F}_{ij}$$

Equation 2.48

To convert the force to acceleration Newton's second law is used, where t is time, $\boldsymbol{a}$ is the acceleration and m is the mass:

$$\boldsymbol{F} = m \cdot \frac{\delta^2 \boldsymbol{r}}{\delta t^2} = m \cdot \boldsymbol{a}$$

Equation 2.49

2.4.2. Time Integration Algorithms

Once the force acting on an atom is obtained, it is possible to write equations to update the positions and velocities of atoms based on the accelerations and the previous positions and velocities:

$$\boldsymbol{r}(t + \Delta t) = \boldsymbol{r}(t) + \boldsymbol{v}(t)\Delta t + \frac{\boldsymbol{a}(t)\Delta t^2}{2}$$

Equation 2.50

$$\boldsymbol{v}(t + \Delta t) = \boldsymbol{v}(t) + \boldsymbol{a}(t)\Delta t$$

Equation 2.51

where $\boldsymbol{r}$ is the position, $\boldsymbol{v}$ is the velocity and $\boldsymbol{a}$ is the acceleration of the atoms. Equation 2.50 and Equation 2.51 are only valid for continuous time and infinitesimally small changes in the acceleration. However, time in molecular dynamics simulations is discretised, which may remove the energy conservation properties of Newton's equations and therefore alternative algorithms are required.

To compensate for the use of finite timesteps, time integration algorithms have been developed based on the Taylor expansion in time. These are time-reversible algorithms which in principle conserve a mean energy over the course of the simulation [176].

2.4.2.1. Störmer-Verlet

The Taylor series expanded about $\boldsymbol{r}(t + \Delta t)$ is given in Equation 2.52 and Equation 2.53.

$$\boldsymbol{r}(t + \Delta t) = \boldsymbol{r}(t) + \boldsymbol{v}(t)\Delta t + \boldsymbol{a}(t)\frac{1}{2!}\Delta t^2 + \boldsymbol{b}(t)\frac{1}{3!}\Delta t^3 + \mathcal{O}(\Delta t^4)$$

Equation 2.52

$$\boldsymbol{r}(t - \Delta t) = \boldsymbol{r}(t) - \boldsymbol{v}(t)\Delta t + \boldsymbol{a}(t)\frac{1}{2!}\Delta t^2 - \boldsymbol{b}(t)\frac{1}{3!}\Delta t^3 + \mathcal{O}(\Delta t^4)$$

Equation 2.53

where $\boldsymbol{b}$ is the third derivative of the position with respect to time, also known as the jerk. $\mathcal{O}(\Delta t^4)$ is the error due to neglecting higher order terms of the expansion. By summing these two expressions and rearranging, Equation 2.54 is obtained:

$$\boldsymbol{r}(t + \Delta t) = 2\boldsymbol{r}(t) - \boldsymbol{r}(t - \Delta t) + \boldsymbol{a}(t)\Delta t^2 + \mathcal{O}(\Delta t^4)$$

Equation 2.54

The advantage of Equation 2.54 is that the third order terms (the jerk) cancel, making this a fourth order integrator. The velocity is not calculated explicitly but can be computed by:

$$\boldsymbol{v}(t) = \frac{\boldsymbol{r}(t + \Delta t) - \boldsymbol{r}(t - \Delta t)}{2\Delta t} + \mathcal{O}(\Delta t^2)$$

Equation 2.55

This approach is known as the Störmer-Verlet algorithm [177]. A significant drawback of this method is that velocities can only be calculated one step behind the positions due to the requirement of the $\boldsymbol{r}(t + \Delta t)$ term. While this does not directly affect the dynamics, it does cause some issue for calculation of properties such as kinetic energy and thus any thermostat applied to the system. Additionally, computational accuracy may suffer by adding a small term, $a(t)\Delta t^2$, to the difference between two very large terms.

2.4.2.2. Verlet Leap-Frog

Other algorithms have been developed which explicitly calculate the velocity. The Verlet Leap-frog algorithm [139] is based on the basic Störmer-Verlet algorithm but calculates the velocities at the half-timestep. These can then be used to calculate the velocities at the timestep without requiring the positions at the next timestep. In this algorithm the half-timestep velocities are calculated by:

$$\boldsymbol{v}\left(t+\frac{\Delta t}{2}\right)=\boldsymbol{v}\left(t-\frac{\Delta t}{2}\right)+\boldsymbol{a}(t)\Delta t$$

Equation 2.56

The velocities at the timestep can then be extrapolated by averaging the time adjacent velocities:

$$\boldsymbol{v}(t)=\frac{\boldsymbol{v}\left(t+\frac{\Delta t}{2}\right)+\boldsymbol{v}\left(t-\frac{\Delta t}{2}\right)}{2}$$

Equation 2.57

The positions are then calculated from the half-timestep:

$$\boldsymbol{r}(t+\Delta t)=\boldsymbol{r}(t)+\boldsymbol{v}\left(t+\frac{\Delta t}{2}\right)\Delta t$$

Equation 2.58

While an improvement over the Störmer-Verlet method there remains a disadvantage in that the positions and velocities are still not synchronised. In this work the Velocity Verlet algorithm has been used which calculates the positions, velocities and accelerations at the same timestep.

2.4.2.3. Velocity Verlet

The algorithm for the Velocity Verlet [178] method is:

1. Calculate the new positions from current positions, velocities and accelerations by Equation 2.59.

$$\boldsymbol{r}(t+\Delta t)=\boldsymbol{r}(t)+\boldsymbol{v}(t)\Delta t+\frac{\boldsymbol{a}(t)\Delta t^2}{2}$$

Equation 2.59

2. Calculate the velocity at the half-timestep with Equation 2.60.

$$\boldsymbol{v}\left(t+\frac{\Delta t}{2}\right)=\boldsymbol{v}(t)+\frac{\boldsymbol{a}(t)\Delta t}{2}$$

Equation 2.60

3. Calculate new forces and thus accelerations using the new atom positions.
4. Calculate new velocities using velocities at the half-timestep and the new accelerations using Equation 2.61.

$$\boldsymbol{v}(t+\Delta t)=\boldsymbol{v}\left(t+\frac{\Delta t}{2}\right)+\frac{\boldsymbol{a}(t+\Delta t)\Delta t}{2}$$

Equation 2.61

At the expense of extra storage for accelerations, the Velocity Verlet method may be shortened to:

1. Calculate the new positions from current positions, velocities and accelerations using Equation 2.59.
2. Calculate new forces and thus accelerations using the new atom positions.
3. Calculate new velocities using current velocities, old accelerations and new accelerations using Equation 2.62.

$$\boldsymbol{v}(t+\Delta t)=\boldsymbol{v}(t)+\frac{\big(\boldsymbol{a}(t)+\boldsymbol{a}(t+\Delta t)\big)\Delta t}{2}$$

Equation 2.62

2.4.2.4. Predictor-Corrector Methods

A class of slightly more complex time integrators are also available which use the Taylor expansion term for acceleration and compare it to the acceleration as predicted from the potential acting upon the system. The difference can be used iteratively to adjust the positions and velocities until the two accelerations match.

The predictor-corrector methods often follow the equations of motion very closely but suffer from the requirement of repeated calculation of the accelerations and therefore forces, which is usually the most expensive part of a molecular dynamics simulation. Additionally, not all predictor-corrector methods are time reversible and conserve energy [179].

A more complete discussion of these methods is given by Leach [134].

2.4.3. Initial Velocities

The Velocity Verlet algorithm requires initial velocities as well as atomic coordinates and thus the velocities must be assigned or carried over from a previous simulation. Equation 2.63 is used to relate average atom velocities to a given temperature.

$$\sum_{i=1}^{N} m_i v_i^2 = 3Nk_BT$$

Equation 2.63

In Equation 2.63 m_i is the mass of each atom and v_i is the velocity. N is the number of atoms, k_B is the Boltzmann constant. The linear momentum of the system is also required to be zero to avoid translation of the simulation cell contents, Equation 2.64.

$$p = \sum_{i=1}^{N} m_i v_i = 0$$

Equation 2.64

Additional constraints may also be placed to ensure there is no net angular momentum either.

2.4.4. Choosing the Timestep

Time integration algorithms require a discrete timestep which is chosen as a balance between simulation accuracy and computation time. A poorly chosen timestep can lead to unphysical dynamics and highly unstable systems.

The timestep must be short enough to accurately reproduce the trajectory of fastest atomic motion present in the system; this is particularly important in systems with light atoms such as hydrogen, or in systems employing the shell model which can move at very high frequencies. However, a timestep that is too small will take an unfeasibly long time to accrue statistics and so a balance must be struck between the two.

Consider a diatomic system such as O_2, when the atomic separation is small there is a repulsive force and there is no initial velocity. The repulsive force felt between the atoms results in movement away from each other. In the case of a reasonable timestep,

the atoms will separate until an attractive force is felt, resulting in vibration. If the timestep is too large the atoms may separate far enough that they bypass the attractive part of the potential, resulting in an unphysical bond breaking.

2.4.5. Equilibration Period

Before any information can be gathered from a simulation, it is important to allow the simulation to equilibrate first, so as to not include any effects from the initialisation.

A key example is that of system volume; when starting from an energy minimised structure (equivalent to zero Kelvin) the structure often has the wrong volume for the simulation temperature and this must be allowed to equilibrate before data collection.

The equilibration period is also the time where additional constraints can be applied to ensure the correct dynamics are reproduced later. In the case of the diatomic of O_2 molecule, if the atoms start too close together, a large force will be exerted within a very short period of time. The large force will lead to a large acceleration and a separation of the molecule. This means the system under study is no longer the O_2 molecule as desired. By applying a maximum force limit during equilibration, the O_2 molecule may remain intact. After the equilibration, the system may then be studied.

Other constraints which may be applied during equilibration include rapid temperature rescaling to bring the system to the desired temperature faster, and repeated momentum zeroing to prevent translation of the entire system.

2.4.6. Neighbour Lists and Verlet Lists

During molecular dynamics simulations all relevant interactions must be calculated at every timestep. Instead of calculating all short-range particle-particle interactions, cutoffs (discussed in Chapter 2.2.2) are used so that only relevant interactions are calculated. To find all particles that are within the cutoff, a search over all particles can be performed to generate a neighbour list. The generation of neighbour lists is very computationally demanding, and scales poorly with number of particles, giving a complexity of $\mathcal{O}(N^2)$. A number of approaches have been developed to reduce the computation time, one such approach is that of Verlet lists.

Verlet lists [177] serve as a data structure to keep track of which particles may be within the short-range cutoff over the next few timesteps. Deciding which particles to include

in the Verlet list is done by adding an extra skin region to the surface of the cutoff region; particles within the skin region are close enough to the central particle that it is possible for them to move within the cutoff over the next few timesteps.

The choice of skin distance must be made carefully; a larger skin distance means less frequent updates of the Verlet list, but an increase in the number of particles that must be checked each timestep. The decision is largely system dependent; a low temperature crystal would need only a moderate skin distance and have its Verlet list updated very infrequently, if ever. Conversely a hot gaseous system would require a large skin distance and still require frequent list rebuilds.

The use of Verlet lists in not infallible, a statistically rare high velocity particle could theoretically move into the cutoff region between Verlet list builds and not be recognised as potentially interacting. However it is relatively simple to check for atoms with such high velocity and when they occur to trigger a rebuild of the Verlet list. A deeper concern is that frequent occurrences of these high velocity particles may indicate that the timestep is too large, leading to generally poor dynamics.

This work has used a skin distance of 2.0 Å and an update interval of 10 timesteps.

2.4.7. Ensembles

Ensembles describe the conditions that molecular dynamics simulations are run under. Each ensemble is represented by a different Hamiltonian, which describes the conserved quantities of the system. The simplest ensemble that can be used in molecular dynamics simulations is the microcanonical (NVE) ensemble.

2.4.7.1. Microcanonical (NVE) Ensemble

In the NVE ensemble the number of atoms (N), volume (V) and energy (E) are held constant. The Hamiltonian of this system is simply the sum of the potential (U) and kinetic ($K.E.$) energies:

$$H_{\mathrm{NVE}} = U + K.E.$$

Equation 2.65

In experiments it is not the total energy that is held constant, but the temperature. To more accurately model these cases it is more appropriate to use a constant temperature ensemble such as the canonical (NVT) ensemble.

2.4.7.2. Canonical (NVT) Ensemble

A number of different methods are available to control the temperature of a simulation. One of the most commonly used methods is the Nosé–Hoover thermostat [180-182] which is also used throughout this work. The Hamiltonian when using the Nosé–Hoover thermostat is the Helmholtz free energy:

$$H_{\mathrm{NVT}} = U + K.E. + \frac{\chi^2 Q}{2} + 3Nk_BT \ln s$$

Equation 2.66

where χ is a friction coefficient, s is a variable used to scale the particle momenta and Q is the effective mass of the thermostat and governs the coupling of the system to the thermostat. The update of particle positions proceeds in the same manner as for the microcanonical ensemble:

$$\frac{d\boldsymbol{r}_i}{dt} = \boldsymbol{v}_i$$

Equation 2.67

However, the accelerations now have an additional component which is coupled to the thermostat:

$$\frac{d\boldsymbol{v}_i}{dt} = \boldsymbol{a}_i - \chi \boldsymbol{v}_i$$

Equation 2.68

The friction coefficient, χ, is updated by:

$$\frac{d\chi}{dt} = \frac{m_i \sum |\boldsymbol{v}_i|^2 - 3Nk_BT}{Q}$$

Equation 2.69

where m_i is the mass of the particle and T is the desired temperature. The scaling factor, s, is then updated by:

$$\frac{d \ln s}{dt} = \chi$$

Equation 2.70

2.4.7.3. Isobaric-isothermal (NPT) Ensemble

The NPT ensemble maintains the number of particles, pressure and temperature. The temperature is maintained as before and a similar expression is used to maintain the pressure, except that it is the cell dimensions which are adjusted. Several variations exist depending on whether the cell dimensions are allowed to vary isotropically, anisotropically and whether the angles between the cell vectors are allowed to change.

2.5. Defects

Crystal systems may contain many types of defects. The simplest type of defect is the point defect which is a change to a single atomic site in the crystal, of which three basic types are possible:

- Vacancies – An empty site that is usually occupied.
- Interstitials – An atom occupying a site that is usually vacant.
- Substitutions – A site that is occupied by a different type of atom than is usual.

More complex defect schemes can be built from these three basic types. A Schottky defect is typically a group of vacancies that constitute one complete stoichiometric unit of the material. A Frenkel defect is a combination of a vacancy and an interstitial such that an atom has essentially moved to another position in the material. This work has not studied point defects and a more complete discussion of their study may be found in Leach [134].

Crystals also contain extended defects, including:

- Line defects.
    - Edge dislocations.
    - Screw dislocations.
- Planar defects.
    - Surfaces.
    - Grain boundaries.

- Stacking faults.

This work has looked at grain boundaries and nanostructured systems, which may also contain internal surfaces. Therefore, in the next section an overview of extended defects is given.

2.5.1. Extended Defects

Extended defects are those which exist over large distances as opposed to localised defects such as dopants and vacancies. Generating such defects is nontrivial and requires several steps. In this work the METADISE code [165] has been used to generate grain boundaries to study their effect on thermal conductivity.

2.5.1.1. Miller Indices

A Miller index defines a normal to a plane in the lattice and consist of three integers which indicate where in a given reciprocal cell the plane cuts the axes. For example the {112} Miller index indicates a family of planes in the real space cell. This Miller index includes the plane which cuts the X axis at 1.0, the Y axis at 1.0 and the Z axis at 0.5 and all parallel planes. Some example Miller indices and their corresponding planes are given in Figure 2.6. The Miller index is a convenient way to describe surfaces; however a single Miller index may give multiple surface geometries depending on where in the crystal the plane is cut and the possible surface reconstructions.

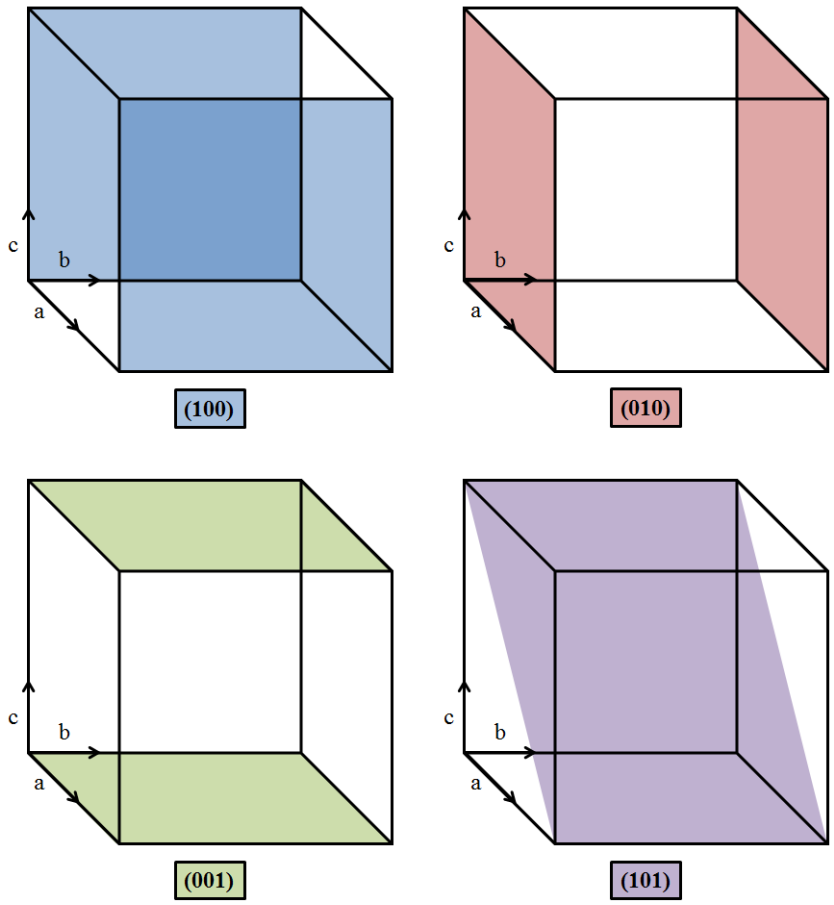

Figure 2.6 Possible planes for different Miller indices.

2.5.1.2. Surfaces

When a crystal is cleaved, two surfaces are formed. The surface is primarily characterised by its Miller index, secondarily by the termination pattern. These different factors influence the stability of the surface. Depending on the termination of the surface, problems relating to the dipole of the materials may arise.

It has been shown [183] that when a dipole perpendicular to the surface is present, the energy of the surface diverges. Such surfaces are therefore unstable and require defects to remove the dipole. These defects can either be adatoms, vacancies or large reconstructions. There are in fact three different types of surface, as described by Tasker [184] and shown in Figure 2.7.

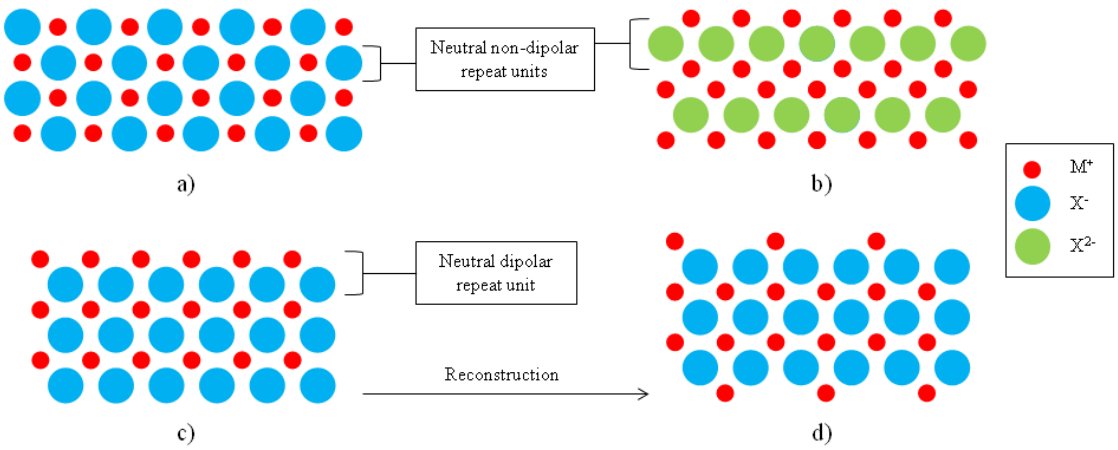

Figure 2.7 Diagram of the three types of surfaces possible when cutting a crystal: a) Type I, b) Type II and c) Type III. The polar repeat units in the Type III surface result in a reconstruction, one possible reconstruction is shown in d).

The three types of surface are defined as:

- Type I –Built from uncharged planes. Each plane contains a stoichiometric amount of cations and anions and thus has no dipole.
- Type II – Built from charged planes, stacked in a way as to produce no overall dipole at the surface.
- Type III – Built from charged planes, stacked in a way that generates a dipole at the surface. It is this type of surface which requires modification to become stable.

Several schemes have been proposed for the modification of Type III surfaces. Oliver et al. [185] suggested moving half of the atoms in the surface plane to the surface at the bottom of the cell, neutralising the dipole. However, the arrangement of the half-filled plane at the surfaces becomes another variable to investigate. A related approach is that of micro-faceting, where rearrangement of the surface to give facets can remove the dipole and lower the surface energy. Very large facets may simply be considered different surfaces which are stepped, Figure 2.8.

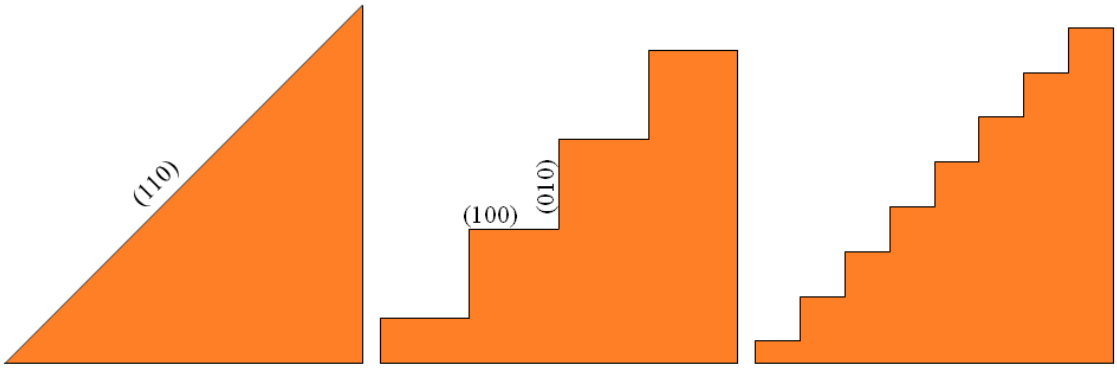

Figure 2.8 Two possible surface geometries generated by faceting of the (110) surface, both using the (100) and (010) surfaces.

To model a surface one can use the approach developed by Tasker [184]. Here the simulation cell consists of two-dimensional periodic charged planes, parallel to the surface. A full crystal may contain millions of layers of charged planes between two opposing surfaces. To overcome this problem Tasker developed the two-region approach. When a surface is formed relaxation of ions occurs and continues several layers into the bulk crystal until bulk like geometry is restored. Therefore the surface/bulk system can be split into two regions; one containing atoms which are near the surface and will explicitly relax (Region I), the other far from the surface where the effect is negligible and so the atoms can be held fixed (Region II).

To minimise the surface energy, a block is made consisting of the two regions (Figure 2.9). The ions in Region II are held fixed at their equilibrium positions to approximate the bulk crystal. The ions in Region I experience all the interactions associated with Region II and are allowed to relax to their favoured positions. The size of the two regions must be tested so that they reach convergence. A small Region II may result in the surface not experience enough bulk-like effects while a small Region I may not be large enough to return to bulk before meeting Region II.

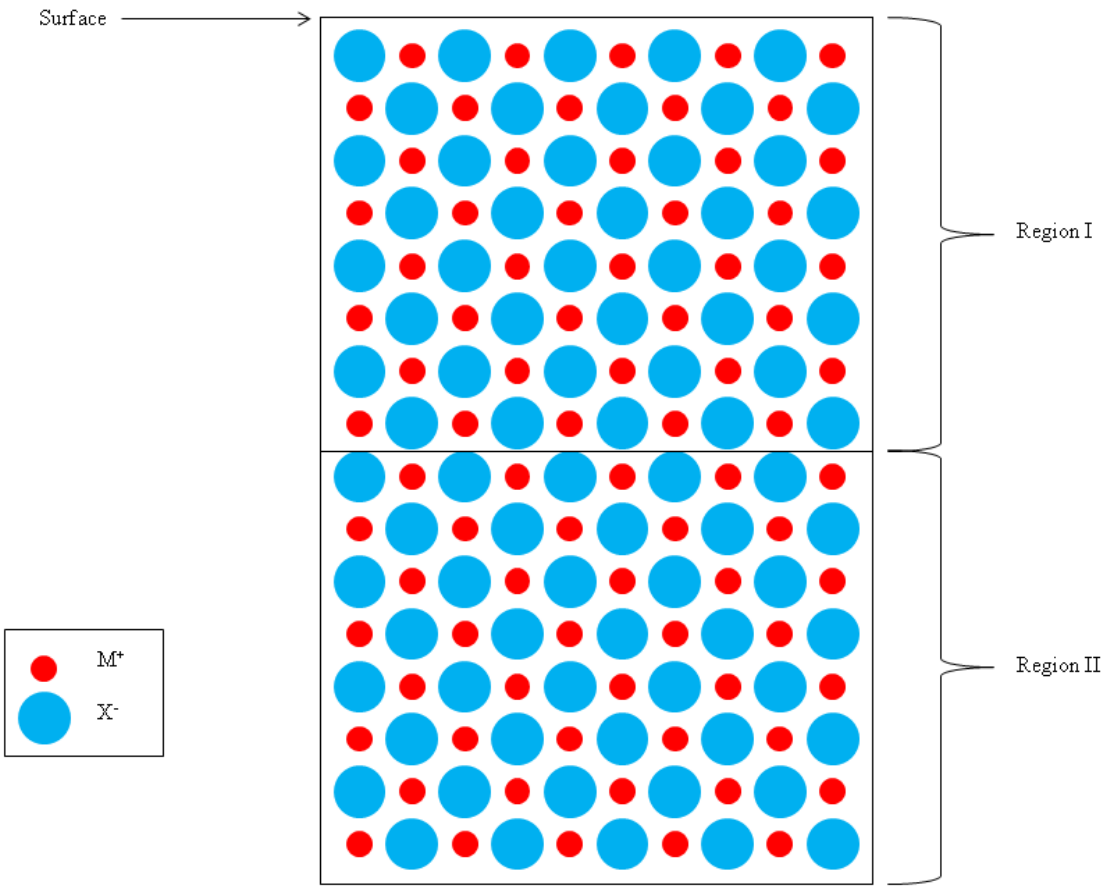

Figure 2.9 Schematic of the two-region approach as used to simulate surfaces. PBCs may be applied perpendicular to the surface.

To compare the energy of the surface to that of the bulk, two blocks instead of one can be used. In this case, the surface is not exposed to vacuum but another surface in the second block such that the two surfaces recover the bulk structure. From this arrangement one can then calculate the bulk (U_{B}) and surface (U_{S}) energies:

$$U_{\mathrm{B}} = (E^{\mathrm{B}}_{I-I} + E^{\mathrm{B}}_{I-II}) + (E^{\mathrm{B}}_{II-I} + E^{\mathrm{B}}_{II-II})$$

Equation 2.71

$$U_{\mathrm{S}} = \left(E^{\mathrm{S}}_{I-I} + E^{\mathrm{S}}_{I-II}\right) + \left(E^{\mathrm{S}}_{II-I} + E^{\mathrm{S}}_{II-II}\right)$$

Equation 2.72

where the superscripts refer to either the energy of the bulk (E^{B}) or the surface (E^{S}) and the subscripts refer to the components of different regions interacting. For example E^{S}_{I-II} refers to the energy of interaction between ions in Regions I and II for the surface calculation.

The energy of a given surface, γ, is the excess in energy of the surface calculation as compared to the bulk, for the same number of atoms per surface area:

$$\gamma = \frac{U_{\mathrm{S}} - U_{\mathrm{B}}}{S}$$

Equation 2.73

where S is the surface area. Using the reasonable approximation of $E_{II-II}^{\mathrm{B}} = E_{II-II}^{\mathrm{S}}$ they will cancel and thus their calculation can be avoided.

2.5.1.3. Crystal Morphology

Using the calculated surface energies it is possible to obtain the equilibrium morphology of a given material. For a crystal of a given volume, the equilibrium morphology will minimise the total surface energy and thus more stable surfaces will have larger surface areas and vice versa. Thus, Equation 2.74 is minimised for a given volume [186]:

$$\gamma = \sum_i \gamma_i S_i$$

Equation 2.74

where γ_i is the surface energy per area and S_i is the surface area of the corresponding crystallographic face. i runs over all possible surfaces, however very high Miller index surfaces tend to be unstable and contribute very little to the final morphology.

Building upon this, Wulff [187] proposed the crystal morphology could be calculated based on the normal vector to a crystallographic face (h_i) and the surface energy of that face γ_i:

$$h_i = \lambda \gamma_i$$

Equation 2.75

where λ is a constant dependent upon the volume of the crystal. By constructing planes at the end of these vectors, the inner surface gives the equilibrium morphology. This is known as the Wulff construction, Figure 2.10.

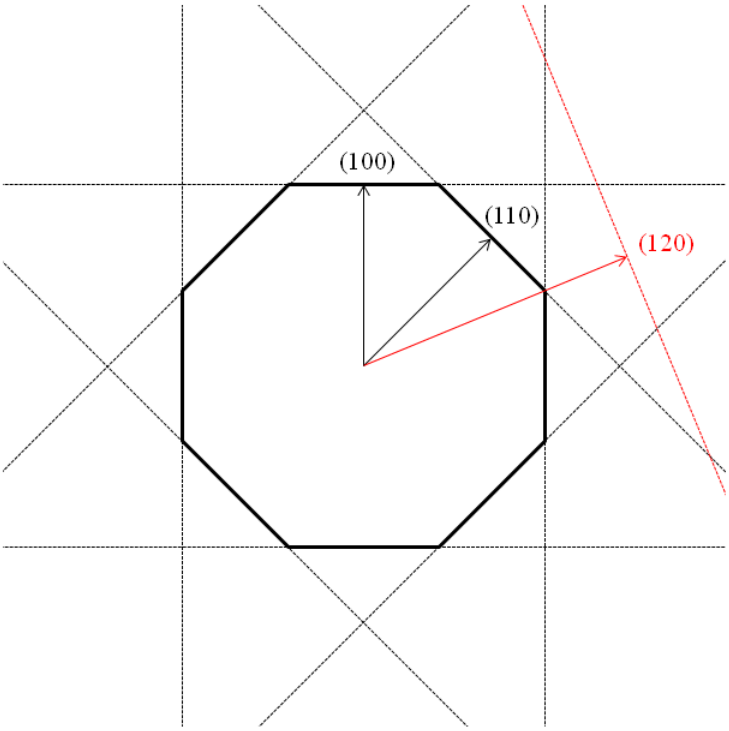

Figure 2.10 The Wulff construction of a crystal. The (120) surface is not expressed due to its high energy.

The Wulff construction only holds true for larger crystals grown in equilibrium. The kinetic morphology may be very different due to the growth speeds of the different surfaces. Additionally, growth of crystals in different mediums will also affect the morphology and the surface calculations should include these effects for accurate comparison to experiments.

2.5.1.4. Grain Boundaries

Extended defects within the bulk such as dislocations and grain boundaries can be modelled by adapting the approach used for surfaces. Grain boundaries are generally considered as the interface between two crystalline grains with differing orientations [188], however dislocations can also be considered to be a special case of grain boundary where no rotation of the grain has occurred, but only displacement.

There exist primarily two types of grain boundary:

- Tilt Grain Boundaries – These boundaries are created when the rotation axis is parallel to the boundary plane.

- Twist Grain Boundaries – These boundaries are created when the rotation axis is perpendicular to the boundary plane.

The definition of grain boundaries follows the coincidence site lattice model which assumes that low formation energy is achieved when there is a high degree of coincidence of the atomic positions across the two grains. The reciprocal density of coincidence sites, Σ, is defined as the sum of the squares of the Miller indices (h, k and l):

$$\Sigma = \delta(h^2 + k^2 + l^2)$$

Equation 2.76

where δ is 1 if sum of the squared indices is odd and 0.5 when they are even. Hence in cubic systems Σ values are always expressed as an odd number. Low Σ values are accepted as representing special boundaries (e.g. a Σ of 3 is a singular boundary. Further details about the coincidence site lattice model may be found elsewhere[189].

Constructing a grain boundary initially follows the same procedure as constructing a surface, diverging just prior to relaxation of the surface. Following the same approach as in surface construction, a block is created containing two regions as before. To build a grain boundary rather than a surface the block is reflected or rotated such that the Region Is of the two blocks are adjacent, Figure 2.11.

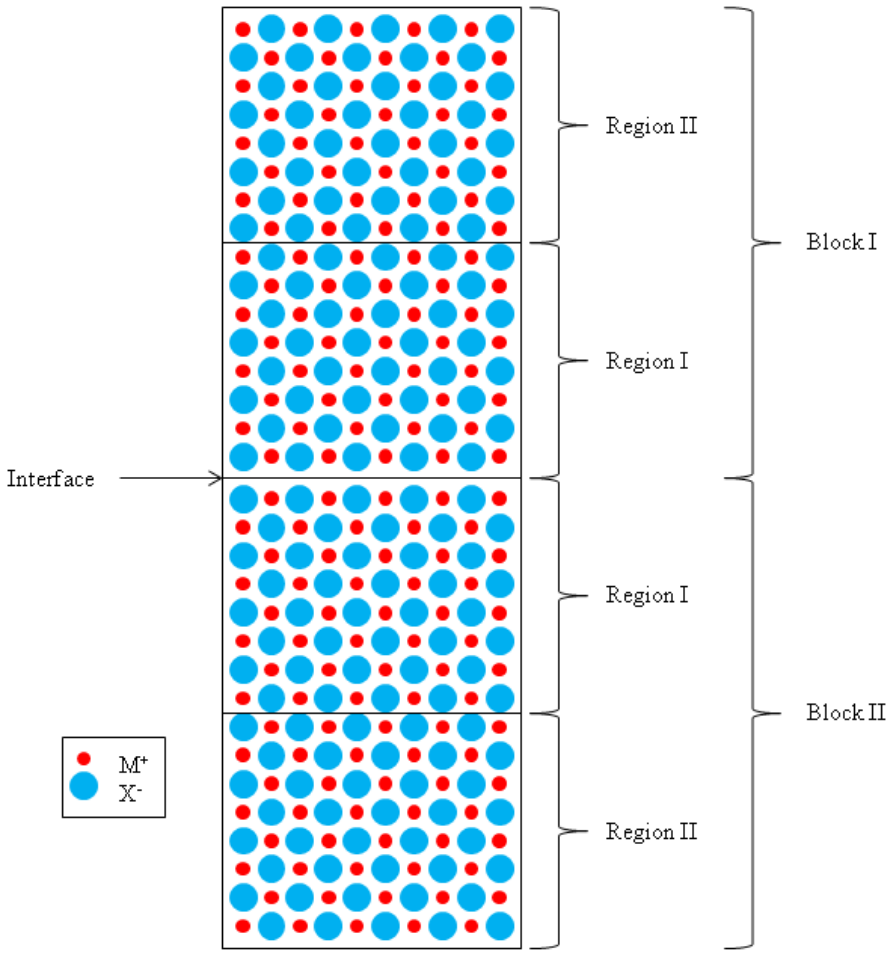

Figure 2.11 The two-region approach applied to a grain boundary (dislocation).

The choice of reflection or rotation must be made carefully depending on the type of material and grain boundary being built. For centrosymmetric materials a reflection is equivalent to a rotation; for non-centrosymmetric materials it is not.

One block is then scanned over the other to determine the displacement which will give the lowest energy structure. In principle the scan could be done over rotations in addition to displacements but for tilt grain boundaries only the displacement is required. These scans are performed with the METADISE code [165].

The scans are conducted by defining a two-dimensional mesh over the surface and displacing the second block to the different points on the mesh. The two Region Is of the blocks are then minimised and the final energy taken. The finer the mesh the more accurate the scan will be, at the expensive of more structures to evaluate. The scan may

also be accelerated by skipping the minimisation but then the lowest energy structure may not be found.

When the lowest energy displacement structure is found the simulation cell is converted to a bulk-like cell and a second boundary half way along the simulation cell is created such that it is the same as the first boundary. The amount of bulk between the two boundaries can be varied to study the effects of inter-boundary distance, related to grain size in real materials.

Two important energetic values can be calculated for grain boundaries. Cleavage energy (E_C) is defined as the energy required to separate the boundary into two surfaces and is representative of how tightly bound the two grains are. Formation energy (E_F) is the energy required to form the grain boundary from the bulk and is related to how likely the boundary is to form. E_C is calculated by:

$$E_C = \frac{E_{gb} - 2E_{surf}}{A}$$

Equation 2.77

where E_{gb} is the energy of the grain boundary, E_{surf} is the energy of the surface and A is the area. Likewise E_F is obtained from:

$$E_F = \frac{E_{gb} - E_{bulk}}{A}$$

Equation 2.78

where E_{bulk} is the energy of the bulk material. It is important that for both these calculations the energy values are for the same number of atoms per area.

3. Thermal Conductivity Methodology

The calculation of thermal conductivity in simulation may be conducted a number of ways. In this chapter a brief overview of phonons is given followed by an outline of three different approaches to the calculation of thermal conductivity. Each of the approaches calculates the thermal conductivity in a different way and each has its strengths and weaknesses.

3.1. Phonon Processes

A phonon is a quasiparticle which represents waves traversing materials via local displacements of atoms. The thermodynamic properties of a material are directly governed by the phonon processes occurring within the material. Heat capacity, thermal expansion and thermal conductivity are just a few thermodynamic properties which are explained by phonons. Heat capacity may be calculated using only the harmonic approximation, but thermal expansion and thermal conductivity require that phonons interact with each other and therefore anharmonic contributions must be included. An initial starting point for anharmonic contributions is the harmonic approximation, which may then be extended to include anharmonic terms.

3.1.1. The Harmonic Approximation

The energy of a material (U) may be described by a Taylor expansion of displacements ($u_{j,a}$), where j is the atom label and a is a particular dimension (x, y or z):

$$U = U_0 + \frac{1}{2}\sum_{\substack{j,j' \\ a,a'}} \frac{\partial^2 U}{\partial u_{a,j}\partial u_{a',j'}} u_{a,j}u_{a',j'} + \frac{1}{n!}\sum_{\substack{j^{(1)},\cdots,j^{(n)} \\ a^{(1)},\cdots,a^{(n)}}} \frac{\partial^n U}{\partial u_{a^{(1)},j^{(1)}}\cdots\partial u_{a^{(n)},j^{(n)}}} u_{a^{(1)},j^{(1)}}\cdots u_{a^{(n)},j^{(n)}} + \cdots$$

Equation 3.1

where U_0 is the equilibrium lattice energy, the second-order term is the harmonic energy and all higher terms (denoted by n) contribute to the anharmonic energy. The first-order term is neglected as for a crystal at equilibrium the forces (negative of the first

derivative of energy) are zero. The harmonic approximation is simply to neglect all terms beyond the harmonic energy.

In the harmonic approximation the phonon frequencies can be calculated using the finite displacement method, where the derivatives with respect to energy are calculated by displacing an atom by a small distance and recording the forces on all other atoms. This obtains a $3n \times 3n$ matrix (where n is now the number of atoms) known as the harmonic matrix. The Fourier transform of the harmonic matrix using a given k-vector (or q-point) is known as the dynamical matrix [190, 191]. The dynamical matrix may be diagonalised to yield the squared phonon frequencies as eigenvalues, with eigenvectors corresponding to atomic motions.

This approach may be extended to include higher order terms and therefore some anharmonic properties, including thermal expansion and conductivity. Including the third-order term requires additional atomic displacements of other atoms so that all possible pairs of atomic displacements are included [122]. Problems such as memory requirements and numerical error on the forces rapidly make the approach intractable above the third-order force constants. However the third-order force constants are sufficient to allow phonon-phonon interactions to be calculated and thence thermal expansion and conductivity.

3.1.2. Anharmonic Processes

The anharmonicity of the interactions between atoms are not accounted for in the harmonic approximation. Including the anharmonic terms allows for both thermal expansion and phonon-phonon interactions [192], which moderate the thermal conductivity. This section is only intended as a brief overview, a more complete explanation is given by Dove [192].

3.1.2.1. Thermal expansion

The thermal expansion of crystals is governed by the anharmonic part of the interaction. In the harmonic approximation the average interatomic distance does not change with temperature and thus the crystal does not expand. When the interaction is anharmonic the bond lengths may change upon changing temperature, Figure 3.1.

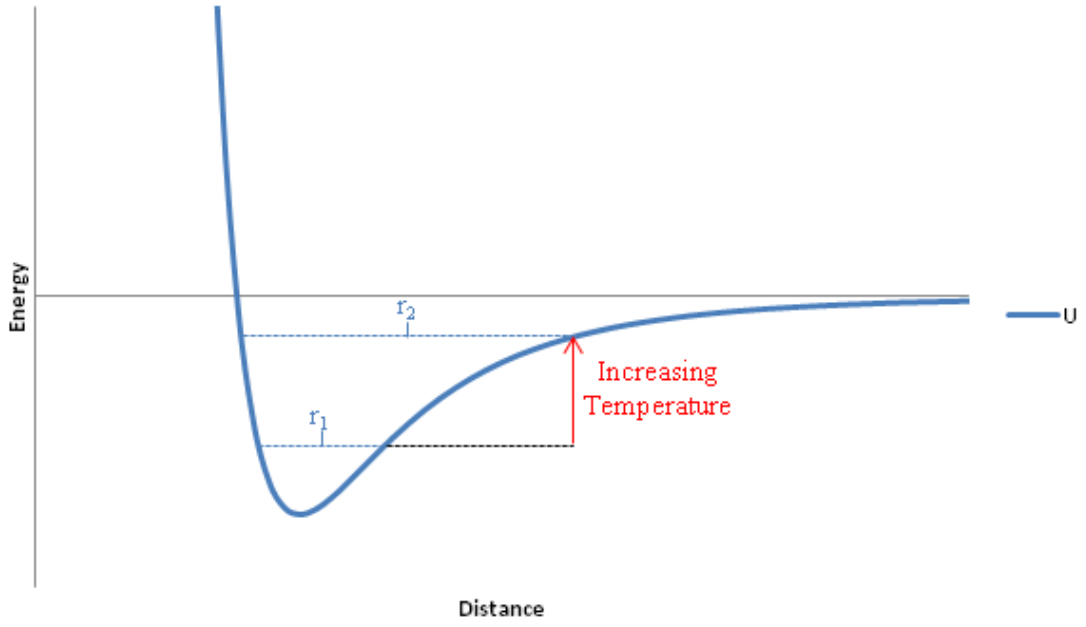

Figure 3.1 The equilibrium distance increases from r_1 to r_2 upon increasing temperature.

The thermal conductivity of a material is also dependent upon anharmonic interactions. In a harmonic system phonon-phonon interactions do not occur and thus the thermal conductivity would be infinite as scattering does not occur.

If the thermal expansion is reproduced well by a potential model then it is likely the potential model will also give good thermal conductivity values, although it is not ensured.

3.1.2.2. Phonon Scattering

There are two possible types of phonon scattering process, Normal and Umklapp.

Normal type scattering processes occur when the interaction of two phonons (k_1 and k_2) results in a third phonon (k_3) with the same total phonon momentum (p) of the original two phonons:

$$p_{k_1} + p_{k_2} = p_{k_3}$$

Equation 3.2

Umklapp type scattering processes occur when the interaction of two phonons (k_1 and k_2) results in a third phonon (k_3) with less total phonon momentum (p) than the original two phonons, but with some transfer of phonon momentum to the lattice (G):

$$p_{k_1} + p_{k_2} = p_{k_3} + G$$

Equation 3.3

The reason behind this is that the k-vectors of the original two phonons push the resultant phonon's k-vector outside of the first Brillouin zone. k-vectors pointing outside the first Brillouin zone can be remapped back into the first Brillouin zone by addition or subtraction of a reciprocal lattice vector, shown schematically in Figure 3.2.

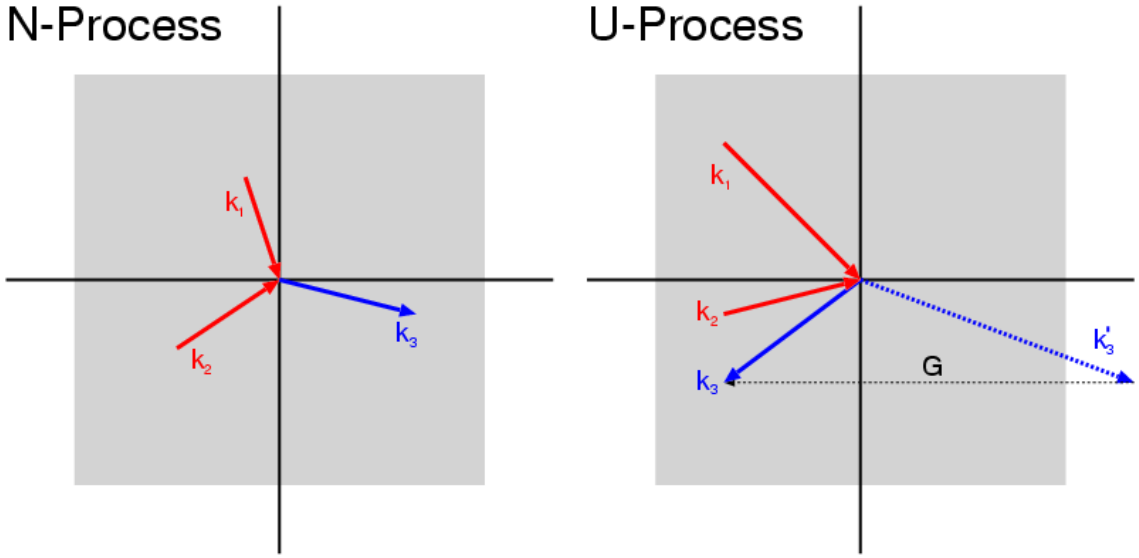

Figure 3.2 Normal and Umklapp type scattering processes [193].

However the distinction between these processes depends upon the definition of the basic cell of the reciprocal lattice [194]. Both phonons scattering processes are capable of reducing the thermal conductivity of the system as the heat-flux of is given by the product of the phonon's energy and group velocity. Therefore as long as a scattering event produces a phonon with a lesser or reversed group velocity the thermal conductivity of the lattice will be reduced. A fuller discussion of these principles is given by Maznev [194].

The thermal conductivity itself can be calculated via a number of methods, which can be broadly categorised into two approaches. The first approach involves solving the

Boltzmann transport equation using lattice dynamics and the other involves measuring the thermal conductivity within molecular dynamics simulation.

The molecular dynamics approaches may be subdivided further into two approaches. The first approach is based on non-equilibrium simulations where a temperature gradient is imposed and the response measured. The second approach is an equilibrium method and relies on obtaining the thermal conductivity the Green-Kubo relations.

3.2. Calculation of Thermal Conductivity

3.2.1. The Boltzmann Transport Equation

The calculation of thermal conductivity via the Boltzmann transport equation is very complex and too extensive to cover here. In brief, the finite displacement method is used to generate the third-order dynamical matrix. The harmonic phonon frequencies (ω_λ) are obtained from the second-order force constants as

discussed in Chapter 3.1.1. Additionally, the third-order force constants are used to obtain the imaginary part of the phonon self-energy (Γ_λ). Next the phonon self-energy and the harmonic phonon frequency (ω_λ) are used to calculate lifetimes of the phonons (τ_λ), Equation 3.4.

$$\tau_\lambda = \frac{1}{2\Gamma_\lambda(\omega_\lambda)}$$

Equation 3.4

It is also assumed that the phonon relaxation time is equivalent to the phonon lifetime under the single mode relaxation time approximation (SMRT), Equation 3.5.

$$\tau_\lambda^{SMRT} \equiv \tau_\lambda$$

Equation 3.5

Finally, the number of unit cells (N), system volume (V_0), mode dependent heat capacities (C_λ), group velocities ($\boldsymbol{v}_\lambda$) and phonon lifetimes (τ_λ^{SMRT}) are used to calculate the thermal conductivity (κ), Equation 3.6.

$$\kappa = \frac{1}{NV_0}\sum_{\lambda} C_\lambda \boldsymbol{v}_\lambda \otimes \boldsymbol{v}_\lambda \tau_\lambda^{SMRT}$$

Equation 3.6

A more complete description of the method is given by Togo et al.[122].

3.2.2. The Direct Method

The direct method has been used extensively to calculate the thermal conductivity of various systems [123, 195-198]. The direct method involves defining two regions in the simulation cell as reservoirs which have thermostats applied to maintain a temperature difference. The use of two thermostatted regions means the system is not in equilibrium, and so this method is also known as the Non-Equilibrium Molecular Dynamics (NEMD) method.

The reservoirs are thin layers, periodic in 2D and perpendicular to the X direction of the simulation cell. They are positioned half the simulation cell apart in the X direction so that they are equally spaced across the periodic boundaries as well, Figure 3.3.

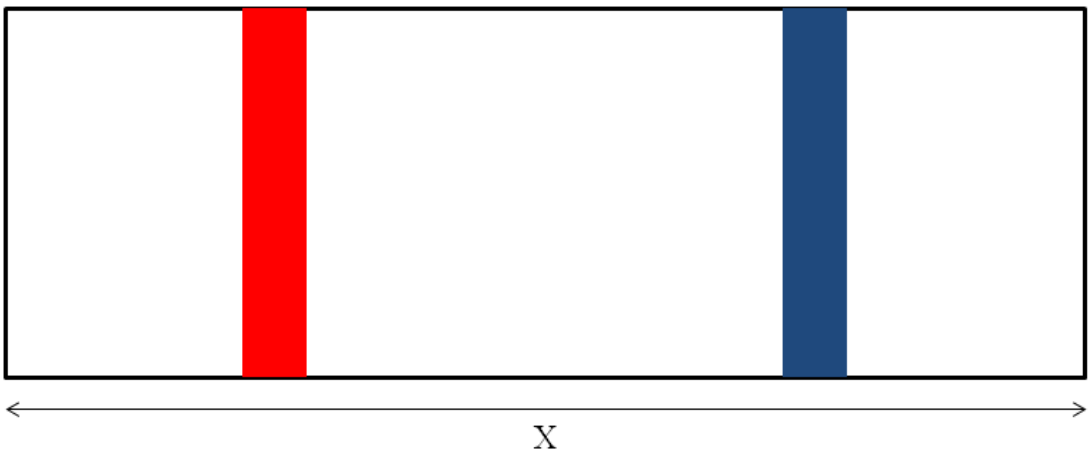

Figure 3.3 Layout of a NEMD simulation cell. Hot slab in red, cold slab in blue.

The total energy removed and added to the system by the thermostats is monitored and is equal to the heat-flux. Then by measuring a temperature profile the thermal conductivity can be calculated using Equation 3.7.

$$\kappa = -\frac{J}{\delta T/\delta x}$$

Equation 3.7

where J is the heat-flux, δT is the temperature difference between the reservoirs and δx is the distance over which the thermal gradient is measured. These types of systems must be large to ensure a diffusive regime is reached and avoid ballistic transport of phonons between the reservoirs.

The effect of having hot and cold reservoirs means the phonon mean free path in the X direction of the unit cell is limited. Therefore simulations of various lengths are often conducted, with the value of thermal conductivity for an infinitely long simulation cell extrapolated using Equation 3.8.

$$\frac{1}{\kappa_L} = \frac{1}{\kappa_\infty} + \frac{\alpha}{L}$$

Equation 3.8

where κ_L is the thermal conductivity for a given simulation cell length, L. α is a coefficient independent of simulation cell length and κ_∞ is the bulk thermal conductivity at infinite length. This expression holds well for most materials but for some it fails to give reasonable values for thermal conductivity.

A general problem with direct methods is that of isotropy. For isotropic systems the calculations need only be done once. However for anisotropic systems the series of calculations must be repeated for each distinct direction.

Further problems are also introduced by the presence of the reservoirs. In the reservoir regions the velocities of the atoms are being constantly adjusted and therefore the reservoir acts much like a barrier to the phonons and hence thermal transport. In bulk materials this is not so much an issue as the material is periodic over short distances and the structure in the region of the reservoir will be repeated elsewhere. However, in complex nanostructured systems there are likely to be large infrequent defects, and a reservoir placed on these defects will exclude their effect on thermal transport.

Issues also arise from using thermostats on the reservoirs as the choice of thermostat parameters can affect the rate of heat transport. Using a constant heat-flux regime where the amount of energy added/removed to the reservoirs per timestep is constant can mitigate this problem.

In the constant heat-flux direct method it is important that the amount of energy removed from the cold reservoir should match the amount of energy added to the hot reservoir. This approach requires scaling of all velocities within the reservoir region; a simpler approach involves swapping of velocities between the two regions, outlined below.

3.2.2.1. The Reverse Non-Equilibrium Molecular Dynamics (RNEMD) Method

The reverse non-equilibrium molecular dynamics (RNEMD) method by Müller-Plathe [126] is a variant of the direct method which is very similar to the constant heat-flux regime as implemented in the standard direct method. The difference of the RNEMD method is that it uses kinetic energy swapping between the hottest atom in the cold reservoir and the coldest atom in the hot reservoir to generate the temperature gradient. Thus the heat-flux between the two reservoirs is equal to the sum of the total energy transferred.

The mechanics of this approach mean that the heat-flux can be finely controlled by adjusting how often the kinetic energy swaps are performed.

The distribution of kinetic energies at the target temperature means that it is usual for the hottest atom in the cold reservoir to have more kinetic energy than the coldest atom in the hot reservoir. Even if this were not the case the swapping of kinetic energies should ensure there is always some overlap between the kinetic energy distributions, and hence a small temperature differential is ensured.

A significant advantage of this method is that the heat-flux is known exactly. The heat-flux in the direct method is measured and subject to large fluctuations, making the value slow to converge. Whereas in the RNEMD method the value to converge is the temperature gradient, which is averaged over atoms and time and thus should be faster to converge.

Despite these advantages the RNEMD method still requires calculation of multiple sizes and orientations of the same system to obtain reasonable results while the issue of reservoir location still remains for large nanostructures. Alternative schemes based on similar principles have also been proposed [199].

3.2.3. The Green-Kubo Method

The thermal conductivity can also be calculated from systems in equilibrium by using the Green-Kubo relations [124, 125]. In the Green-Kubo method the heat-flux of the system is calculated at intervals and the processed to give the thermal conductivity. The advantages are that the system is always in a steady state regime with no artificial boundaries and finite size effects are somewhat minimised.

First the heat-flux of the system is calculated using:

$$\boldsymbol{J} = \left[\sum_i e_i \boldsymbol{v}_i - \sum_i \boldsymbol{S}_i \boldsymbol{v}_i\right]$$

Equation 3.9

where $\boldsymbol{J}$ is the heat-flux, e_i is the energy of atom i, $\boldsymbol{v}_i$ is the velocity vector for atom i and $\boldsymbol{S}_i$ is the stress tensor. This may also be expanded to give:

$$\boldsymbol{J} = \left[\sum_i e_i \boldsymbol{v}_i - \sum_{i<j} (\boldsymbol{f}_{ij} \cdot \boldsymbol{v}_j)\boldsymbol{r}_{ij}\right]$$

Equation 3.10

and further:

$$\boldsymbol{J} = \left[\sum_i e_i \boldsymbol{v}_i - \frac{1}{2}\sum_{i<j} \left(\boldsymbol{f}_{ij} \cdot (\boldsymbol{v}_i + \boldsymbol{v}_j)\right)\boldsymbol{r}_{ij}\right]$$

Equation 3.11

where $\boldsymbol{f}_{ij}$ represents the force and $\boldsymbol{r}_{ij}$ the separation between atoms i and j.

A time averaged autocorrelation of the heat-flux is then taken and integrated, yielding a value proportional to the thermal conductivity:

$$\boldsymbol{\kappa} = \frac{s\Delta t}{V k_B T^2} \int_0^\infty \langle \boldsymbol{J}(0) \cdot \boldsymbol{J}(t) \rangle \Delta t$$

Equation 3.12

where s is the integer number of steps between heat-flux sampling, Δt is the timestep of the simulation, V is the volume of the system, k_B is Boltzmann's constant and T is the temperature of the system.

It is important to select the timestep such that the highest frequency vibration in the system is accurately reproduced to ensure physical dynamics. Furthermore, the choice of heat-flux sampling interval is important as it must accurately capture the highest frequency mode which partakes in phonon scattering.

The Green-Kubo method gives a thermal conductivity tensor as a result, instead of a single scalar value. The advantage gained over the direct method is that only one calculation is required for any material, as opposed to multiple calculations at different systems and lengths and in different directions. The advantage of the tensor output also extends to anisotropic materials (such as quartz), extended defects (such as grain boundaries) and highly nanostructured materials.

A drawback of the Green-Kubo method is that long simulations/multiple simulations are required to properly sample the ensemble average. It may require tens of ns for the heat-flux autocorrelation function to converge. Additionally, the point of convergence and thus the error may be difficult to identify.

3.2.3.1. Deciding The Integral Cutoff

The autocorrelation function for a bulk ionic solid tends to be quite simple. It resembles an exponential damped cosine wave, Figure 3.4 and Figure 3.5.

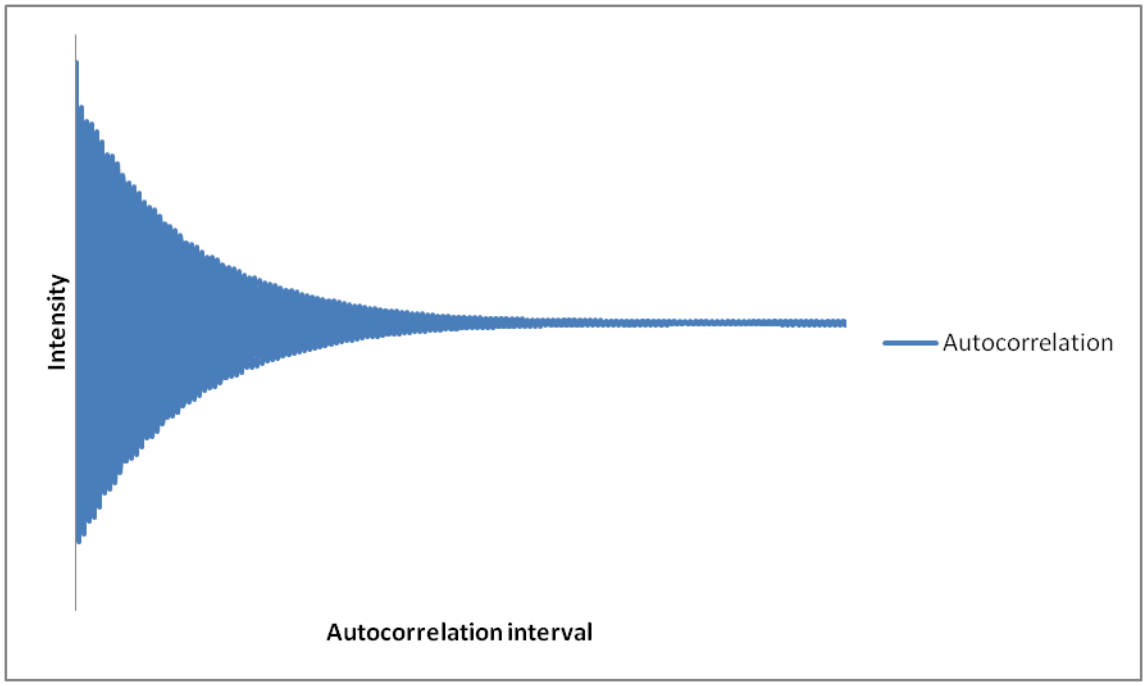

Figure 3.4 Heat-flux autocorrelation.

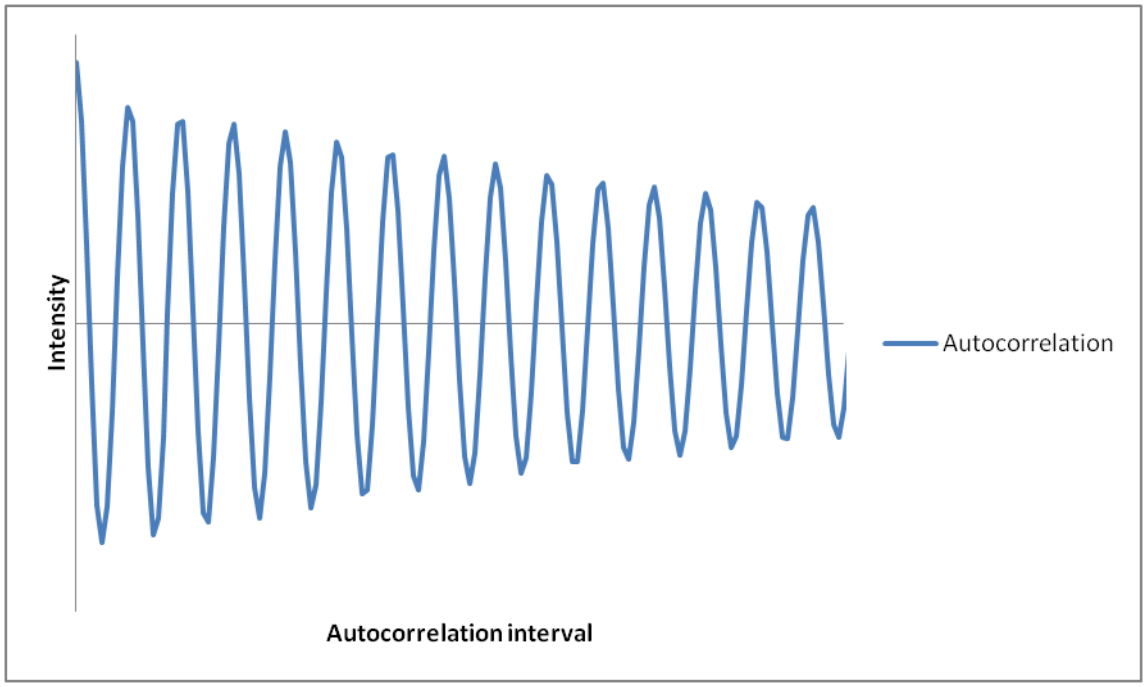

Figure 3.5 Heat-flux autocorrelation (fine detail).

Indeed, for simple systems fitting the data points to such an expression is possible, with the integral then calculated analytically. However for more complex systems this type of fitting becomes very difficult.

The exponential decay component of the autocorrelation is related to the lifetime of the acoustic modes and the sinusoidal component is related to optical phonons that are transporting heat locally but not contributing to long range transport. The more complex a system is, the more modes must be included to get a reasonable fit. For defective systems the fit becomes more difficult still due to the large range of frequencies a defect may operate over.

For the complex systems presented here a numerical integration must be used and requires the choice of an integration cutoff. As there will always be some thermal noise it is necessary to average over a portion of the integral [200]. The averaging aims to remove random noise while preserving the signal underneath. The choice of parameters is somewhat arbitrary and difficult to define with this method, and error calculation is also difficult [201].

An example of a Green-Kubo integral is given in Figure 3.6 for the MgO system detailed later in Chapter 4.2.2. The value at each time interval is the thermal conductivity should the autocorrelation be integrated only up to that point.

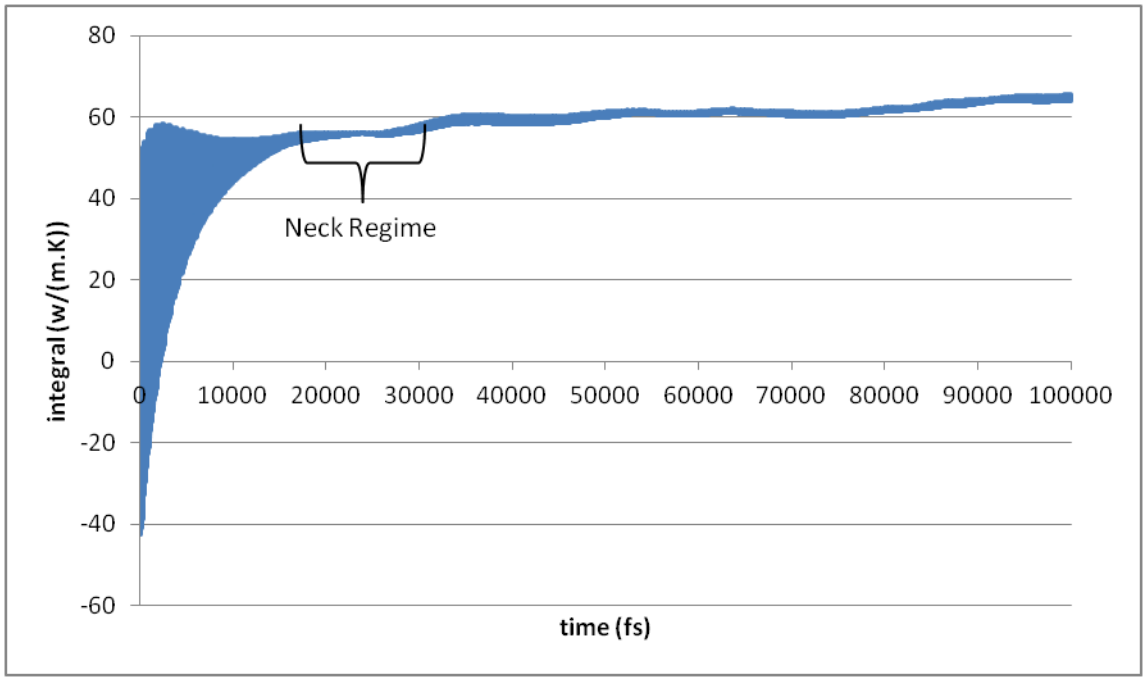

Figure 3.6 Example at 300 K with increasing integration. Example neck regime highlighted.

In this work the method of McGaughey [202] has been used where the thermal conductivity integral is averaged over a period called the neck regime. The neck regime

occurs when the value for thermal conductivity plateaus and before statistical error begins to contribute significantly to the thermal conductivity, Figure 3.6. The start and finish of the neck regime itself may also change significantly between materials, temperature and nanostructure. For this work, the neck regime has been defined for each bulk material independently to simplify analysis, and kept the same for nanostructures of the same material.

3.2.3.2. Green-Kubo Error Analysis

The error on the thermal conductivity as calculated by the Green-Kubo method is very hard to define [203, 204]. To ensure maximum accuracy the thermal conductivity is calculated by passing heat-flux values as calculated by LAMMPS (Appendix C) to an in-house code (Appendix D) which performs the autocorrelation and integration. This code uses the heat-flux values from the entire data set rather than using windowed time-frames as is done natively in LAMMPS. The advantage gained is that a shifting initial timestep can be used in the autocorrelation calculation, boosting accuracy. Additionally, the full cross-correlation tensor can be computed, giving access to the diagonal X, Y and Z components as well as the off-diagonal values (which should be zero).

There are several sources of error on both the heat-flux values and originating within the method itself. The contributing factors include:

- Error of autocorrelation point. Each point of the autocorrelation is generated by averaging the correlation between a large number of time intervals and so the accuracy of this value depends upon the number of time intervals available.
- The error of integration. The exact calculation of thermal conductivity from the autocorrelation requires integration over continuous time. However only discrete time is available in molecular dynamics and so errors are present stemming from interpolation over the gaps in the data. This work has used a sampling frequency of 10 fs and integration of the autocorrelation was performed using a running trapezoidal rule.
- The cut-off time for the integration. The final value of thermal conductivity is given by integrating up to a given time where the autocorrelation has completely decayed. As the Green-Kubo method relies on sampling the thermal noise of the system and relating it to thermal conductivity there is always some noise

remaining in the autocorrelation. Thus deciding the point at which the autocorrelation has fully decayed is extremely challenging as including values after the decay point only serves to add error from random noise. Choosing the cut-off point is not simple and varies from temperature to temperature, material to material and between different nanostructures/defects.

The calculation of error is still not simple as each point within the neck regime is dependent upon the previous points and influenced by the errors outlined above. Therefore a simple standard error cannot be calculated and instead the error in this work is represented as the difference between the maximum and minimum values within the neck regime. With this approach some representation of the fluctuation in thermal conductivity values is retained.

3.2.3.1. The Green-Kubo Spectrum

If the Fourier transform of the heat-flux autocorrelation function is taken, a spectrum is yielded which relates to the periodic oscillations observable in the heat-flux autocorrelation function [202].

These oscillations have been shown to arise from a certain subset of optical phonon modes at the gamma point of the first Brillouin zone [115]. The subset of allowed phonon modes in the Green-Kubo spectrum seems to be related to the symmetry of the vibrational mode; modes which are symmetrical do not appear whereas the asymmetrical modes do.

While these optical modes do not transport a significant portion of heat they are still capable of interacting with the heat carrying acoustic modes and thus the heat-flux of the system [115, 205].

3.2.3.2. Serial and Parallel Heat-Flux Collection

The calculation of the heat-flux autocorrelation requires heat-flux data to be continuous as the important property is the strength of the relation between the heat-flux at one time and the heat-flux at another time. However, at longer intervals the heat-flux is not expected to be strongly correlated and thus the simulation may be divided into several different runs and then averaged later. By dividing the simulation into different runs, each starting with different velocities, the amount of data available for smaller time

intervals will also be reduced. An expression may be derived to predict the number of fewer data points available at any given time interval within the autocorrelation by the splitting of the calculation across several simulations.

The set of parallel simulations may be considered a single serial simulation with discontinuities in the heat-flux data set. In this pseudo-serial run there will be $n-1$ discontinuities in the heat-flux data set.

The total number of missing data points contributing to the autocorrelation in a set of parallel simulations as compared to a serial simulation is a function of the interval length and the number of discontinuities.

At a timestep interval of zero there are no missing data points in a set of parallel simulations as compared to a serial simulation as there is no need to cross a discontinuity. At a timestep interval of 1 the number of missing data points is $1 \times (n-1)$ as there will be one missing autocorrelation values per discontinuity. Similarly at a timestep interval of 2 timesteps the autocorrelation will have $2 \times (n-1)$ missing values in the autocorrelation. The general expression is given by:

$$m_p = p(n-1)$$

Equation 3.13

where m_p is the number of missing heat-flux data points at point p of the autocorrelation and n is the number of parallel simulations. The number of data points contributing directly to any autocorrelation point in a sequential simulation can also be stated:

$$s_p = t - p$$

Equation 3.14

where s_p is the number of data points contributing to the autocorrelation at timestep interval p and t is the total number of heat-flux data points in the data set. By dividing m_p by s_p the fraction of missing values contributing to any autocorrelation point may be derived.

As the fraction of missing data points increases linearly with the autocorrelation interval these values remain insignificant well beyond the point of decay for simulations

containing several ns of data collection for each parallel simulation. Additionally the additional averaging over phase space may offset the introduced error entirely [206].

3.2.4. Finite Size Effects

Thermal conductivity calculations are particularly susceptible to finite size effects due to their reliance on vibrational modes of the system. If the wavelength of the vibration is limited (such as by periodic boundary conditions) then the number of heat conducting modes is also limited.

An example of the extreme case is a single particle in a periodic box. As there is a single particle in the primitive unit cell and the number of vibrational modes is $3N - 3$, no vibrational modes are present. Acoustic modes are technically present in the form of lattice translations, however their frequency is imaginary. Clearly the thermal conductivity of such a system makes no sense as heat cannot be transported internally.

It is by expanding the simulation cell for the system that vibrational modes become accessible. These may be acoustic or optical, which may or may not interact with the acoustic modes. Figure 3.7 shows various simulation cell sizes and their respective lowest frequency optical mode. Note that expansion of the cell may lose modes allowed in smaller systems (e.g. lowest frequency mode in a x2 expansion in the x3 expansion).

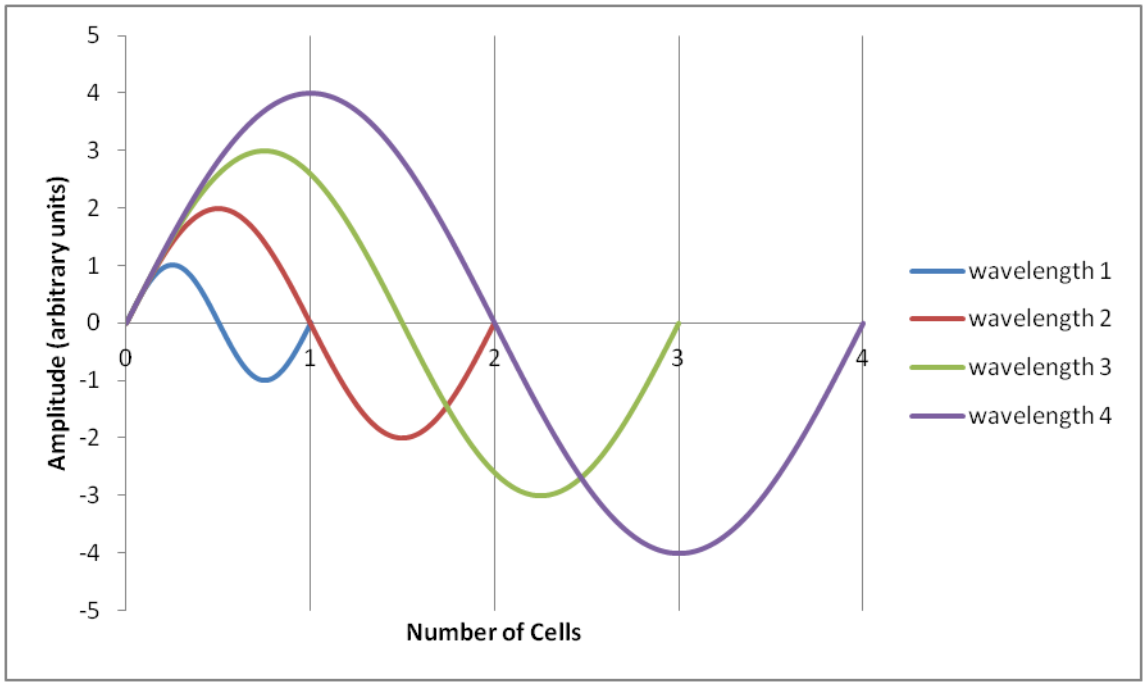

Figure 3.7 The lowest frequency allowed optical modes in different simulation cell expansions. Note that the wave of wavelength 2 is forbidden in the x3 expansion of the cell and likewise the wave of wavelength 3 is forbidden in the x4 expansion of the cell.

The complex interaction of phonons in a small simulation cell can lead to spurious effects where acoustic phonons do not scatter before crossing a region they have only recently passed. The effect may result in constructive or destructive interference depending on the size of the simulation cell and the wavelength of the phonons.

Finite size effects in defective materials are less important than in their bulk counterparts. The scattering centres introduced by the defects lead to a much shorter phonon mean free path and thus the limited size of the simulation may become less of an issue. However different defects interact or scatter phonons to different degrees, meaning some finite size effects may still remain.

3.2.4.1. BTE Methods

BTE methods employing lattice dynamics calculations are most susceptible to neglecting longer wavelength phonons due to the large memory requirements of the dynamical matrix, and thus small simulation cells. The problem of incommensurate waves outlined in Figure 3.7 is also present but may be compensated for by using multiple simulation cells of different sizes to better to describe the first Brillouin zone;

however this leads to the risk of small simulation cells and thus spurious force constants.

3.2.4.2. Direct Methods

Finite size effects are most important in direct method simulations where the temperature gradient is sustained over a finite distance. The distance between the two reservoir regions acts to limit the allowed wavelength of the phonons and thus multiple simulations are often required. The calculated thermal conductivity of these systems is then extrapolated to infinite length.

3.2.4.3. Green-Kubo Method

Green-Kubo calculations are performed at equilibrium and the lack of reservoirs allows acoustic phonons to pass through the system multiple times before scattering, thus reducing the problem of finite size. However, the maximum allowed wavelength of a phonon is still limited by periodic boundary conditions and interference is now possible. Therefore, convergence of the thermal conductivity with respect to system size must still be ensured.

4. The Effect of Nanostructuring on the Thermal Conductivity of Magnesium Oxide (MgO)

The aim of the work in this chapter is to apply potential based techniques to calculate the thermal conductivity of bulk MgO via the Green-Kubo method and investigate the effect of extended defects and nanostructures. These systems are expected to give a significant reduction in the thermal conductivity which depends upon the structure of the boundary and nanostructure.

Before presenting the results, a brief overview of MgO is given discussing the importance of MgO as a material and why its thermal conductivity is studied. Previous computational work on the thermal conductivity of MgO is also discussed. Throughout this work thermal conductivity is used to refer specifically to lattice thermal conductivity, excluding electronic and radiative contributions.

4.1. MgO Overview

Magnesium oxide (MgO) is one of the most abundant materials on the planet and comprises a significant portion of the earth's lower mantle [207, 208]. In this context MgO is also known as periclase and when in conjunction with iron, ferropericlase. As this material exists deep in the earth's mantle it is subject to extreme temperature and pressure conditions. These conditions are difficult to access experimentally but can be simulated relatively easily.

In addition to being important geochemically, MgO and other binary metal oxides have found many uses in industrial applications such as in ceramics and in refractory materials [209-211] and as a potential component of immobilisation matrices for nuclear fuels [212, 213]. Many of these applications involve high temperature conditions and can benefit from a greater understanding of the thermal transport in these materials.

MgO is a simple binary oxide compound with the rocksalt structure. The ionic nature of bonding in MgO and its simple structure means that thermal transport processes and the effect of defects can be understood more easily than in systems with complex structures and bonding. Some materials structurally similar to MgO are NiO, FeO, MnO and CoO,

which are of interest as possible thermoelectric materials [214], as they contain relatively cheap transition metal cations. Thus, MgO is a good model system.

Previous work has been performed on MgO, both experimentally and computationally. The thermal conductivity of MgO has been measured experimentally and has given fairly consistent results [215-217]. The calculation of thermal conductivity computationally is somewhat more challenging due to many factors such as simulation size, timescale and most importantly accurate representation of interactions. Despite these challenges, the thermal conductivity of MgO has been calculated using several different techniques.

Ab initio techniques derive the interatomic interactions from first principles calculations on the electronic structure. These types of calculations are computationally expensive and so most often use lattice dynamics to solve the Boltzmann transport equation [121, 122, 218] using very small simulation cells. Other approaches to calculate the thermal conductivity using ab initio methods have also been tried. Ab initio non-equilibrium molecular dynamics (NEMD) simulations have also been used to calculate the thermal conductivity of MgO and produced a good match to experimental values [219]. Hybrid approaches using data from both ab initio molecular dynamics and ab initio lattice dynamics have also been demonstrated [220].

Classical modelling has also been successfully applied to MgO as the simple ionic interactions can be well described by pair potentials. There are many potential models available [127, 145, 221, 222] which have been applied to calculate many bulk and defect properties [165, 222, 223]. However, care must be taken when selecting a potential model for calculation of the thermal conductivity as the anharmonic properties of the potential [192] have a significant effect, meaning that it is important for the potential model to be accurate away from equilibrium.

To date, there have been relatively few studies calculating the thermal conductivity of MgO due to the long time and length scales required to achieve a converged and accurate result. Despite these problems, some work has been done to calculate the thermal conductivity of MgO using computational methods. Shukla et al. [127] used the NEMD method to calculate the thermal conductivity of both bulk and polycrystalline MgO to assess its possible inclusion with other materials as an inert matrix for nuclear fuels. The high thermal conductivity of MgO is appealing in these circumstances but it

must be mixed with other materials to reduce the solubility of the matrix in water [212, 213]. The same study also demonstrated an order of magnitude reduction in thermal conductivity when a polycrystalline sample of MgO was simulated. However, the polycrystalline system studied was a simple approximation constructed from a collection of hexagonal grains, infinite in one direction and tiling in the other two. Within each grain the bulk MgO material was randomly orientated around the {001} axis, meaning the boundaries formed are likely far from the most energetically favourable.

Thus a more systematic study of the effect of different grain boundaries on the thermal conductivity is required. By studying individual boundaries more information can be gained about the phonon scattering mechanisms at a specific interface. This knowledge can then be used to generate materials with desirable thermal characteristics.

The potential model used in this work for MgO was developed by Shukla et al. [127] and was chosen as it was specifically designed for accurate thermal conductivity calculations. The model has been fitted against the structure, lattice parameter and thermal expansion. As this model is rigid ion, there may be some small discrepancies from experiment due to the non-polarisable nature of the ions.

Initially, the bulk properties of MgO will be calculated and compared against experimental values, Chapter 4.2. This is important as both the potential model and the approaches used to calculate thermal conductivity in this work must be verified. Additional information will also be derived to explain the scattering mechanism in bulk MgO.

The work will then be extended to study two different grain boundary systems in Chapter 4.3. The two systems are expected to scatter phonons differently due to their different structures and whether the difference in scattering mechanism leads to significantly different thermal conductivities will be examined.

The same methods are finally applied to different complex nanostructures in Chapter 4.4. The nanostructures used in this work originate from Sayle et al. [224] and were built by positioning molten MgO on crystallographic sites and then allowing them to cool and form complex hierarchical nanostructures. This method is known as amorphisation and recrystallisation.

By using this hierarchical approach a more nuanced understanding of the phonon scattering in MgO is obtained and can be used to guide the engineering of nanomaterials to either enhance or reduce the thermal conductivity. These methods may then be applied to more promising thermoelectric materials with similar structure to MgO.

4.2. Bulk MgO

MgO has a simple face-centred cubic structure with the space group $Fm\bar{3}m$. Both magnesium and oxygen atoms within the lattice are 6-fold coordinated. The calculated lattice parameter and independent elastic constants have been calculated using the potential model of Shukla et al. [127] using METADISE [165] and are compared to experiment in Table 4.1.

Property	Calculated	Experiment	% Difference
a (Å)	4.20	4.21	-0.24
c_{11} (GPa)	279.90	298.96	-6.37
c_{12} (GPa)	128.32	96.42	33.08
c_{44} (GPa)	128.32	157.13	-18.34

Table 4.1 Calculated and experimental [225, 226] structural properties of MgO.

Some deviation from experimental values is expected due to the finite temperature at which experiments are performed, whereas energy minimisation gives the values at effectively zero Kelvin (excluding even zero-point motion). The lattice parameter and c_{11} elastic constant are reproduced well but the c_{12} and c_{44} elastic constants deviate from experimental values. This deviation is a well-known artefact of rigid-ion pair potentials in the rocksalt structure and is caused by the Cauchy condition [227].

The Cauchy condition arises from the high symmetry found in some materials. For the Cauchy condition to apply the material must be of cubic symmetry, there is no initial stress, forces must be central and all atoms must be at a centre of symmetry. The reason this does not arise experimentally is that the magnesium oxygen interaction is not central due to the polarisability of the species, whereas the potential model here is rigid-ion. A more complete discussion may be found in Kittel [135].

Despite the limitations imposed by the Cauchy condition, the c_{12} and c_{44} lattice constants are still acceptable as their value falls between those of the experimental c_{12} and c_{44} elastic constants. The elastic constants are an important property for a potential model to reproduce well as they are dependent on the curvature of the potential interactions which will have a significant impact on the thermal expansion and conductivity.

As the property of interest in this work (thermal conductivity) is only available at finite temperatures, having static lattice properties is not sufficient to determine the applicability of the potential model. However, as a full thermal conductivity calculation is computationally expensive, it is wise to explore other properties, which arise from anharmonic interactions and which converge faster before proceeding with a full thermal conductivity calculation. The thermal expansion is a good measure of the potential models applicability as it derives directly from anharmonic phonon interactions [127, 228] and is relatively quick to calculate from molecular dynamics simulations.

4.2.1. Thermal Expansion

The thermal expansion of bulk MgO was calculated using molecular dynamics simulations under an NPT ensemble (using a Nosé–Hoover thermostat and barostat) within the LAMMPS [166] simulation code. A simulation cell of 10 x 10 x 10 eight atom cubic unit cells (approximately 42 Å along each side) was prepared, containing a total of 8,000 atoms. The a, b and c lattice vectors were allowed to vary independently while the angles α, β and γ were held fixed at 90°. Six different temperatures (300 K, 500 K, 700 K, 900 K, 1100 K and 1300 K) were simulated for 0.5 ns and the lattice vectors recorded every 10 timesteps. A timestep of 1.0 fs was used due to the potential model being rigid-ion. The simulation was deemed to converge if the energy fluctuations were consistently less than 0.1% of the average energy value and the volume fluctuations were less than 0.5% of the average volume; these criteria are applied to all NPT simulations in all materials. The converged lattice constant of MgO is plotted alongside experimental data in Figure 4.1.

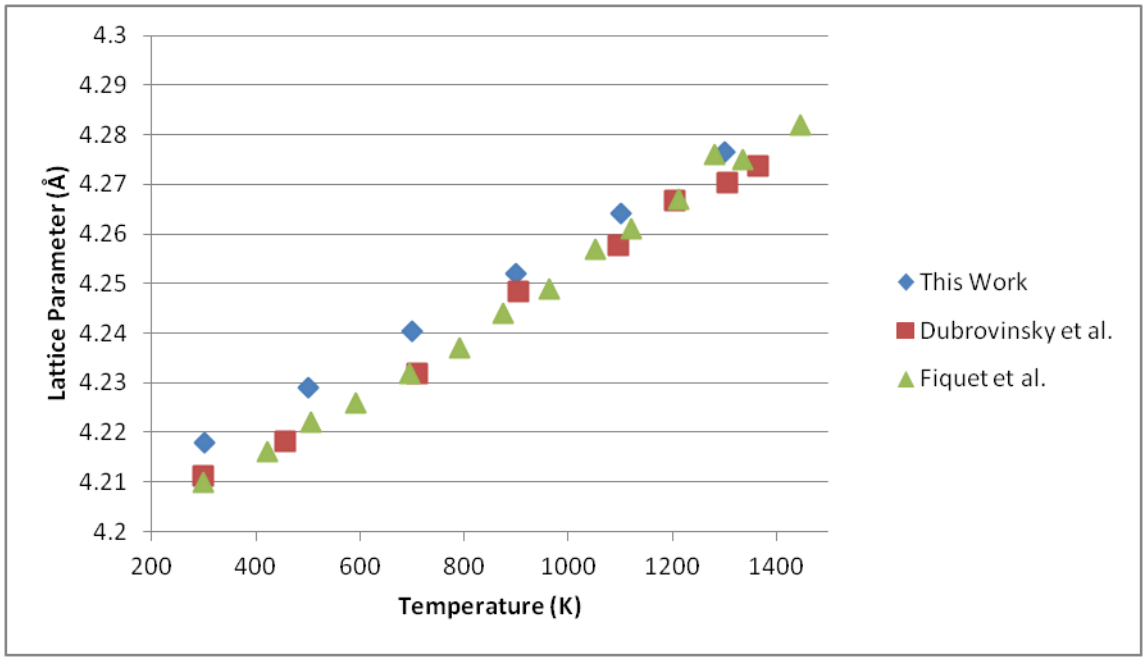

Figure 4.1 Thermal expansion of a MgO supercell using the potential model of Shukla et al. [127] compared to experiments [229, 230].

The experimental values of Dubrovinsky et al. [229] and Fiquet et al. [230] were both obtained using X-Ray experiments. The values of Dubrovinsky et al. were estimated to have an error of less than $5x10^{-4}$ Å at the temperatures presented here. The work of Fiquet et al. demonstrated very similar results across many previous studies using multiple techniques.

The thermal expansion is reproduced very well by the potential model and matches experimental data very closely; the lattice parameter is within 1% of the experimental values at all temperatures. Additionally the thermal expansion coefficients match reasonably well over the temperature range of 300 K to 1300 K. A linear fit is made to the values within the range of interest for all data sets. The gradient of the fit may then be used to compare the calculated expansion of MgO. The calculated value of the gradient in this work is $1.38x10^{-5}$ K^{-1} which compares favourably with the values of $1.95x10^{-5}$ K^{-1} for Dubrovinsky et al. and $1.66x10^{-5}$ K^{-1} for Fiquet et al..

As the thermal expansion is reproduced well by the potential model, it can be concluded that the anharmonic interactions are reasonable and that an equally reasonable thermal conductivity may be produced.

4.2.2. Thermal Conductivity

The thermal conductivity of a material may be calculated in many ways. Two very different approaches to calculating the thermal conductivity are via molecular dynamics and lattice dynamics. The Green-Kubo method calculates the thermal conductivity from heat-flux data generated via long timescale molecular dynamics simulations. The lattice dynamics method utilises the Boltzmann transport equation (BTE) to calculate the thermal conductivity from the dynamical matrix obtained via the finite displacement method [122].

The results from the Green-Kubo calculations and the lattice dynamics calculations are not expected to be identical. Where one method fails the other excels. Green-Kubo calculations include all anharmonic terms whereas the lattice dynamics calculations tend only to include up to the third-order force constants. While lattice dynamics calculations are in principle exact within the approximations made, in Green-Kubo calculations it is more difficult to know when a converged result is achieved (Chapter 3.2.3.1) although there are methods available to assist in the determination [202].

Thus the Green-Kubo and lattice dynamics methods are expected to give complimentary information. Furthermore lattice dynamics calculations are able to give additional information on the phonon modes contributing to scattering.

4.2.2.1. Green-Kubo Results

Molecular dynamics simulations to calculate thermal conductivity via the Green-Kubo method were performed under the NVT ensemble (with a Nosé–Hoover thermostat) to better control the temperature fluctuations in the finite sized cell. Early tests showed no significant deviation in thermal conductivity from an NVE ensemble. The timestep used was 1.0 fs.

The simulation cell used was the same as that for the thermal expansion calculation (cubic supercell of 8,000 atoms), with the lattice vectors set to their average at each temperature. A run of 0.5 ns of NVT equilibration was conducted to ensure thorough thermalisation of the system and that the initial velocities had no spurious effect on the final result. Subsequently, heat-flux data was collected for 10 ns with the heat-flux being sampled every 10 fs. Due to the isotropic nature of magnesium oxide, further averaging can also be done over the three independent directions X, Y and Z.

As discussed in Chapter 3.2.3, the thermal conductivity will be extracted from the integrated heat-flux autocorrelation by selecting a convergence region. This region is known as the neck regime and has been chosen so that the maximum fluctuation within the region is as small as possible. Figure 4.2 gives a plot of the average thermal conductivity with fluctuations as a function of possible neck regime for the 500 K simulation. Each possible regime spans 5,000 fs and each point is set to be at the midpoint of the regime.

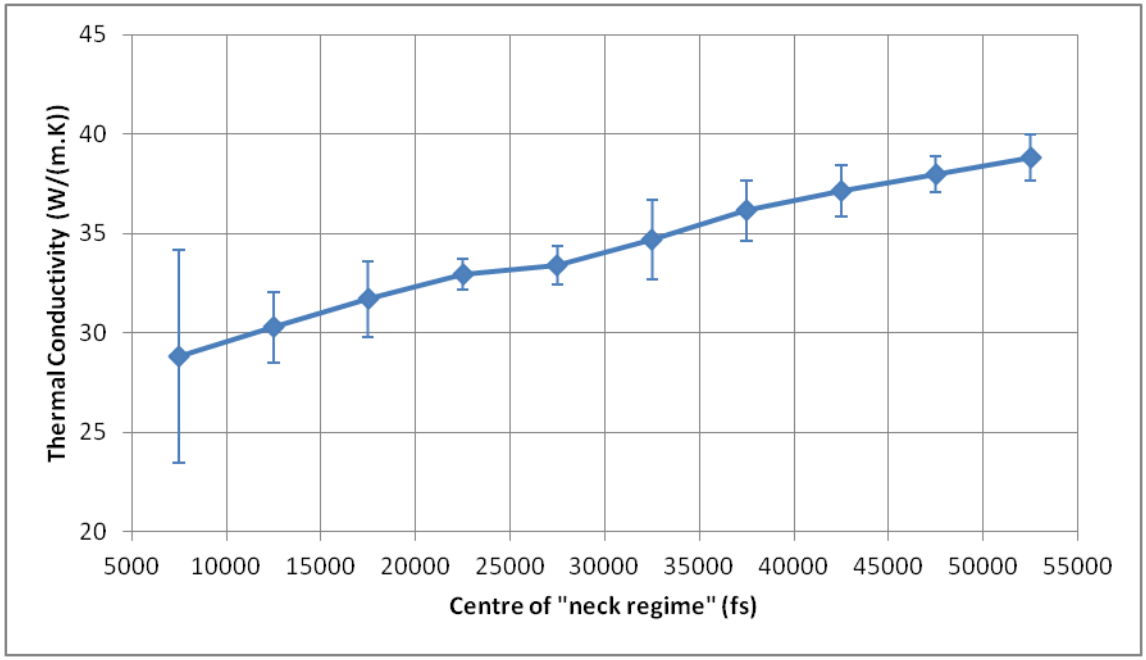

Figure 4.2 The average value of thermal conductivity at 500 K within different possible neck regimes. Each data point is set to the midpoint of a 5,000 fs window. Error bars represent the size of the fluctuation.

The neck regime for this temperature is found to be between 20,000 and 25,000 fs as the size of the fluctuations is minimised. The neck regime remains valid as long as the autocorrelation lifetime is the same length or shorter, additionally significant deviations should not arise at longer timescales. These requirements are fulfilled at higher temperatures and in nanostructured materials. Thus the neck regime is kept fixed for all MgO simulations across temperatures and nanostructures. Neck regimes for other materials are likewise chosen based on the neck regime of the lowest temperature bulk simulation.

While this approach simplifies analysis greatly, it must be applied carefully to avoid spurious values appearing in other systems; however the thermal conductivity integral at

lower temperatures tends to have larger fluctuations than at higher temperatures and so having a non-optimal neck regime at higher temperatures causes less difficulties.

When this approach is used across all temperatures for bulk MgO a smooth curve for the thermal conductivity is obtained, Figure 4.3. The smooth transition from one value to another supports the approach outlined above as there is no significant deviation from the expected inverse power law behaviour.

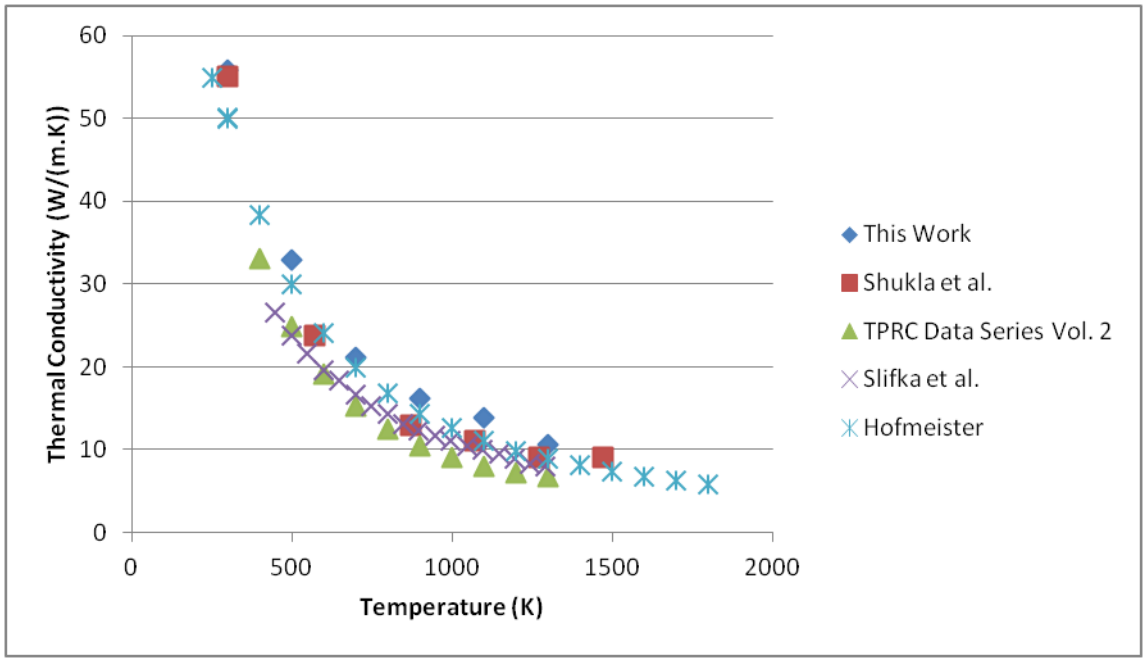

Figure 4.3 Calculated [127] and experimental [215-217] thermal conductivity of bulk MgO.

The thermal conductivity as calculated by the Green-Kubo method displays the expected inverse power law behaviour [231] characteristic of materials with dominating phonon-phonon processes. The values themselves match almost exactly with the values previously calculated by Shukla et al. [127] using the same potential model but using the NEMD approach. The values calculated in this work give a good match at low and high temperatures but deviate slightly between 900 K and 1100 K. The deviation may stem either from larger finite size effects found in the NEMD method or from the longer convergence time required in the Green-Kubo method.

The experimental work of Slifka et al. [216] used samples with 93% theoretical density and a grain size of 25 μm. Three MgO samples of various sizes were used in the experiment to allow the effect of interfacial resistance of the equipment to be factored

out. The different sized samples were combined in various ways to give the final values. Combination a) used the thermal conductivity from the 2.59 mm and 5.04 mm samples, b) used the 2.59 mm and 7.64mm samples while c) used data from the 5.04 mm and 7.64 mm samples. The thermal conductivity for each of these approaches was almost identical and so only the a) combination has been presented.

Deviations in the experimental results of Slifka et al. found at ~1300 K are noted as likely arising from failure of the experimental apparatus. The calculated thermal conductivity using the potential model is higher than these values as may be expected due to the perfect 100% density within the simulation.

The experimental work of Hofmeister [217] gave better agreement to calculated values as a sample of 96% theoretical density was used and thus the measured thermal conductivity values are higher and closer to the values calculated from simulation. This result also shows the difficulty with comparing directly with experiment, as a 3% change in density resulted in ~25% difference in the measured values at 500 K for experimental values. In simulations the system is a 100% perfectly dense infinite single crystal and it is thus expected that the calculated thermal conductivity will always be higher than experimental values.

The overall trend of the thermal conductivity values calculated from simulation matches very well to the standardised data from the TPRC Data Series [215] and the work of Hofmeister [217]. This similarity indicates that the response to temperature is being reproduced very well by the potential model and thus indicating that the phonon-phonon scattering processes are being well represented.

Additional information can be gained from the molecular dynamics simulations by applying a Fourier transform to the autocorrelation of the heat-flux. The frequencies obtained are of the optical phonon modes which interact with the heat-flux; these modes transport thermal energy locally but may also interact with the acoustic phonon modes which transport heat non-locally.

The Fourier transform of the heat-flux is called by the name Green-Kubo spectrum within this work but is known elsewhere as the spectrum of the heat-flux autocorrelation function (HFACF) or the spectrum of the heat-current autocorrelation function (HCACF). The Green-Kubo spectra for all temperatures are presented in Figure 4.4.

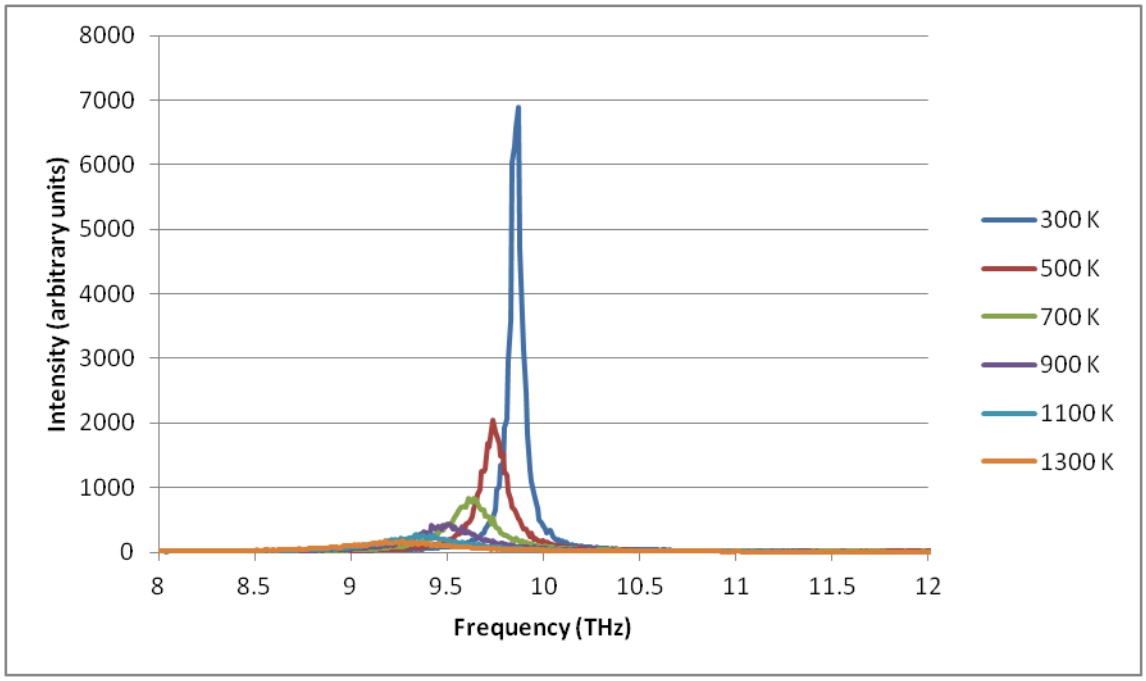

Figure 4.4 The Fourier transform of the heat-flux autocorrelation function for each temperature (Green-Kubo spectra).

It is clear from the Green-Kubo spectra that there is a single optical phonon mode with a frequency slightly less than 10 THz which reduces in frequency as temperature increases. The lowering of the frequency is partially due to the expansion of the lattice as the temperature increases, making the wavelength of the phonon longer and hence the frequency lower. The frequency shift also partially originates from the anharmonicity of the potential.

As the frequency of the mode is reduced, the probability of scattering an acoustic phonon increases due to the Bose-Einstein distribution (i.e. a greater population of acoustic phonons at lower frequency). As the scattering of acoustic phonons is increased, less thermal energy is being transported and thus the thermal conductivity decreases. A more thorough discussion is given by Dove [192].

The shape of the peaks may be understood in terms of the lifetime of the phonon mode. The autocorrelation function can be considered as a sine function (due to the optical modes) multiplied by an exponential decay (due to the acoustic modes). The peaks in the Green-Kubo spectra are thus Lorentzian (due to the exponential decay), centred at the frequency of the sine function. As the decay of the exponential function becomes shorter-lived the width of the Lorentzian increases. Thus, the width of the peaks in the

spectra are inversely proportional to the lifetime of the phonon modes [192]. The broadening of the peaks with increasing temperature is thus due to a reduction in the lifetime of the associated phonon mode.

The motion of atoms associated with the modes appearing in the Green-Kubo spectrum cannot be easily obtained directly but may be derived from lattice dynamics calculations as will be demonstrated later in the next section (Chapter 4.2.2.2).

In the next section the thermal conductivity of magnesium oxide is calculated using the same potential model but an alternative approach. The results from the two methods can then be compared to highlight the advantages and deficiencies of each.

4.2.2.2. Lattice Dynamics Results

Calculation of the lattice thermal conductivity can also be performed using lattice dynamics techniques. Phono3py [121, 122, 218] uses small finite displacements to calculate phonon-phonon interactions lifetimes and then uses the relaxation time approximation (RTA) within the Boltzmann transport equation (BTE) to calculate the thermal conductivity.

The forces used to calculate the phonon-phonon interactions were calculated using the METADISE code [165] and used the same potential model as in the Green-Kubo calculations. Thus, convergence with the Green-Kubo calculations for a suitably sized supercell and q-point sampling mesh is expected.

The following calculations were performed on a 3 x 3 x 3 expansion of the cubic unit cell of magnesium oxide (a total of 216 atoms). Larger supercells were attempted but problems were encountered involving excessive memory requirements exceeding the limitations of the machine. The convergence of q-points was tested and plotted in Figure 4.5 for some temperatures.

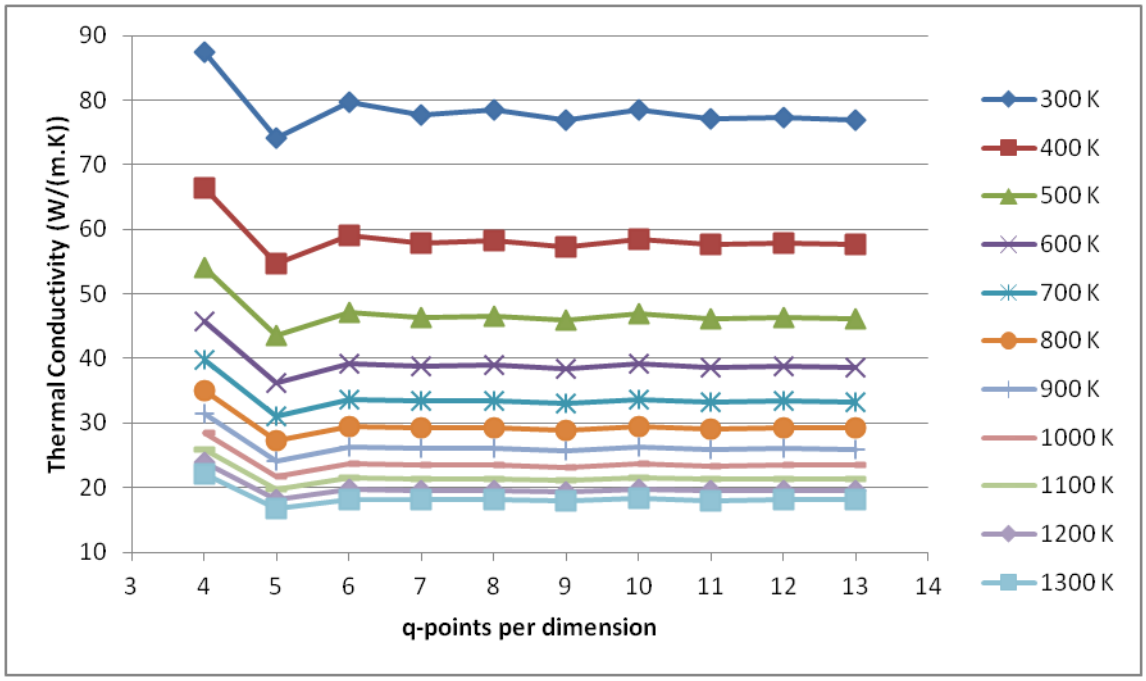

Figure 4.5 Convergence of thermal conductivity for number of q-points (per dimension).

The dynamical matrix as generated from the supercell gives the force constants at a number of points within the first Brillouin zone. A Fourier interpolation to these points can theoretically give the force constants at any point within the first Brillouin zone if the force constants vary smoothly. By sampling these q-points for the thermal conductivity calculation as opposed to just the explicitly calculated points a more exact thermal conductivity can be obtained, though care must be taken to ensure the force constants vary smoothly over the Brillouin zone (a large enough supercell is used). Convergence with respect to q-points occurred in the region of 6 q-points per dimension for this system.

The converged BTE results for all temperatures are compared against both the Green-Kubo and experimental results are plotted in Figure 4.6 (only one experimental result shown for clarity).

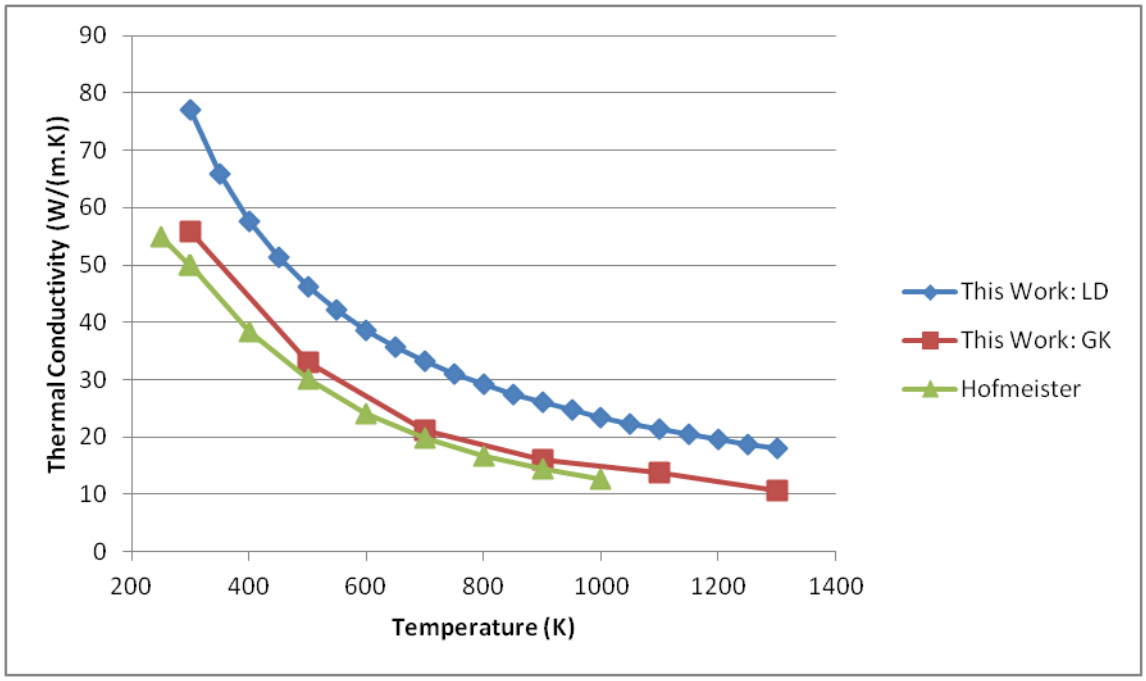

Figure 4.6 Calculated thermal conductivity of bulk magnesium oxide via the Green-Kubo and lattice dynamics methods compared with experiment.

The thermal conductivity values as calculated via lattice dynamics are shifted to higher values than those calculated using the Green-Kubo method, but the overall trend remains the same. The upwards shift of thermal conductivity values as given by lattice dynamics calculation may have many sources. The simulation cell used was not adjusted for volume expansion and the fourth-order and above anharmonic terms are not computed, meaning the frequencies of the phonon modes do not change as a function of temperature.

Another possible source of the shift is the small supercell size used in the calculation, meaning longer wavelength acoustic phonons are by necessity excluded, reducing acoustic-acoustic scattering. These problems are not apparent in the Green-Kubo calculation where all anharmonic terms are included and much longer wavelength phonons are allowed.

Lattice dynamics calculations can also be used to generate the phonon density of states (DOS) which should show some similarity to the Green-Kubo spectrum as the thermal conductivity is dependent upon phonon-phonon scattering.

The calculation of the phonon DOS (gamma point) was performed on the primitive two atom MgO unit cell with the lattice vectors were a=b=c=2.97 Å and α=β=γ=60° using the Phonopy code [121].

Performing the calculation at the gamma point means the modes visible are strictly optical modes and thus will not transport significant portions of heat. However, these modes may still scatter acoustic modes and alter the heat-flux [205].

The phonon DOS spectrum of magnesium oxide is displayed in Figure 4.7. The potential model used for the calculation was the same as for the Green-Kubo and BTE calculations.

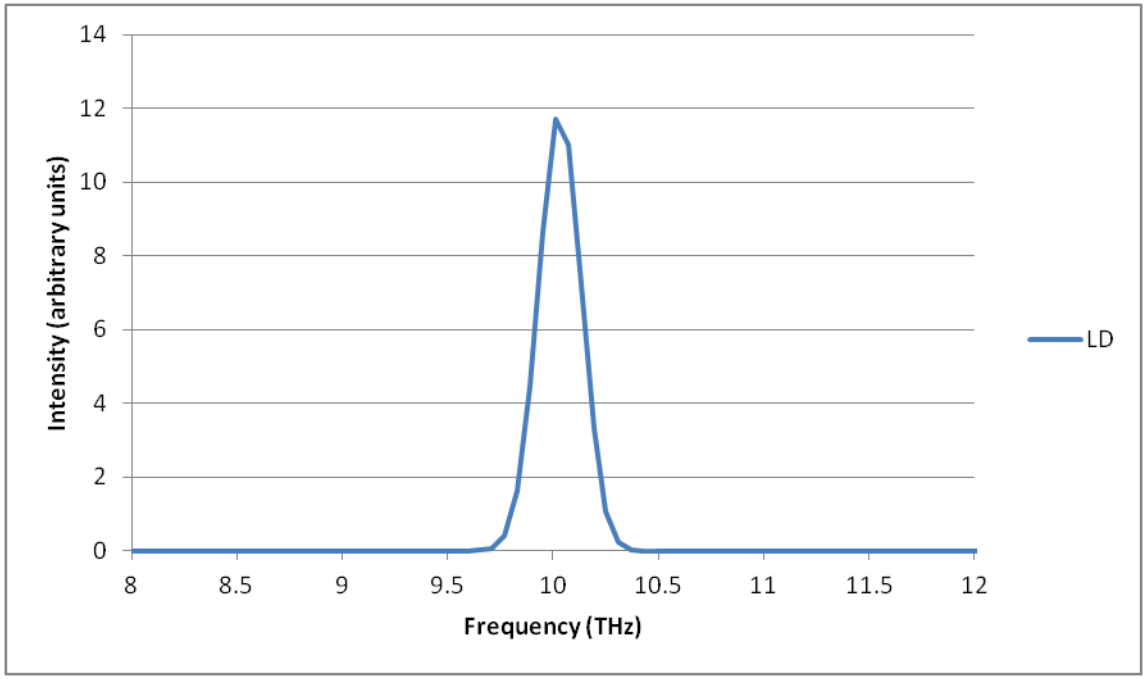

Figure 4.7 Phonon density of states (DOS) for magnesium oxide at the gamma point.

The phonon DOS shows three identical modes at ~10 THz corresponding to optical phonons in each of the three lattice directions. The equivalence of the frequencies is expected due to the isotropic nature of magnesium oxide. An additional set of three vibrational modes are also present at 0 THz corresponding to the translation of the entire lattice, these have been removed for clarity from all phonon DOS spectra.

The atomic motions corresponding to the phonon mode of each frequency in the phonon DOS may be obtained by examining the eigenvectors and mapping them to each atom. The result for bulk magnesium oxide reveals the motion at ~10 THz is that of the

magnesium and oxygen sublattices being displaced relative to each other. This type of motion may be considered a simple rattling motion which is often theorised to reduce thermal conductivity, especially when involving high mass substitutional defects or guest species [232]. The motion of the ~10 THz mode is displayed schematically in Figure 4.8.

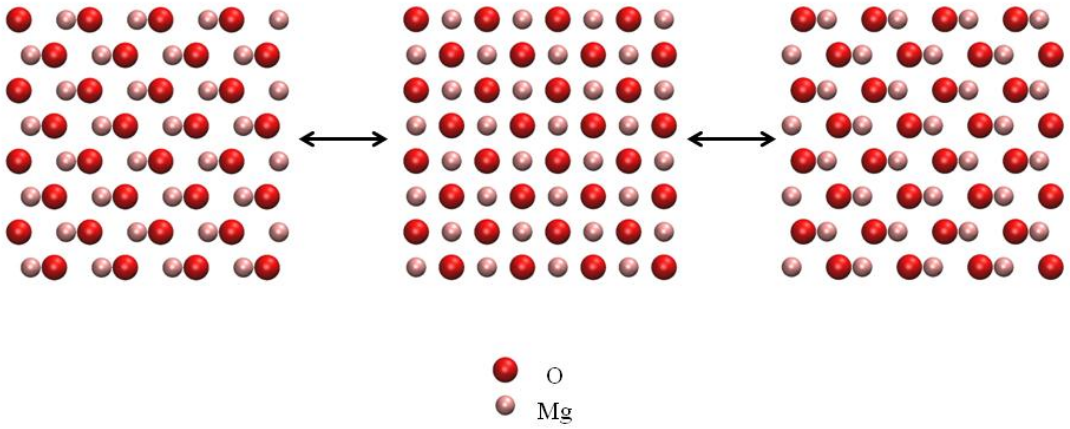

Figure 4.8 Schematic of the vibrational mode at 10 THz in a single layer of the MgO lattice.

The lattice dynamics phonon DOS can be compared with those obtained from the Green-Kubo calculations, Figure 4.9.

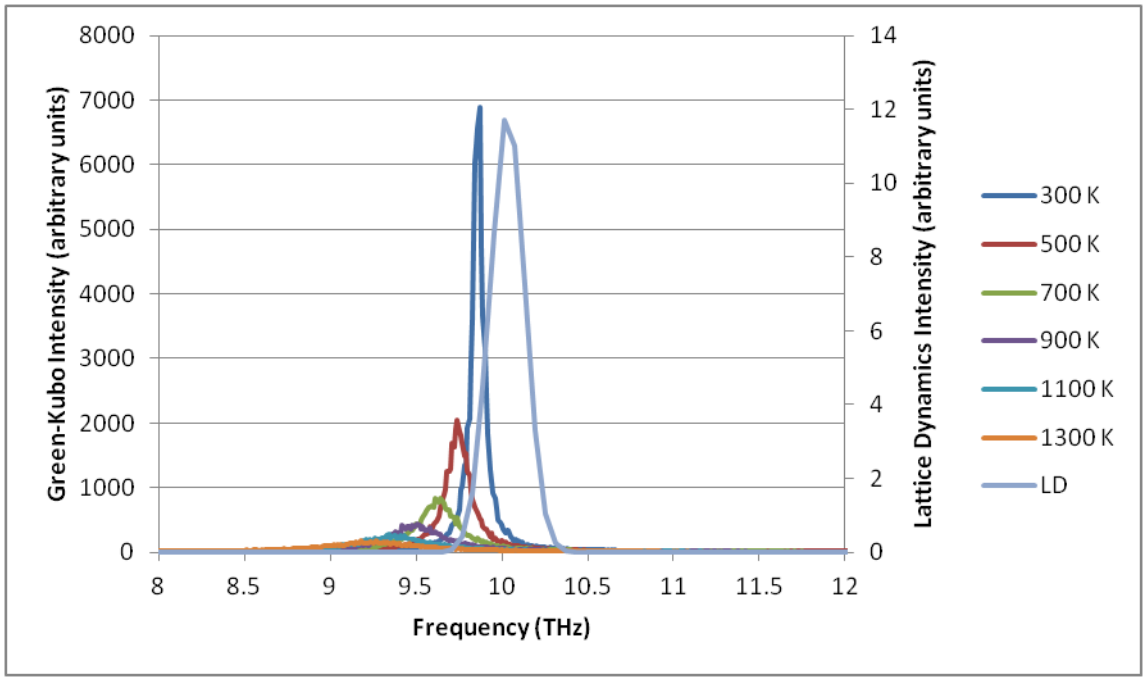

Figure 4.9 Lattice dynamics phonon DOS and Green-Kubo spectra of bulk MgO.

The frequency as calculated from lattice dynamics matches extremely well with those as calculated from the Green-Kubo method. A shift to higher frequency is observed and is expected due to the lattice dynamics calculation being performed at effectively zero Kelvin. This effect has been noted previously in the literature as arising from anharmonic effects at finite temperature [115].

The thermal conductivity of magnesium oxide has been calculated over a range of temperatures by both the Green-Kubo method and lattice dynamics employing the BTE. The BTE over predicts the thermal conductivity of magnesium oxide at all temperatures but has highlighted deficiencies in the BTE method for magnesium oxide. Lattice dynamics calculations also reveal which optical phonons can contribute to scattering and their atomic motions within the material.

By applying these methods to more complex systems, an enhanced understanding of scattering processes may be obtained. Thus in the next section two different grain boundary systems are studied using the Green-Kubo method with additional information coming from lattice dynamics calculations.

4.3. MgO Grain Boundaries

There are many types of grain boundaries in oxide materials, however this study only accounts for two types, mirror tilt and twist. A mirror tilt boundary is constructed by having two grains expressing the same surface joining together. A twist boundary is constructed by rotating the mirrored surface to allow the formation of the boundary. These two boundary types will thus have significantly different environments due to the mismatch generated by the adjoining grains and may show different behaviours with respect to thermal conductivity.

This work explores the Σ5{210}/[001]θ=26.57° tilt boundary and the {100}36.87° twist boundary (for simplicity referred to as Σ5{210} and {100}twist respectively), which are both constructed using the methodology outlined in Chapter 2.5.1.4. Both grain boundary systems have an inter-boundary distance of approximately 16 Å.

The thermal conductivity of these systems is calculated using the Green-Kubo method with additional information again being derived using lattice dynamics. This simple

study acts as a proof of principle in distinguishing the effect of two very different grain boundary systems on the thermal conductivity.

4.3.1. Mirror Tilt Grain Boundary

The Σ5{210} tilt grain boundary is fairly simple and representative of many other magnesium oxide tilt grain boundaries [165]. The Σ5{210} boundary can be considered as two stepped surfaces (the {210} surfaces) coming together to form a reduced density layer, Figure 4.10.

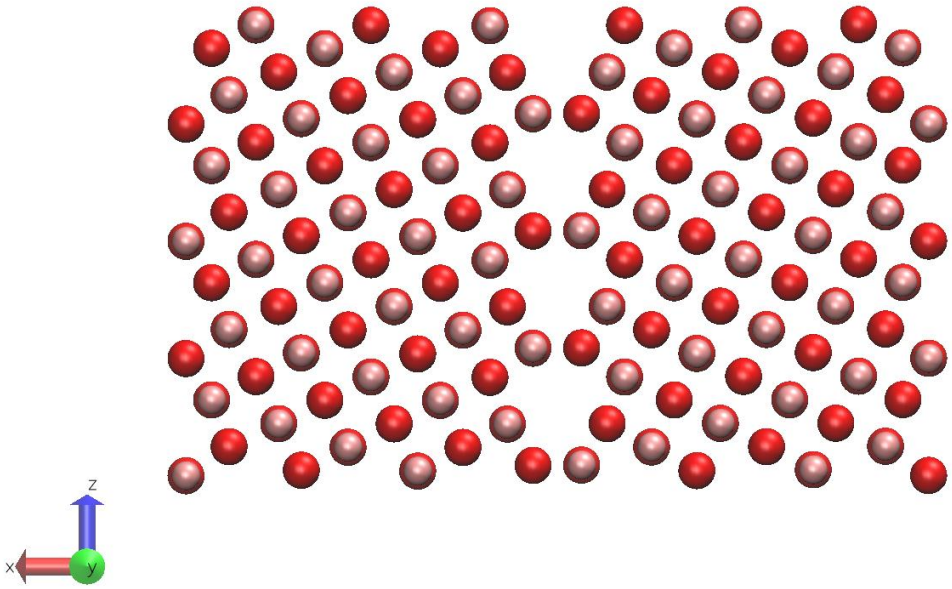

Figure 4.10 The energy minimised Σ5{210} boundary.

Previous work by Watson et al. found the Σ5{210} boundary to be the most stable of the family of MgO grain boundaries [165] with the exception of the {110} boundary which may be considered a special case of a stacking fault grain boundary. The formation energy of this boundary has been calculated to be 1.33 Jm^{-2}. The potential model of Lewis and Catlow [145] has also been used to calculate the formation energy of this system and has given a value of 1.73 Jm^{-2}.

The simulation cell used for the Green-Kubo calculation comprised of 1,280 atoms in a periodic cell of approximately 32 Å x 21 Å x 19 Å with a 500 K density ~94% that of bulk magnesium oxide. The simulation cell contains two identical Σ5{210} mirror tilt boundaries lying parallel to the Y-Z plane and perpendicular to the X axis, running in two opposite directions. The distance between the boundaries is much smaller than in a

real system and should have a significant effect on thermal conductivity by limiting allowed phonon frequencies.

As before the simulation cells underwent 0.5 ns of NPT equilibration to obtain the averaged lattice vectors. A further 0.5 ns of NVT equilibration was then conducted to ensure thorough thermalisation of the system. Data were collected as three sets of 5 ns NVT simulations, whose autocorrelations are then averaged; this approach differs from the bulk calculation but will only have a significant effect on very large sample intervals, where the correlation should be negligible anyway. Additionally, the convergence is improved by sampling a more varied region of phase space [206]. The additional 5 ns of simulation time were added to improve convergence of the boundaries due to their lower thermal conductivities. Despite the increased simulation time the 300 K simulation was dropped due to extremely poor convergence, as may have been expected from observations of the error from the bulk calculations.

The average thermal conductivity at each temperature is calculated from the averaged integrals and is displayed in Figure 4.11.

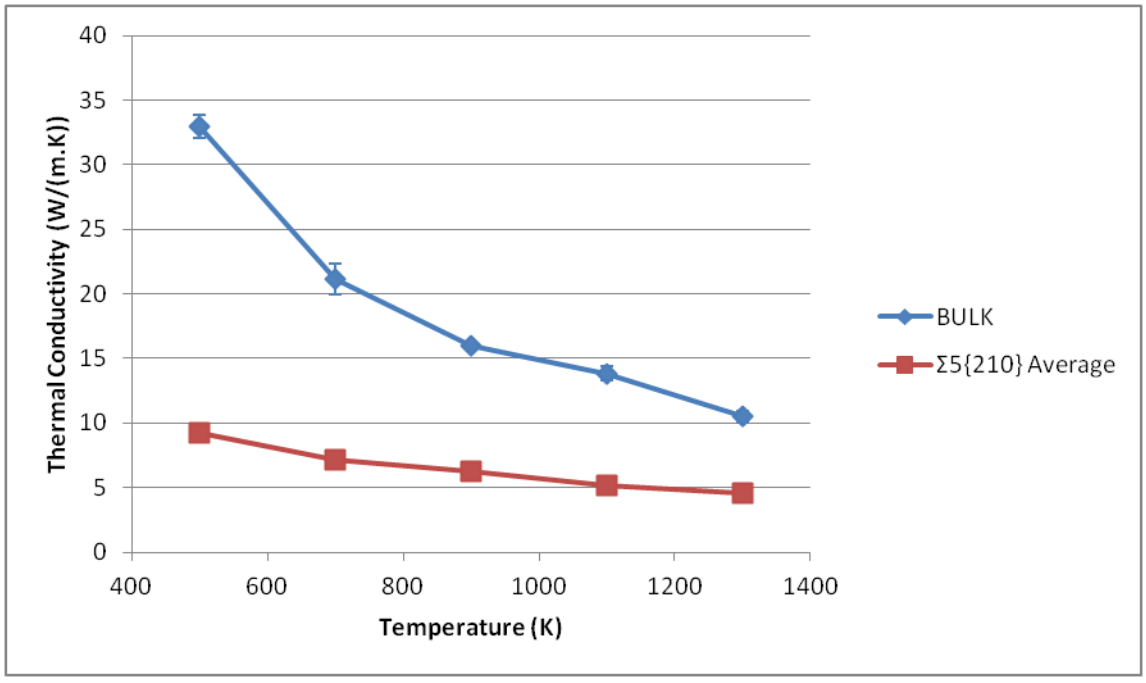

Figure 4.11 Average thermal conductivity of the Σ5{210} tilt boundary.

Initial observations reveal the thermal conductivity is more than halved by introduction of grain boundaries at intervals of ~16 Å. The decrease in thermal conductivity with temperature is now less steep.

In the Σ5{210} system the X direction corresponds to the direction perpendicular to the boundary plane, the Y direction corresponds to the direction of the pipes in the boundary and the Z direction corresponds to the direction across the pipes. These three directions are structurally different at the boundary and so a difference in thermal conductivity is expected. The thermal conductivities for these three directions are presented in Figure 4.12.

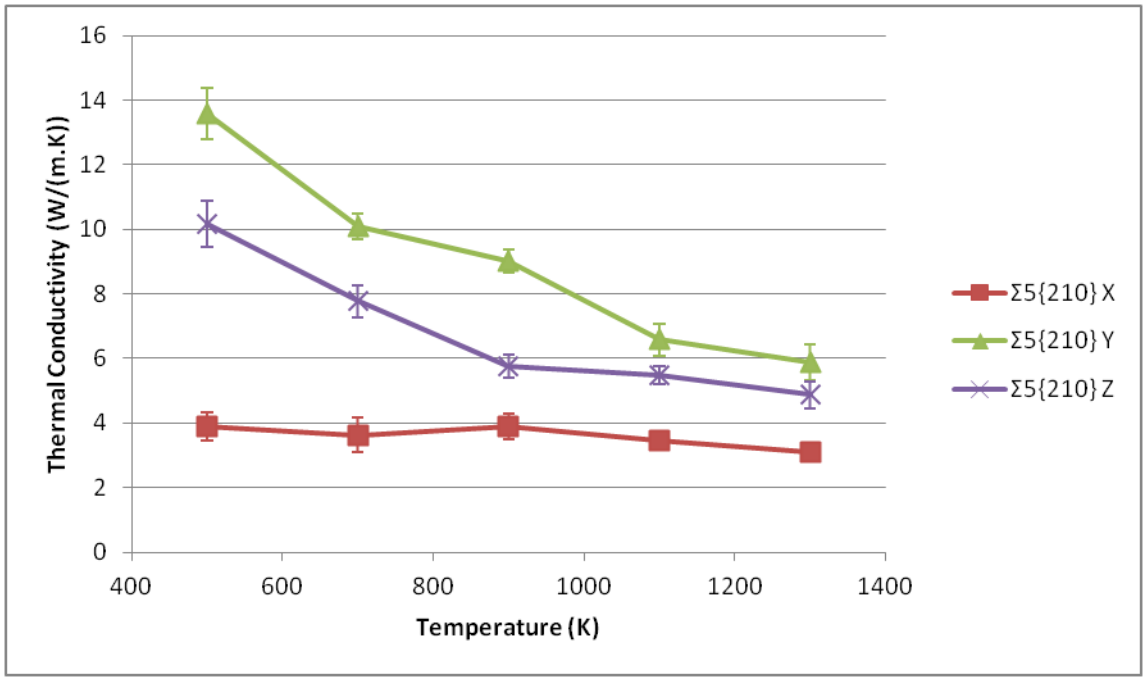

Figure 4.12 Directional thermal conductivities of the Σ5{210} tilt boundary.

The inverse power law trend usually observed [231] in the bulk is no longer clear as the primary scattering mechanism is no longer phonon-phonon and the system now contains defects which also scatter phonons.

As expected the thermal conductivity in the X direction, which goes through the boundary, is the lowest at ~4 W/(m.K) and shows effectively no sensitivity to temperature. The insensitivity to temperature likely results from the domination of phonon-boundary scattering up to 900 K and then increasing contribution of phonon-phonon scattering at higher temperatures. The Y and Z direction are also reduced due to oblique scattering off the boundaries, i.e. scattering of phonons with some X component as well as other directions. The Z direction also has a noticeable behaviour change at 900 K where the gradient of the thermal conductivity changes. The Z direction may also have a change in trend but it is less clear.

The Green-Kubo spectra may also reveal how the scattering mode of bulk magnesium oxide has changed. The spectra for the X, Y and Z direction are plotted in Figure 4.13, Figure 4.14and Figure 4.15.

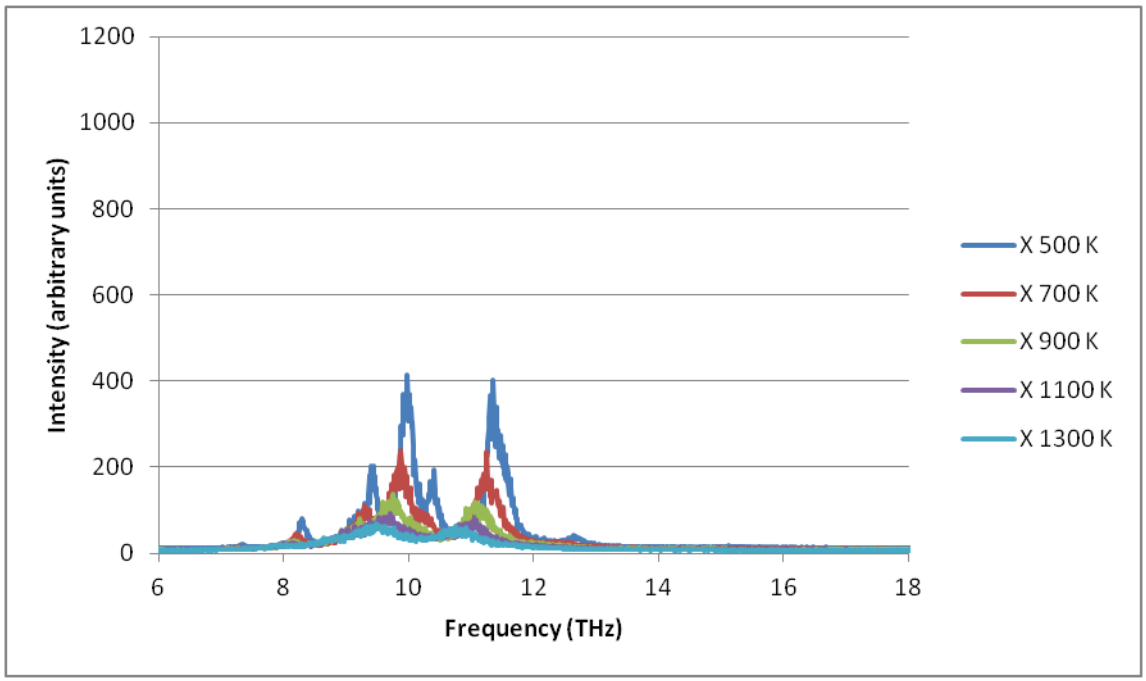

Figure 4.13 Σ5{210} tilt boundary Green-Kubo spectra in the X direction.

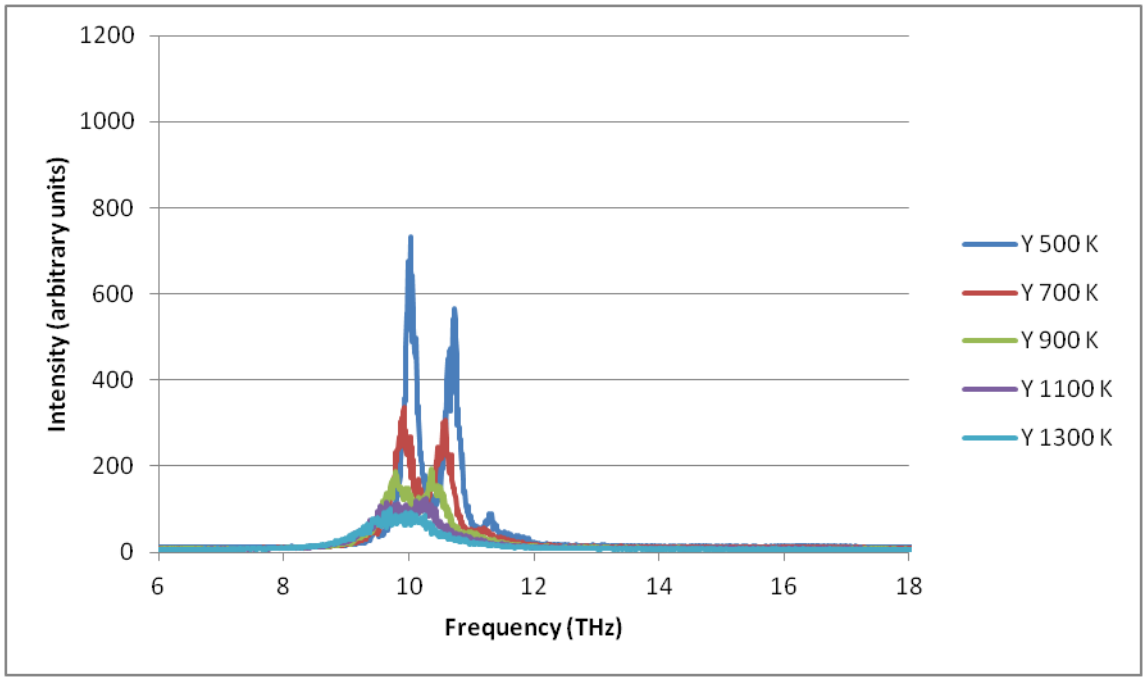

Figure 4.14 Σ5{210} tilt boundary Green-Kubo spectra, Y direction.

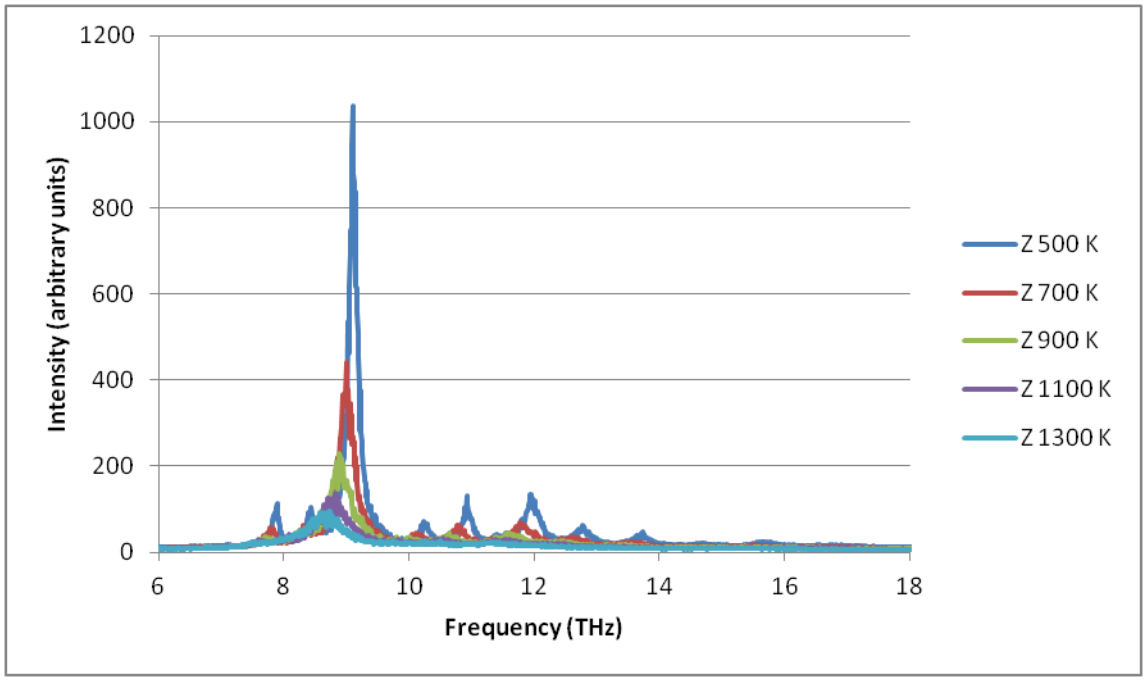

Figure 4.15 Σ5{210} tilt boundary Green-Kubo spectra, Z direction.

The most striking change to the spectra from the bulk is the very large number of additional modes now present. While the bulk spectra only had a single mode corresponding to vibration of the magnesium/oxygen sublattices, the grain boundary spectra shows many more modes available for interaction with the acoustic phonons. The increased number of modes results from the different environments created by the introduction of the grain boundary, so although the primary scattering mechanism is now phonon-boundary, it is via boundary vibrational modes that this occurs.

Some unusual features are presented by these spectra. There is an extremely large additional mode in the X direction at ~11.5 THz which is equal in magnitude to the primary 10 THz peak. A similar, but smaller peak appears in the Y direction at ~10.7 THz. The Z direction does not show an additional peak of very large magnitude but does have very many smaller peaks and the main peak has been shifted to ~9 THz.

It is also noted that the usual shift to lower frequencies and broadening of the modes is occurring with increased temperature. However, the additional boundary modes become less distinct at higher temperatures, leaving only the optical mode inherent in the bulk material. This type of behaviour indicates a return to bulk-like scattering at higher temperatures as more phonons scatter via bulk optical modes before encountering

boundary based optical modes. However, the thermal conductivity remains lower than the bulk and so some effect of the grain boundary remains.

The phonon DOS for the Σ5{210} mirror tilt boundary can be calculated using lattice dynamics methods implemented in the Phonopy code [121] to better analyse the modes appearing in the Green-Kubo calculation. The phonon DOS was computed at the gamma point and used the smallest symmetry reduced representation of the cell possible (128 atom orthorhombic cell of a=32.05 Å, b=4.16 Å and c=9.49 Å). The total phonon DOS is displayed in Figure 4.16 (the peak centred at 0 THz is a set of three translational modes).

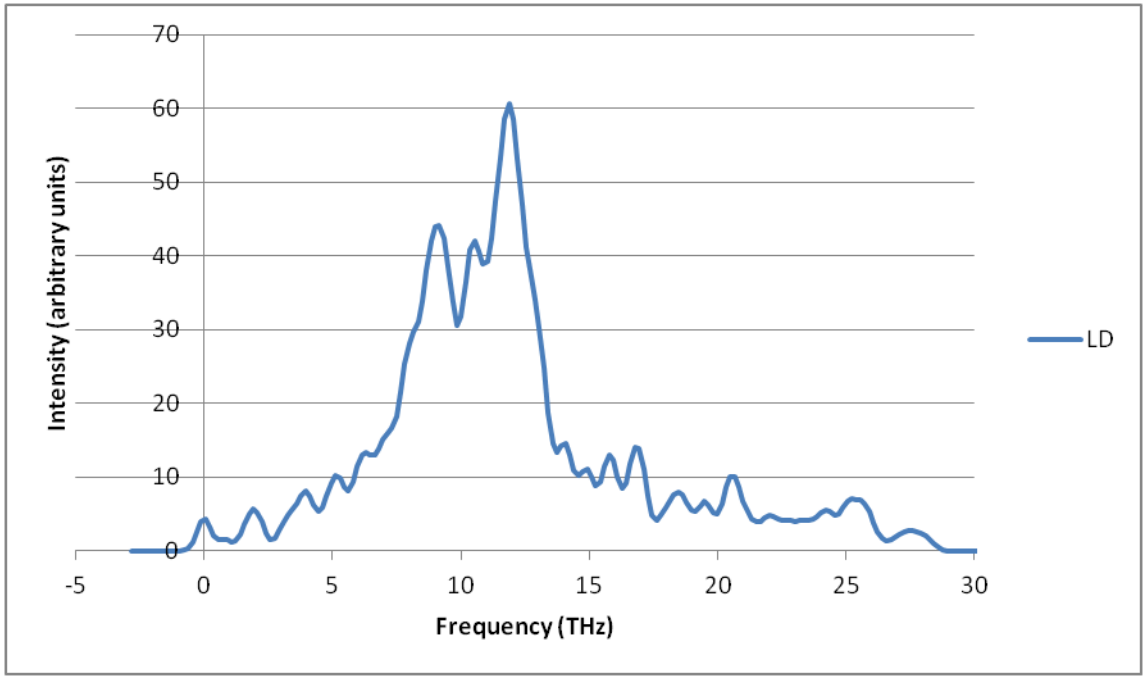

Figure 4.16 Σ5{210} tilt phonon DOS.

It is immediately clear that the phonon DOS is much more complex for the Σ5{210} tilt boundary than the bulk material, although a series of strong mode are still present in the region of ~10 THz. It is possible to simplify the interpretation of the phonon DOS by removing all modes which should not appear in the Green-Kubo spectrum.

The simplest way of removing those modes which do not appear in the Green-Kubo spectrum is to sum the non-mass-weighted eigenvectors produced for each frequency by the lattice dynamics calculation. Any mode that has a non-zero sum of non-mass-weighted eigenvectors is asymmetric and should therefore interact with the heat-flux and appear in the Green-Kubo spectra.

While not a rigorous treatment, this simple analysis makes it very easy to identify which modes will interact with the acoustic modes of the system. A more rigorous analysis method is given by Landry et al. [115] in "Complex superlattice unit cell designs for reduced thermal conductivity", Equation A13.

In practice, a lower bound cutoff of 0.1 (dimensionless units) is used on the sum of non-mass-weighted eigenvectors in each direction so that only the most significant modes are presented. A cutoff value of 0.1 will be used for all MgO calculations for consistency.

An additional benefit is that this type of analysis gives directionally independent spectra, which can be useful for complex defective structures. Once the participating modes have been isolated, a Gaussian distribution is applied for easier comparison and is meant only to serve as a guide to the eye, Equation 4.1.

$$f(x) = a \exp\left(-\frac{(x-b)^2}{2c^2}\right)$$

Equation 4.1

a is set to be the magnitude of the sum of eigenvectors for the mode, b is the frequency of the mode and c is an arbitrary broadening parameter, set to 0.1 for all modes. The use of a Gaussian distribution makes it easier to see where certain modes may overlap and become difficult to distinguish. Comparison to the Green-Kubo calculations is now possible in a more systematic way; the lowest temperature Green-Kubo calculations (500 K in this case) are used for comparison as it should be the closest to the lattice dynamics calculations (effectively 0 K). The separate dimension comparisons are plotted in Figure 4.17, Figure 4.18 and Figure 4.19.

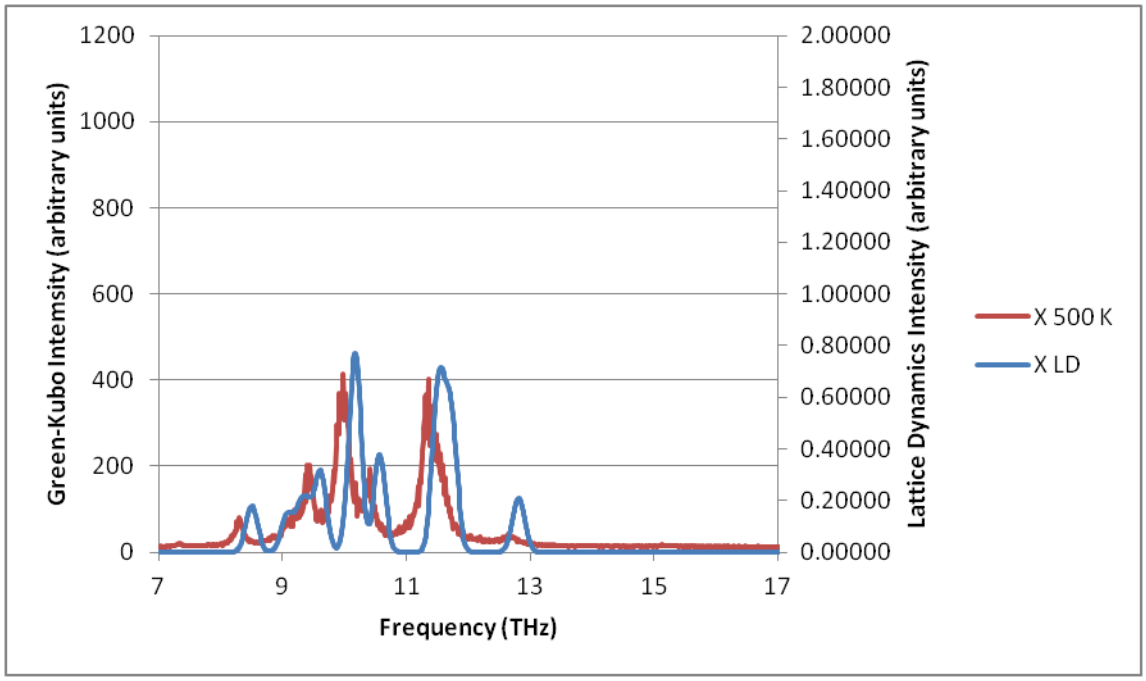

Figure 4.17 Comparison of the Green-Kubo at 500 K and lattice dynamics spectra for the Σ5{210} tilt boundary, X direction.

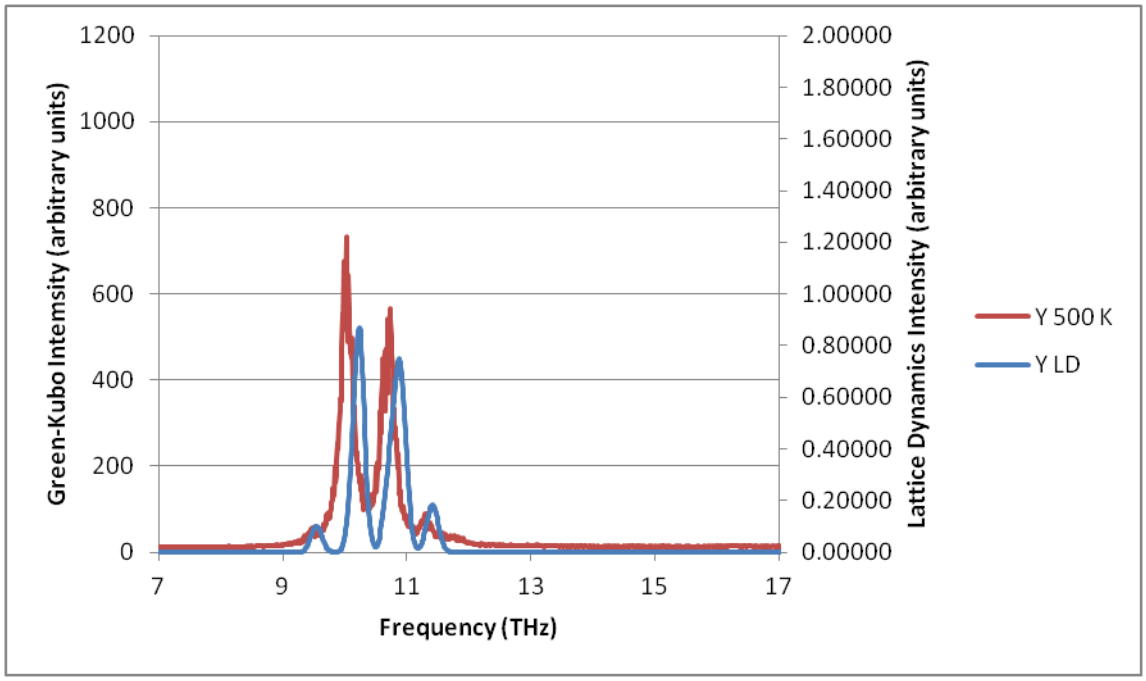

Figure 4.18 Comparison of the Green-Kubo at 500 K and lattice dynamics spectra for the Σ5{210} tilt boundary, Y direction.

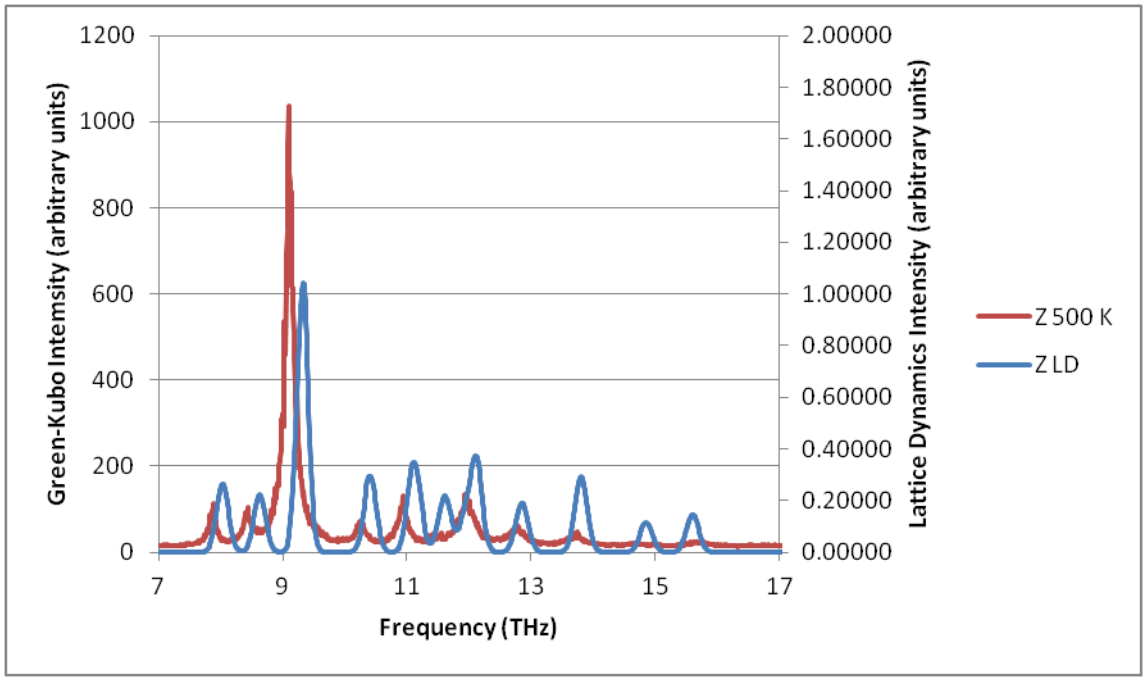

Figure 4.19 Comparison of the Green-Kubo at 500 K and lattice dynamics spectra for the Σ5{210} tilt boundary, Z direction.

Once again the positions of the peaks match with the Green-Kubo calculations with only a small shift to higher frequencies associated with the lattice dynamics calculation being performed neglecting temperature. The relative heights of the peaks match very well in some instances and poorly in others. The mismatch is likely due to more complex factors affecting the probability of the optical phonon partaking in scattering processes, such as the temperature. Indeed the peaks that show the greatest mismatch are the ones that show the greatest temperature dependence in the Green-Kubo spectra.

Additional peaks appear at greater than 14 THz in the Z direction of the lattice dynamics phonon DOS calculation which are not immediately apparent in the Green-Kubo spectrum. By applying a logarithmic scale to the Green-Kubo spectrum the additional peaks become apparent and their frequencies match very well with those in the phonon DOS calculation, Figure 4.20.

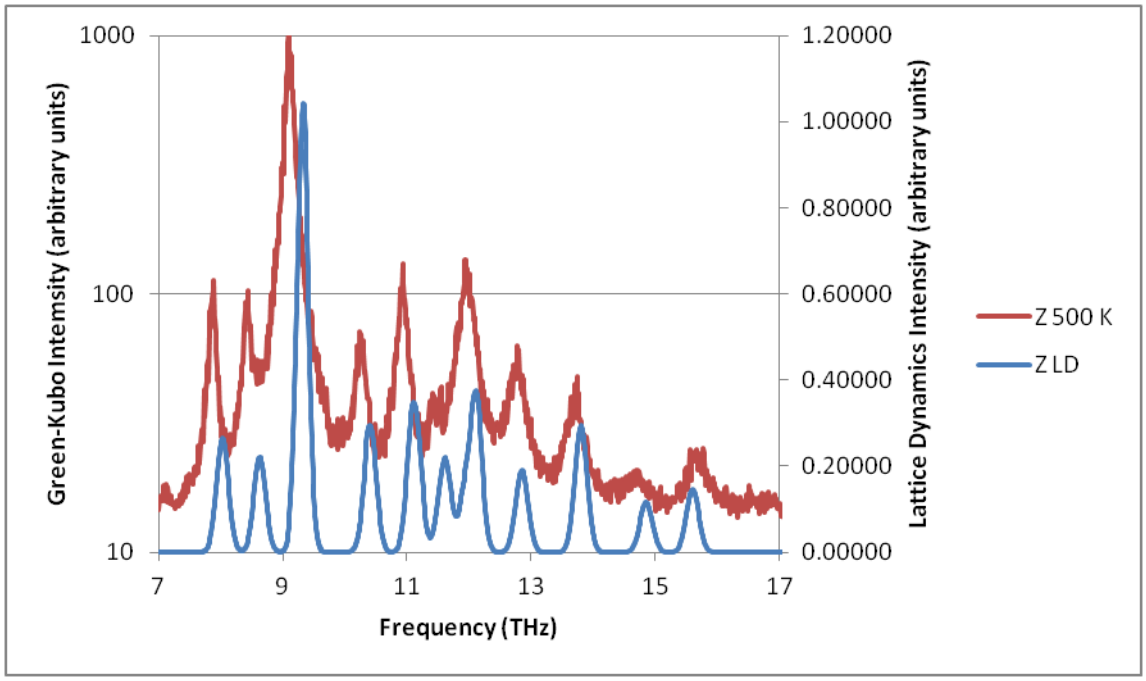

Figure 4.20 Comparison of the Green-Kubo at 500 K and lattice dynamics spectra for the Σ5{210} tilt boundary, Z direction. Log_{10} scale on Green-Kubo intensity.

The use of a logarithmic scale reveals several peaks that were not originally visible (primarily above 13 THz) and most of these peaks now match with those observed in the lattice dynamics calculations. A couple of the smaller peaks are also visible at very high and at very low frequencies that do not to have a counterpart in the lattice dynamics calculation, however this is as a result of the eigenvector cutoff used when analysing the phonon DOS and the very low significance of these modes.

The changes to the modes present in the Green-Kubo spectra can now be understood by examining the eigenvectors as applied to the structure as atomic motions.

The X direction spectrum shows many peaks, the majority of which are difficult to categorise due to the complex motion of atoms within the structure. The only mode that is easily described is at 9.34 THz where the oxygen atoms in the bulk portions of the system are vibrating symmetrically in the Z direction. This motion is almost entirely stopped at the boundary except for a small motion of magnesium atoms which makes the mode asymmetric in the X direction.

In the Y direction only four modes are present and are easily categorised. The modes appearing at 9.62 and 10.88 THz are complicated and involve motion of all ions within the system. The mode appearing at 10.33 THz involves the vibration of ions within the

boundary only (within ~5 Å of the core of the boundary). The mode appearing at 11.06 THz only has vibration of ions outside of the boundary region. This result demonstrates how local boundary structure can lead to new boundary modes that effectively scatter acoustic phonons.

The strongest peak in the Z direction displays a significant shift and appears at 9.36 THz. This is the same mode which is easily categorised in the X direction, except the motions of the grains are now concerted in the Z direction. The remaining modes are once again too complex to describe.

4.3.2. Twist Grain Boundaries

Another type of grain boundary is a twist boundary. Here the second grain is reflected across the cutting plane and then rotated about an axis perpendicular to the plane. The grain boundary chosen for this work was the {100}36.87° twist boundary which has been found to be extremely stable when the density at the boundary is reduced by removal of Mg and O atoms which are in close proximity. The 36.87° rotation angle has been frequently observed experimentally [234] and is very stable due to the good coincidence of the lattice sites across the boundary [235]. The formation energy of this system has been calculated as 1.51 Jm^{-2}, slightly higher than the Σ5{210} tilt boundary. Once again the potential model of Lewis and Catlow has additionally been used to calculate the formation energy of this system and gives a value of 2.00 Jm^{-2}.

Figure 4.21 shows the boundary layer to be very thin. Figure 4.22 shows the internal structure of the grain boundary. The 8-fold and 4-fold interconnecting rings which comprise the core of the boundary are highlighted.

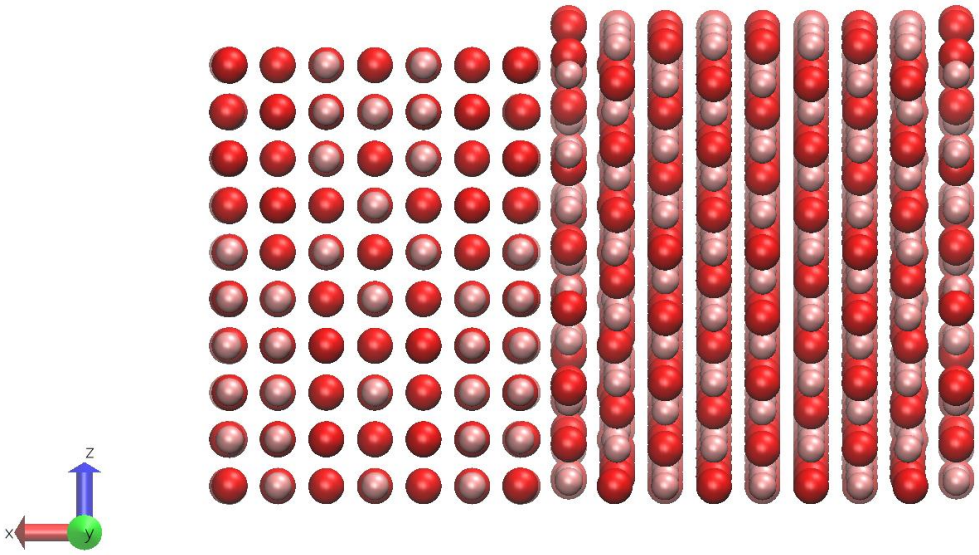

Figure 4.21 Side view of the relaxed {100}twist boundary.

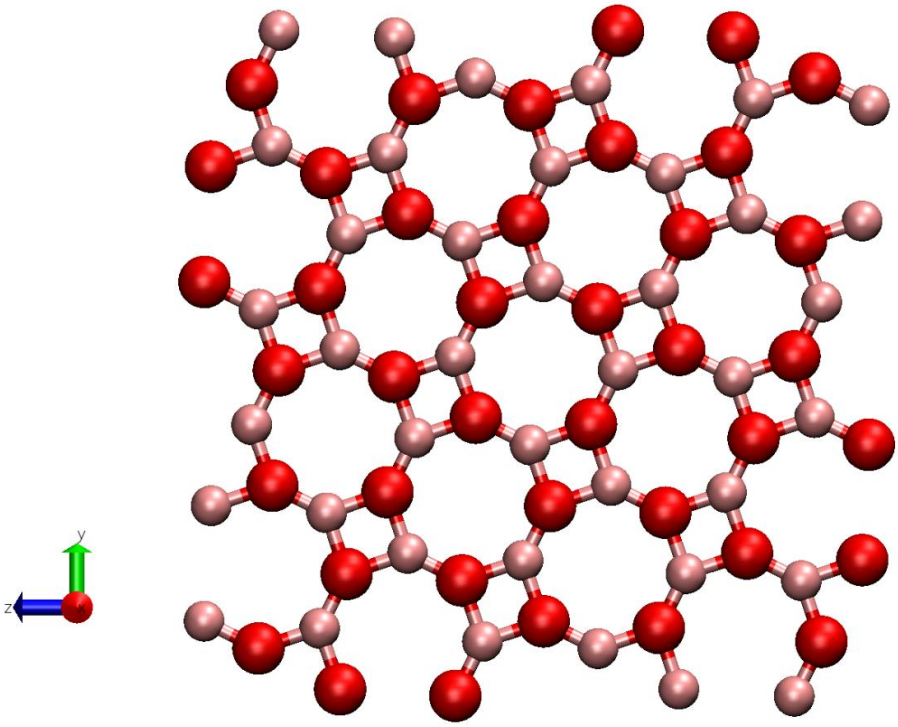

Figure 4.22 Internal structure of the relaxed {100}twist boundary plane with 8-fold and 4-fold rings highlighted.

The simulation cell used in these calculations was a 2,808 atoms supercell with lattice vectors of approximately 37 Å x 28 Å x 28 Å with a 500 K density of ~97% that of bulk magnesium oxide. Once again the system contains two grain boundaries running in opposite directions to allow for periodic boundaries. The grain boundaries again lie perpendicular to the X direction. The simulation procedure was the same as for the

Σ5{210} tilt boundary with 0.5 ns NPT equilibration, 0.5 ns NVT equilibration and three sets of 5 ns NVT data collection. The average thermal conductivity results for the {100}twist boundary are plotted in Figure 4.23.

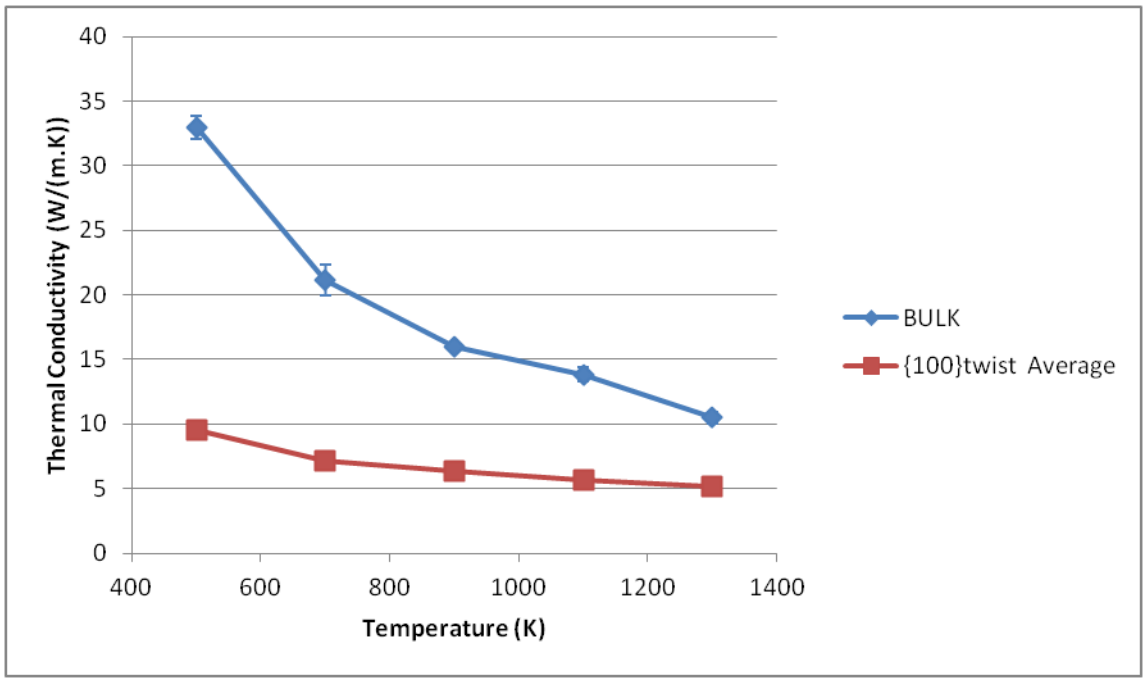

Figure 4.23 Average thermal conductivity of the {100}twist boundary.

The thermal conductivity of the {100}twist boundary shows remarkably similar reduction in thermal conductivity as the Σ5{210} tilt boundary. However, it is unclear whether the contribution from each direction is the same as from the Σ5{210} tilt boundary. If some difference is present then it is expected that as the inter-grain distance increases the Y and Z direction thermal conductivities will tend towards bulk whereas the X direction thermal conductivity will diverge between the two boundary types due to structural differences.

The structure of the {100}twist boundary is generally contained to a single atomic plane with only minor disruption to the lattice in adjacent planes. This narrow boundary means that the system is more dense than the Σ5{210} tilt boundary and only ~3% less dense than the perfect bulk material. Thus a higher thermal conductivity in the X direction compared to the Σ5{210} tilt boundary is expected as phonons are more likely to transmit some thermal energy across the boundary as it is more dense. The Y and Z directions in the {100}twist boundary are identical under symmetry and so it is expected

they will have near identical thermal conductivities. The directionally independent thermal conductivities are presented in Figure 4.24.

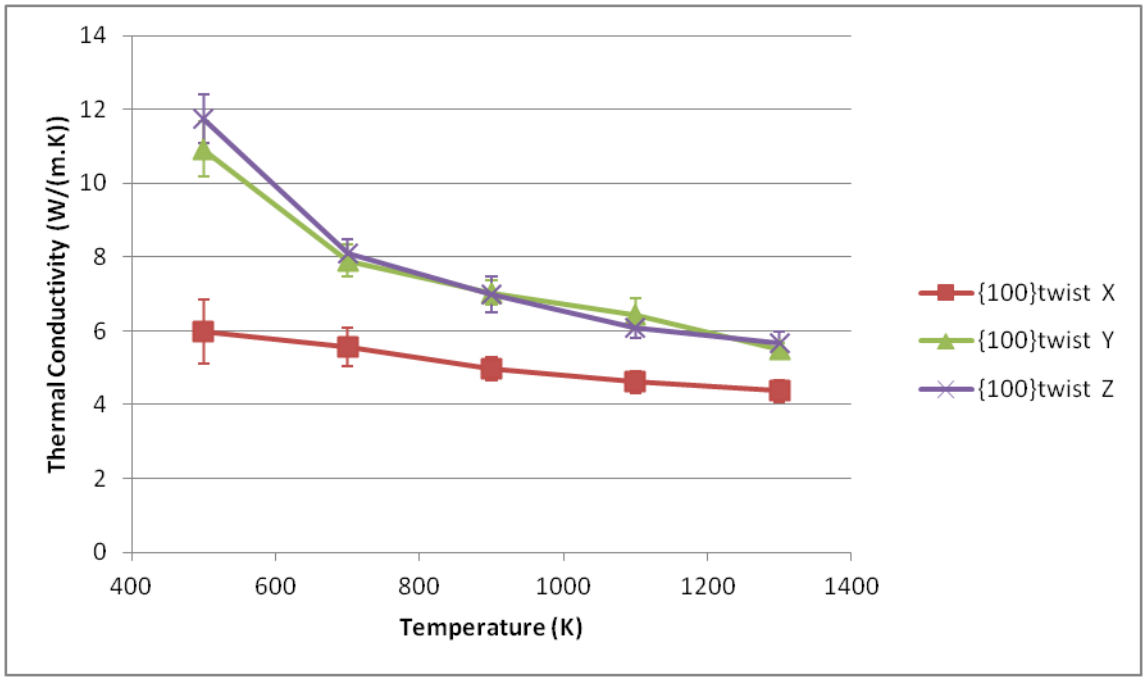

Figure 4.24 Directional thermal conductivities of the {100}twist boundary.

As was the case for the tilt boundary the X direction (through boundary) yields the lowest thermal conductivity. The X direction values also descend almost linearly from 500 K to 1300 K, showing temperature dependence entirely absent from the tilt boundary. The Y and Z directions exhibit almost identical values across the temperature range as is expected as the two directions are symmetrically equivalent; this result also indicates the real error is much smaller than the fluctuations in the autocorrelation. The values in the Y and Z directions are also much reduced from the bulk values but not as much as the X direction.

The spectra from these calculations are plotted in Figure 4.25, Figure 4.26 and Figure 4.27.

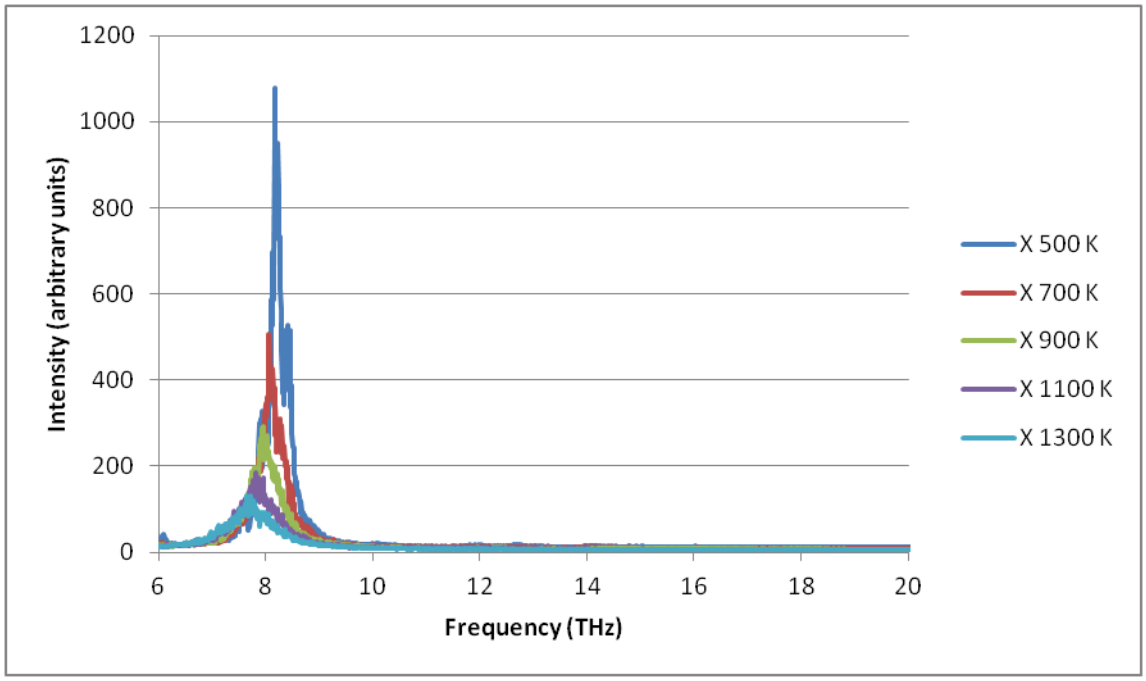

Figure 4.25 {100}twist boundary Green-Kubo spectra, X direction.

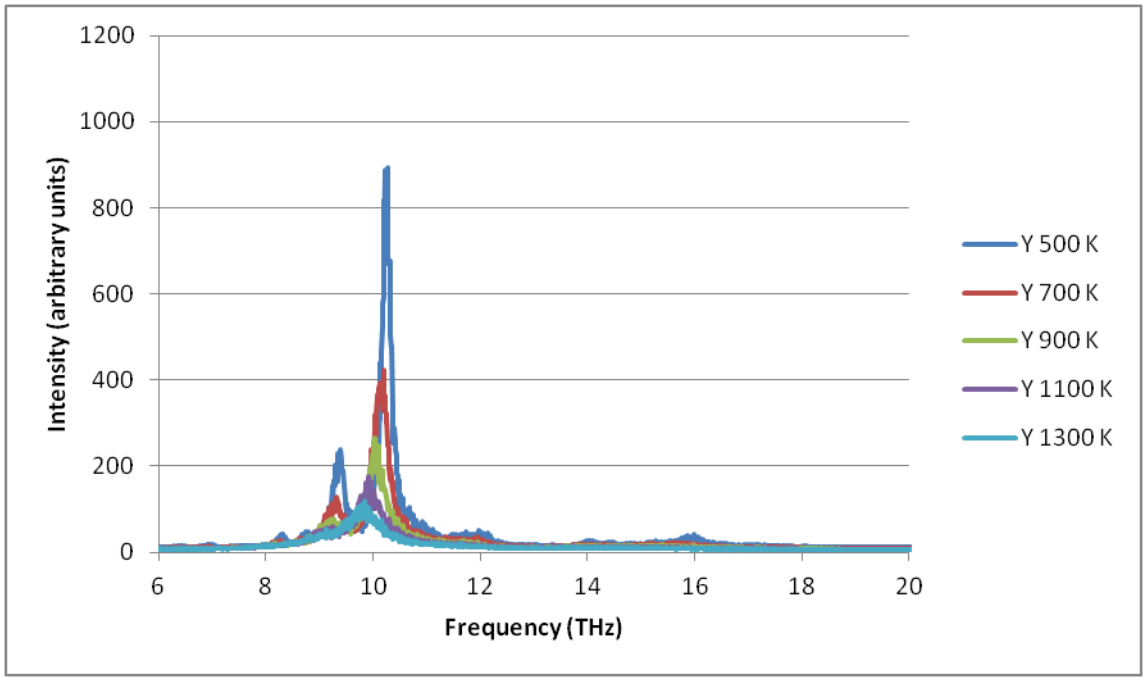

Figure 4.26 {100}twist boundary Green-Kubo spectra, Y direction.

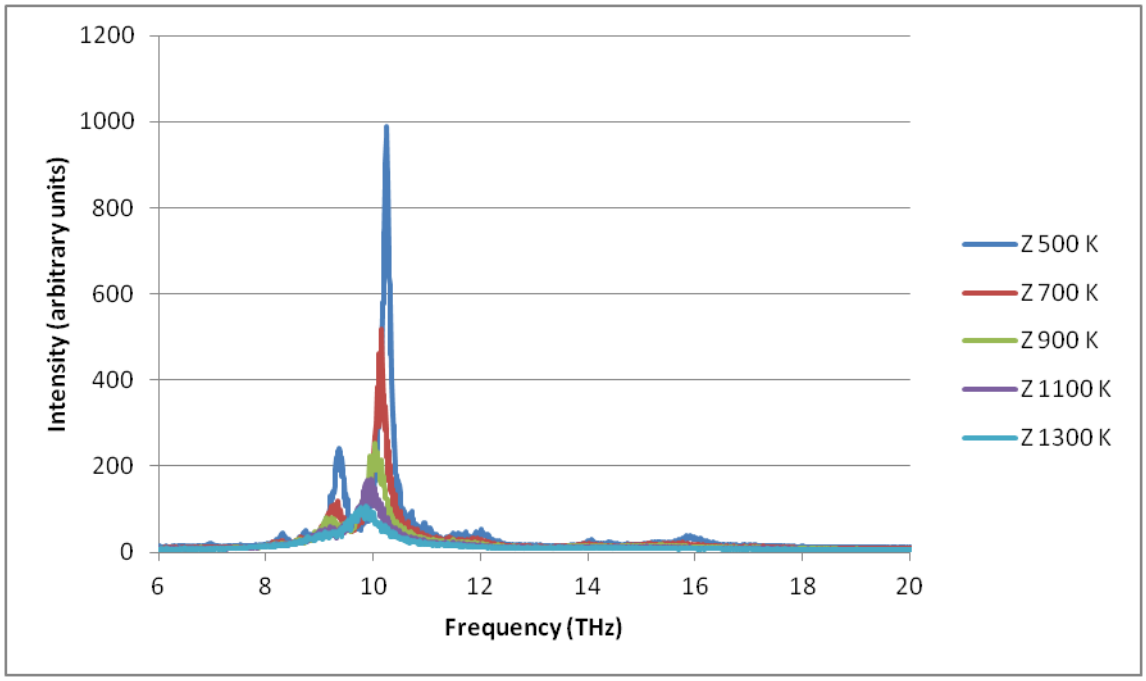

Figure 4.27 {100}twist boundary Green-Kubo spectra, Z direction.

The Green-Kubo spectra of the twist boundary show significantly less splitting of peaks in all directions than the tilt boundary. The fewer extra peaks are a result of fewer distinct environments at the boundary due to rotational symmetry as well as very little reconstruction in the planes between the boundary and the bulk. The same shift to lower frequency with higher temperature is still present.

The largest peak in the X direction shows a large shift in frequency from ~10 THz to ~8 THz, similar to the Z direction peak of the tilt boundary. The origins of this shift may also be similar, being due to the boundary blocking the vibration.

Unlike the Σ5{210} tilt boundary, the Y and Z direction spectra for the {100}twist boundary are essentially identical due to their relation by symmetry. The main peak has remained at ~10 THz as the primary phonon vector is travelling through bulk, with edge scattering possibly causing the extra peak at ~9 THz.

Performing the lattice dynamics analysis (using a 156 atom orthorhombic cell of a=34.00 Å and b=c=6.61 Å) shows a reasonable match to the Green-Kubo spectra. The results are plotted in Figure 4.28, Figure 4.29 and Figure 4.30.

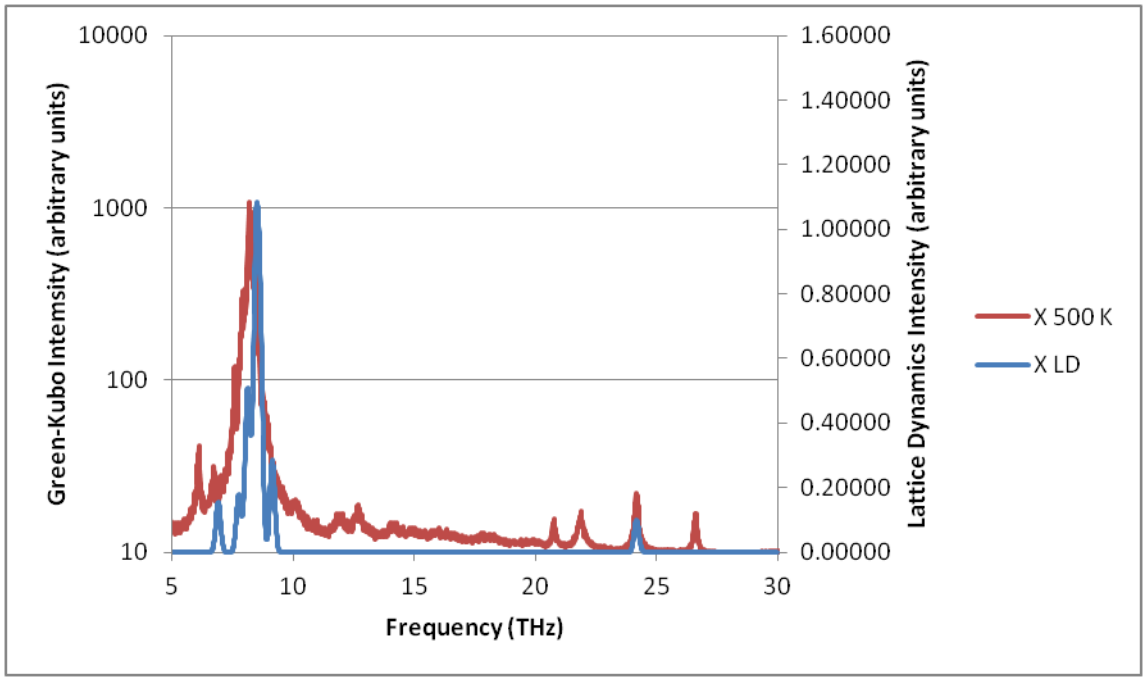

Figure 4.28 Comparison of the Green-Kubo at 500 K and lattice dynamics spectra for the {100}twist boundary, X direction. Log_{10} scale on Green-Kubo intensity.

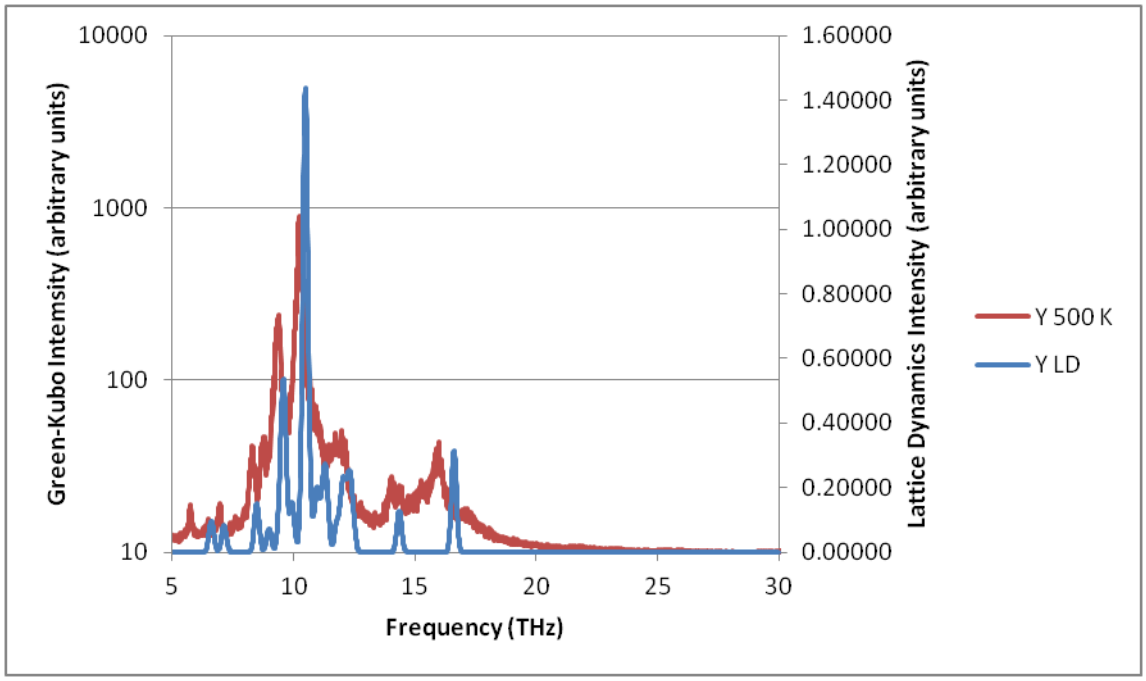

Figure 4.29 Comparison of the Green-Kubo at 500 K and lattice dynamics spectra for the {100}twist boundary, Y direction. Log_{10} scale on Green-Kubo intensity.

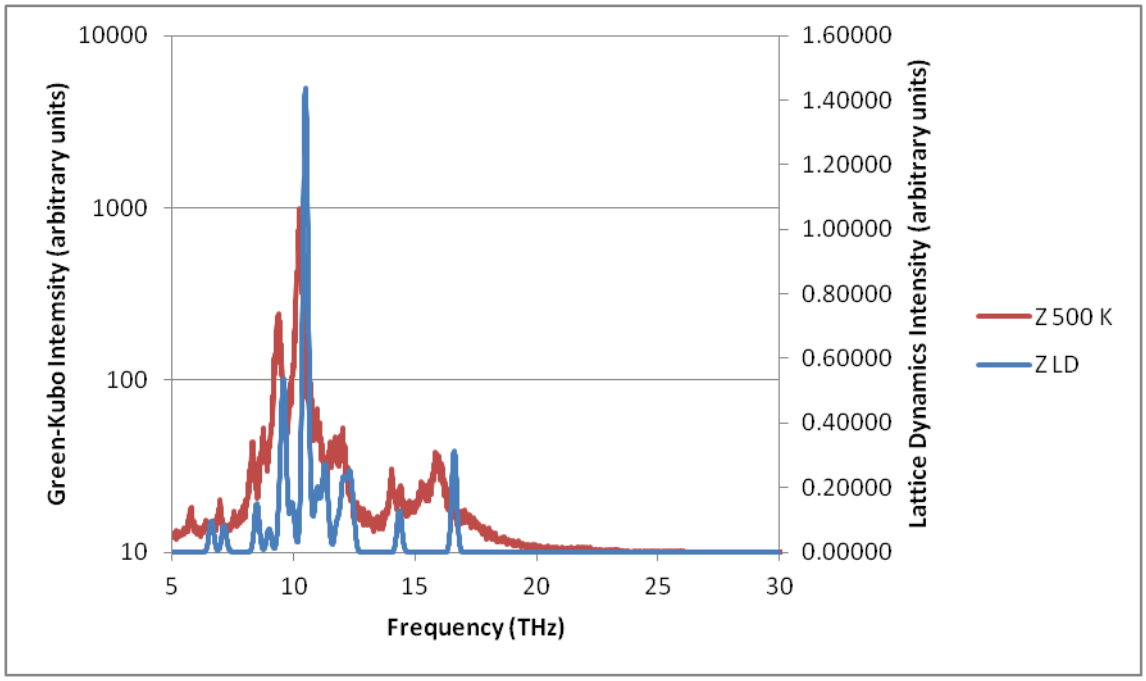

Figure 4.30 Comparison of the Green-Kubo at 500 K and lattice dynamics spectra for the {100}twist boundary, Z direction. Log_{10} scale on Green-Kubo intensity.

The spectra show reasonably good agreement. Where the spectra diverge can be explained by temperature effects and possibly the noise remaining in the Green-Kubo spectra. Additionally, it becomes clear that the main peak at 8 THz in the X direction is in fact a collection of several peaks of similar atomic motions; information which was not available from the Green-Kubo calculation alone.

The large shift of the main peak to lower frequency in the X direction is a result of a rotational twisting element now associated with the vibration of the sublattices. The origin of this mode is at the boundary where the magnesium/oxygen sublattices in the plane vibrates purely in the X direction, but the interactions with the surrounding atoms induce an additional Y and Z movement.

In previous lattice dynamics calculations each vibrational mode was asymmetric in only one direction. An unusual result for the twist boundary is that several frequencies now contain asymmetry in more than one direction simultaneously. All the frequencies showing this behaviour have peaks in both the Y and Z directions and never in the X direction. These frequencies with asymmetry in two dimensions are plotted in Figure 4.31.

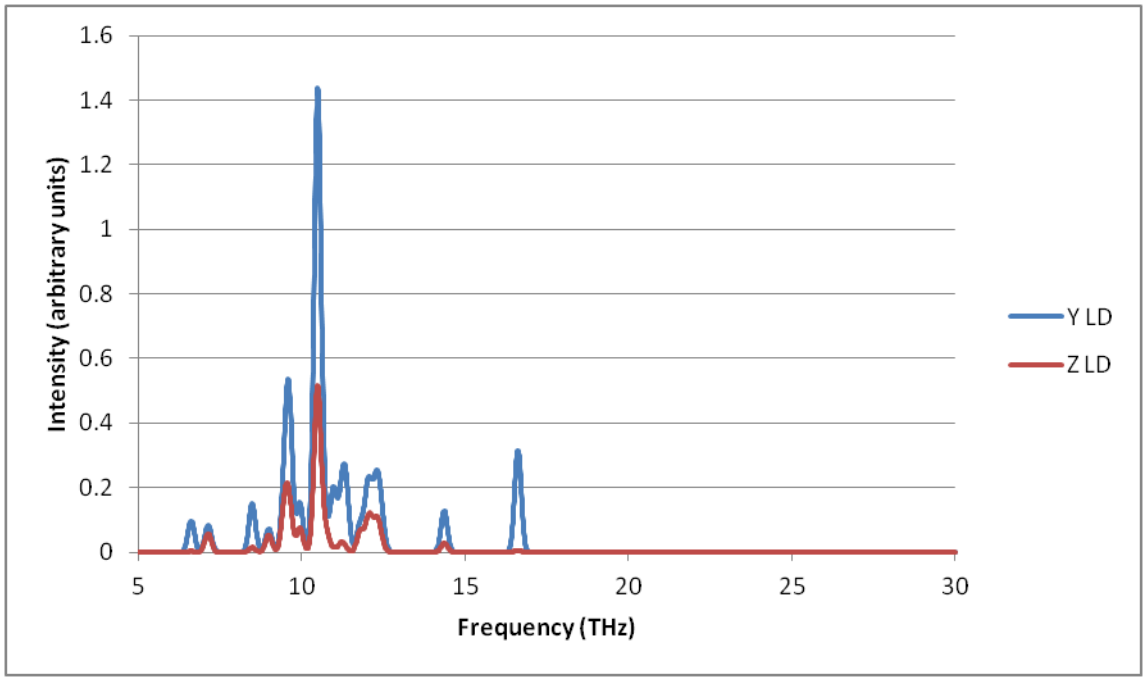

Figure 4.31 Lattice dynamics frequencies with greatest magnitude in both the Y direction and the Z direction for the {100}grain boundary. An identical set is found with the directions reversed.

These additional contributions stem from the symmetry of the structure and partial continuity of the structure across the grain boundary. Simply, the motion in the Y direction of one grain is instigating a corresponding motion in the Z direction of the other grain. Thus the dimensional contributions cannot be completely separated.

When considering only the X direction the Σ5{210} tilt boundary has a slightly lower thermal conductivity across all temperatures than the {100}twist boundary, likely due to the lower density of the Σ5{210} boundary (94% compared to 97%). The average thermal conductivity for the whole system is however very similar indicating a strong influence of the proximity of the boundaries at these sizes. Whether this relationship holds at greater inter-boundary distance is unclear.

The simulations described here have demonstrated that the thermal conductivity is significantly reduced in the direction perpendicular to the grain boundary and that the structure of the grain boundary also has an impact on the thermal conductivity. The thermal conductivity parallel to the grain boundaries is also affected due to confinement of the phonons to the core of the grains, leading to a variation in thermal conductivity along with grain size.

By applying the same techniques to more complex polycrystalline systems the effect of different grain boundaries, grain sizes, surfaces and disorder may be elucidated.

4.4. MgO Nanostructures

Nanostructures are a promising approach to improve the ZT of thermoelectric materials as they can begin to approach the Phonon-Glass Electron-Crystal (PGEC) idea put forth by Slack [21, 44]. By offering many scattering areas mixed with regions of unmodified bulk it is possible to tune the scattering to affect primarily phonons and not electrons. However, there is some evidence that energy filtering by grain boundaries can also be beneficial to the power factor by boosting the Seebeck coefficient [54].

Rocksalt type nanostructures have been explored previously [224] and are produced via amorphisation and recrystallisation. The nanostructures used in this work were chosen to be geometrically distinct to each other. Thus one nanostructure is based on a hexagonal superlattice and one on a cubic superlattice.

The large size and very low density of these systems pose a particular challenge for molecular dynamics simulation. As the LAMMPS code [166] distributes the calculations in a domain decomposition scheme, empty space can have a significantly detrimental effect of calculation speed and efficiency, even after optimisation of the domain sizes.

Thus the calculations were split into several shorter simulations rather than attempt a single very long simulation. The splitting of the calculation into smaller runs will not have a significant effect on the statistical accuracy as the autocorrelations are expected to be short lived and thus longer correlation times are not statistically significant.

A complication arises for the Green-Kubo calculation with these low density systems. In the grain boundary systems the density was near bulk levels (>90%), whereas this is not the case for the nanostructures. The Green-Kubo method require a system volume to calculate the thermal conductivity but it is somewhat unclear whether this volume should be of the entire system, or just the occupied space. This work uses the volume of the entire system as the nanostructure is the only object within the simulation cell and therefore the thermal conductivity should be correct for the given region of space which contains the nanostructure.

The next section presents the morphology, density and thermal conductivity of the two nanostructures. The Green-Kubo spectra are also discussed along with data from a model slab system to assist interpretation of the spectra.

4.4.1. Nanostructure 1: Hexagonal Superlattice

The first nanostructure studied is based on a hexagonal superlattice and contains 50,400 atoms in a simulation cell approximately 96 Å x 164 Å x 68 Å in size with a 500 K density ~46% that of bulk magnesium oxide. The structure is presented in Figure 4.32.

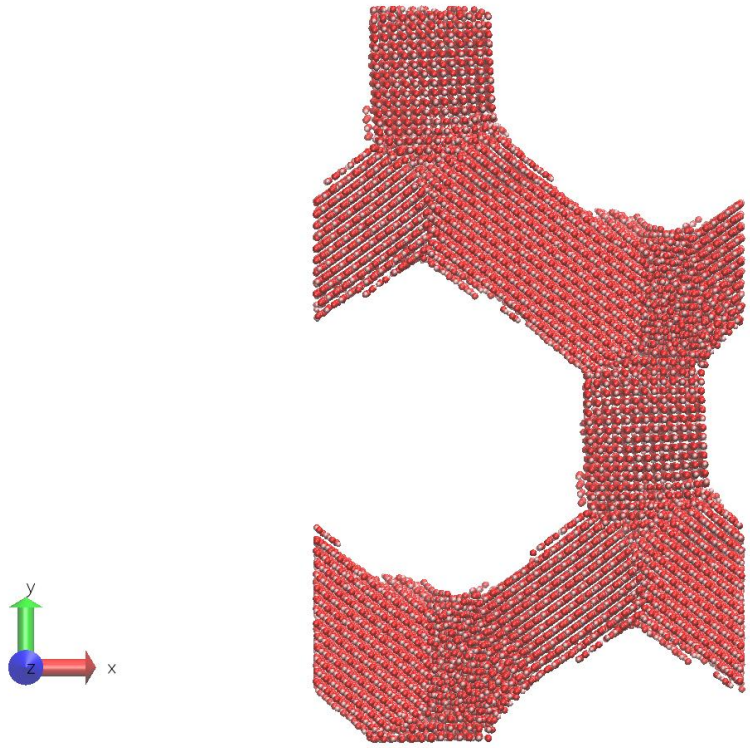

Figure 4.32 Simulation cell of the hexagonal nanostructure.

A feature particular to this nanostructure is that the grain boundaries are only present perpendicular to the X-Y plane and the structure is symmetrically similar in 6 directions related by 60° rotations around the Z axis. Figure 4.33 shows a 3 x 3 x 3 expansion of the simulation cell coloured to highlight different density environments, such as surfaces and grain boundaries, which will act as scattering centres.

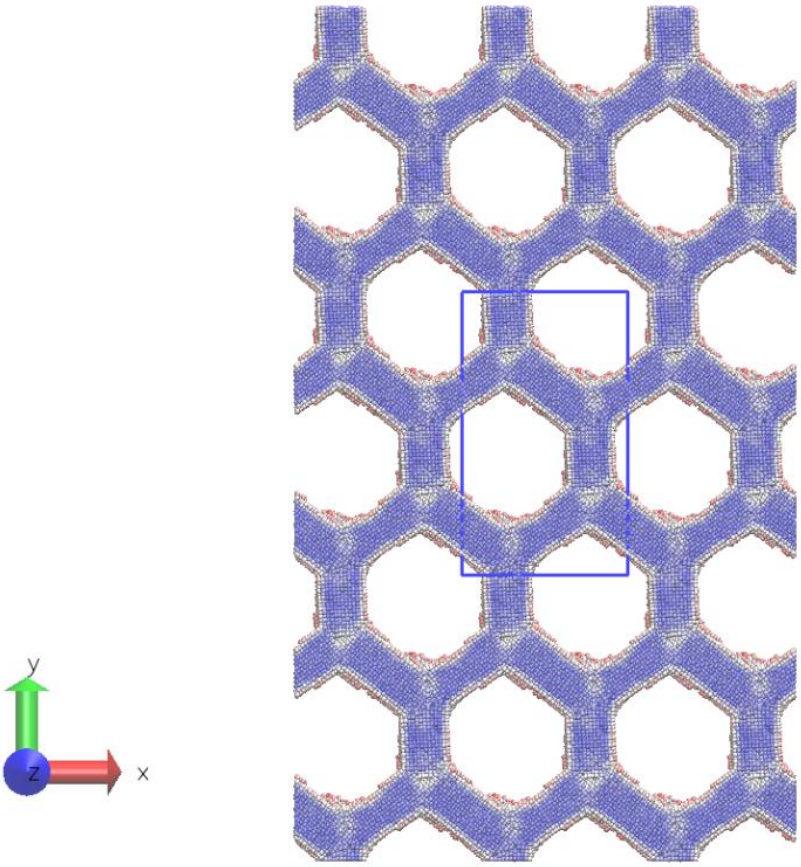

Figure 4.33 The hexagonal nanostructure (expanded 3 x 3 x 3) coloured to highlight different density environments. Blue is high density and red/white is low density. The blue box highlights the original simulation cell.

The simulation was equilibrated at each temperature for 500,000 steps in an NPT ensemble, next the lattice vectors of the systems were set to their average values for the appropriate temperature. Subsequently 8 copies of the system were made and given new random initial velocities and equilibrated briefly (100 fs) in an NVT ensemble to remove any effect of initial conditions. The systems were then simulated in an NVT ensemble for 0.6 ns to collect heat-flux data. The autocorrelation was calculated up to 100,000 steps. The averaging of the converged value was taken over the same region of the autocorrelation integral as for previous magnesium oxide calculations. The results are displayed in Figure 4.34 and Figure 4.35.

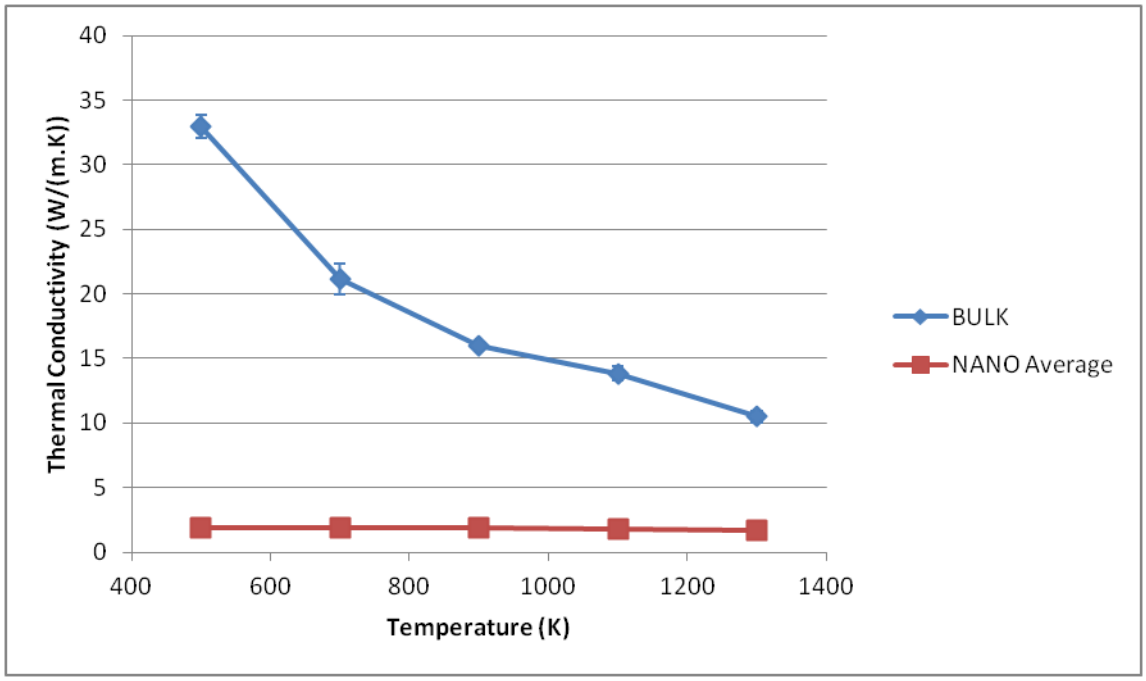

Figure 4.34 The average thermal conductivity for the hexagonal nanostructure compared to bulk.

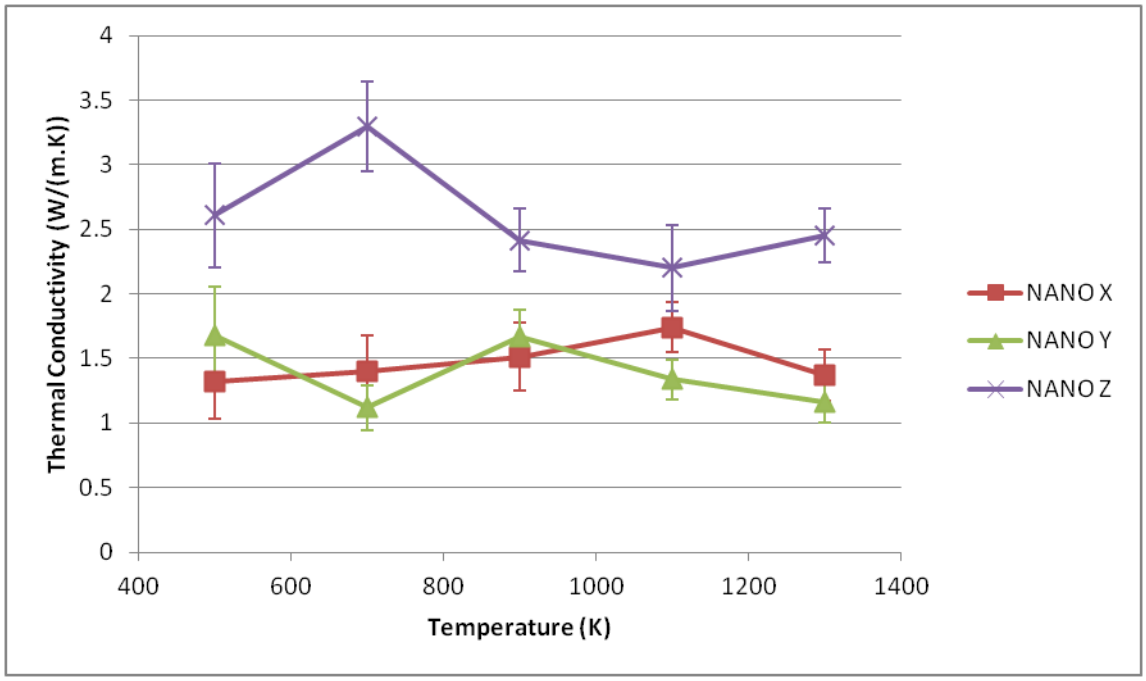

Figure 4.35 The directional thermal conductivity for the hexagonal nanostructure.

The thermal conductivities for the hexagonal nanostructure show no temperature dependence, indicating a significant increase in scattering due to defects at all temperatures. The X and Y direction thermal conductivities are all between 1 and 2 W/(m.K) and are essentially identical within the error, which is expected as the

nanostructure is symmetrically equivalent in these directions. This effect was also observed in the {100}twist boundary.

The Z direction thermal conductivity is distinctly higher than the X and Y directions due to the grain boundaries being parallel to the Z direction instead of perpendicular. However scattering still occurs off the parallel boundaries and accounts for the large reduction in thermal conductivity.

One concern for these calculations is the limited size of the nanostructure motif. While the simulation is large in terms of the magnesium oxide unit cell, the nanostructure itself only contains two repeat units of its smallest representation. To accurately reproduce extremely long wavelength, and thus low frequency, phonons relating to the movement of the lattice itself would require several repeat units of the superlattice as a minimum. However, it is not known for certain whether such low frequency phonons will contribute significantly to the thermal conductivity of this structure.

The Green-Kubo spectra for hexagonal nanostructure are presented in Figure 4.36, Figure 4.37 and Figure 4.38.

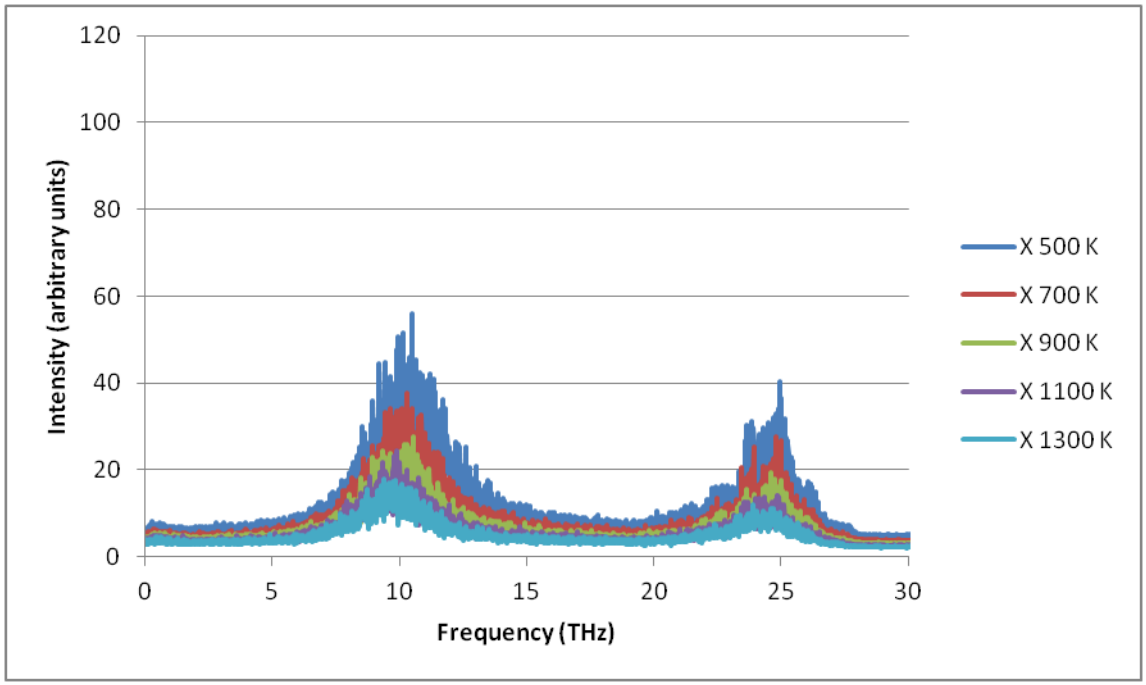

Figure 4.36 Green-Kubo spectra for the hexagonal nanostructure in the X direction.

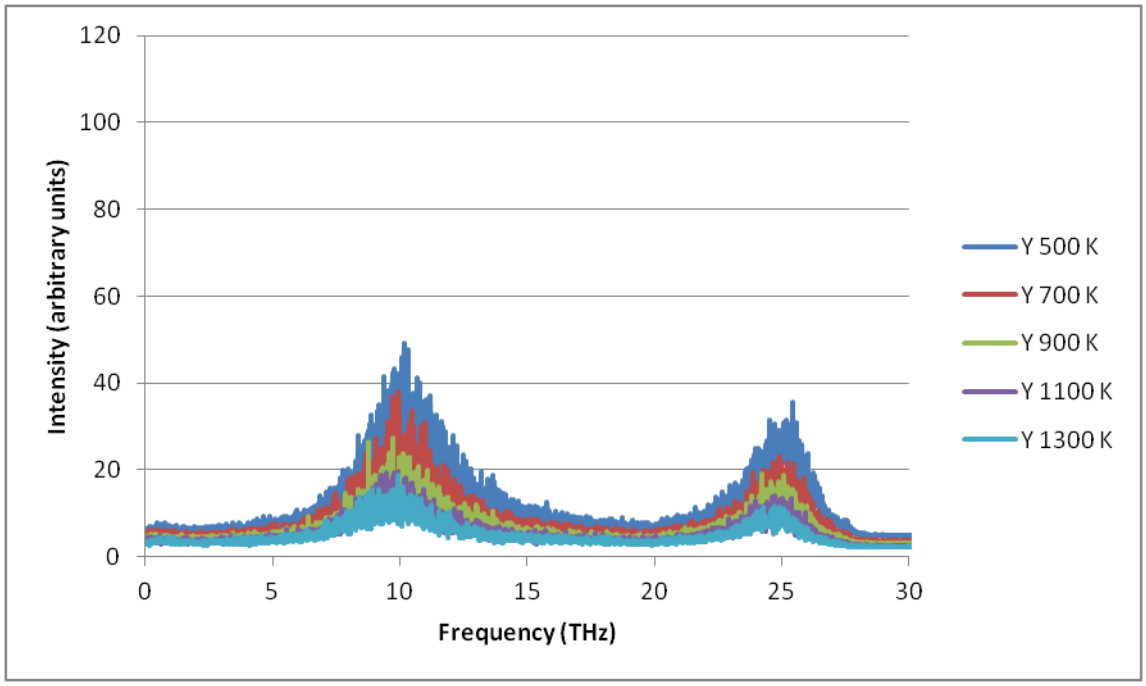

Figure 4.37 Green-Kubo spectra for the hexagonal nanostructure in the Y direction.

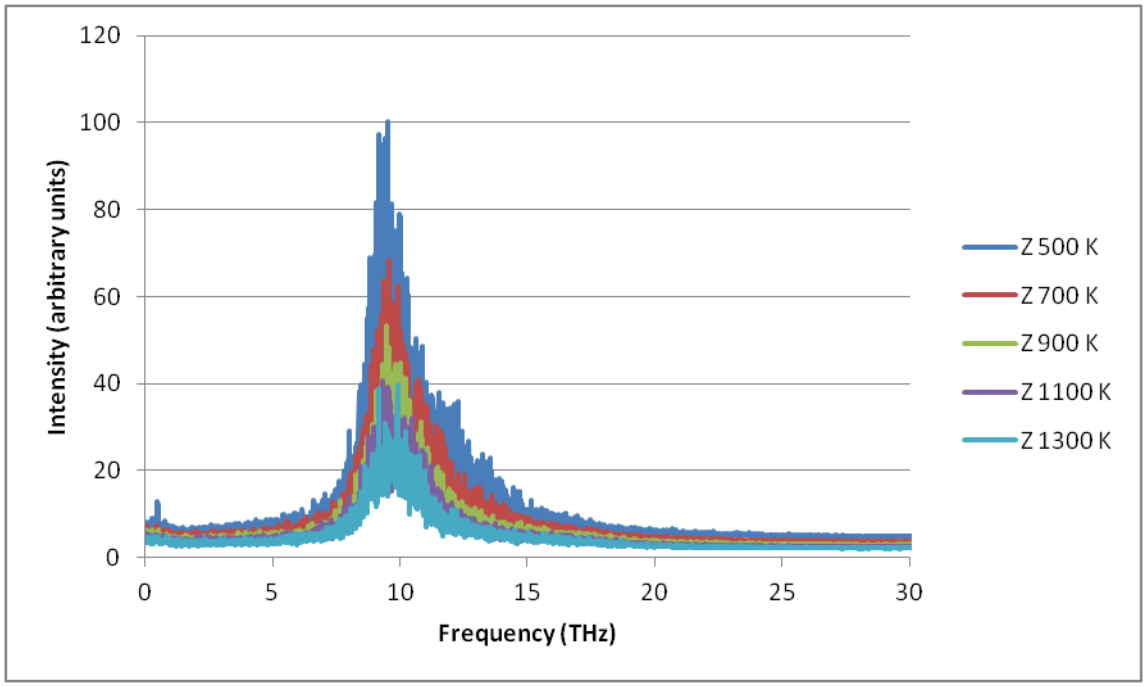

Figure 4.38 Green-Kubo spectra for the hexagonal nanostructure in the Z direction.

The most obvious effect of nanostructuring is the broadening of the peaks. The broader peaks generally mean a shorter phonon lifetime. However, it is also possible that the increased variability of magnesium and oxygen environments has resulted in a large number of very similar modes clustered around ~10 THz, as was seen in the grain

boundary systems and discussed in Chapter 4.3. More intriguing is the additional peak which appears around 25 THz in the X and Y directions.

The peak at ~25 THz in the X and Y directions is entirely missing from the Z direction spectra and thus is related to a feature found specifically in the X and Y directions and not the Z direction. Possible origins for the additional peak include the complex three grain boundary intersection, the separate tilt grain boundaries or the numerous surfaces (which are almost entirely <001> surfaces).

However, from the grain boundary calculation in Chapter 4.3 it is clear that most grain boundary vibrational modes occur in the region of ~10 THz and so it is much more likely that the new modes originate from the large <001> orientated surfaces found perpendicular to the X and Y directions.

The full hexagonal nanostructure contains 50,400 atoms and is much too large to be studied directly using lattice dynamics. Therefore a model system must be used to determine whether <001> surfaces are the origin of the ~25 THz peak.

4.4.2. Model System

A series of magnesium oxide slabs were generated and energy minimised. Each slab is made up of a number of layers (each layer is two atoms thick) with a surface termination of {001}. The slabs are separated enough from their periodic images to remove slab-slab interactions. The phonon DOS was calculated for each slab system and then processed to remove modes that do not interact with the heat-flux, leaving a spectrum which is directly comparable to the Green-Kubo spectrum. Figure 4.39 shows the frequency with the largest magnitude in the direction perpendicular to the slab plane as a function of slab thickness.

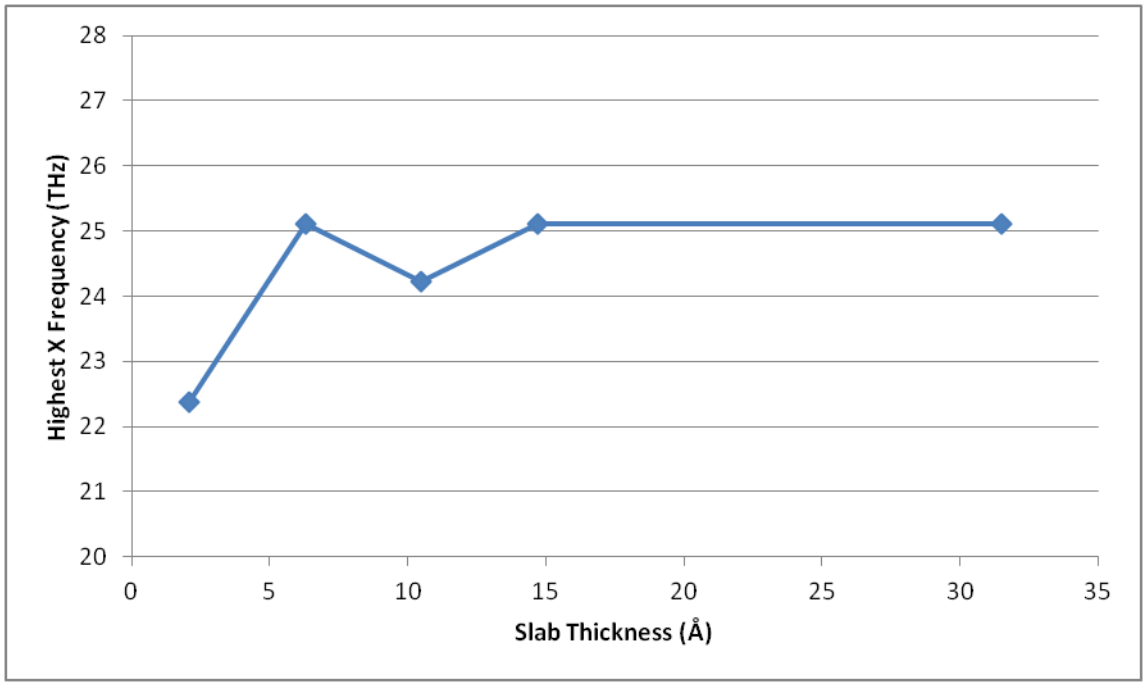

Figure 4.39 Frequencies of a magnesium oxide slab in the X direction as a function of slab thickness.

Figure 4.39 demonstrates that the {001} surface of MgO introduces an additional scattering mode appearing above 20 THz, originating from the species at the surface being undercoordinated. It can also be seen that the thickness of the slab also has an effect on the frequency, converging to ~25 THz for thicker slabs. The thickness of crystallites in the hexagonal nanostructure are on the order of ~25 Å which is in the middle of the converged region of Figure 4.39; thus it is reasonably certain that the source of the new ~25 THz mode in the hexagonal nanostructure stems from surface scattering.

Additional vibrational modes clustered around ~25 THz are also visible in the processed phonon DOS and stem from the subtly varying environments present at increasing distances from the surface. This result also goes some way to explaining the large broadening of the peaks seen in the Green-Kubo spectra.

It is noted that the thickest slab in these calculation still did not recover any bulk-like frequencies (i.e. ~10 THz) in the direction perpendicular to the slab, indicating the dominance of surface scattering at these sizes. However, the Green-Kubo spectra retains modes around 10 THz which likely stem from phonons travelling lengthways through the grain and scattering at non-perpendicular surfaces or grain boundaries.

Combined with the fact that the grain boundary calculations showed no significant modes above ~20 THz it can be concluded that the additional ~25 THz peak appearing in the X and Y direction spectra of the hexagonal nanostructure originate from surface scattering rather than grain boundary scattering, which from the grain boundary calculations tends to show peaks around ~10 THz, i.e. more bulk like.

4.4.3. Nanostructure 2: Cubic Superlattice

The second nanostructure chosen is constructed the same way as the hexagonal nanostructure but on a cubic superlattice instead. The cell itself is comprised of 2,744 atoms in a cell 41 Å x 39 Å x 41 Å in size with a 500 K density ~39% that of bulk magnesium oxide, Figure 4.40.

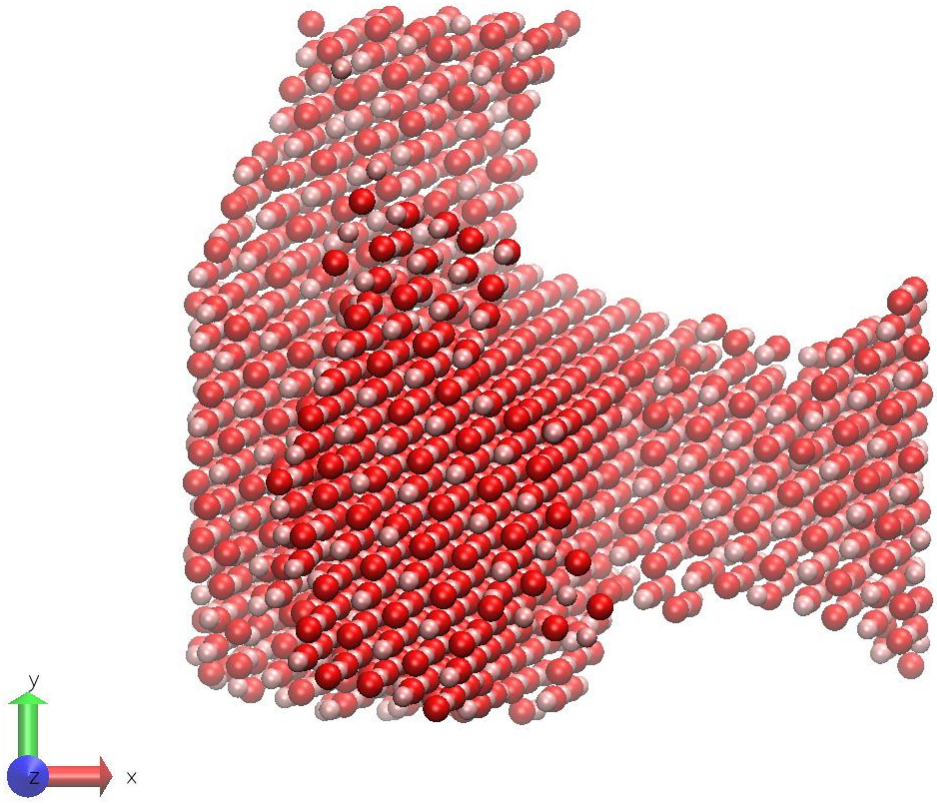

Figure 4.40 Simulation cell of the cubic nanostructure.

During recrystallisation no grain boundaries were formed, leaving a continuous crystal except for interconnected voids in a 3D grid arrangement; these voids lead to a large number of surfaces. The 3 x 3 x 3 expanded crystal structure is shown in Figure 4.41 and shaded according to local density. The crystal-like core (blue) is surrounded by lower coordinated surfaces (white).

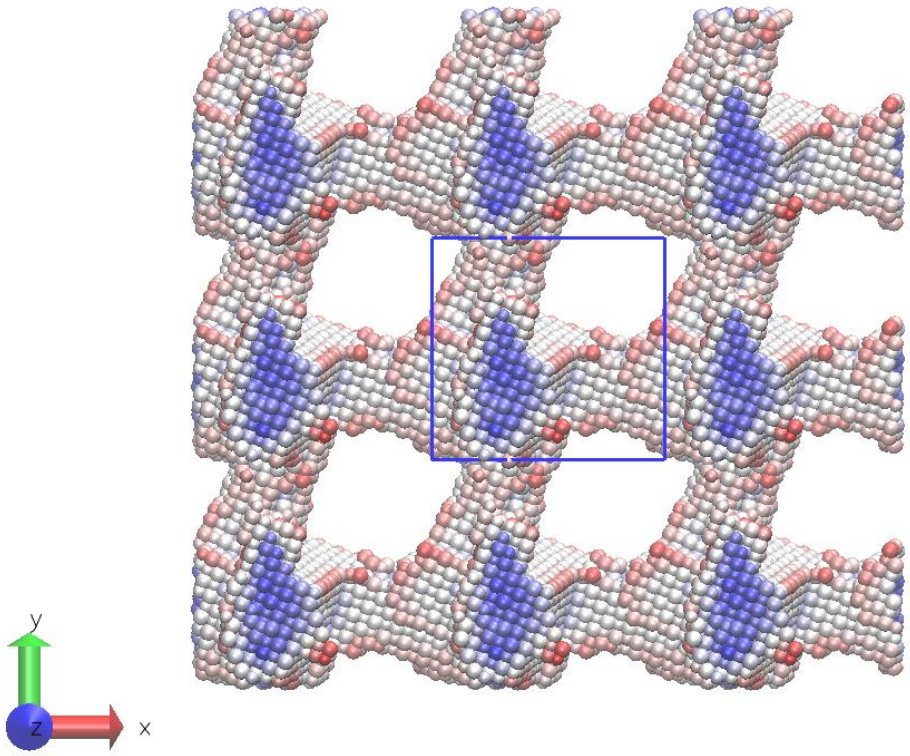

Figure 4.41 The cubic nanostructure (expanded 3 x 3 x 3) coloured to highlight different density environments. Blue is high density and red/white is low density. The blue box highlights the simulation cell.

The same equilibration process was applied as in the first nanostructure. However, due to the much smaller simulation cell than the hexagonal nanostructure the simulations were split into three groups of 5,000,000 steps. The thermal conductivities are presented in Figure 4.42 and Figure 4.43.

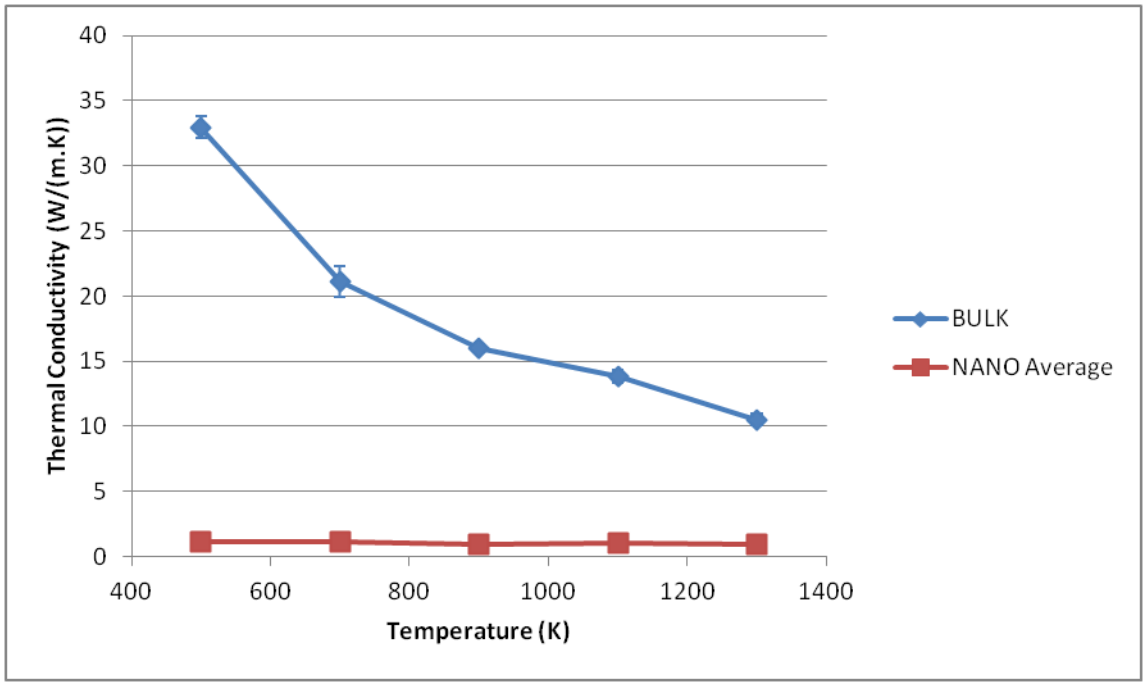

Figure 4.42 The average thermal conductivity for the cubic nanostructure compared to bulk.

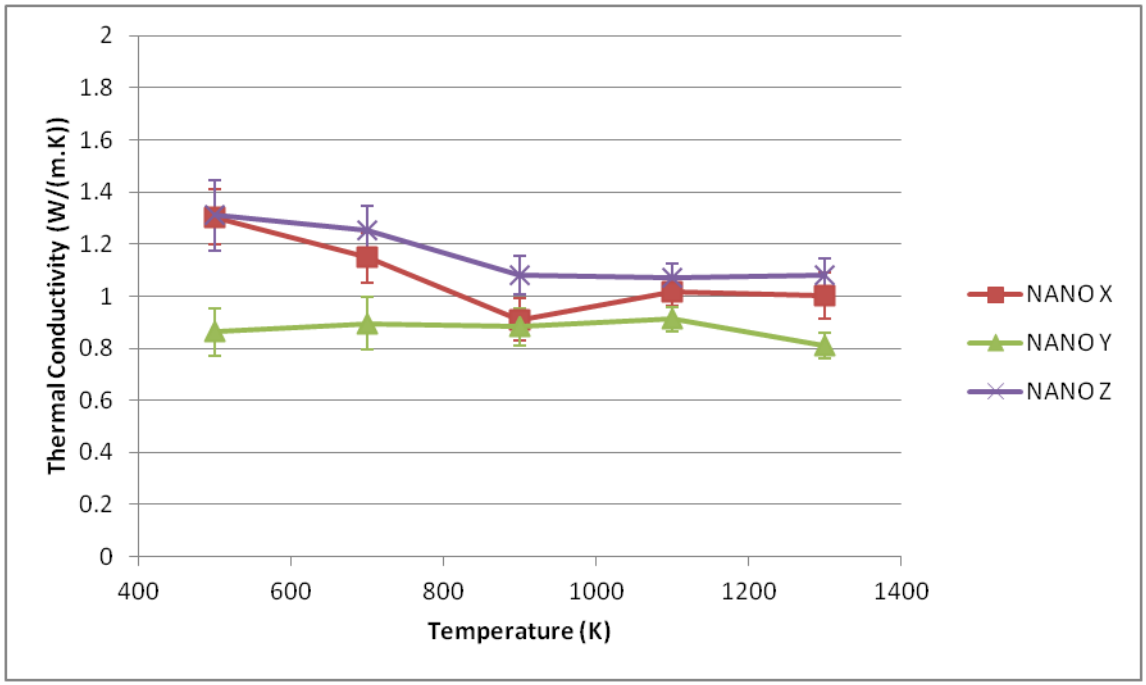

Figure 4.43 The directional thermal conductivity for the cubic nanostructure.

The thermal conductivity in each direction for the cubic nanostructure is lower than that of the hexagonal nanostructure. Once again there is little temperature dependence in the thermal conductivities, having approximately the same thermal conductivity across the range of temperatures studied.

As for previous systems a strong peak at ~10 THz is observed corresponding to the bulk-like vibrational mode. An additional peak is also visible which stems from the large number of surfaces in the system and the extremely small channels of MgO, leading to a large amount of scattering from surfaces. Due to the dominance of surface scattering a peak is expected at approximately 25 THz in the Green-Kubo spectra, Figure 4.44, Figure 4.45 and Figure 4.46.

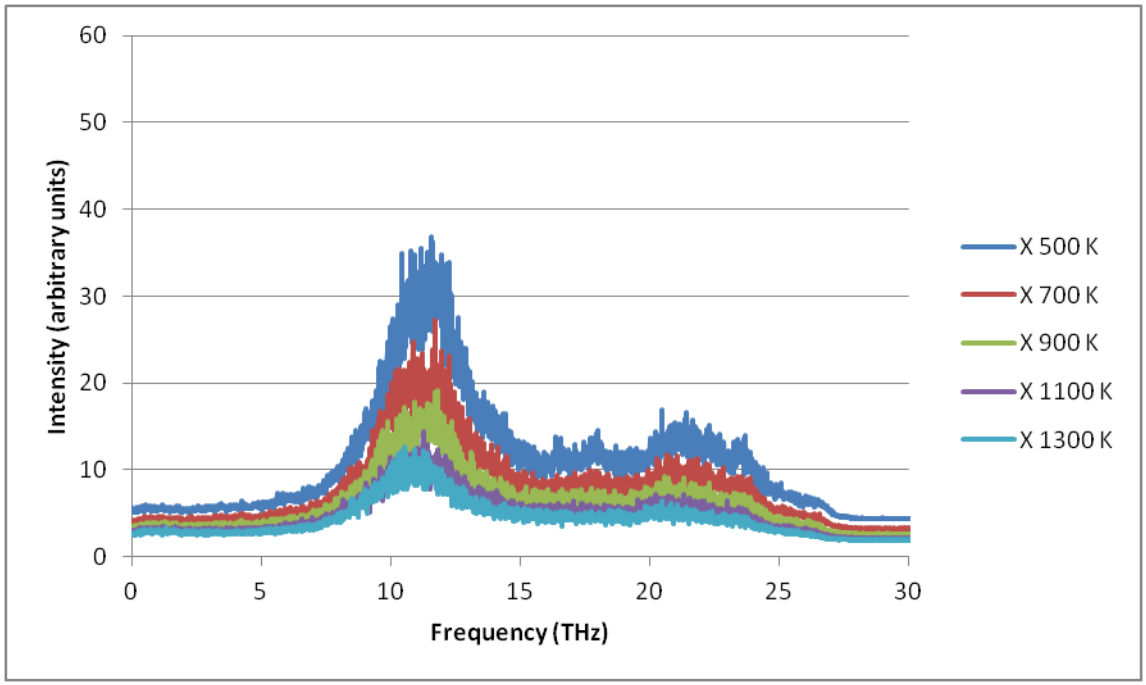

Figure 4.44 Green-Kubo spectra for the cubic nanostructure in the X direction.

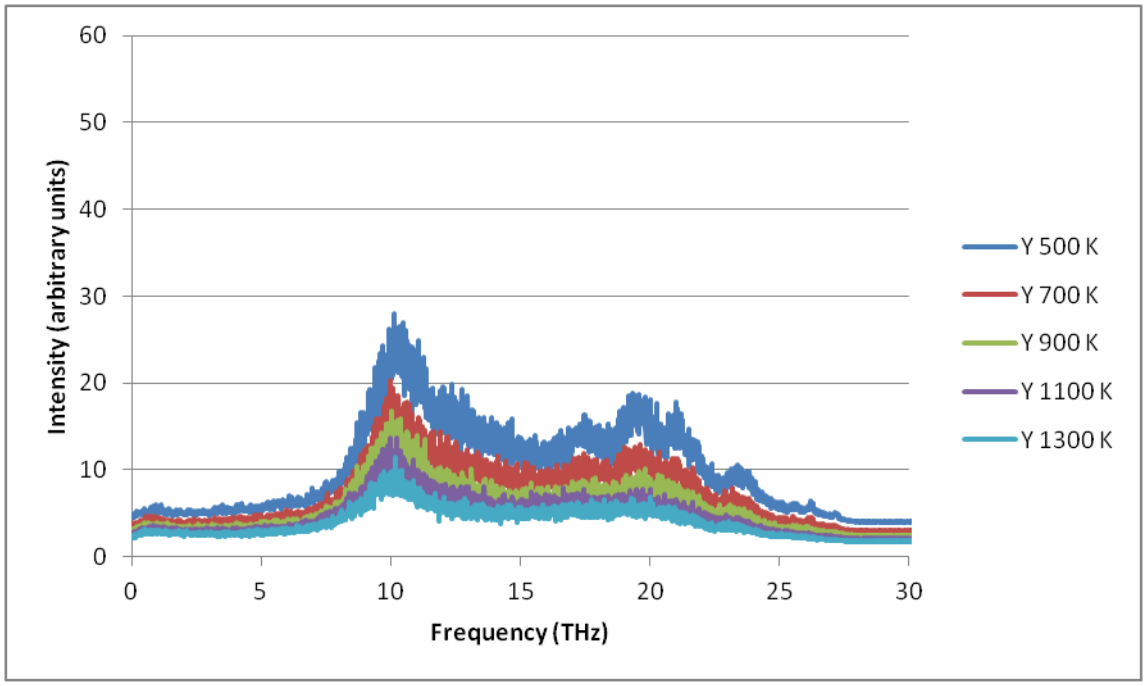

Figure 4.45 Green-Kubo spectra for the cubic nanostructure in the Y direction.

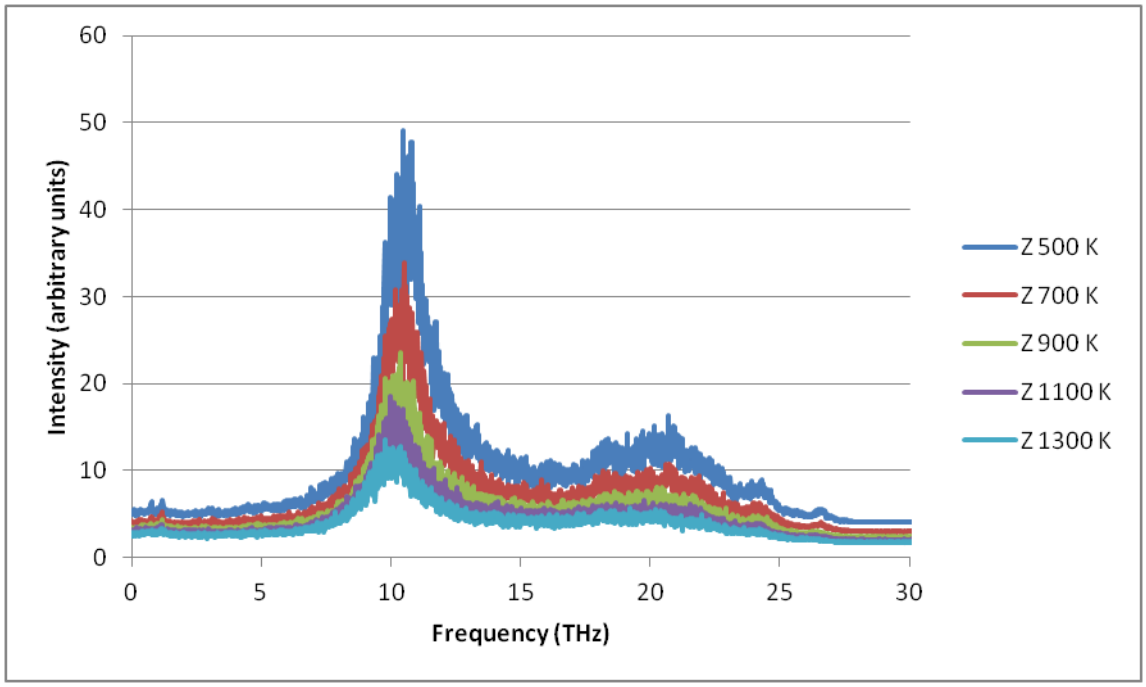

Figure 4.46 Green-Kubo spectra for the cubic nanostructure in the Z direction.

The three spectra are similar to each other but vary in the magnitude of the peaks. Once again a secondary peak occurs, but in this case at ~20 THz instead of ~25 THz. The change in peak position can be related to the very small size magnesium oxide channels and thus the very short surface-surface distance. The surface-surface distances in the cubic nanostructure are on the order of 8 Å to 15 Å and correspond to a frequency of

~24 THz in Figure 4.39, which is slightly higher than the values found in the Green-Kubo spectra. However, other effects such as cross-sectional area and surface roughness may also play a role in reducing the frequency further.

4.5. MgO Summary

The simulation of magnesium oxide has revealed that Green-Kubo calculations can give well converged thermal conductivities and an estimate of the error. Furthermore, the method gives access to phonon information that can be used to understand the scattering process going on at different temperatures and in different systems.

Lattice dynamics and molecular dynamics calculations can be used to provide complementary information. Using the Boltzmann transport equation provides an alternative route to calculating thermal conductivity but very quickly becomes resource intensive with respect to system size and is not applicable for nanostructured or large defective systems. An additional issue arises for high thermal conductivity systems where the phonon mean free path is long and hence larger supercells are required.

Lattice dynamics calculation of the phonon density of states (DOS) also provides additional information to aid understanding of the vibrational modes appearing in the Green-Kubo calculations. With this information it becomes clear which structural features are contributing the most to phonon scattering and hence lowering thermal conductivity. New nanostructures can then be designed with the most promising features to either maximise or minimise the thermal conductivity depending upon the application.

For magnesium oxide the type of boundary seems to have only a small effect on the overall reduction in thermal conductivity. Both the tilt and twist boundary reduce the thermal conductivity to between 5 and 10 W/(m.K). What seems to be important is the disruption to the bulk by introduction of the grain boundary and limiting of allowed frequencies between the two boundaries in each simulation cell. Work on $SrTiO_3$ grain boundary systems presented in Chapter 6.3 will explore the effect of different grain sizes on the thermal conductivity. There is however an effect on the modes available for scattering introduced by the boundaries.

Complex nanostructures successfully reduce the thermal conductivity several orders of magnitude, however a correction may have to be applied to account for the porosity of the structures. Defects and grain boundaries will reduce the thermal conductivity but surfaces play the largest role for nanostructures as seen from the peaks of the Green-Kubo spectra. The exact positioning of the additional surface peak varies depending on the characteristic size of the grains. While grains are rarely this small in experiments the result may have important implications for other materials such as 2DEG materials which tend to have extremely small layers [236].

An important result for both grain boundaries and nanostructures is that an increase in defect scattering modifies the behavioural trend of thermal conductivity with respect to temperature. Phonon-phonon scattering is the only scattering mechanism available for pure materials and increases with temperature; however defect scattering is active at all temperatures. Thus all defective structures display a reduced response as temperature increases. The density of the system can also give a good indication of the thermal conductivity reduction, with lower densities equalling lower thermal conductivity, but no clear trend presents itself.

In summary, the results demonstrate that the thermal conductivity can be calculated reliably for the ionic material, and that the modes that have the largest effect on the thermal conductivity. Different boundaries and nanostructures have also been studied and their influence on thermal conductivity evaluated.

Furthermore, the results suggest that if analogous oxide materials were used as part of a thermoelectric device a reduction in the thermal conductivity (and hence an increase in ZT) of a factor of ~30 could be achieved, which may mean the difference between the device being usable or not.

In the following Chapter SiO_2 is considered. SiO_2 based materials offer a chance to study the behaviour of thermal transport in a covalent system instead of the purely ionic system presented by MgO.

5. The Thermal Conductivity of Silica (SiO_2) Structures with Complex Vibrational Modes

The aim of this chapter is to extend the range of thermal conductivity simulations to covalent materials. This study has opted to look at silica, SiO_2, which is not only highly abundant, being one of the most naturally abundant oxides, but is also used in a range of devices and in its amorphous forms constitutes a major component of glasses.

Additionally, mesoporous silica has been used as an additive to Nb-doped $SrTiO_3$, which increased the ZT five fold via an increase in the electrical conductivity and reduction of thermal conductivity caused by the growth of $Sr_2TiSi_2O_8$ at the grain boundaries, while the Seebeck coefficient remained unchanged [237]. The reduction in thermal conductivity and enhancement of electrical conductivity is of particular interest as the system is now approaching the PGEC concept [44]. The PGEC-like behaviour of the material may originate from the $Sr_2TiSi_2O_8$ phase found at the boundary which is capable of rigid unit motion [238], leading to very low frequency RUMs which may be highly effective at scattering acoustic phonons. Silica systems are also known to contain rigid unit modes (RUMs) [239] and so can act as a model system.

Hence, a detailed analysis of heat transfer in silica materials is also of great technological interest. Structurally, most silica polymorphs contain silicon atoms tetrahedrally coordinated by oxygen atoms, although there are some exceptions [240], such as the high pressure forms which may adopt octahedral coordination. These tetrahedra are then corner linked to form a variety of different crystalline structures, the most stable of which is quartz, but there are many other naturally occurring metastable forms, such as cristobalite and tridymite [241]. A number of more complex silica systems also exist, such as those synthesised within the zeolite community. One of these zeolite materials is silicalite, which is the basis of an important class of acid catalysts used for cracking hydrocarbons [242].

5.1. SiO_2 Overview

The wide variety of silica structures, which can undergo complex phase transitions, has meant that the structural properties, including the effects of temperature, have been studied extensively using computer simulation techniques [243-245]. One reason for the

structural complexity, which makes the vibrational properties of silica structures distinctive, is the presence of rigid unit modes (RUMs) [246-248], which are vibrational modes of silica frameworks with very low frequency. RUMs are often also associated with negative Grüneisen parameters and can be used to explain the mechanisms for the various phase transitions as well as the distinctive auxetic properties (negative Poisson's ratio), most notably the negative thermal expansion coefficient [249]. A further question that then needs addressing is how this auxetic behaviour affect the thermal conductivity.

Thus, in this chapter two distinct structures will be considered. Firstly the thermal conductivity of quartz will be studied with particular interest in effect of the phase transition to β-quartz at higher temperatures. Secondly the thermal conductivity of a microporous material, silicalite, will be studied. However, before modelling the thermal conductivity of silica polymorphs a potential model must be identified that can reproduce the vibrational and structural parameters with sufficient accuracy, which is described in Chapter 5.2.

Reproducing the structural and vibrational properties of these different materials with a single potential model is very important. There are many potential models available for silica materials [250], including very complex reactive potentials [251]. However, a relatively simple potential model is desirable for the calculation of thermal conductivity due to the large system sizes and long simulation times required for a converged result. Thus, the requirement is for a comparatively simple functional form that has been used to model structural [252], elastic [253] and vibrational [254] properties.

The potential model of van Beest, Kramer and van Stanten (BKS) [161, 162] has been selected for the work detailed here as it satisfies the requirement for a simple yet accurate model. The BKS potential has been used frequently and has been applied to a wide range of silicate materials. Examples showing the success of the BKS potential include shock-wave compression of quartz [255], pressure induced amorphisation [256, 257], many amorphous glass studies [258-260] and the α-quartz to β-quartz transition [261]. Additionally the phase diagram for SiO_2 using the BKS potential is at least partially known [262].

The BKS potential uses a simple Buckingham form for the short range interactions where the parameters were adjusted to reproduce the results of a number of electronic structure calculations along with experimental structural data. As indicated, it has been

used extensively in the calculation of many other properties and silicate systems. Indeed, the convention of using the oxygen charge of -1.2 e has also been adopted by the other potential models [156, 163].

More complex potential models than the BKS potential are available which include additional terms such as a three-body interaction [263, 264] or the shell model [265]. While improving on some properties over the BKS potential, the additional complexity will slow calculation significantly and make the potential unsuitable for thermal conductivity calculations. Thus the BKS potential is used for all silica materials detailed in this chapter.

5.2. Quartz

Quartz constitutes a significant proportion of the earth's crust, coming second only to feldspar in abundance. Quartz also has numerous industrial and commercial applications due to its piezoelectric and pyroelectric properties, which arise out of the complex structure of the material.

The quartz structure is complex due to the many types of symmetry present. Quartz is a non-centrosymmetric material meaning there is not a centre of inversion. This in turn gives rise to the piezoelectric and pyroelectric properties as dipoles may be formed across the material under stress/heating. Additionally, this property means there exists left and right handed polymorphs of quartz (Brazil twins) [266] related through a mirroring of the structure (enantiomorphism).

Quartz may also exhibit further polymorphs related by the tilting of the SiO_4 tetrahedra. At low temperatures quartz is in the form of α-quartz, where the tetrahedra are relaxed and tilted by 16.3° [267]. The tetrahedral tilt angle found in α-quartz may be positive or negative, giving rise to two polymorphs which are related through a 60° rotation about the c axis; when both forms are present in a single crystal the system is known as a Dauphiné twin.

Upon heating above ~846 K [268], the α-quartz polymorph transforms into the higher symmetry β-quartz polymorph. The difference between α-quartz and β-quartz is in the average angle of tilt of the silicate tetrahedra. When the structure is α-quartz the

tetrahedral are tilted by approximately 16.3° on average, transitioning to an average tilt of 0° in β-quartz.

The vibrational mode involved in the phase transformation is thus known as a rigid unit mode (RUM) [239]. RUMs have unusual vibrational properties [269-271] and leads to the negative thermal expansion of quartz at higher temperatures [249]. The presence of RUMs may also have some impact on the thermal conductivity of quartz and other silica polymorphs.

Previous simulation work with the BKS potential model by Yoon et al. showed little variation of thermal conductivity with respect to temperature [272] at around ~5 W/(m.K) between 500 K and 1100 K. The approach used was that of a NEMD simulation with data collected over the course of 2-12 ns. The thermal conductivity is then extrapolated from three different simulation sizes. The poor thermal conductivity values can be attributed to the setup of the simulation which had only a small region of diffusive thermal transport, the rest being dominated by ballistic transport introduced by thermostated hot/cold regions. Additionally, the extrapolation to infinite size thermal conductivity was only calculated with three system sizes, which is not enough to discern a trend in the data. Thus, to obtain reasonable values larger bulk regions or a smaller temperature difference are required in conjunction with more system sizes.

Work by McGaughey et al. on the thermal conductivity of quartz also used the BKS potential but calculated the thermal conductivity with the Green-Kubo method instead and gave results which were in much better agreement with experiments [200, 202] than the NEMD work by Yoon et al., although at low temperatures only.

The work by McGaughey et al. [200, 202] used the Wolf method [273] for electrostatics as it was found that the long range interactions were on the order of ~1% that of the short range interactions; the advantage of this method is that the electrostatic interactions are approximated as a medium range potential and hence the calculations are significantly faster. The calculations were performed on temperatures between 100 K and 350 K at 50 K steps. Each temperature had five separate ~1 ns simulations performed and averaged to better sample phase space (with the exception of the 100 K series which required 10 separate ~1 ns simulations). The final thermal conductivity was located by using overlapping averages on the integral to identify the point of convergence. The results are very close to experimental values in both absolute value

and trend, supporting the use of both the BKS potential and the Green-Kubo method in calculating the thermal conductivity.

Thus, the aim of this component of the work was firstly to demonstrate that not only can the thermal conductivity of α-quartz be calculated efficiently, but using the procedures described in the previous chapter the extent to which the optical modes are involved in heat transfer may be identified.

The second aim is to investigate whether the effect of the α-quartz to β-quartz phase transition can be evaluated and if domains play a role in lowering the thermal conductivity. However, before describing the results of the thermal conductivity simulations, an assessment of the potential model in calculating more routine bulk properties is discussed.

The structures of α-quartz and the high temperature polymorph β-quartz have been well determined experimentally [274] having the space groups $P3_221$ [274] and $P6_222$ [275] respectively. Images of the structures are given in Figure 5.1, which shows the increased symmetry in β-quartz.

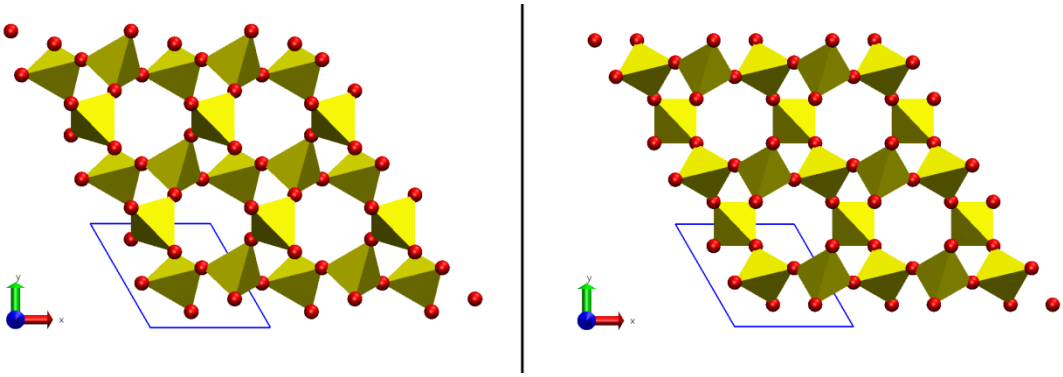

Figure 5.1 View down the c axis of α-quartz (left) and β-quartz (right). α-quartz is related to its Dauphiné twin by a 60°/180° rotation around the c axis. The hexagonal unit cell is displayed in the blue box.

As already mentioned in the previous chapter the thermal conductivity depends directly on the structure and lattice properties, including the elastic constants. The lattice parameter and elastic constants of α-quartz have been calculated via energy minimisation in the METADISE code [165] and are presented in Table 5.1.

Property	Calculated	Experiment	% Difference
a (Å)	4.922	4.913	0.18
c (Å)	5.434	5.405	0.54
c_{11} (GPa)	89.5	86.8	3.11
c_{33} (GPa)	111.73	105.75	5.65
c_{12} (GPa)	1.01	7.04	-85.65
c_{13} (GPa)	16.85	11.91	41.48
c_{44} (GPa)	50.6	58.2	-13.06
c_{66} (GPa)	39.69	39.88	-0.48
c_{14} (GPa)	-16.87	-18.04	-6.49

Table 5.1 Calculated and experimental [276, 277] properties of α-quartz.

The agreement with experimental values is excellent. The lattice parameters are within 0.05 Å of their experimental values. The elastic constants are also reproduced very well which is to be expected considering the BKS potential has been developed with the elastic constants as one of the fitting parameters. One further detail to note is that the BKS potential over predicts the Si-O-Si bond angle by ~6° at room temperature, which has been noted previously [278].

The temperature induced phase change present in quartz is closely linked to RUMs as the difference between α-quartz and β-quartz is in the positioning of the tetrahedra. Above the phase transition (~846 K) [268] the RUMs also play a role in the negative thermal expansion. How well the BKS potential performs in reproducing the phase change will also help indicate how well temperature dependent changes in the phonon frequencies are being reproduced.

5.2.1. Thermal Expansion

The thermal expansion of quartz was calculated as for magnesium oxide. In these simulations the BKS potential has been used due to the wealth of study and testing done on it previously [161, 162, 202, 255, 258-261]. The simulation cell used was a 7 x 4 x 6 expansion of the orthorhombic unit cell consisting of 18 atoms and measuring approximately 4.9 Å x 8.5 Å x 5.4 Å, giving a final simulation cell of 3,024 atoms and

measuring approximately 34.5 Å x 34.1 Å x 32.6 Å. The crystallographic c direction of quartz is aligned along the Z direction.

The thermal expansion was measured using the same procedure as for magnesium oxide. A series of 5 different 0.5 ns anisotropic NPT (Nosé–Hoover thermostat and barostat) molecular dynamics simulations were run on 6 different temperatures. A timestep of 1.0 fs was again used. The lattice vectors were sampled every 10.0 fs and averaged over the course of the simulations. Due to the anisotropic nature of the underlying material the lattice vectors were averaged independently.

The resulting cell dimensions were converted back to the primitive hexagonal unit cell for easier comparison with experiments. The calculated a and b lattice parameters were found to be almost identical and that the maximum difference between them was less than $5x10^{-4}$ Å at high temperatures. Additionally the standard error between the 5 separate runs was also on the order of $5x10^{-4}$ Å. The final results are plotted in Figure 5.2, only the a and c parameters are presented.

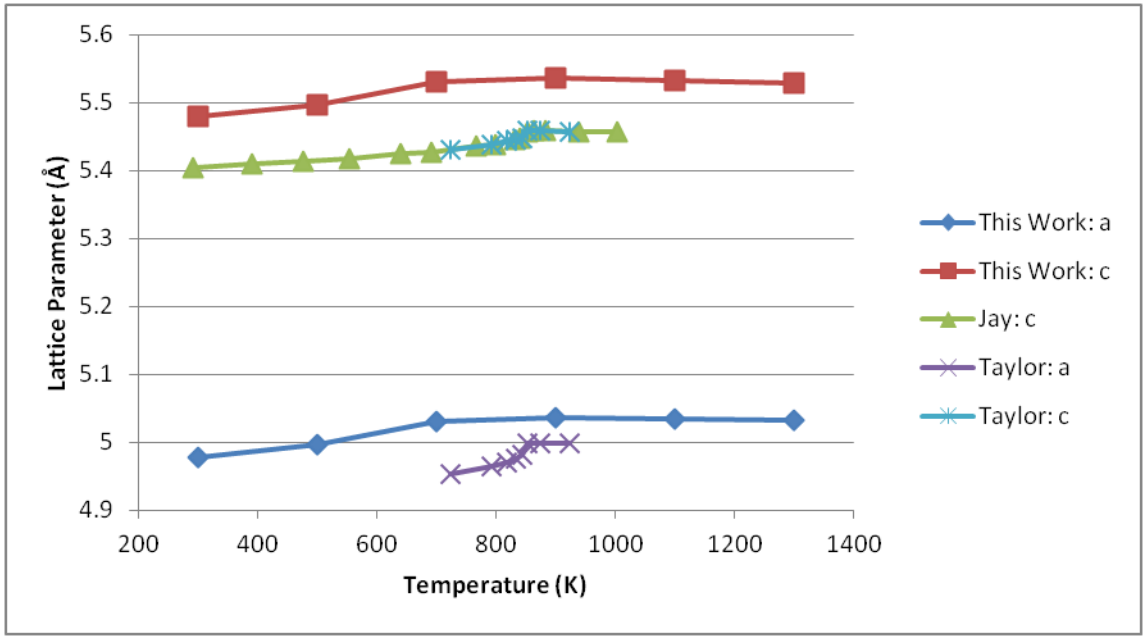

Figure 5.2 Calculated and experimental [279, 280] lattice parameters of quartz.

The experimental c parameters of Jay and Taylor are effectively identical and are overlaid in Figure 5.2. However, the a parameter from the experiments of Jay (not shown) is significantly lower than the calculated values (in the region of 4.25 Å to 4.32 Å). The discrepancy is because the a values of Jay were extrapolations based on the c direction rather than measurements and so are not included. Due to the remarkable

similarity of the c lattice parameters and the untrustworthiness of the Jay a lattice parameter only the experimental values of Taylor will be used from this point onwards.

The calculated lattice parameters of quartz are reproduced well with a deviation of less than 3% compared to experiments. However, there is a consistent shift to higher values in simulation as compared to experiments. The c lattice parameter is consistently shifted upwards by 0.08 Å compared to experimental values. The a direction has a more variable shift of between 0.04 Å and 0.08 Å above experimental values.

The trends seen in both the a and c directions are relatively well reproduced. The phase transition from α-quartz to β-quartz appears to occur in the region of 700 K-900 K in the calculations which matches well with the experimentally known value of 846 K [268]. The thermal expansion coefficient has been calculated for α-quartz and β-quartz separately using the values presented above and split across the phase transition temperature. The thermal expansion coefficients for α-quartz were calculated using the lattice parameter at 300 K as a baseline for the calculated expansion and the lattice parameter at 720 K as a baseline for the experimental expansion. Within these regions the expansion is essentially linear and thus this difference in baseline is not expected to cause much difficulty. The thermal expansion coefficients for α-quartz are presented in Table 5.2 and those for β-quartz in Table 5.3.

Direction	**This Work**	**Taylor**
a=b (K^{-1})	2.613×10^{-5}	4.317×10^{-5}
c (K^{-1})	2.342×10^{-5}	2.675×10^{-5}

Table 5.2 Thermal expansion coefficients of α-quartz.

Direction	**This Work**	**Taylor**
a=b (K^{-1})	-1.800×10^{-6}	0.0
c (K^{-1})	-3.575×10^{-6}	-2.819×10^{-6}

Table 5.3 Thermal expansion coefficients of β-quartz.

The thermal expansion coefficients are reasonably good matches to experimental values. All calculated thermal expansion coefficient are within an order of magnitude of the experimental values except for the a parameter of β-quartz where the experimental differences were too small to give a valid expansion coefficient.

The thermal expansion of quartz has also been calculated previously using the BKS potential model and gave slightly different results [252], Figure 5.3.

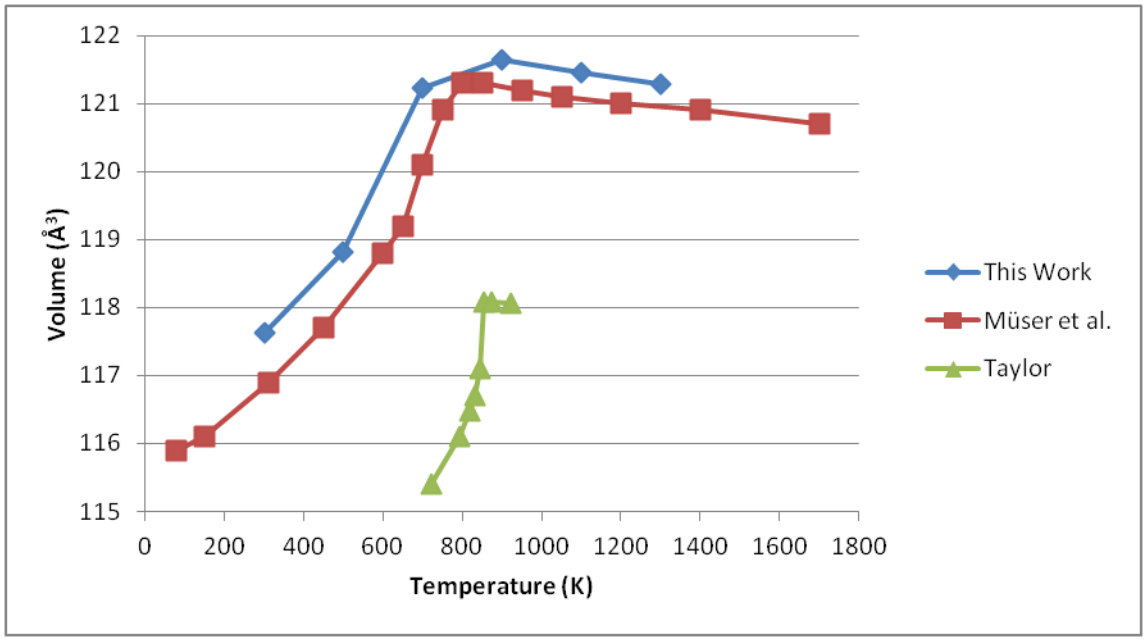

Figure 5.3 Volume expansion of quartz calculated with the BKS potential compared to experiments [252].

Figure 5.3 clearly shows an increase in the volume as calculated by Müser et al., although the expansion behaviour is essentially identical. The difference between the two BKS calculations is attributed to the cutoff used in the simulations. In this work a cutoff of 8.5 Å has been used whereas in the work of Müser et al. used a cutoff of 9.5 Å. The requirement to simulate large systems for long time periods means a compromise must be made to accelerate the simulations and so a cutoff of 8.5 Å will be used.

Both calculated data sets and the experimental data set indicate that the lattice parameters begin to decrease in the region of 850 K, indicating transition to the β-quartz phase. The change in thermal expansion is a result of a change in the behaviour of vibrational modes and thus could have a significant effect on the thermal conductivity.

The negative thermal expansion of β-quartz at least partially originates from the tilting of the rigid tetrahedra. A simple two-dimensional example using squares is given in Figure 5.4 [249].

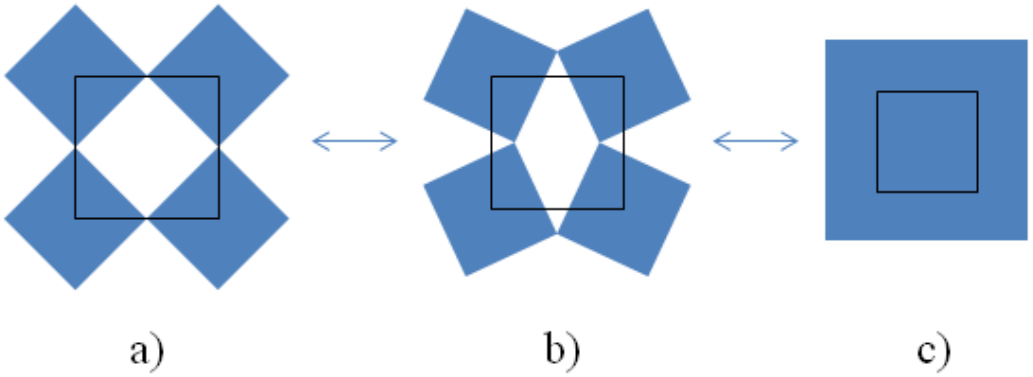

Figure 5.4 As the rigid units (blue squares) rotate the total area occupied by the system decreases. The black box indicates the area required to hold one square in each motif. The area in a) is 4, the area in b) is 3.5 and the area in c is 2.

Figure 5.4 b) may be considered a two-dimensional analogue of α-quartz and upon heating may transform to β-quartz, most similar to Figure 5.4 a). The transformation is accompanied by an increase in volume. The β-quartz structure is only stable dynamically and exists as a time average of the rigid tetrahedra occupying many tilt angles. By increasing the temperature further the system spends longer at one extreme or another of tilt and the time averaged volume is less than the perfect β-quartz structure.

5.2.2. Thermal Conductivity

Quartz is a complex material, constructed from a network of semi-rigid tetrahedra. The changes in orientation of the tetrahedra give rise to a phase change at approximately 850 K, accompanied with a change to negative thermal expansion. These properties are also likely to have an impact on the thermal conductivity.

5.2.2.1. Green-Kubo Results

The thermal conductivity of quartz was calculated by dividing the simulation into 5 individual sets. As discussed in Chapter 3.2.3.2 the calculation of thermal conductivity will theoretically converge faster when using multiple simulations with different starting velocities as a larger portion of phase space is sampled [206]. Each set of simulations comprised 6 temperatures (with lattice vectors set to the corresponding thermal expansion calculation values). The cell volume for each temperature was taken from the averaged thermal expansion calculations, each system was then equilibrated

for a further 0.5 ns in an NVT ensemble (with a Nosé–Hoover thermostat), followed by 3 ns NVT data collection, sampling the heat-flux every 10 fs (1 fs timestep was once again used). Again, the crystallographic c direction of quartz is aligned along the Z direction, the X direction is equivalent to the crystallographic a direction and the Y direction is perpendicular to both the X and Z directions.

The collected heat-flux data is then treated in the usual manner as discussed in Chapter 3.2.3. It is autocorrelated, integrated and then averaged over all the sets for each temperature to give thermal conductivity values with respect to integral length. For simulations on SiO_2 based materials, it was found that the convergence regime has occurred in the region of 20,000-25,000 steps for all temperatures. The values in the convergence region are thus averaged to give the final thermal conductivity values with half the difference between the maximum and minimum values used as a measure of the noise in the autocorrelation. Again the error presented here is likely much larger than the true error which is extremely difficult to calculate [201].

The experimental thermal conductivities for quartz are presented in Figure 5.5 and the calculated thermal conductivities are presented in Figure 5.6.

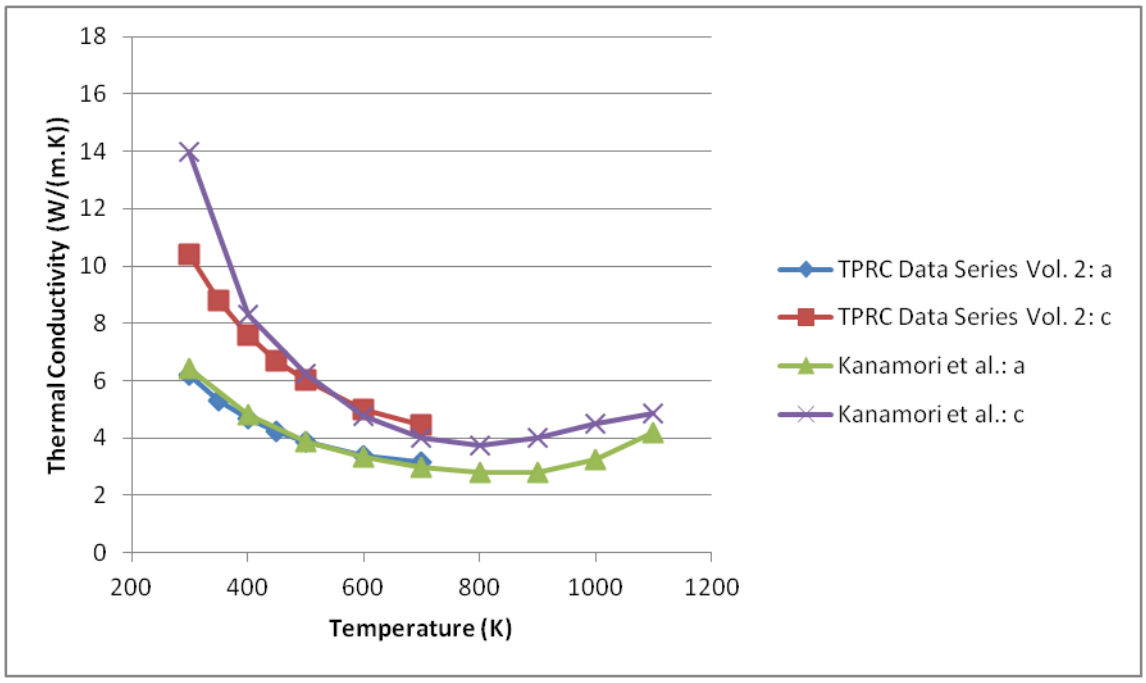

Figure 5.5 Experimental thermal conductivity of quartz [49, 215].

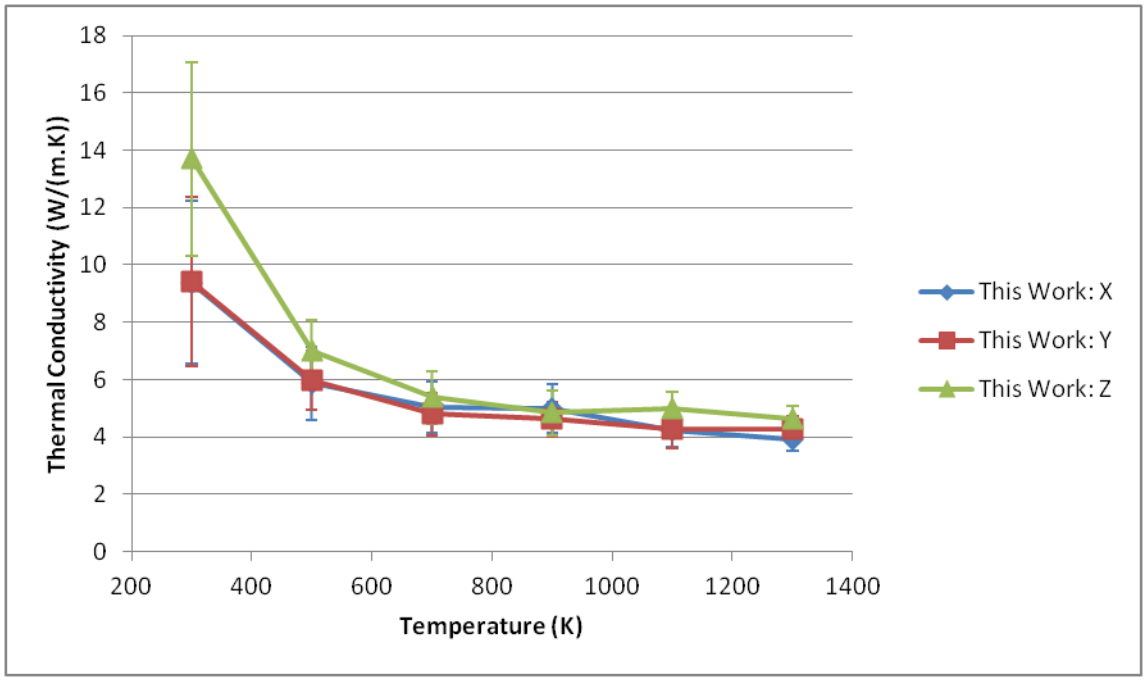

Figure 5.6 Calculated thermal conductivity of quartz for the three directions.

The experimental thermal conductivities in Figure 5.5 show a clear splitting between the a and c directions, with the c direction thermal conductivity being consistently higher. An unusual trend is seen beyond the α-quartz to β-quartz at 846 K where the thermal conductivity increases. The unusual increase may be either related to the negative thermal expansion or to the presence of Dauphiné twins, discussed later in Chapter 5.2.2.2.

The calculated thermal conductivities in Figure 5.6 also show a clear split between the a direction (X and Y directions in the simulation) and the c direction (Z direction in the simulation). The absolute values are also fairly similar, although a constant shift to higher values is seen in the calculations, possibly due to the choice of cutoff as discussed in Chapter 5.2.1. Alternatively the experimental samples may contain trace defects not present in simulations, and would therefore have a lower thermal conductivity.

The X and Z directions in the calculations correspond directly to the experimental a and c directions respectively. However, the Y direction in the calculations does not correspond directly to the b direction but does show effectively identical thermal conductivity to the X direction. The reason for this is that the X and Y directions are still related through symmetry, whereas the Z direction is not.

The minimum in the experimental thermal conductivities at 846 K is not observed in simulation. It could be argued this minimum is related to the negative thermal expansion above 846 K, however the negative thermal expansion is seen in both experiments and calculations but the minimum in thermal conductivity is only seen in experiments, making this explanation less likely. An alternative explanation is that of Dauphiné twins, the effect of which is difficult to capture in a comparatively small simulation cell.

The calculated thermal conductivity values presented here represents an improvement on those calculated by Yoon et al. using the same potential model, but an alternative method [272]. The values of Yoon et al. are consistently around 5 W/(m.K) +/-0.5 between 500 K and 1100 K. The thermal conductivity values calculated by Yoon et al. do however match the values calculated here at temperatures above ~850 K, showing the significance of the α-quartz to β-quartz transition and the possible presence of Dauphiné twinning in the simulation cell that becomes possible with NEMD methods.

Green-Kubo methods preclude this possibility by having the entire simulation cell at one temperature, which does not make Dauphiné twinning impossible, but much less likely over the timescales simulated. Additionally the NEMD methods are known to be more sensitive to finite size effects, especially at lower temperatures, where the phonon mean free path is very long [281].

Other work by McGaughey et al. [202] using both the same potential model and simulation methodology has resulted in close agreement with experimental values, although at temperatures lower than presented here. The values calculated by McGaughey et al. also match well with the values presented here within the small region of overlap, Figure 5.7. The slight difference in values may be attributed to a different potential cutoff (which was not specified) or the use of the Wolf method [273] of solving electrostatic interactions.

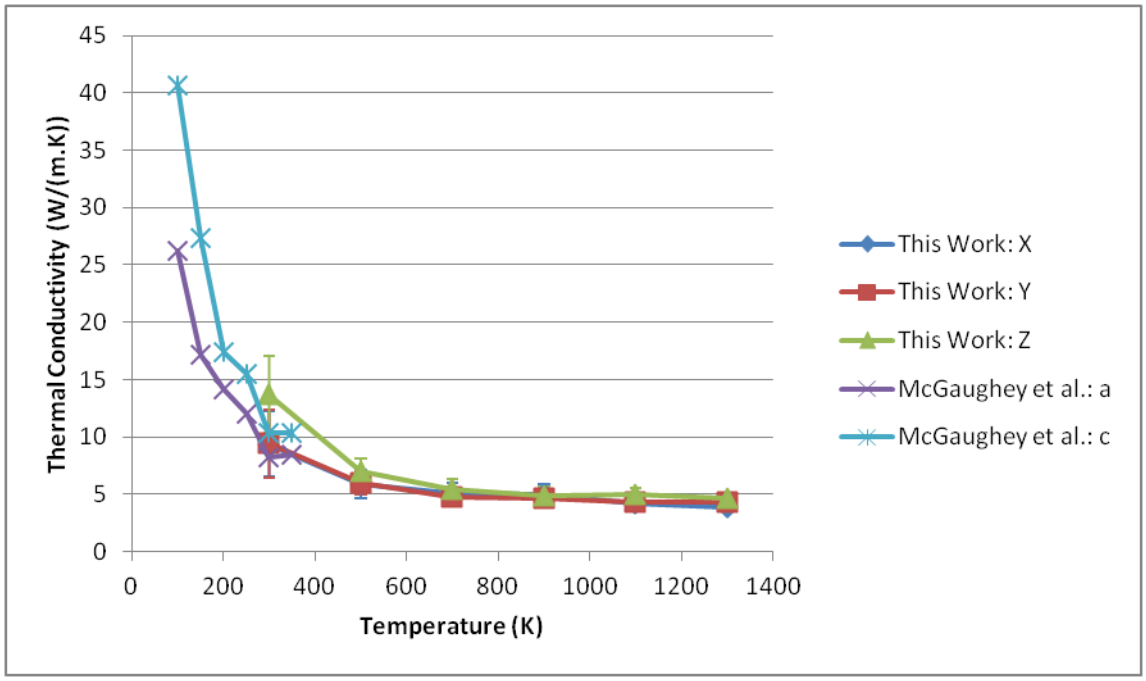

Figure 5.7 Calculated thermal conductivity of bulk quartz in this work and by McGaughey et al. the a direction of McGaughey et al. is equivalent to the X and Y directions in this work.

5.2.2.1. Lattice Dynamics Results

Attempts to calculate the thermal conductivity of quartz via lattice dynamics failed to give a converged result with respect to supercell size and q-points. Furthermore, the phase change found in quartz is likely to complicate interpretation of any results.

The unconverged values are presented in Appendix A.

5.2.2.2. The Effect of Dauphiné Twinning

Experimentally a minimum in the thermal conductivity is observed in the region of the α-quartz to β-quartz transition temperature. The origin of the minimum in thermal conductivity may be due to Dauphiné twinning found at temperatures near the α-quartz to β-quartz transition and in this section the aim is to generate a twinned structure for investigating whether they may cause the experimentally observed change in thermal conductivity.

Dauphiné twins are related through a 60° rotation of the α-quartz structure. One Dauphiné domain may transform into another via the β-quartz structure i.e. a reorientation of the tetrahedra [282]. The boundaries between Dauphiné domains could

result in additional scattering as the phonons move from one orientation of quartz to another and therefore lower the thermal conductivity; additional scattering may also be caused by the local structure of the boundary itself.

Dauphiné twins can only occur in α-quartz and not β-quartz, therefore it may be expected that they will only impact the thermal conductivity at temperatures below the α-quartz to β-quartz transition. At temperatures significantly above the α-quartz to β-quartz transition the domains will not occur and phonons will experience the lattice as pure β-quartz.

Thus the thermal conductivity at temperature much below the α-quartz to β-quartz transition is likely to be reduced by static Dauphiné twin domains. At temperatures above the α-quartz to β-quartz transition the phonons experience the lattice as β-quartz, resulting in less scattering.

This complex trend in thermal conductivity is not seen in the calculated thermal conductivity (Figure 5.6) due to the relatively small system size. At larger sizes Dauphiné twins are able to form below the transition temperature and act as additional scattering centres.

The general approach for generating a simulation cell containing Dauphiné twins was to first heat quartz above the transition temperature and then rapidly quench to low temperatures. By doing this different regions of the crystal crystallise to α-quartz independently and there is insufficient time for one orientation to exert dominance and remove the other orientation. However, below the transition temperature in small systems the twin boundaries are metastable and hence the simulation cell may simply recrystallise into one form of α-quartz.

During creation of the Dauphiné twin system, it was found that the stability was dependent upon the size of the system. At small system sizes Dauphiné twins were unable to form as one orientation exerted dominance over the other, possibly due to strain effects in a small system. At intermediate sizes the twin boundaries would approach over time and anneal out of the structure. At large system sizes the twin boundaries were at such large separation that they were effectively independent and did not approach each other. Thus at the system sizes used for thermal conductivity

calculation Dauphiné twins are not expected to form and therefore will not be able to reduce the thermal conductivity in the region of the phase transition.

A large orthorhombic simulation cell of α-quartz measuring approximately 193 Å x 22 Å x 226 Å and containing 74,160 atoms was created. The crystallographic c direction was orientated along the Y direction while the crystallographic a direction was slightly misorientated from the X direction in an attempt to avoid spurious periodicity. The system was heated to 2000 K and maintained at that temperature for 10 ps, using a timestep of 1.0 fs in an NVT ensemble. The system is then rapidly cooled to 100 K over the course of 20 ps. The system was then energy minimised to remove any residual strain and thermal noise in the position of the atoms.

Analysis of such boundaries is challenging because of the subtle difference in structures, i.e. tilting of tetrahedral, which distinguish the separate regions. To picture the boundaries within the system the density of atoms within a 4.5 Å radius of a silicon atom is calculated and the tetrahedra centred on that silicon is coloured depending upon that density. This system (expanded 2 x 2 x 2) is shown in Figure 5.8.

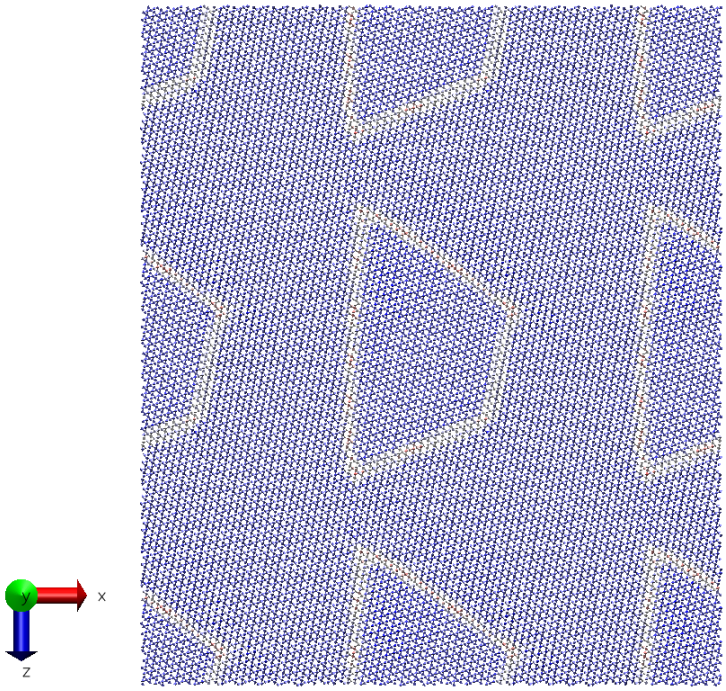

Figure 5.8 The 74,160 atom Dauphiné twin system (expanded 2 x 2 x 2). Domain boundaries are coloured white.

One twin region is entirely enclosed by the other and takes on a trapezoidal shape with two ~60° and two ~120° angles, reflecting the symmetry of the α-quartz material. Interestingly the domain boundaries do not align along the crystallographic a or b directions and has a small misorientation angle of ~10°, an effect which has been noted before experimentally [283] and is the subject of a joint experimental/computational paper by Eder et al. [284]. This misorientation was observed in many systems regardless of whether the crystallographic a direction was misorientated from the X direction or not.

Annealing this system at 300 K resulted in the inner domain being annealed to the same orientation as the outer domain. The reconstruction to one orientation of α-quartz is likely expedited by the strain generated by the twin boundary on the underlying crystal. By having the twin boundaries in close proximity there is a driving force for them to approach as the strain between them is relieved until the boundaries meet and remove the inner domain. In a sufficiently large system the boundaries should be so well separated as to have no driving force to move in any given direction, thus the stability of Dauphiné twins is expected to be extremely sensitive to system size.

In an attempt to create a dynamically stable Dauphiné twin system an even larger system of approximately 386 Å x 22 Å x 452 Å (c axis orientated along the Y direction) containing 296,640 atoms was constructed and treated in the same manner as the 74,160 atom system. The calculation of local density was performed as before and the coloured system is presented in Figure 5.9.

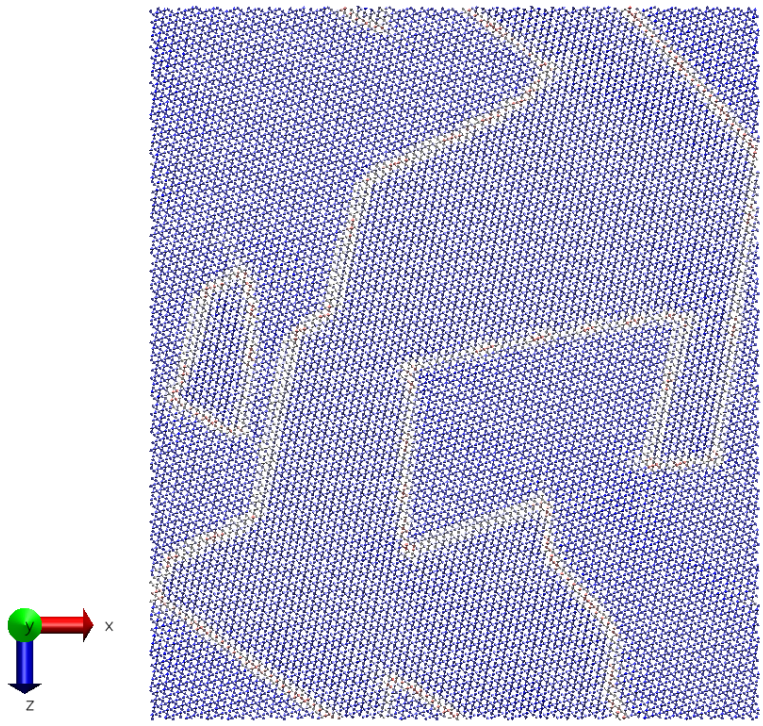

Figure 5.9 The 296,640 atom Dauphiné twin system. Domain boundaries are coloured white.

Once again the system displayed an abundance of ~60° and ~120° angles in the boundary while the boundaries themselves are again slightly misorientated from the crystallographic a and b directions. This system was further annealed for 20 ps at 300 K, followed by 10 ps of cooling to 100 K and then energy minimised. The final system is shown in Figure 5.10.

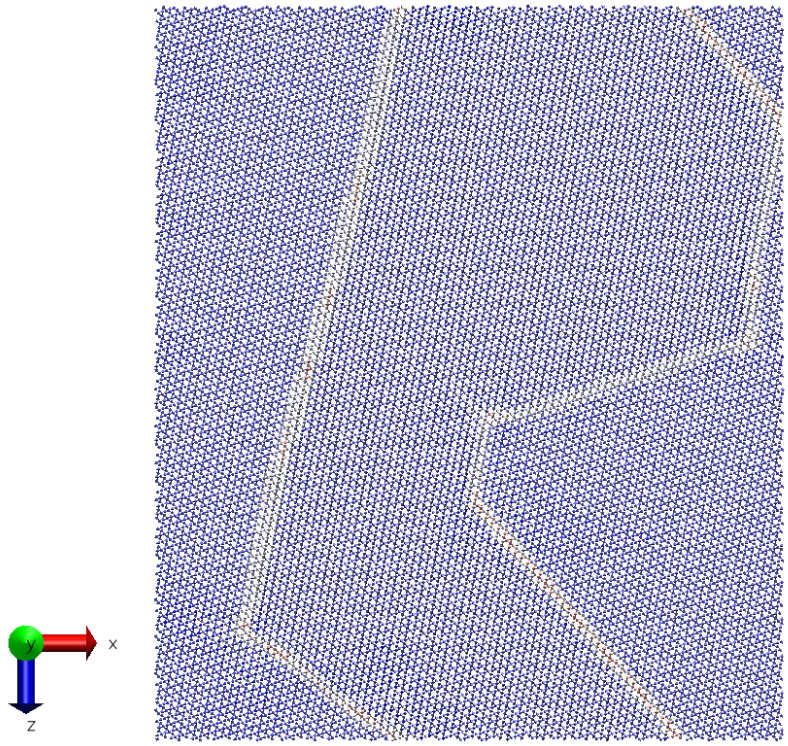

Figure 5.10 The 296,640 atom Dauphiné twin system after annealing at 300 K. Domain boundaries are coloured white.

Annealing at 300 K has resulted in longer and straighter twin boundaries, while retaining six individual ~120° angles. This system is stable at 300 K for short time periods due to the large distances between oppositely orientated boundaries; even larger systems should remain stable for longer periods and higher temperatures.

A thermal conductivity calculation was attempted on this system but was not possible as the Dauphiné twins annealed away at 500 K and longer timescales necessary for thermal conductivity calculations. One possible solution is to increase the thickness (Y direction) of the system so that there is a greater barrier to diffusion of the domain boundary, however this would result in a system of more than a million atoms which would take an unfeasibly long time to simulate in order to gain enough data for a converged thermal conductivity.

The calculation of thermal conductivity in these systems is further complicated by the changing geometry in these systems, meaning that the calculated thermal conductivity can change over the course of the simulation.

In summary, small scale (length and time) simulations have significant difficulty in capturing the effect of domains on the thermal conductivity of quartz. If the simulation cell is too small then two opposite domain boundaries may interact with each other, approach and annihilate. Furthermore the correct concentration and orientation of domains is exceptionally difficult to achieve, partially due to the constraints of periodic boundary conditions and simulation cell geometry.

The magnitude of the impact of Dauphiné twins is thus still unknown. Future work may concentrate on creating more ordered, and more stable Dauphiné twin system which are capable of being simulated for the requisite amount of time. The concentration of Dauphiné domains is also an important aspect to be studied but is expected to be temperature sensitive and require even larger systems.

Experimental results must also be carefully considered as the thermal conductivity should be dependent on the thermal history of the crystal, via Dauphiné twinning. If the crystal is cooled slowly at temperatures below the transition, then there is a greater amount of time for Dauphiné twins to be removed, conversely if the crystal is quenched quickly then many Dauphiné twins are expected to form and the thermal conductivity will consequently be lower.

As shown in the previous chapter, it is also possible to analyse the lattice dynamics to identify the optical modes that interact with the acoustic and hence heat transport. Clearly, this is not possible for the domain structures, but α-quartz and β-quartz can still be considered.

5.2.2.3. Green-Kubo and Lattice Dynamics Spectra

The Green-Kubo spectra of quartz are expected to show significant changes with temperature due to the phase transition from α-quartz to β-quartz. The Green-Kubo spectra are presented in Figure 5.11, Figure 5.12 and Figure 5.13.

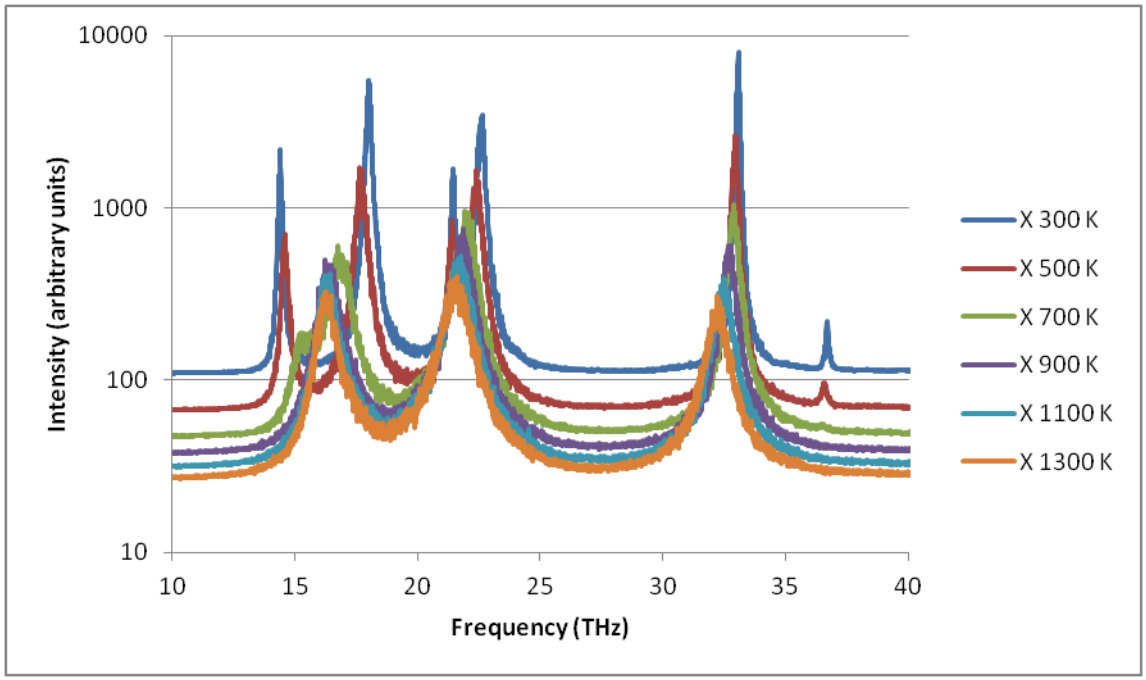

Figure 5.11 Green-Kubo spectra of quartz in the X direction, Log_{10} scale.

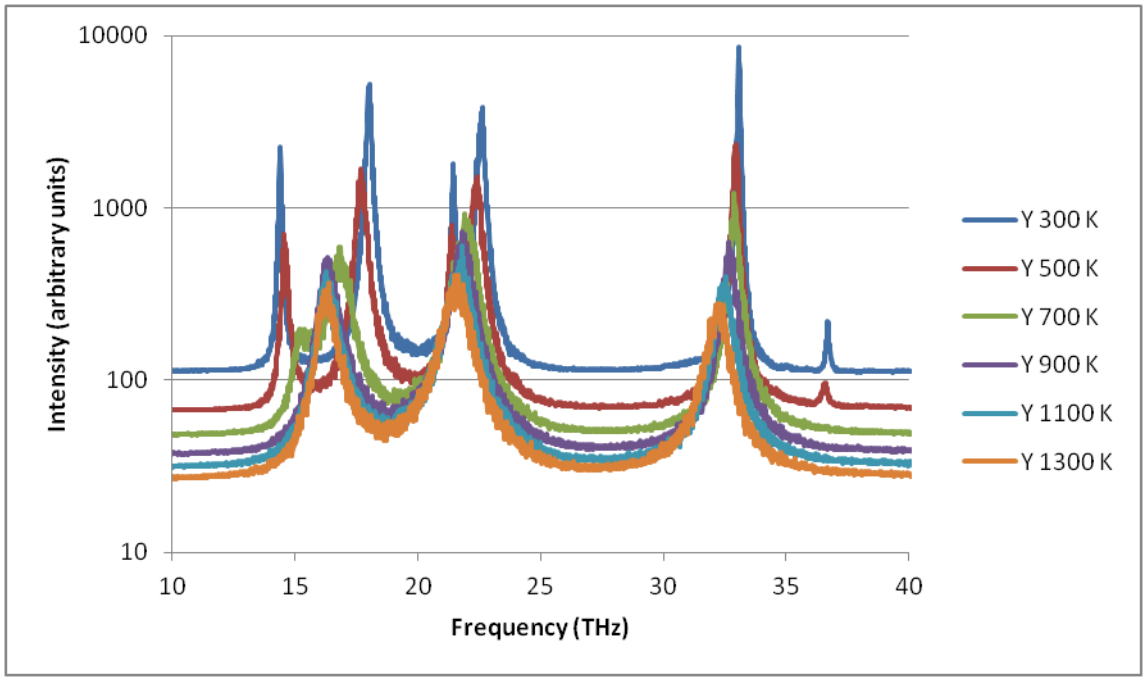

Figure 5.12 Green-Kubo spectra of quartz in the Y direction, Log_{10} scale.

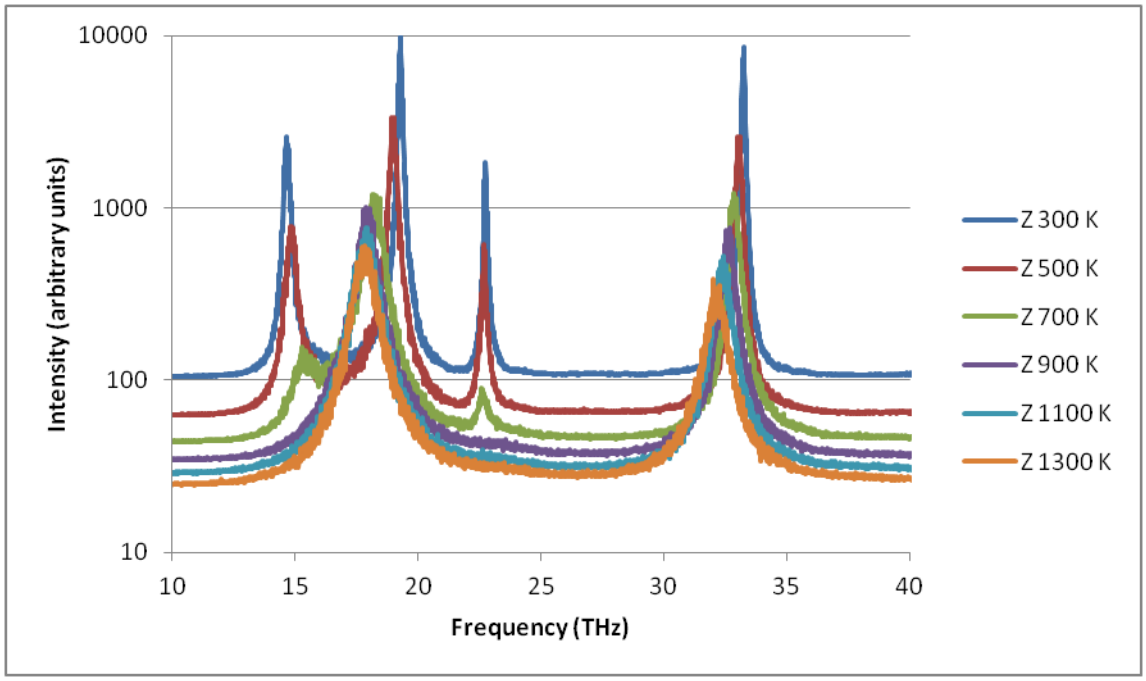

Figure 5.13 Green-Kubo spectra of quartz in the Z direction, Log_{10} scale.

The spectra show once again that the X and Y directions are equivalent. All peaks occur between 10 THz and 40 THz and are in two main groups; those above ~25 THz and those below. Some peaks move to lower frequency with increasing temperature as was seen for MgO. Other peaks show the reverse trend, moving to higher frequency with increasing temperature and eventually merge with other peaks. Furthermore, some peaks disappear entirely with increasing temperature (~37 THz in X and Y, ~23 THz in Z).

The most unusual feature of the Green-Kubo spectra is that some peaks shift to higher frequencies as temperature increase (a negative mode Grüneisen parameter), as opposed to the previously observed decrease in frequency with higher temperatures (a positive mode Grüneisen parameter). These frequencies are attributed to the transition from α-quartz to β-quartz and the accompanying increase in symmetry. As the material changes phase, several previously distinct environments become identical and thus many phonon modes involving those environments also become identical. The increase in frequency is likely due to the increasing lattice parameter removing slack from tetrahedral chains, the chains thus become tighter and resulting in higher frequencies.

A secondary feature of the spectra transformation is that some peaks (X and Y directions ~18 and ~23 THz and Z direction ~19 THz) which do shift to lower

frequency with higher temperature cease moving somewhere between 700 K and 900 K while other peaks (X,Y and Z direction ~33 THz) continue to shift towards lower frequencies.

Additionally, the 36.6 THz peak in the X and Y directions and the 22.7 THz peak in the Z direction decrease in magnitude with increasing temperature until disappearing entirely in the region of 700 K to 900 K.

These phenomena occur in the region of the quartz transition temperature and show that α-quartz and β-quartz present distinct systems with respect to thermal conductivity calculation. Thus the spectra support the idea that the NEMD molecular dynamics approach to calculating thermal conductivity may be unsuitable as the thermal conductivity will depend strongly upon the temperature gradient i.e. there may be α-quartz in one portion of the system but β-quartz in another. The Green-Kubo method however maintains a single temperature throughout the system and may only experience the problem of Dauphiné twinning in large systems and close to the phase transition temperature.

Calculating the thermal conductivity via BTE methods may also fail as they cannot directly account for the structural changes at the phase transition and thus a poor representation of the phonon-phonon scattering processes.

The lattice dynamics phonon DOS can once again be used to give a physical interpretation of the modes appearing in the Green-Kubo spectra. The phonon DOS for α-quartz was calculated as previously, but now using a total eigenvector cutoff of 0.01. The simulation cell used for this calculation contained 9 atoms with lattice vectors of a=b=4.92 Å, c=5.43 Å, α=β=90° and γ=120°. The phonon DOS spectra of α-quartz and the 300 K Green-Kubo spectra for quartz are presented in Figure 5.14, Figure 5.15 and Figure 5.16.

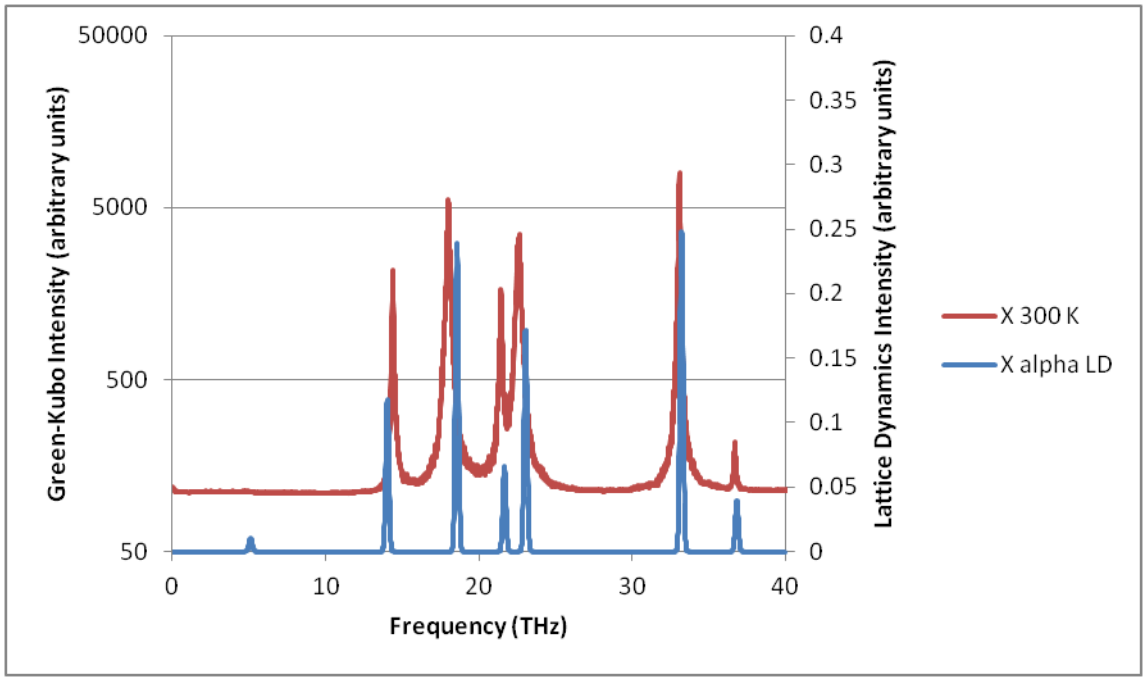

Figure 5.14 Comparison of the Green-Kubo at 300 K and lattice dynamics spectra for α-quartz, X direction. Log_{10} scale on Green-Kubo intensity.

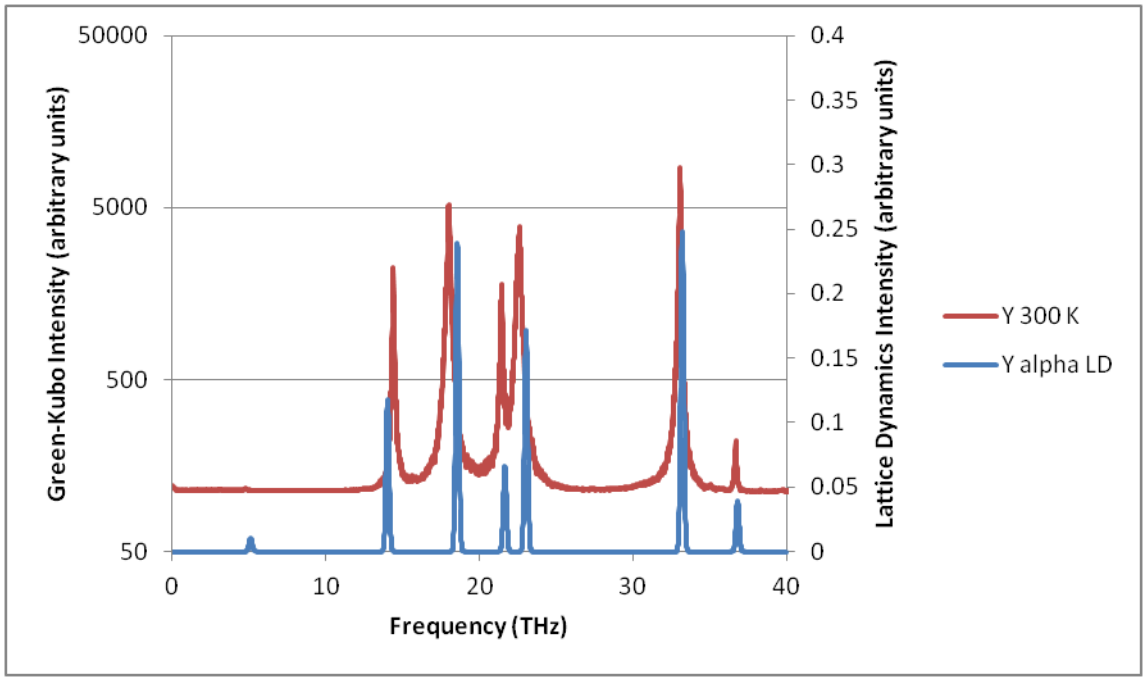

Figure 5.15 Comparison of the Green-Kubo at 300 K and lattice dynamics spectra for α-quartz, Y direction. Log_{10} scale on Green-Kubo intensity.

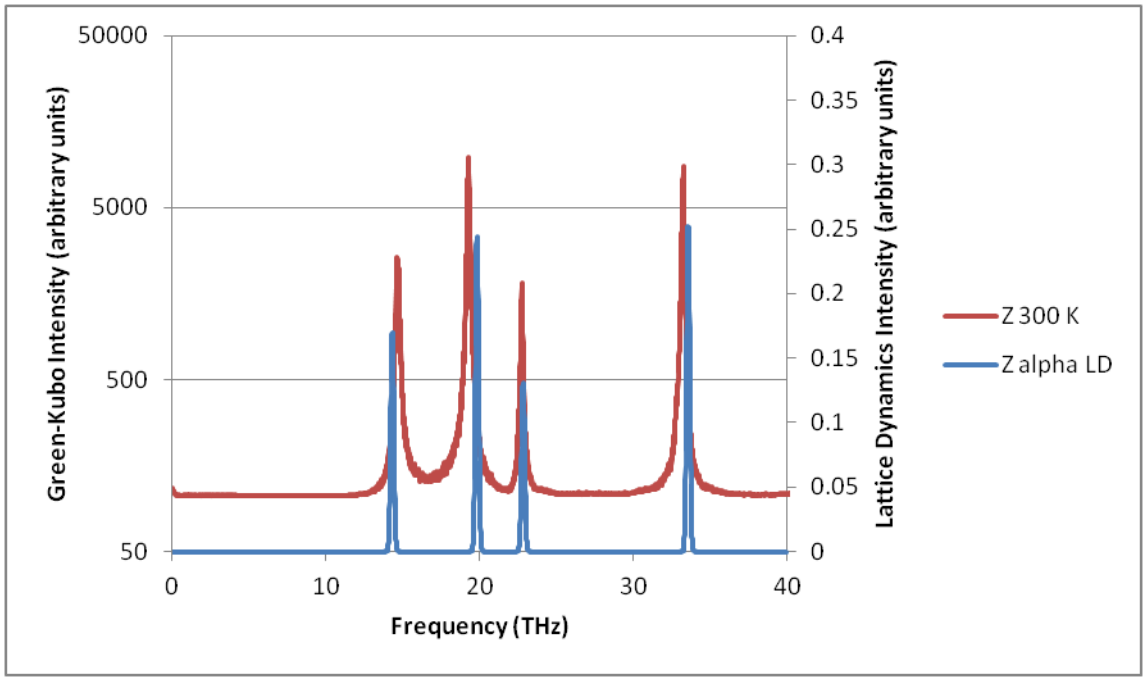

Figure 5.16 Comparison of the Green-Kubo at 300 K and lattice dynamics spectra for α-quartz, Z direction. Log_{10} scale on Green-Kubo intensity.

The peaks arising from the Green-Kubo calculation at 300 K can now be indexed, Table 5.4.

Frequency (THz)	Direction	Motion
5.104	X/Y	Rigid Unit Mode (RUM)
14.03	X/Y	Tetrahedra distortion/Si-O bending
14.32	Z	Tetrahedra distortion/Si-O bending
18.57	X/Y	Tetrahedra distortion/Si-O bending
19.84	Z	Tetrahedra distortion/Si-O bending
21.67	X/Y	Tetrahedra distortion/Si-O bending
22.84	Z	Si rattling in tetrahedra/Si-O bending
23.05	X/Y	Tetrahedra distortion/Si-O bending
33.23	X/Y	Tetrahedra distortion/Si-O stretching
33.58	Z	Tetrahedra distortion/Si-O stretching
36.83	X/Y	Tetrahedra breathing and distortion/Si-O stretching

Table 5.4 Assigned vibrational modes of α-quartz.

By indexing the peaks via lattice dynamics calculations it becomes clear that the modes present above ~25 THz are related to Si-O bond stretching, the modes between ~10 THz and ~25 THz are related to Si-O bond bending. An additional single mode appears below 10 THz which is a rigid unit mode (RUM).

The vibrational frequencies for α-quartz as calculated by Green-Kubo and lattice dynamics match almost exactly. One exception appears to be the very low magnitude rigid unit mode (RUM) appearing at 5.1 THz in the X and Y directions of the lattice dynamics calculation which initially appears to have no counterpart in the Green-Kubo calculation. Closer inspection of the Green-Kubo spectra reveals this mode is indeed present in the X and Y directions but at exceptionally low intensity, matching fairly well with the relatively low magnitude found for this mode in the lattice dynamics calculation, Figure 5.17.

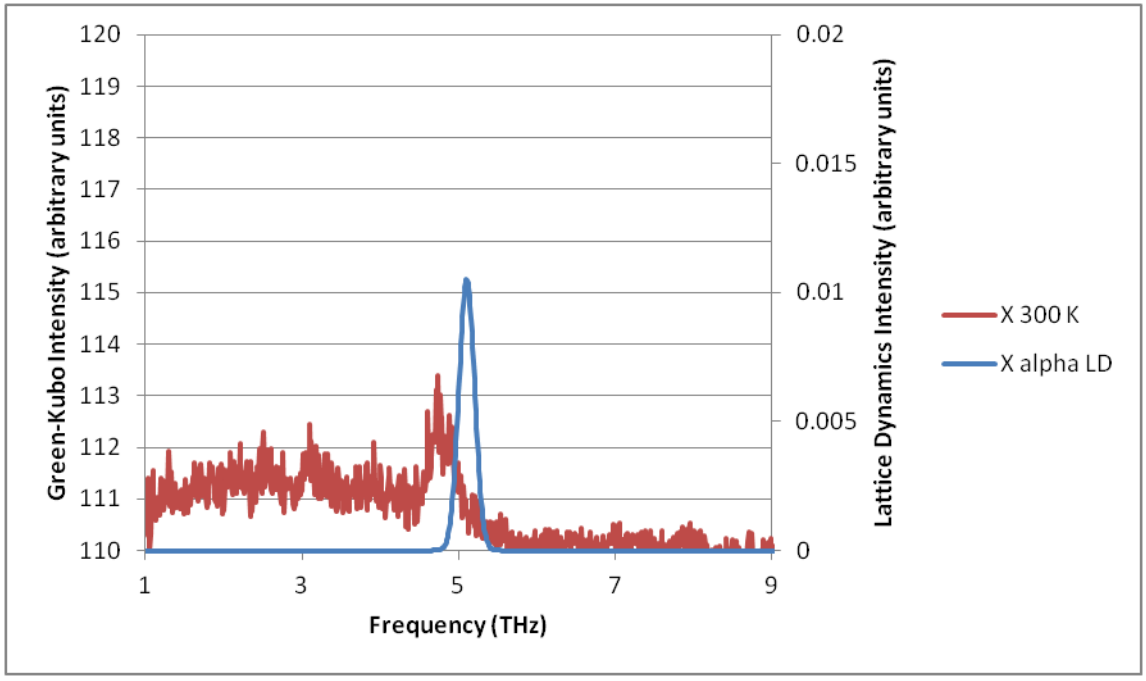

Figure 5.17 Low frequency RUM in the X direction of α-quartz. Green-Kubo values are at 300 K.

This mode is unusual in that it is the only RUM to appear in the Green-Kubo spectra and the lattice dynamics phonon DOS (after removing symmetric modes). However, other RUMs may be present but do not appear because the sum of their non-mass-weighted eigenvectors is less than the cutoff; indeed there may be some evidence of further RUMs between 1.0 THz and 5.1 THz in the Green-Kubo spectrum, but these are

not conclusive. Furthermore the mode at 5.1 THz is absent from the β-quartz calculations, indicating that this mode becomes symmetric during the phase transition.

The lattice dynamics phonon DOS is much harder to obtain for β-quartz as the structure is not stable to energy minimisation. Therefore a fictional β-quartz unit cell was created using the cell volume as calculated from molecular dynamics at 1300 K and the corresponding average atomic positions. The cell is then minimised under constant volume using the same potential parameters. By being precisely on the saddle point between the two possible orientations of α-quartz, relaxation to either state is avoided and the β-quartz structure is maintained.

As β-quartz is not a stable structure at 0 K, imaginary modes are expected to appear in the spectra; however the rest of the modes in the spectra may give some insight into the vibrational modes interacting with the heat-flux. The β-quartz phonon DOS spectra and the 1300 K Green-Kubo spectra for quartz are presented in Figure 5.18, Figure 5.19 and Figure 5.20 and shows good agreement with the Green-Kubo spectra.

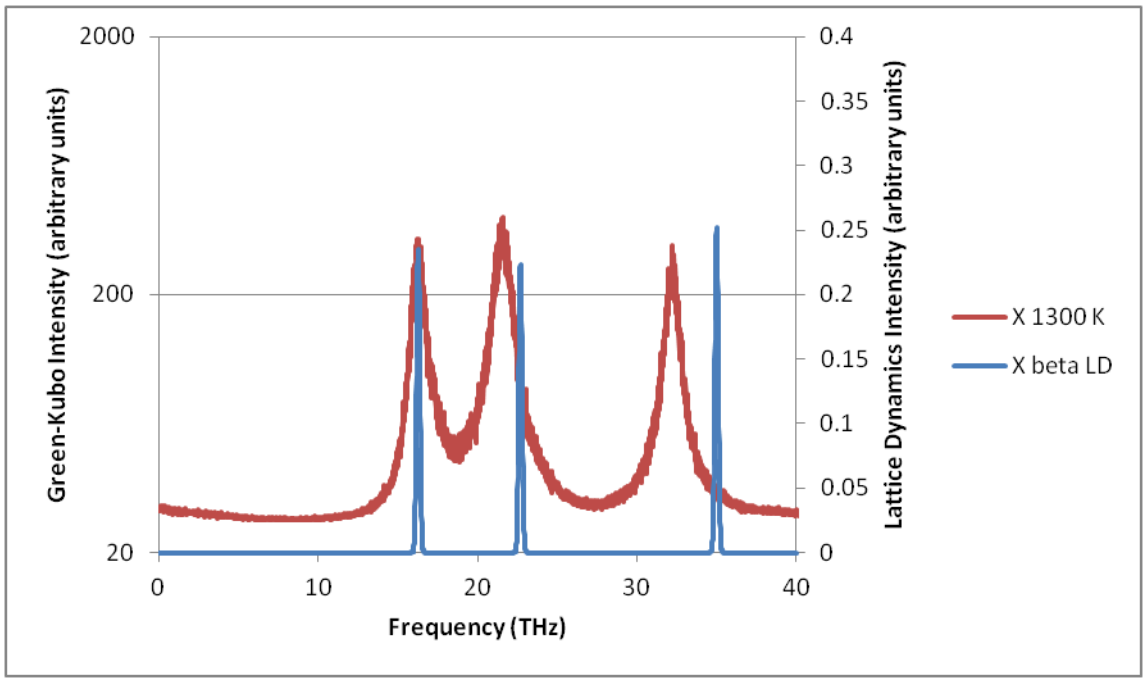

Figure 5.18 Comparison of the Green-Kubo at 1300 K and lattice dynamics spectra for β-quartz, X direction. Log_{10} scale on Green-Kubo intensity.

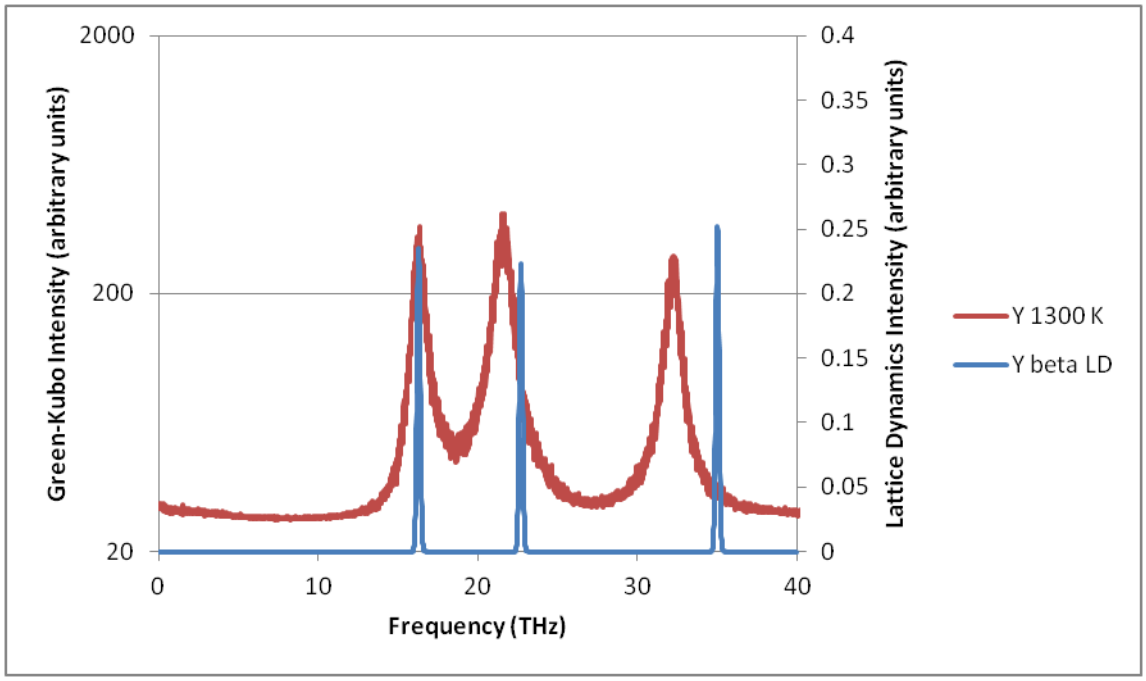

Figure 5.19 Comparison of the Green-Kubo at 1300 K and lattice dynamics spectra for β-quartz, Y direction. Log_{10} scale on Green-Kubo intensity.

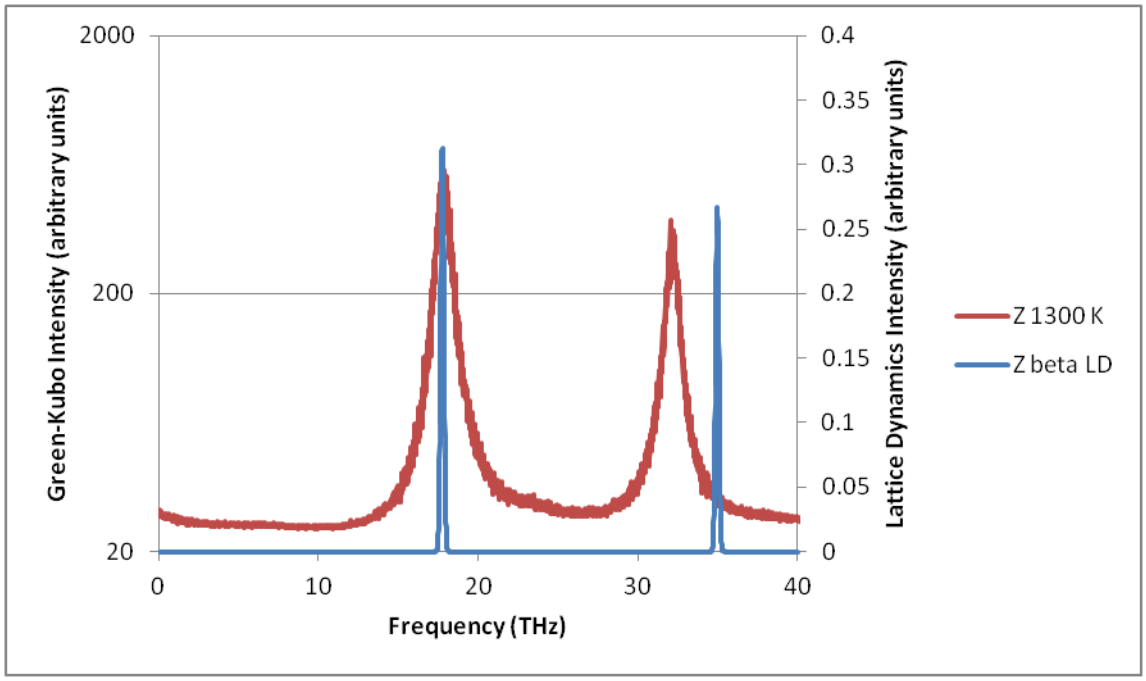

Figure 5.20 Comparison of the Green-Kubo at 1300 K and lattice dynamics spectra for β-quartz, Z direction. Log_{10} scale on Green-Kubo intensity.

There are many fewer peaks for β-quartz than α-quartz and a good match is achieved to the Green-Kubo spectra. One exception is the overestimation of the highest frequency peak which appears at 35 THz, a 3 THz overestimation on the Green-Kubo spectra.

These peaks may now be indexed according to their atomic motions; the results are displayed in Table 5.5.

Frequency (THz)	Direction	Motion
16.28	X/Y	Tetrahedra distortion/Si-O bending
17.75	Z	Tetrahedra distortion/Si-O bending
22.70	X/Y	Si rattling in tetrahedra/Si-O bending
34.97	Z	Tetrahedra distortion/Si-O stretching
35.01	X/Y	Tetrahedra distortion/Si-O stretching

Table 5.5 Assigned vibrational modes of β-quartz.

The expected imaginary frequency for β-quartz is present and appears at approximately 3.8i THz. The low frequency of the imaginary mode is due to the α-quartz to β-quartz transition being based on changes in tetrahedral positioning, and is thus an imaginary rigid unit mode (RUM). The imaginary frequency is symmetric and thus does not appear in the treated phonon DOS and it is not expected to directly affect the thermal conductivity. However, the existence of the phase transition itself is likely to lead to secondary effects that do have an impact on the thermal conductivity.

The β-quartz structure shows a significant peak shift of the ~32 THz modes in the Green-Kubo spectra to ~35 THz in the lattice dynamics phonon DOS spectra. Additionally, the 21.5 THz mode in the X and Y directions of the Green-Kubo spectra is overestimated to 22.5 THz in the lattice dynamics phonon DOS.

The shift of some modes to higher frequency in the lattice dynamics phonon DOS of β-quartz originates from the fact that β-quartz is not a stable structure at 0 K and only exists as a dynamical average of many tetrahedral tilt angles. Thus at any given moment in time the SiO_4 tetrahedra are not occupying the β-quartz average and the Si-O distances are closer to their low temperature bond lengths (1.60 Å). When the average atomic coordinates of β-quartz are used the Si-O bonds must become shorter to allow the tetrahedra to fit (1.59 Å). The Si-O bond is thus strained and not at its 0 K equilibrium distance, causing a slight change in the observed frequencies. The remaining modes which do not involve a stretching of the Si-O bond show a much better match to the Green-Kubo spectra.

The lattice dynamics spectra of both α-quartz and β-quartz can also help reveal the origin of changes in the Green-Kubo spectra as a function of temperature. The frequency at 22.84 THz in the Z direction disappears as the structure transitions from α-quartz to β-quartz. The lattice dynamics calculation shows that this mode originates from the vibration of a Si atom within the tetrahedra, oscillating between two opposite edges. The vibration of the Si occurs mainly in the X-Y plane but also has some small Z component due to the tilt of the tetrahedra in α-quartz. The motion of all the tetrahedra in the system results symmetric mode in the X-Y plane but a concerted asymmetric motion in the Z direction, giving rise to the mode seen in the spectrum. At higher temperatures, the edges of the tetrahedra align perfectly in the X-Y plane and the concerted motion in the Z direction is removed, thus resulting in the mode reducing and disappearing at higher temperatures.

The vibrational modes present at 14.32 THz and 19.84 THz in the Z direction of the α-quartz spectrum (Figure 5.16) share identical motion of Si atoms, differing only in the motions of the O atoms. The two distinct frequencies arise out of the tetrahedral tilt and splitting of the vibrational environment. As the temperature increases and the environments become identical in β-quartz the frequencies merge into a single frequency at 17.75 THz in the Z direction of the β-quartz spectrum (Figure 5.20). Similar processes are likely the cause of other peak merging seen in the X and Y directions (14.03 THz with 18.57 THz and 21.67 THz with 23.05 THz) although the exact mechanism is unclear.

The study of quartz has allowed a basic understanding of the thermal properties of silica materials to be developed which can aid in the interpretation of data coming from a more complex silica phase. In the next section a zeolite material, silicalite is studied, which has a much greater variety of environments and is much lower in density, both of which are factors which can greatly influence thermal conductivity.

5.3. Silicalite

The zeolites are a related class of silicate materials, which have a much lower density than quartz. There are over 200 known zeolite structures [285], both natural and synthetic. Their uses primarily stem from their highly porous structure, making them suited to catalysis [286], gas separation [287, 288] and ion exchange [289, 290]; these

process are often temperature dependent. Furthermore, zeolites are of interest for nuclear waste remediation and hence knowledge of their thermal properties is of great benefit [291].

The structure of zeolites also somewhat mirrors that of several promising thermoelectric material classes such as clathrates [68] by having a porous frame with the possibility of guest species. Thus the study of thermal transport in zeolite structures may give guidance on other materials for thermoelectric applications.

Most zeolites incorporate aluminium into the structure and accommodate charge balancing cations in the pores such as alkali metals [292], alkaline earth metals or rare earth metals. It is however still possible for purely silicious versions of several zeolites to be synthesised.

The thermal conductivity of zeolites has been studied computationally using the BKS potential. The work by McGaughey et al. [202] which calculated the thermal conductivity of quartz also calculated the thermal conductivity of a few zeolite structures (SOD, FAU and LTA) using the same approach. They found that in zeolites there are two primary mechanisms for heat transfer:

1. A short range mechanism linked to optical phonons and short wavelength acoustic phonons and is heavily influenced by the geometry of the structure. This mechanism is temperature insensitive.
2. A long range mechanism which is related to longer wavelength acoustic phonons. This mechanism is temperature sensitive and accounts for a significant portion of the thermal conductivity.

Other potential models have also been used to calculate the thermal conductivity of zeolites. Schnell et al. [293] used a simplistic model [294, 295] in a NEMD simulation similar to that of Müller-Plathe[126] but with some minor modifications. This work found that the introduction of organic guest molecules into the zeolite structures had little effect on the thermal conductivity, likely due to weak interactions of the guests with the zeolite cages. This result gives an interesting contrast with clathrate materials where the guest ions are included specifically to reduce thermal conductivity, indicating the importance of both cage size and interaction strength. Therefore it may be expected

that introducing highly interacting cations may have a larger impact on the thermal conductivity.

Hudiono et al. [296] used a more complex potential model incorporating electrostatic interactions, two-body interactions, three-body interactions and polarisation [297] to calculate the thermal conductivity of MFI within a BTE calculation. This study found increasing thermal conductivities with temperature between 150 K and 450 K, from ~1.0 W/(m.K) to ~1.4 W/(m.K) with varying Si/Al ratio, matching closely the values from experiments conducted concurrently.

Silicalite is a purely silicious version of the zeolite commonly known as MFI or ZSM-5 [285]. The silicalite structure (Figure 5.21) contains large sinusoidal channels in the X direction and large straight channels in the Y direction, forming a network through which species may diffuse. This pore network is often used for catalysis, sequestration etc.

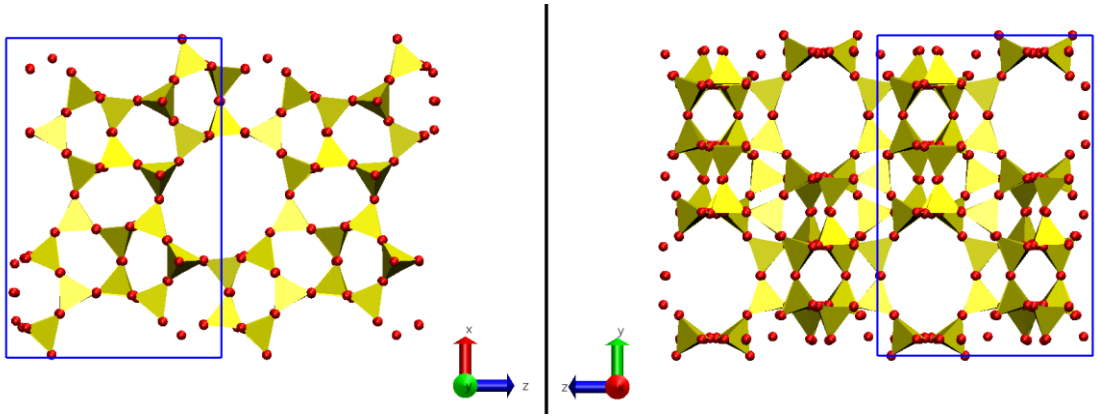

Figure 5.21 Silicalite framework. Expanded x2 in the Z direction for clarity. The orthorhombic unit cell is displayed in the blue box.

The structure of silicalite used here has space group *Pnma* and is constructed from the same tetrahedral units as quartz, but arranged in a more complex motif. The crystallographic a, b and c directions correspond to the simulation X, Y and Z directions respectively. To test how well the potential model reproduces silicalite, the lattice parameters and elastic constants were calculated and are presented in Table 5.6.

Property	Calculated	Experiment	% Difference
a (Å)	20.286	19.963	1.62
b (Å)	20.323	20.019	1.52
c (Å)	13.655	13.388	1.99
c_{11} (GPa)	33.7	68.2	-50.59
c_{22} (GPa)	78.5	84.5	-7.10
c_{33} (GPa)	79.1	79.0	0.13
c_{44} (GPa)	18.8	23.5	-20.00
c_{55} (GPa)	19.9	22.6	-11.95
c_{66} (GPa)	20.3	21.2	-4.25
c_{12} (GPa)	14.2	-1.52	-1034.21
c_{13} (GPa)	-3.42	10.3	-133.20
c_{23} (GPa)	24.4	19.9	22.61

Table 5.6 Calculated and experimental [298] properties of silicalite. The crystallographic a and b directions used in this work have been swapped for this comparison due to differences in space group definition.

The experimental values for the elastic constants come from a sample which still contains the tetrapropylammonium (TPA) fluoride template. However, measuring the elastic constants for synthetic zeolites is particularly challenging due to the difficulties in growing sufficiently large crystals for analysis [298]. Thus, the values presented in Table 5.6 are presented as a closest match, with some deviation expected from the calculated values.

Overall the match with experiment is reasonable, although the calculated lattice parameters are consistently ~0.3 Å higher than experimental values. The c_{11} constant is significantly underestimated compared to experiments, although this may be the result of the TPA-F guests making the structure stiffer. The c_{12} and c_{13} elastic constants also show significant deviation.

To confirm whether the deviation from experiments is due to the presence of TPA-F in the structure or whether the potential model is not accurate enough, higher levels of theory may be applied in future to calculate the elastic constants, e.g. DFT.

5.3.1. Thermal Expansion

The thermal expansion and conductivity of silicalite were calculated using the BKS potential [161] to facilitate direct comparison with the quartz results. The simulation cell used was a 2 x 2 x 3 expansion of the orthorhombic unit cell consisting of 288 atoms and measuring approximately 20.3 Å x 20.3 Å x 13.7 Å, giving a final simulation cell of 3,456 atoms, measuring approximately 40.8 Å x 40.8 Å x 41.0 Å.

The thermal expansion was measured using the same procedure as for all other materials in this work. A 0.5 ns anisotropic NPT molecular dynamics simulation was run on 6 different temperatures with a timestep of 1 fs. The lattice vectors were again sampled every 10 fs and averaged over the course of the simulation. The lattice vectors were averaged independently due to the anisotropic structure. The final lattice parameters are plotted against temperature in Figure 5.22.

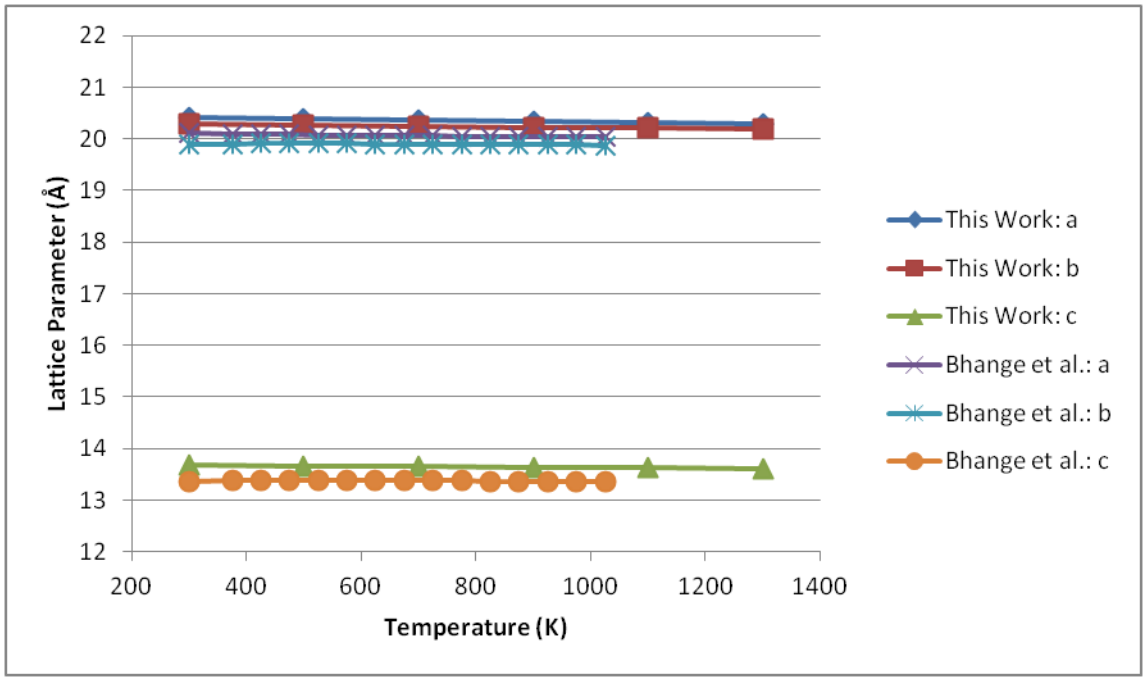

Figure 5.22 Calculated and experimental [299] lattice parameters.

The calculated lattice parameters are within 3% of the experimental values [299] across the whole temperature range and in each direction. The thermal expansion coefficients were calculated for each direction using the lattice parameter at 500 K as the baseline. The thermal expansion values are presented in Table 5.7.

Direction	This Work	Bhange et al.
a (K^{-1})	-5.266×10^{-6}	-3.998×10^{-6}
b (K^{-1})	-5.232×10^{-6}	-3.427×10^{-6}
c (K^{-1})	-4.149×10^{-6}	-2.364×10^{-6}

Table 5.7 Thermal expansion coefficients of silicalite from 500 K to 1000 K.

The thermal expansion coefficients are reproduced within a factor of two in each direction. A deviation occurs below 500 K where the expansion is positive in the b and c directions.

5.3.2. Thermal Conductivity

The thermal conductivity of silicalite was calculated by dividing the simulations into a set of 5 molecular dynamics calculations for each of the 6 temperatures and then averaging the final Green-Kubo integrals for each temperature. Each temperature used the averaged lattice vectors as computed by the thermal expansion calculation. The simulations were given different random starting velocities and were equilibrated under an NVT ensemble for 0.5 ns before heat-flux data was collected for 4 ns under an NVT ensemble sampling every 10 timesteps (10 fs). The separate sets were then averaged together to give the final integrals from which the thermal conductivity was extracted.

The thermal conductivity of silicalite with respect to temperature is presented in Figure 5.23.

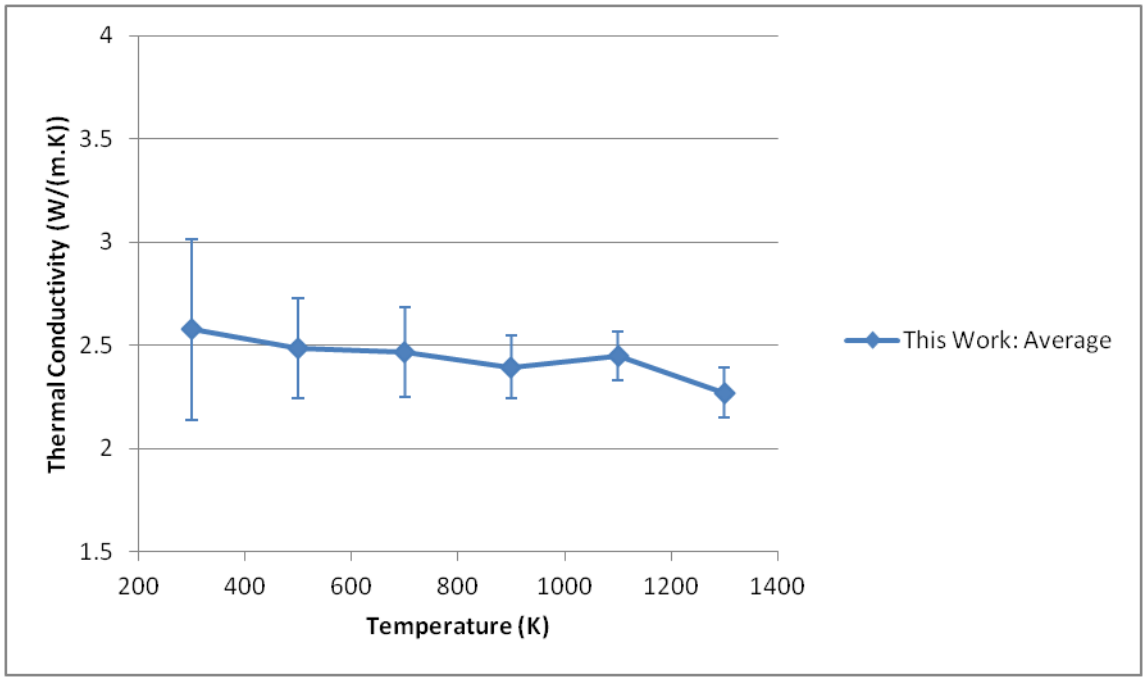

Figure 5.23 Average thermal conductivity of silicalite with respect to temperature.

The calculated thermal conductivities lie within a narrow band between 2 and 3 W/(m.K) and show essentially no response to temperature within the error. Experimental values tend to have increasing thermal conductivity values up to ~400 K and plateau at between 1 and 2 W/(m.K) [296, 300, 301]. As these experimental samples are not purely crystalline the higher thermal conductivities found in simulation are to be expected.

As silicalite is an anisotropic material the thermal conductivities in different directions may be different, as was seen for quartz. The directionally dependent thermal conductivities are presented in Figure 5.24.

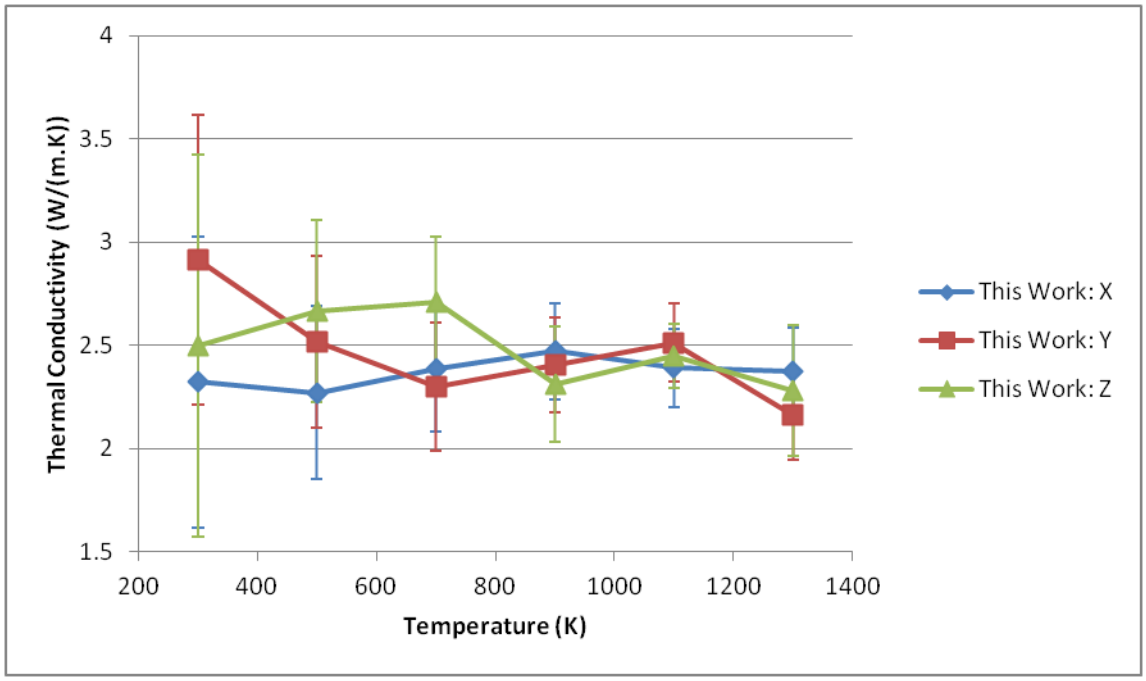

Figure 5.24 Directional thermal conductivities of silicalite with respect to temperature.

The three directions appear to have almost equivalent thermal conductivities despite the structure being very different. The combination of these factors indicates that the main scattering mechanism is via the internal surfaces of the structure and thus the phonon mean free path is limited by surfaces and has very little variation with temperature.

Below are presented the Green-Kubo spectra for silicalite in Figure 5.25, Figure 5.26 and Figure 5.27.

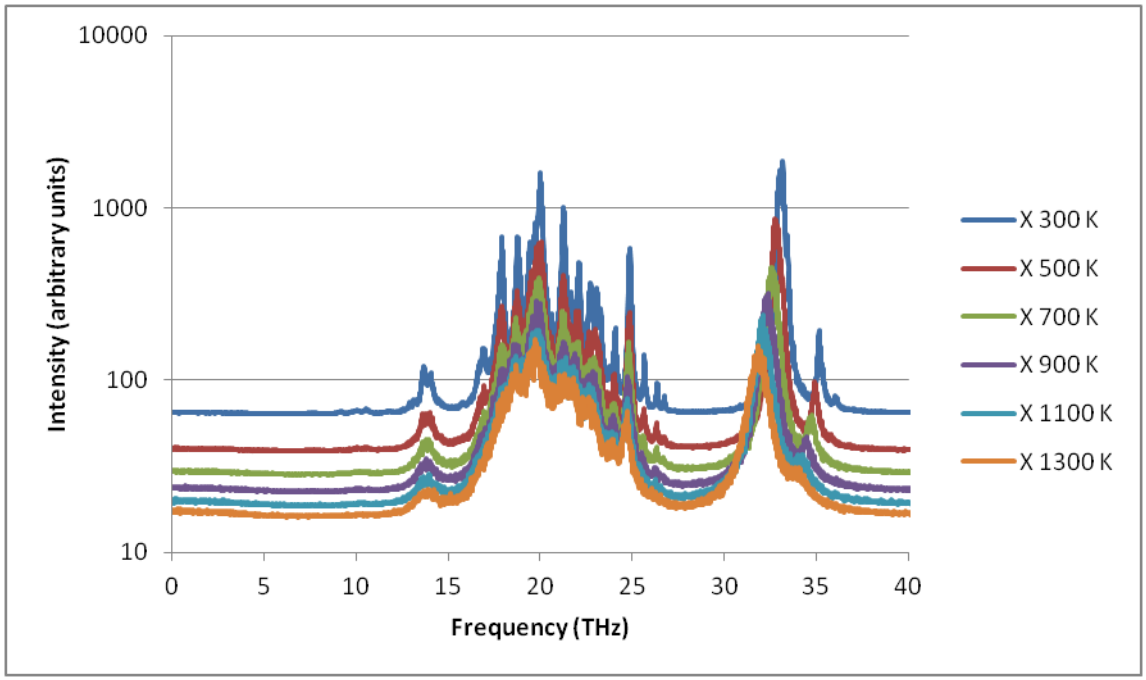

Figure 5.25 Green-Kubo spectra of silicalite in the X direction, Log_{10} scale.

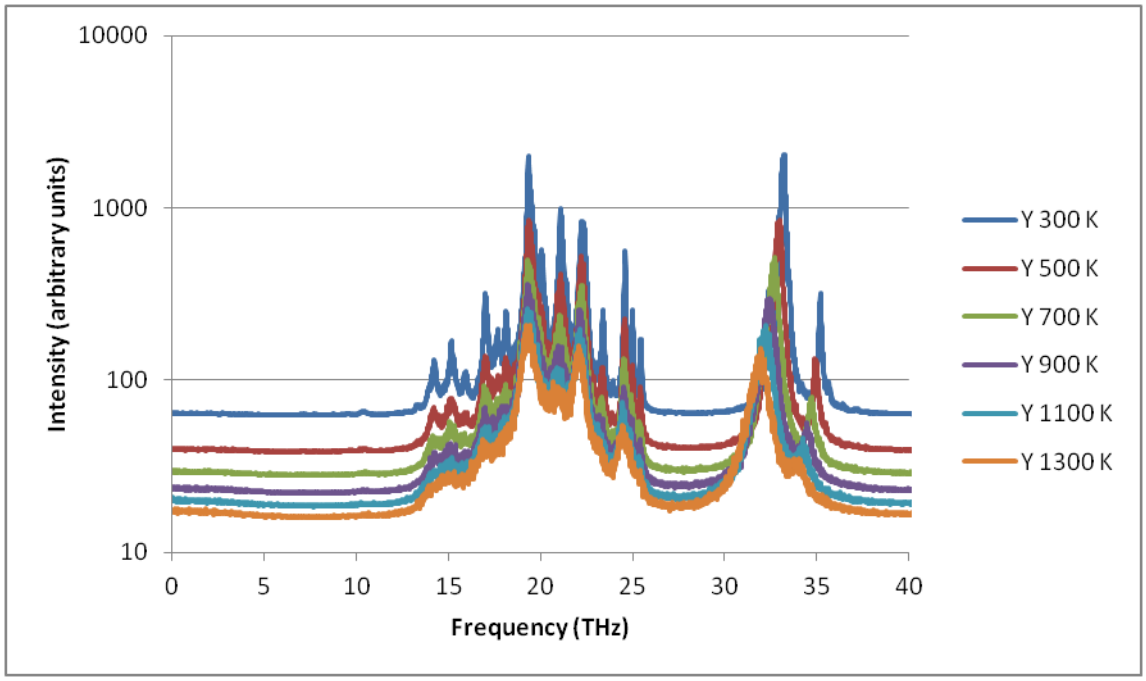

Figure 5.26 Green-Kubo spectra of silicalite in the Y direction, Log_{10} scale.

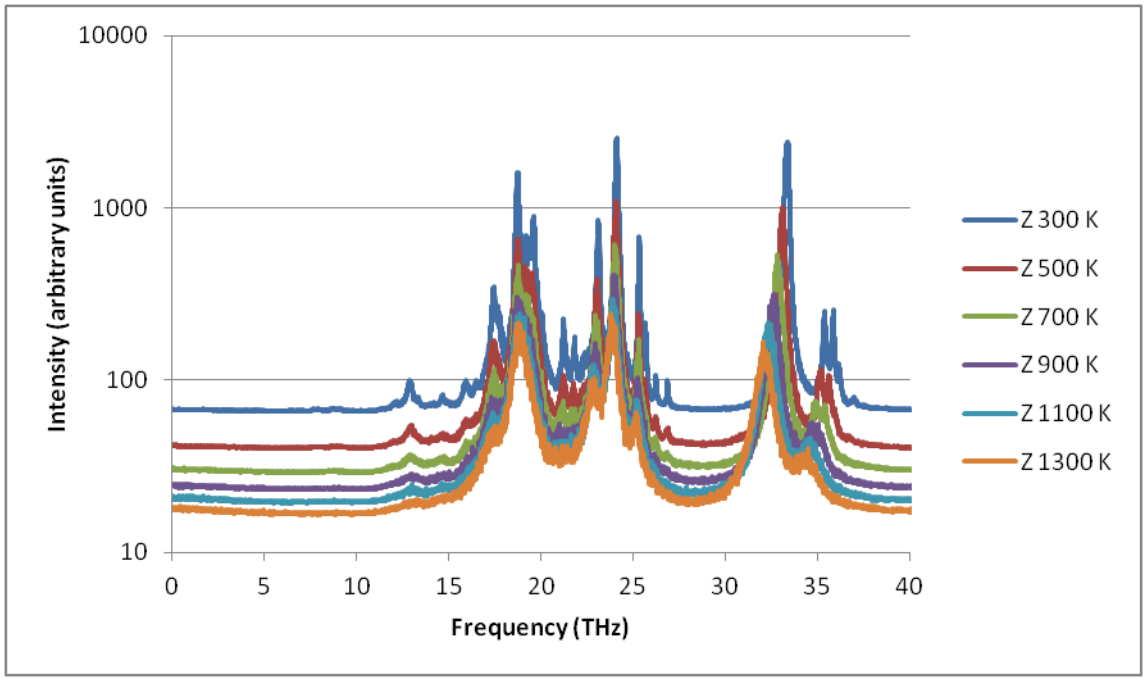

Figure 5.27 Green-Kubo spectra of silicalite in the Z direction, Log_{10} scale.

Each of the three directions gives distinct spectra although the overall regions for different types of modes match well with those of the spectra of quartz. The two regions are centred on 10-27 THz and 30-40 THz respectively. The 10-27 THz region contains Si-O bending modes while the 27-40 THz region contains Si-O stretching modes. The bending region of the spectra shows many more vibrational modes than for the quartz structures, with which acoustic phonons may interact. As was found for quartz the stretching region shows a frequency shift at increasing temperatures but the bending region does not. The very large widths of the peaks indicate short lived phonons as peak width is inversely proportional to phonon lifetime [192].

As the temperature increases, the number of independent modes decreases. The decrease in the apparent number of modes may stem from the same mechanism that reduced the number of modes in quartz i.e. increase in symmetry. However, the symmetry of the system (*Pnma*) remains the same for both the energy minimised structure and the 1300 K average molecular dynamics structure. Therefore, it is more likely that the reduction in modes is due to the broadening of the peaks leading to overlap and obscuring the separate modes.

The lattice dynamics phonon DOS was calculated on the 288 atom orthorhombic cell with lattice vectors a=20.3 Å, b=20.3 Å and c=13.7 Å. The results provide an excellent

match to the Green-Kubo spectra and are presented in Figure 5.28, Figure 5.29 and Figure 5.30.

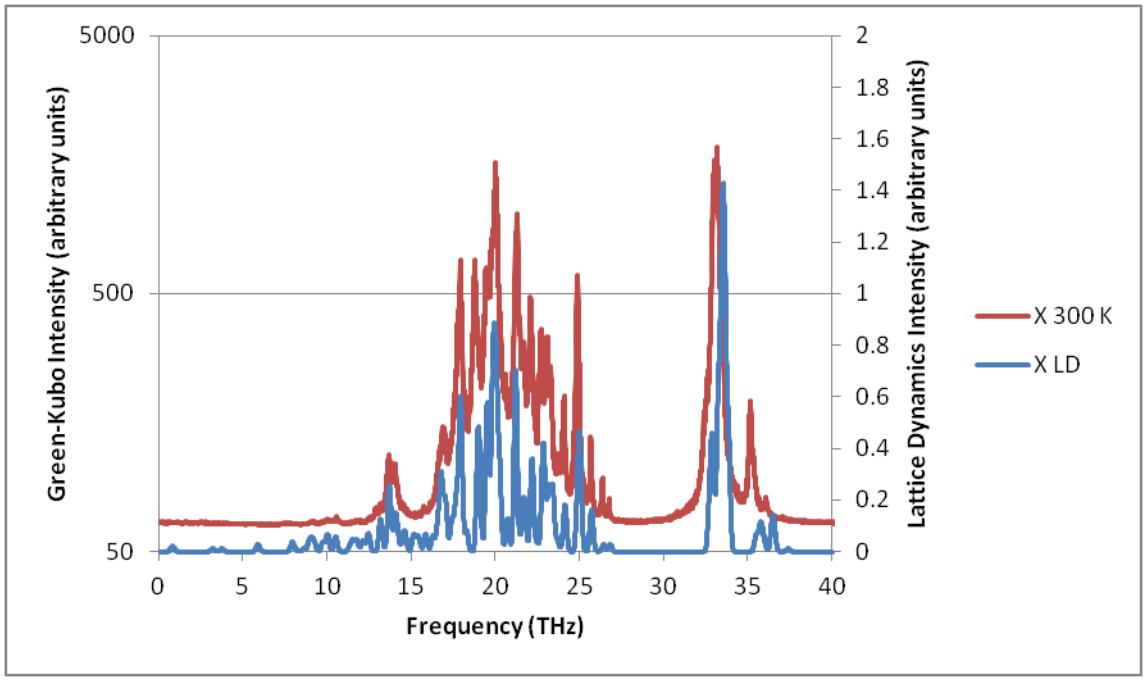

Figure 5.28 Comparison of the Green-Kubo at 300 K and lattice dynamics spectra for silicalite, X direction. Log_{10} scale on Green-Kubo intensity.

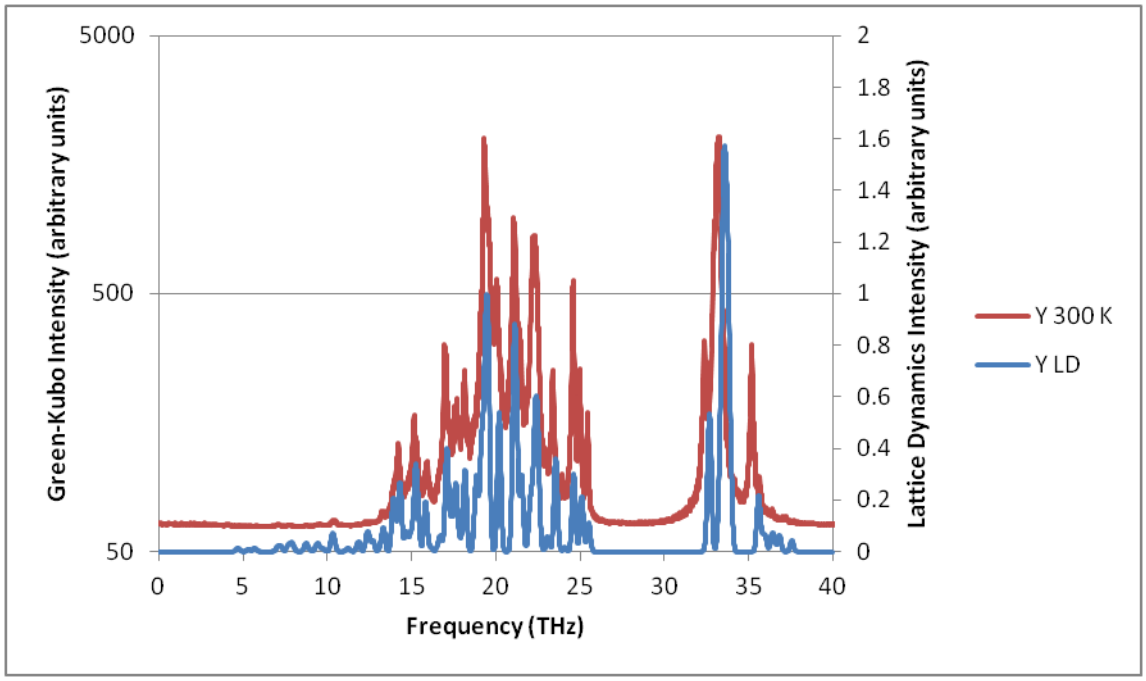

Figure 5.29 Comparison of the Green-Kubo at 300 K and lattice dynamics spectra for silicalite, Y direction. Log_{10} scale on Green-Kubo intensity.

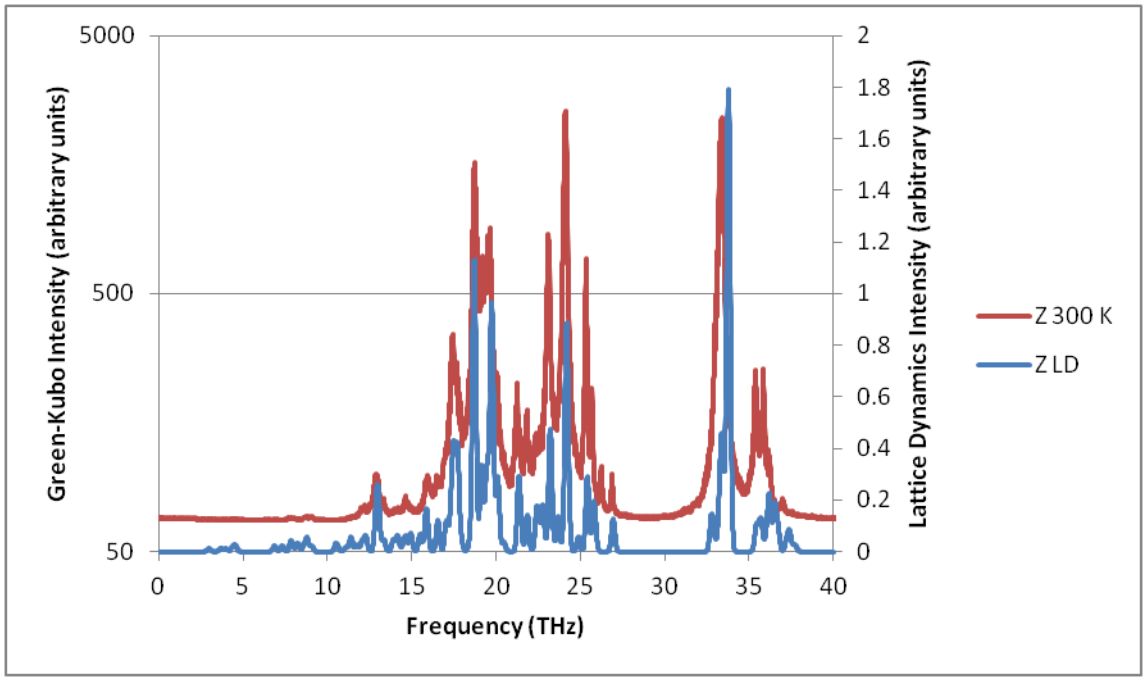

Figure 5.30 Comparison of the Green-Kubo at 300 K and lattice dynamics spectra for silicalite, Z direction. Log_{10} scale on Green-Kubo intensity.

The lattice dynamics phonon DOS spectra confirm that the higher frequency modes (30-40 THz) are related to Si-O stretching and the middle frequency modes (10-25 THz) are related to Si-O bending. Additionally, the lattice dynamics calculations show that silicalite does have a small contribution from the low frequency RUM modes (<10 THz), similar to quartz.

Interestingly, the Z direction of silicalite is the high density direction, containing no channels, and is distinct compared to the X and Y direction in having three main peaks instead of two. The three main Z direction peaks also match well with the X and Y direction peaks of the β-quartz spectra and share broadly similar atomic motions Table 5.8.

β-quartz Frequency (THz)	Silicalite Frequency (THz)	Motion
16.28	~19	Tetrahedra distortion/Si-O bending
22.70	~24	Si rattling in tetrahedra/Si-O bending
35.01	~34	Tetrahedra distortion/Si-O stretching

Table 5.8 Major vibrational modes in β-quartz (X/Y direction) compared to silicalite (Z direction).

The β-quartz structure contains the silica tetrahedra fully expanded. Furthermore, the silicalite structure does not undergo a phase transition and thus the similarity of the dense direction to β-quartz may be expected.

Another feature of note is that the frequencies have generally increased in the silicalite calculation, except for the stretching mode which reduced in frequency. The reduction in frequency of the stretching mode is not real as the stretching mode in the β-quartz was already an overestimation due to the calculation being conducted on a transition structure.

Overall the silicalite structure displays exceptionally low thermal conductivities on the order of 2.5 W/(m.K) and may be similar to a glass (Appendix B). However, the structure retains some similarities in its vibrational modes to bulk quartz.

5.4. SiO_2 Summary

The effect of the phase transition seen in quartz can have a profound effect on the thermal conductivity due to the significant changes to the phonon modes in the system. While some modes display the expected shift to lower frequencies with increasing temperature, some display the opposite behaviour, indicative of a negative mode Grüneisen parameter. As the distribution of acoustic phonons obeys a Bose-Einstein distribution [192], optical modes at lower frequencies are expected to have a higher probability of scattering the heat carrying acoustic phonons and lower thermal conductivity. For the modes with a negative mode Grüneisen parameter this results in less scattering as temperature increases and therefore higher thermal conductivity due to

these modes. However, there are still many modes which display positive mode Grüneisen parameters and these tend to dominate the thermal conductivity. Looking back at Figure 5.5 it now seems possible that the minimum in thermal conductivity is at least partially due to these modes, although the effect of Dauphiné twinning cannot be discounted.

The tetrahedral units which make up the structure of quartz give rise to very low frequency RUMs. However, most of these do not interact with the heat-flux and therefore cannot scatter heat-carrying phonons. Some RUMs are able to interact with the heat-flux at low temperatures within α-quartz but lose this ability as the temperature increases and the structure transitions to β-quartz. This change would also result in an increase of thermal conductivity if it was the only mode present, but is hidden by the reduction in thermal conductivity caused by the majority of other vibrational modes.

The existence of RUMs in silicate materials results in interesting behaviour that can have applications in tuning the thermal conductivity. The RUMs present in quartz leads directly to the phase change and negative thermal expansion [249] which both alter the number and frequency of phonon modes present in the material.

While the RUMs themselves do not significantly contribute to phonon scattering in the silica materials studied here (except at very low temperatures in quartz), their existence creates opportunities to scatter phonons by related mechanisms. Firstly, dynamic Dauphiné domain formation and destruction below the phase transition temperature may lead to the observed experimental thermal conductivity minimum seen in the work of Kanamori et al. [49]. However, extremely large (physical and time scales) molecular dynamics simulations would be required to capture these effects and lattice dynamics calculations may never be able to reproduce such effects as the memory requirements become unmanageable for large systems.

The use of other silica tetrahedra based materials such as silicalite or even mesoporous silica offer many more opportunities for reducing thermal conductivity. The increased number of environments in the unit cell combined with lower density leads to an enormous reduction in thermal conductivity and hence may represent an excellent substrate material for thermoelectric devices.

The thermal conductivity of silicalite was found to be generally insensitive to temperature with a low thermal conductivity of ~2.5 W/(m.K), which is very close to preliminary calculations on silica glass (Appendix B). The primary differences in the systems are that of density and disorder. The density in the glass system is much higher as is the disorder. Therefore, density alone cannot be the only factor affecting thermal conductivity. It is the diversity of environments which leads to many optical phonon capable of interacting with the heat-flux and thus phonon scattering is greatly increased in silicalite.

Although quartz and silicalite are not thermoelectric materials, the understanding gained from their study can now be applied to thermoelectric materials. Searching for a material with strong RUMs and/or which undergoes phase changes in the temperature region of operation may significantly reduce thermal conductivity and boost performance.

In the next chapter the promising thermoelectric material $SrTiO_3$/STO is discussed which combines a covalent framework with an ionic guest atom and may show behaviour similar to either/both MgO and SiO_2. The role of grain boundaries and nanostructured materials in reducing thermal conductivity will also be explored further.

6. The Thermal Conductivity of Systems Based on the Thermoelectric Material Strontium Titanate ($SrTiO_3$/STO)

Strontium titanate ($SrTiO_3$/STO) is a perovskite type material which may have applications in future high temperature thermoelectric devices. STO has advantages over more traditional thermoelectric materials in that its constituent elements are non-toxic, abundant, cheap and stable to oxidation. These properties make STO suitable for use in high temperature applications as it is less likely to degrade in oxidising conditions. The relatively low cost of STO combined with the use of non-toxic elements, stability over a wide temperature range and its ready conversion to an n-type semiconductor makes STO an attractive material for thermoelectric applications.

6.1. STO Overview

STO is a perovskite material and exists in two phases; below ~105 K, the structure is tetragonal (I4/mcm) and above, the structure is cubic ($Pm\bar{3}m$) [302]. This work is concerned primarily with the high temperature thermal conductivity of STO and so only the cubic phase is considered.

The cubic phase STO contains strontium atoms on the A sites coordinated by 12 oxygen atoms and titanium atoms on the B sites and are coordinated by 6 oxygen atoms. At room temperature, the perovskite structure is cubic with a lattice parameter of ~3.9 Å. The bonding arrangement in STO has a strong covalent interaction between titanium and oxygen, while the strontium interaction with the Ti-O framework is ionic [303, 304], Figure 6.1.

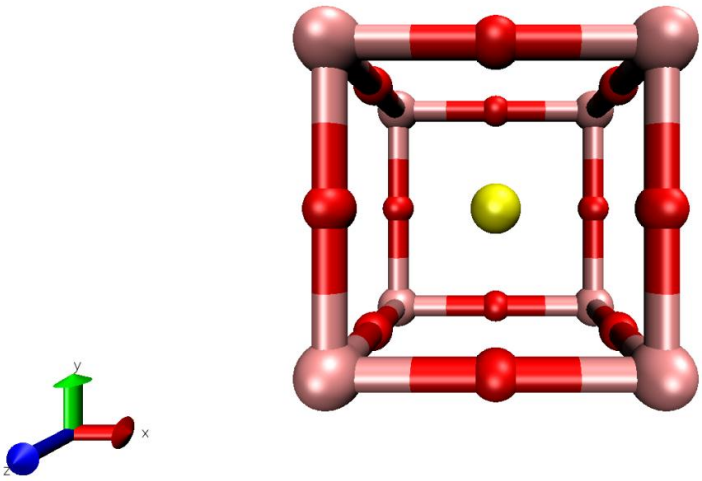

Figure 6.1 Perspective view of a cubic $SrTiO_3$ unit cell. The structure displayed contains 1x Sr atom, 8x 1/8 Ti atoms and 12x 1/4 O atoms.

While STO is an electrical insulator when stoichiometric, it can readily be made an n-type semiconductor by introduction of defects. For example, by making the structure oxygen deficient, i.e. $SrTiO_{3-x}$, Ti^{3+} species are generated [305, 306]. The perovskite structure has another notable feature, namely it can accommodate a wide range of guest species while maintaining its structural integrity, normally by substitution. In general, large low charged cations prefer to be at the Sr site while smaller higher charged cations prefer to be at the Ti site [307].

Despite its attractive TE properties, the thermoelectric figure of merit (ZT) for STO remains stubbornly low. Typical values of ZT for STO are on the order of ~0.37 [308, 309] at ~1000 K via doping with rare earth elements [310] or transition metals [311]. Lanthanum and niobium are particularly popular dopants [28, 312-315]. The low ZT values are generally due to the high thermal conductivity found in oxide materials.

There have been several approaches adopted for reducing the lattice thermal conductivity of STO, which include doping with heavy atoms and nanostructuring to enhance phonon scattering. As STO systems are generally doped to improve the electrical properties, further improvements in ZT are most likely to be gained via nanostructuring [316]. Nanostructuring may take on many forms and can impact on both the electrical and thermal properties and hence is a very active research area [316-318].

Introduction of grain boundaries is the most basic form of nanostructuring and are inherently present in polycrystalline systems. The presence of grain boundaries can greatly reduce the thermal conductivity by scattering phonons [319]. Unfortunately, charge carriers may also be scattered, reducing electrical conductivity. Thus more careful control of the grain boundary morphology and orientation may lead to more efficient thermoelectric materials, particularly if experiment could be guided as to which is the most effective microstructure.

Reducing the dimensionality of the system is another approach to nanostructuring. Interesting quantum effects occur when STO is confined to a thin two dimensional layer [236, 320], these effects are referred to as a two dimensional electron gas or 2DEG. A significant increase in the absolute value of the Seebeck coefficient is obtained for a system of niobium doped STO layers embedded in pure STO when the thickness of the layers is less than 4 unit cells; achieving a maximum estimated ZT of 2.4 at 300 K using the thermal conductivity of pure bulk STO. However, this value refers only to the 2DEG while the corresponding polycrystalline bulk ZT is only 0.24.

By combining the nanostructuring approaches of grain boundaries and 2DEG systems, a promising approach to increasing the ZT of STO may be obtained. One such approach is in the development of ordered arrays of nanoparticles. In the case of STO, these would be nanocubes [318, 319]. Nanocube systems contain small STO crystals connected by a 3D network of 2DEG planes; thus, the system has many scattering planes for phonons while the scattering planes themselves increase the electrical properties.

Nanocubes have been predicted to have a high theoretical ZT, approaching the values required for commercial applications [316]. A theoretical model based on DFT derived values was performed on assembled nanocubes. DFT calculations were used to obtain parameters for the STO nanocubes which contained 10% lanthanum doping and were held together by a variable sized “mortar” of 20% doped niobium STO. Calculations on the transport coefficients found that a ZT of 1.2 at 300 K is possible when the minimum thermal conductivity is used [321]. An alternative treatment of the thermal conductivity gave an alternative value of 0.8 at 300 K [316].

Simulations may provide additional information about the atomic scale processes which make STO a good thermoelectric material. A fundamental problem arises however as it

is very difficult to calculate all relevant transport coefficients using a single method. Ab initio methods are useful for calculating electronic properties as the electrons are included explicitly; ab initio methods may also be used to calculate the thermal conductivity, but are limited by system size and the approximations present in the BTE. Conversely, atomistic methods can extend to large system sizes to calculate the thermal conductivity via several methods, but have no accurate representation of the electronic processes.

Atomistic methods are much more appropriate for studying thermal transport in STO as much larger systems may be used. Additionally by using molecular dynamics rather than lattice dynamics higher order anharmonicity may be included directly, however due to the simulation cell size certain phonons may be forbidden, see Chapter 3.2.4 for details. Therefore, lattice dynamics and molecular dynamics each have their own strengths and weaknesses and the selection of a method must be made carefully. A drawback of potential model techniques compared to ab initio methods is that they may struggle to accurately represent the interactions between species, particularly away from equilibrium and so care must be taken in their selection.

The Shell model is often used in the study of oxide materials to better represent the ionic polarisability of the oxygen species. However, it has been found that for STO the shell model brings no significant benefit for either bulk or grain boundaries in terms of relative energies and structures [322]. Combined with the fact that shell model calculations are much more computationally expensive most potential models used for STO are rigid-ion, often containing partial charges.

A potential model developed by Tosawat et al. [323] appears to give exceptionally good thermal conductivity values at first look. However, it has been pointed out by Goh et al. [128] that the Sr-O interaction in particular has a spurious attraction at close distances, which risks unphysical fusion of atoms at high temperatures.

Goh et al. also propose an alternative potential model which performs well for thermal conductivity calculations, but has the issue of unequal charge distribution [128]. Most potential models either use formal charges or uniformly scaled partial charges; the model of Goh et al. uses partial charges of +2.0 for strontium, +2.2 for titanium and -1.4 for oxygen. These charges seem to have been chosen to mirror the covalent nature of the Ti-O interaction and the ionic interaction of strontium atoms with the Ti-O network

[304]. However this distribution of charges results in non-neutral partial Schottky defects (i.e. SrO and TiO_2) and renders the model almost unusable for any simulations beyond the bulk as most surfaces, grain boundaries and nanostructures will be non-stoichiometric.

Thus a potential model is required that is stable at high temperatures, can readily be used to examine the defect chemistry of STO, and ideally has interaction parameters available for a large range of dopant species. Such a potential model must also be able accurately reproduce the thermal conductivity of bulk STO. With this potential model the thermal conductivity of more defective structures can also be predicted.

Defects within STO reduce the thermal conductivity by scattering the heat transporting acoustic phonons. Much work has been done experimentally to study the effect of grain size on thermal conductivity. However, little is known about the impact of grain boundary structure on the thermal conductivity.

Thus, the aim of this work study the effect of different grain boundary structures, grain sizes and complex nanostructuring on the thermal conductivity of STO based materials. The Teter potential model [163] will be used as it has been fitted to many materials and has many interaction potentials available for future defect work. One drawback of this model is that the interactions are based on Buckingham potentials and so still include spurious attractions at small separations, however the energy barrier is high and thus unphysical fusion is unlikely at the temperatures studied here.

The same techniques outlined and developed in previous chapters will be used again to calculate not only the thermal conductivity of various grain boundary systems but also their Green-Kubo spectra, which may be interpreted with help from lattice dynamics calculations. Thus, information about the specific structural features of the boundaries contributing most to scattering may be derived.

6.2. Bulk STO

The potential model used in this chapter was developed by Teter [163] (parameters are given in Chapter 2.1.5). When applied to the STO structure the symmetry is retained (space group $Pm\bar{3}m$) along with the coordination environments of each of the atoms.

The lattice parameter and independent elastic constants have been calculated using the potential model and are compared to experimental values in Table 6.1.

Property	Calculated	Experiment	% Difference
a (Å)	3.88	3.91	-0.77
c_{11} (GPa)	337.10	~330	2.15
c_{12} (GPa)	133.69	~105	27.32
c_{44} (GPa)	133.69	~126	6.10

Table 6.1 Calculated and experimental [324, 325] properties of STO.

The lattice parameter differs from experiment by less than 1%. The c_{11} elastic constant is very close to the experimental value, differing by only ~2%. The c_{12} and c_{44} are once again identical due to the Cauchy condition and are slightly higher than the c_{44} experimental elastic constant. It must be noted however that the experimental values were obtained at 298 K for the lattice parameter and 133 K for the elastic constants.

As described in Chapter 3.1.2.1 the thermal expansion is an important property for a potential model to reproduce and so the thermal expansion of STO has been evaluated using the same procedure as for MgO and SiO_2.

6.2.1. Thermal Expansion

A 12 x 12 x 12 supercell of the 5 atom STO cubic unit cell was generated containing a total of 8,640 atoms. A 0.5 ns isotropic NPT (with a Nosé–Hoover thermostat and barostat) molecular dynamics simulation was conducted; averaging the lattice vectors every 10 timesteps. The final lattice vectors converted back to the single unit cell are plotted as a function of temperature in Figure 6.2.

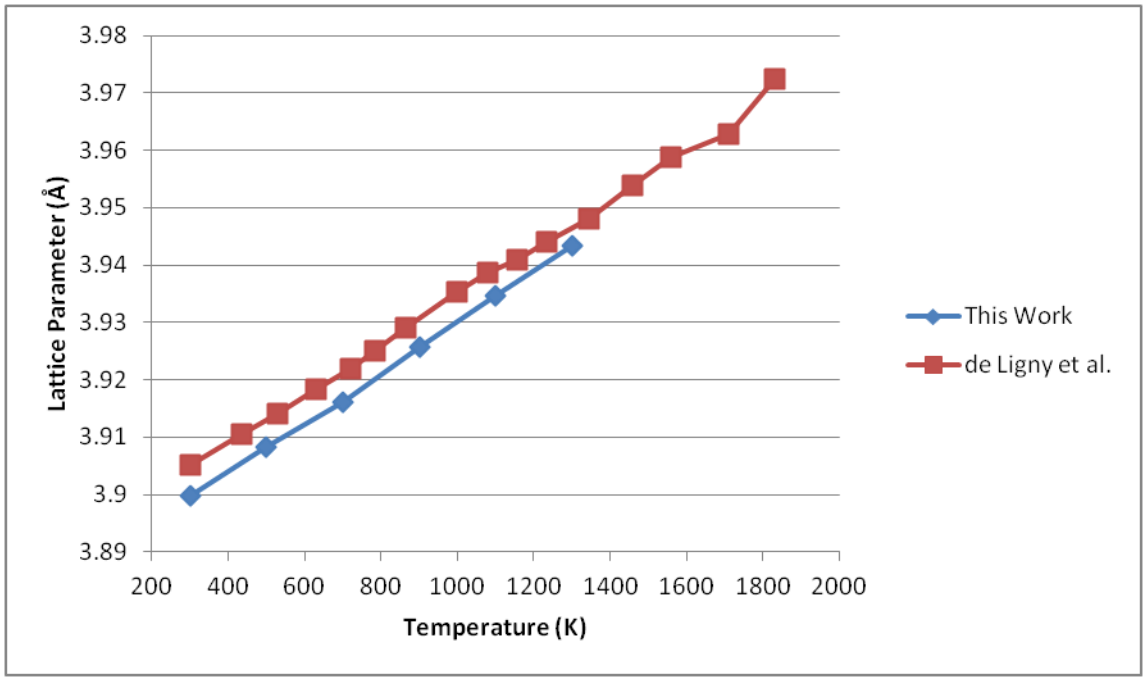

Figure 6.2 Calculated thermal expansion of STO compared to experiment [326].

The lattice parameters stay within 2% of the experimental values across the range to be studied. Additionally the calculated thermal expansion in the simulations is 1.13×10^{-5} K^{-1} while the experimental thermal expansion is calculated to be 1.10×10^{-5} K^{-1}, indicating the potential model is reproducing the anharmonic interactions well and reasonable thermal conductivity values may be expected.

6.2.2. Thermal Conductivity

The thermal conductivity of STO was calculated using the same procedure as the other materials (see Chapter 3.2.3). The same supercells were used as for the thermal expansion calculations with the lattice vectors set to their averaged value. A 0.5 ns NVT equilibration period (with a Nosé–Hoover thermostat) was conducted followed by a 20 ns NVT heat-flux data collection period. The averaging window for STO was found to be optimal between 50,000-55,000 timesteps, although large fluctuations in the integral remained, leading to a large apparent error at low temperatures. The results are plotted against experimental values in Figure 6.3.

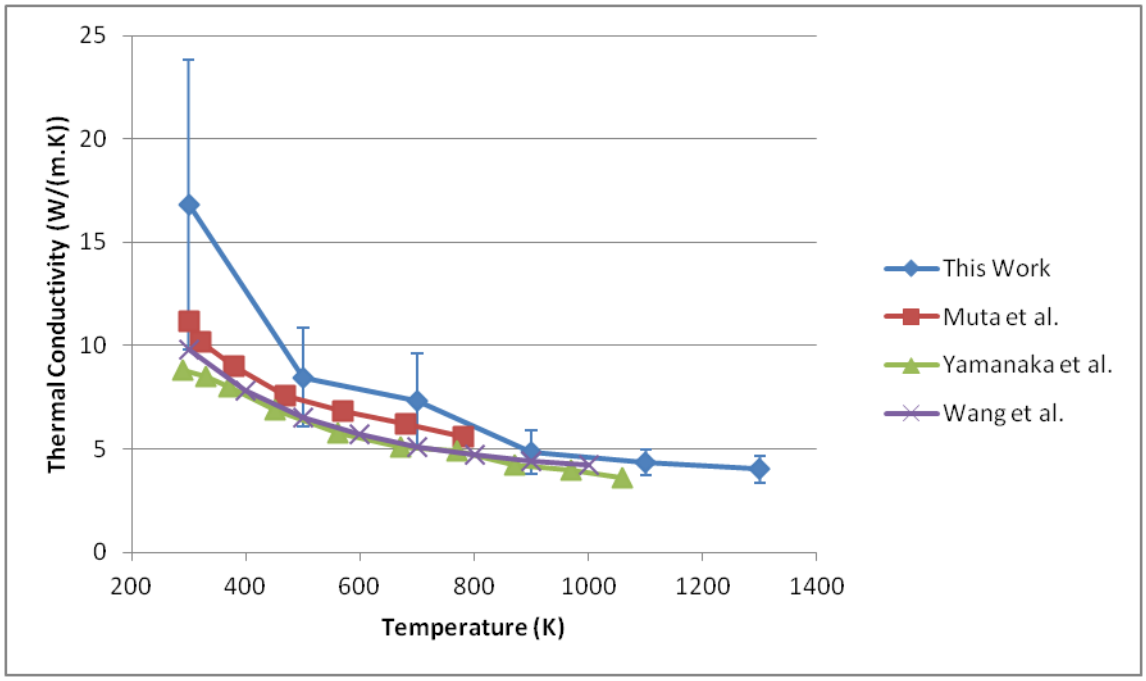

Figure 6.3 Thermal conductivity of bulk STO compared to experiments [319, 327, 328].

The values calculated using the Green-Kubo method appear to be slightly higher than those from experiments. The thermal conductivity values also obey the usual power law indicating the primary scattering mechanism is phonon-phonon.

The thermal conductivity was also calculated via the BTE using the Phono3py code [121, 122]. The Teter potential model [163] was used to calculate the forces within the METADISE code [165]. Convergence was achieved with respect to supercell size and q-point mesh. The final results using a 4 x 4 x 4 supercell and a 20 x 20 x 20 q-point mesh are presented in Figure 6.4 compared to Green-Kubo calculation and experiment.

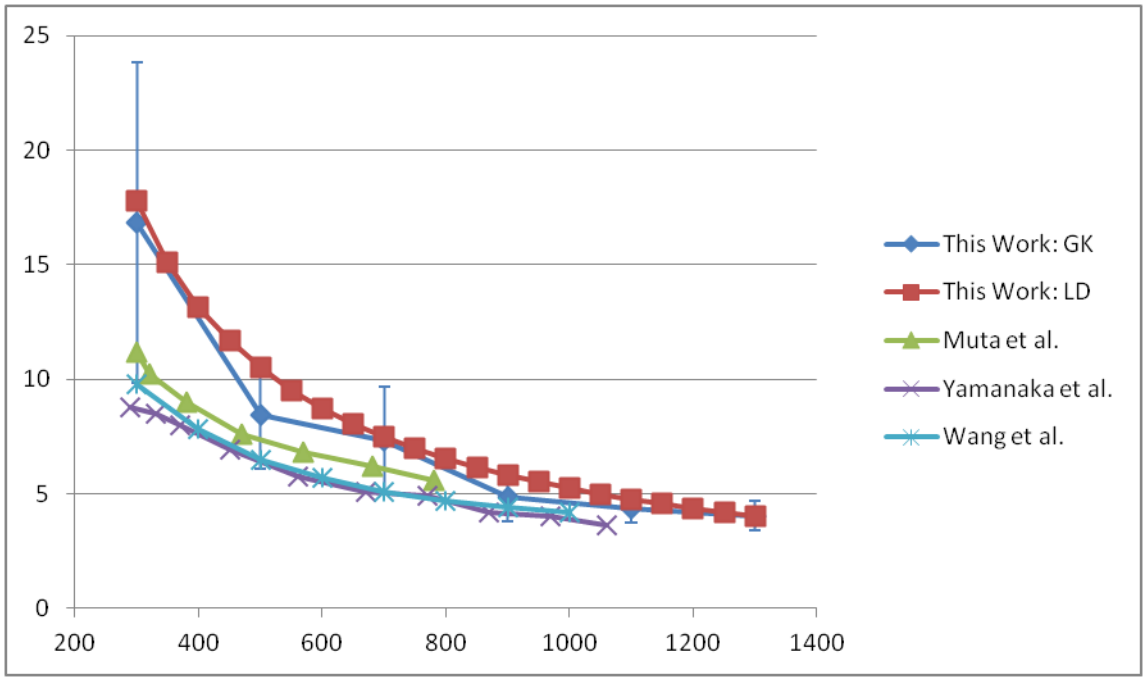

Figure 6.4 Calculated thermal conductivity of bulk STO via two methods compared with experiments [319, 327, 328].

An extremely good match to the Green-Kubo calculations is achieved. The match indicates that the lattice dynamics calculations approximations hold well for STO (i.e. there is no need to go above third order force constants and that the relaxation time approximation holds well) and that a 4 x 4 x 4 supercell is sufficiently large to include important long wavelength phonons in stoichiometric STO.

The close agreement between the lattice dynamics calculation and molecular dynamics calculation indicates that the Green-Kubo results are indeed well converged. It can also be concluded that the potential model is overestimating the thermal conductivity compared to experimental values, particularly at lower temperatures.

To better understand the scattering processes involved in the thermal conductivity the Fourier transform of the heat-flux autocorrelation can again be taken. Additionally, the lattice dynamics phonon DOS at the gamma point can be calculated and treated to obtain a more quantifiable frequency for each mode in addition to the motions of atoms involved in that mode.

6.2.3. Green-Kubo and Lattice Dynamics Spectra

Despite the large fluctuation in the autocorrelations, their Fourier transforms give well resolved Green-Kubo spectra which are displayed in Figure 6.5. The well resolved spectra indicate that the large fluctuations seen in the autocorrelations are consistent long-lived optical modes, rather than random noise. As these optical phonon modes do not transport a significant portion of heat themselves then their truncation in the integration should not lead to a significant underestimation of the thermal conductivity.

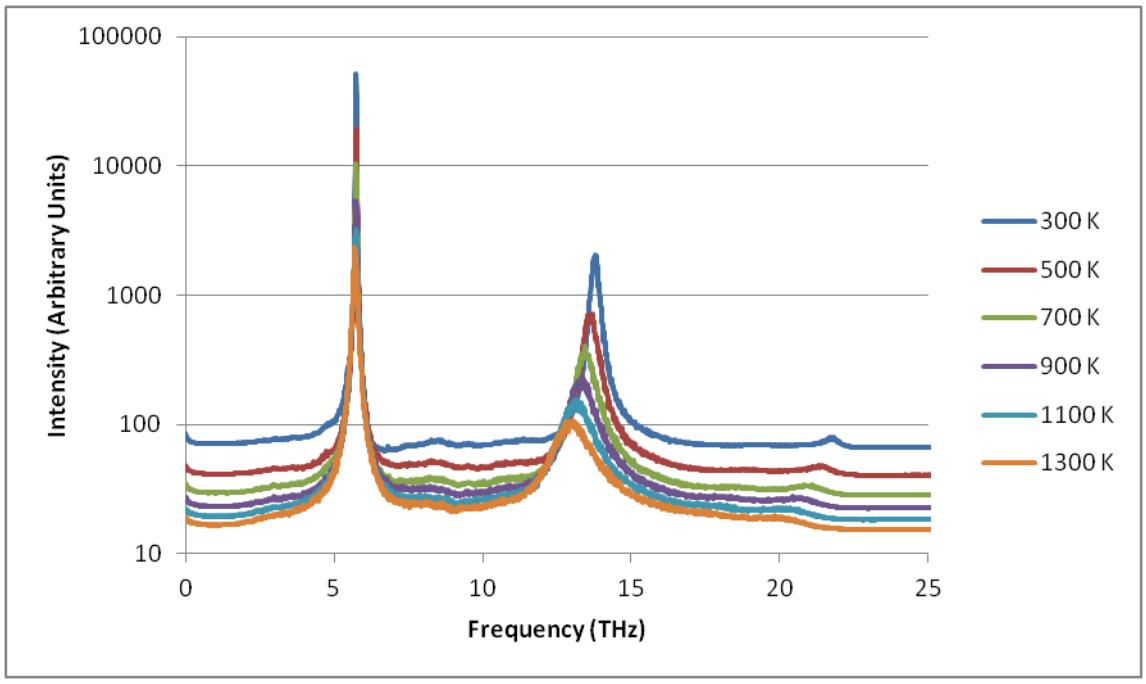

Figure 6.5 The Fourier transform of the heat-flux autocorrelation, Log_{10} scale.

The Green-Kubo spectra for STO display three modes at ~5.7 THz, ~13.9 THz and a very small mode appearing at ~21.7 THz (depending on temperature). The mode appearing at ~5.7 THz seems entirely insensitive to temperature whereas the other two modes shift to lower frequencies with higher temperatures, as seen for previous bulk materials (Chapters 4 and 5).

To index the peaks from the Green-Kubo spectra the total phonon DOS (gamma point) is calculated using the Phonopy code [121] using the 5 atom cubic cell with lattice vectors a=b=c=3.88 Å. The full phonon DOS at the gamma point reveals four distinct optical modes and is displayed in Figure 6.6 (a fifth mode of zero frequency has been removed which corresponds to a translation of the entire lattice).

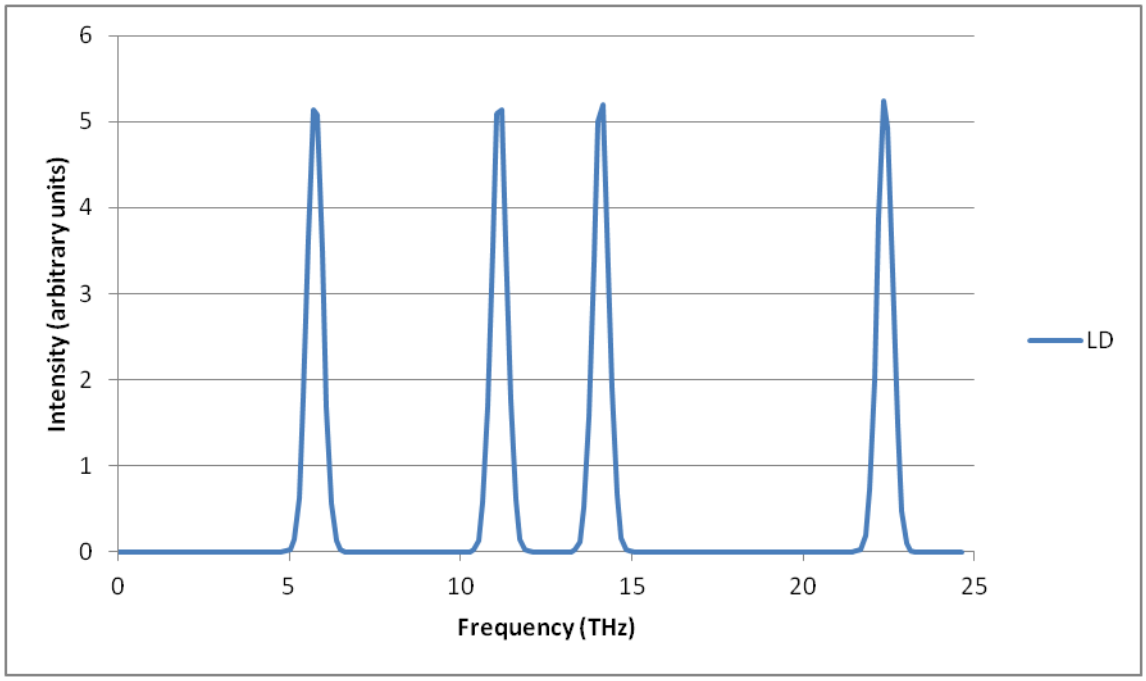

Figure 6.6 Phonon density of states (DOS) for STO at the gamma point.

The DOS has an extra mode at 11.13 THz when compared to the Green-Kubo spectra. This mode is expected to be symmetric and thus will be removed upon analysis. A dimensionless eigenvector cutoff of 0.01 is used for STO to remove the symmetric optical phonon modes. The cutoff value must be chosen carefully otherwise some modes are missed which do appear in the Green-Kubo spectra. The value of 0.01 was chosen to allow the mode at ~22.4 THz in the Green-Kubo spectra to be identified.

As the three directions of STO are equivalent, only the X direction is plotted and compared with the low temperature Green-Kubo calculation in Figure 6.7.

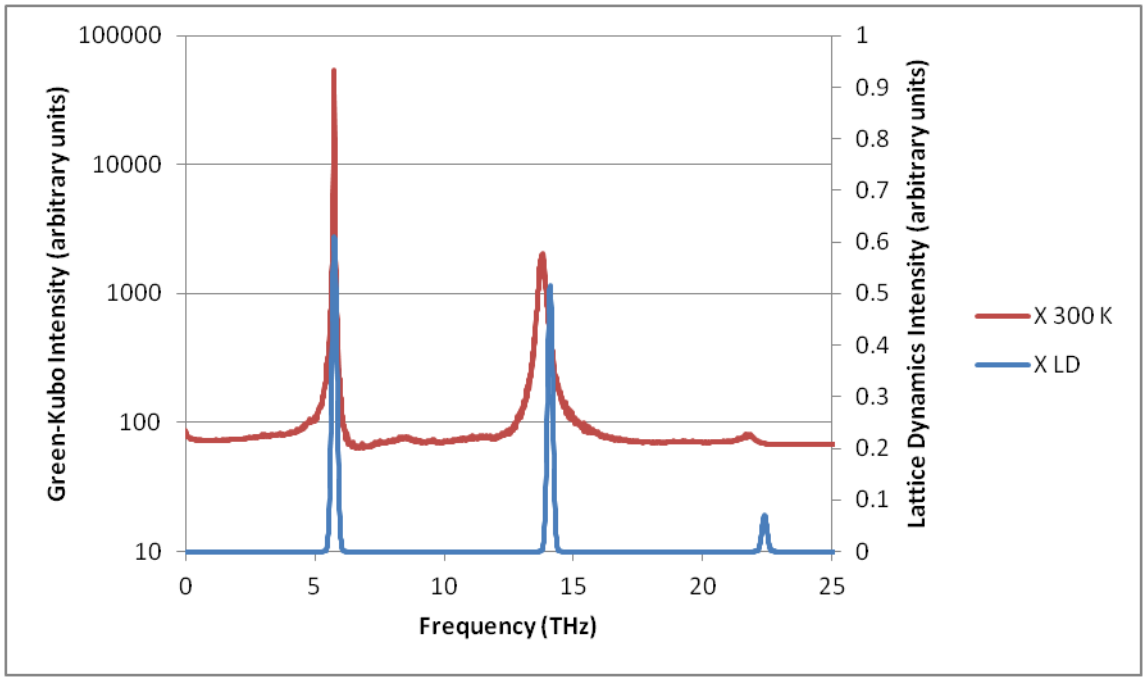

Figure 6.7 Lattice dynamics phonon DOS and Green-Kubo spectra at 300 K of bulk STO. Log_{10} scale on Green-Kubo intensity.

The frequencies as calculated by lattice dynamics are almost identical to those as calculated by Green-Kubo, with a relatively small deviation observed at ~14.1 THz and ~22.4 THz. These two modes displayed significant shift with temperature in the Green-Kubo calculations and so it can be safely assumed that the deviation of the frequencies is due to the lattice dynamics calculation not including temperature effects.

The relative heights of the peaks correlate quite well when the Green-Kubo spectrum is plotted on a logarithmic scale. This indicates that there may be some exponential function involved in the peak heights for the Green-Kubo calculations as opposed to the lattice dynamics calculations; this is almost certainly down to Bose-Einstein statistics and the increased population of acoustic phonons at lower frequencies.

Due to the low number of modes present in the gamma point phonon DOS, the vibrational modes can be examined and motions assigned, given in Table 6.2.

Frequency (THz)	Motion
5.75	Sr atoms vibrating within cubic Ti-O cages
11.1	O tetrahedra distorting around Ti – SYMMETRIC MODE
14.1	Ti atoms vibrating in O tetrahedra with tetrahedra distortion
22.4	O atoms vibrating between Ti atoms

Table 6.2 Assigned vibrational modes of bulk STO.

The three modes, which are present in the Green-Kubo spectra, have motions which may be considered rattling type modes. Low frequency rattling modes are often introduced into thermoelectric materials via doping in order to reduce the thermal conductivity [66, 70, 329]. The low frequency of these modes maximises interaction with acoustic phonons due to the Bose-Einstein distribution of acoustic phonon populations, making them very effective at scattering acoustic phonons and reducing lattice thermal conductivity.

The vibrational mode at ~11.1 THz is a distortion of the oxygen tetrahedra around titanium. The oxygen atoms distort in such a way that the centre of mass does not change during the vibration, making the mode symmetric and explaining its absence from the Green-Kubo spectra.

These modes are expected to be present within grain boundary systems in addition to new modes created by new environments present at the boundary. The effect of the new modes should be to lower the thermal conductivity as there will be more ways to scatter acoustic phonons. Thus the thermal conductivities of three distinct grain boundaries, with either a large (~100 Å) or short (~15-20 Å) separation, have been calculated in order to understand the impact of varying system geometry.

6.3. STO Grain Boundaries

The results in Chapter 4.3 show that for magnesium oxide, the orientation of the grain boundaries is important due to the differing atomic environments found at the boundary. Whether or not the grain boundary will scatter a phonon will depend upon the environments found at the grain boundary. If there are no environments suitable for scattering a particular frequency then the phonon of that frequency may pass unimpeded [330, 331].

The existence of two grain boundaries parallel to each other will also act to limit the allowed phonon wavelengths depending on the distance between them, and thus have some impact on the thermal conductivity.

Three different grain boundaries, which have been identified in experimental studies on STO, have been constructed using the methodology outlined in Chapter 2.5.1.4 and then annealed at 1300 K for more than 5 ns. The boundaries are displayed in Figure 6.8 subsequent to annealing, each showing distinctly different environments.

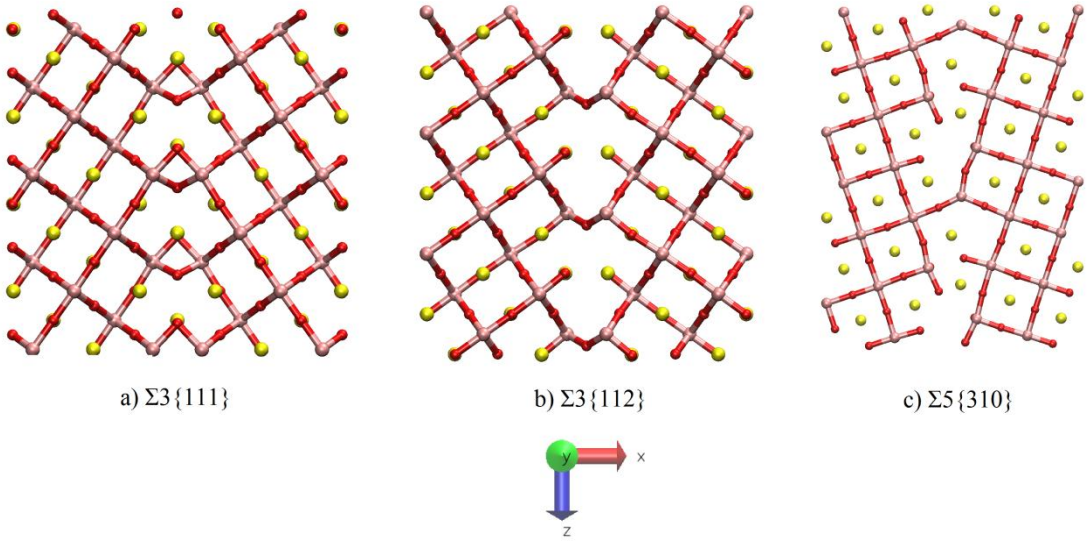

Figure 6.8 The a) Σ3{111}, b) Σ3{112} and c) Σ5{310} STO grain boundary structures. Sr = yellow, Ti = pink, O = red.

The structure of the Σ3{111} boundary is known experimentally from HRTEM studies [332]. DFT calculations [333] have shown that the Ti-O bonding network is partially preserved across the boundary, indicating the possibility of good electrical conductivity while effectively lowering the thermal conductivity. It has also been found that shear stress can alter the structure of the Σ3{111} boundary [334], and may have significant impact on the transport properties.

The Σ3{111} grain boundary used here is found to be identical to those found experimentally and with DFT. The boundary itself is constructed from face sharing Ti-O octahedra while the Sr atoms at the centre of the boundary remain 12-fold coordinate, although in a slightly different arrangement (now at the centre of a HCP packed polyhedra rather than the FCC packed polyhedra found in the bulk). The extent of

relaxation into the bulk caused by the Σ3{111} boundary is minimal and the bulk lattice is relatively unperturbed until very close to the centre of the boundary.

The Σ3{112} grain boundary has two proposed structures, one is mirror symmetric and the other is mirror-glide symmetric. Both of these structures have been studied using DFT and were found to have almost identical energy [322]. Other work has managed to observe the mirror symmetric form experimentally using HRTEM [335]. This work has used the mirror-glide form of the boundary for calculation of thermal conductivity, which was found to remain stable after being annealed at temperatures greater than 1000 K for several ns and displayed no tendencies to reconstruct. The structure of the mirror-glide symmetric Σ3{112} boundary has a larger range of reconstruction into the bulk material than the Σ3{111} boundary and contains square-based pyramidal Ti-O groups and 8-fold coordinate strontium at the boundary.

Combined experimental work (scanning transmission electron microscopy) and first principles calculations have also been conducted on the Σ5{310} boundary and concluded that the structure is asymmetric [336]. It has also been found that the structure of the Σ5{310} grain boundary demonstrates temperature dependent faceting [337]. These complexities mean that there are a large number of candidate structures for the Σ5{310} boundary. An atomistic study using interatomic potentials looked at many possible structures and found many had similar energies [338].

The Σ5{310} structure used for these calculations has been annealed at 1300 K for 2 ns, resulting in a structure that is at least metastable at the temperatures under study and may be the most stable for this potential model. The Ti-O groups at the boundary adopt a mixture of square-based pyramids and distorted square-based pyramids. An interesting property of the Σ5{310} boundary is that the strontium atoms within the boundary display some disorder between two sites, which may give rise to interesting vibrational effects.

Thus, the structures used for these calculations are either a match for experiment or are local minima which may still exist experimentally under certain conditions. Furthermore, due to the simplistic nature of interatomic potentials there is a reasonable possibility that the Σ3{112} and Σ5{310} boundary structures used are the global minima for this potential model, though determining this would require a full enumeration of all possible boundary structures.

While having accurate boundary structures is important, grain size is another factor which is likely to have a significant effect of the thermal conductivity in polycrystalline materials [339, 340]. For the systems under study, this is equivalent to the distance between the two grain boundaries as the other two directions are effectively infinite.

The CPU time overhead for running these simulations meant that the effect of different distances between grain boundaries was studied by considering two separations for each grain boundary structure. The system with a large separation between the boundaries was used to model the isolated case while the system with small separation between the grain boundaries was used to study the interacting case. Thus, six systems in total were generated.

Each system contains two identical grain boundaries (within symmetry) aligned perpendicular to the simulation cells X direction. The isolated systems have approximately 100 Å of bulk between the boundaries (giving a system of ~200 Å long); the interacting systems contain ~15-20 Å of bulk between the boundaries (~30-40 Å system total).

The deviations in distance originate with the structure of each boundary and the thickness of the repeating bulk unit perpendicular to the boundary. The size of the systems in the other dimensions was set to be at least 20 Å. The small size deviations between systems are expected to have negligible influence on the final thermal conductivities as compared to the boundaries.

Each system was simulated at 5 temperatures, 500 K, 700 K, 900 K, 1100 K and 1300 K. The system was not simulated at 300 K due to large fluctuations and hence the concern for the quality of the convergence of the autocorrelation for the bulk material at this temperature. A timestep of 1.0 fs was once again used. Each temperature for each system was equilibrated for 0.5 ns using an NPT ensemble to obtain the time averaged lattice vectors. Subsequent NVT data collection simulations used these lattice vectors. The data collection simulation used an NVT ensemble collecting heat-flux data every 10 fs for 20 ns.

6.3.1. The Σ3{111} Boundary

The Σ3{111} grain boundary has been studied at both long separation (isolated) and short separation (interacting). These different arrangements are expected to give

different thermal conductivities despite having the same structure due to the limiting of phonon wavelengths between the boundaries.

The Σ3{111} grain boundary structure contains face sharing Ti-O octahedra and Sr atoms in a different coordination environment to the bulk. While both the bulk and grain boundary Sr atoms are 12-fold coordinate, in the bulk the packing is HCP and at the boundary the packing is FCC. The arrangement of the simulation cell is such that the grain boundary lies perpendicular to the X direction, while the Y and Z directions are parallel. In the case of the Σ3{111} grain boundary, the Y and Z directions are symmetrically equivalent and are expected to give equivalent thermal conductivities and Green-Kubo spectra.

It must be noted that these simulations cannot be compared directly to polycrystalline systems as they are infinite in the Y and Z directions and thus are much more similar to multilayer thin film systems where two directions are effectively infinite bulk, while the third direction contains multiple grain boundaries aligned in parallel.

The first simulation discussed is that where the grain boundaries are isolated (~100 Å apart), which is expected to have a thermal conductivity slightly less than bulk STO. Additionally, by having the grain boundaries isolated it becomes easier to discern whether distinct grain boundary structures have any significant individual effects. It is expected that at large separations the distance between boundaries will dominate the thermal conductivity, whereas at small grain sizes the types of boundary will become more important due to boundary-boundary interactions.

6.3.1.1. Thermal Conductivity of the Σ3{111} Boundary

The study of the isolated boundary gives a starting point for comparison of boundary-boundary effects when studying interacting boundaries. Additionally, it may be possible to infer whether the boundary has a significantly long range effect, or whether it is the inter-boundary distance alone that is important.

The isolated Σ3{111} grain boundary system is orthorhombic and is approximately 203 Å x 22 Å x 19 Å and contains 7,200 atoms. The formation energy is 0.894 J/m^2, calculated as outlined in Chapter 2.5.1.4.

It is also possible to calculate the amount of additional length in the simulation cell caused by the presence of the grain boundary. To calculate this value, first the volume of an equivalent bulk unit cell is calculated and then divided by the cross-sectional area of the grain boundary system (parallel to the grain boundary), which gives the length of the grain boundary system should the grain boundaries be absent. This length is subtracted from the true length of the grain boundary system and divided by two to give the excess length per grain boundary. For the isolated Σ3{111} grain boundary the excess length is found to be 0.265 Å.

The thermal conductivity of the isolated Σ3{111} grain boundary has been calculated using the Green-Kubo method as described above. The average thermal conductivity compared to bulk is presented in Figure 6.9.

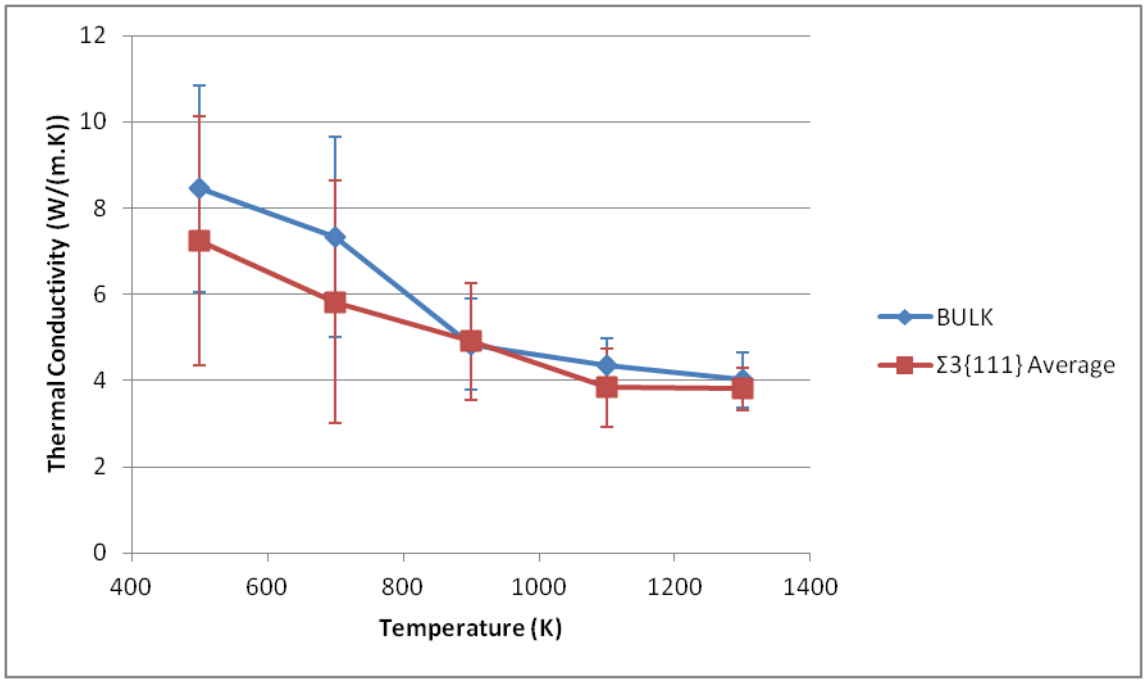

Figure 6.9 Average thermal conductivity of the isolated Σ3{111} boundary.

The grain boundary thermal conductivities appear very close to the corresponding bulk values, a result of the large amount of bulk between the boundaries and thus the average thermal conductivity of the system is much closer to bulk. This effect is more pronounced at higher temperatures, whereas low temperature thermal conductivities are lower than bulk values by 1-2 W/(m.K).

As the Σ3{111} grain boundary system is anisotropic the thermal conductivity is again expected to be anisotropic. The X direction passes directly through the grain boundary

and is expected to display the lowest thermal conductivity; the Y and Z directions are equivalent due to symmetry and are expected to have identical thermal conductivities, Figure 6.10.

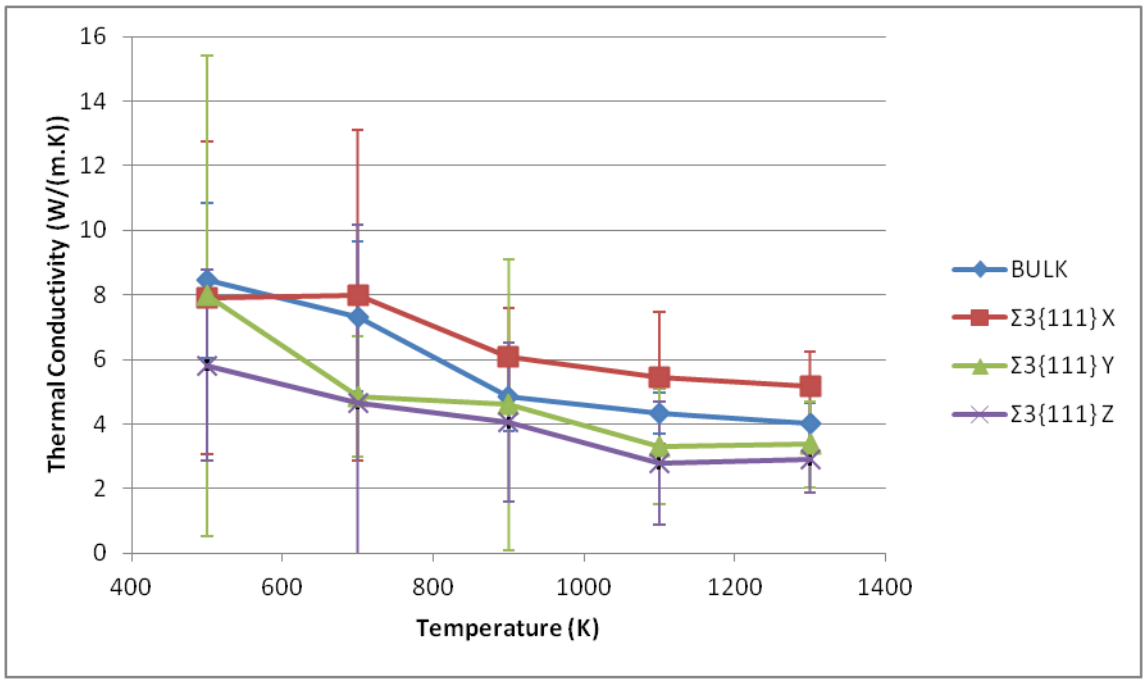

Figure 6.10 Directional thermal conductivity of the isolated Σ3{111} boundary.

Counter to what was expected, the X direction (through the boundary) has higher thermal conductivity than the Y and Z directions as well as bulk, although the difference is small and the fluctuations on the integral are large. One explanation for the possible increase in thermal conductivity may be that the large degree of Ti-O cross-linking at the boundary is facilitating thermal transport. Alternatively, the introduction of the boundary may introduce new scattering modes but also remove other scattering modes found in the bulk structure.

By studying the Σ3{111} at a much shorter separation (~15-20 Å), the bulk component of the thermal conductivity is reduced; additionally the two grain boundaries within the system are more likely to interact with each other. By reducing the bulk component of the autocorrelation the new modes introduced by the boundary become clearer; modes created by boundary-boundary interactions may also be evident.

The interacting Σ3{111} grain boundary system is orthorhombic and is approximately 27 Å x 22 Å x 19 Å and contains 960 atoms. The formation energy is 0.875 J/m^2, indicating a slight stabilisation over the isolated Σ3{111} grain boundary (0.894 J/m^2)

due to boundary-boundary interaction. Furthermore, the excess length of the interacting Σ3{111} grain boundary has also been increased to 0.270 Å from 0.265 Å.

The thermal conductivity of the interacting Σ3{111} grain boundary has also been calculated using the Green-Kubo method as described above. The average thermal conductivity compared to bulk is presented in Figure 6.11.

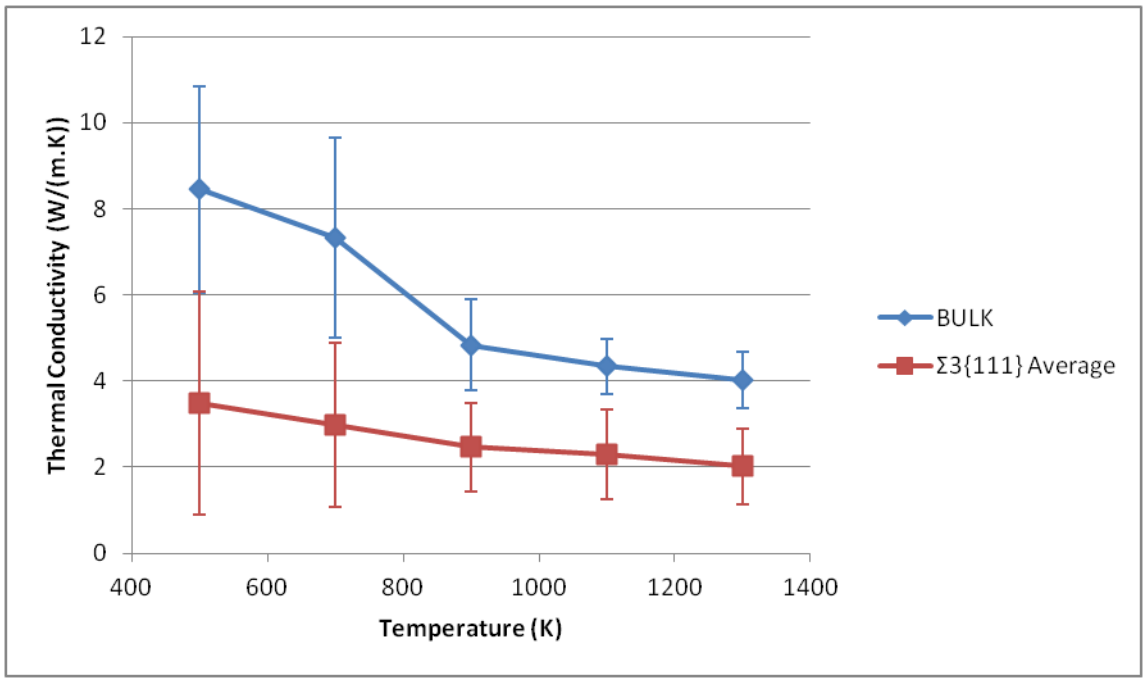

Figure 6.11 Average thermal conductivity of the interacting Σ3{111} boundary.

The thermal conductivity for the interacting Σ3{111} boundary is lower compared to bulk STO as may be expected for a system with a relatively high defect concentration (grain boundaries). The overall trend with temperature is flat indicating phonon-defect scattering is dominating over phonon-phonon scattering. To see whether the X direction still displays a higher thermal conductivity than the Y and Z directions the thermal conductivity is again split into directional components, Figure 6.12.

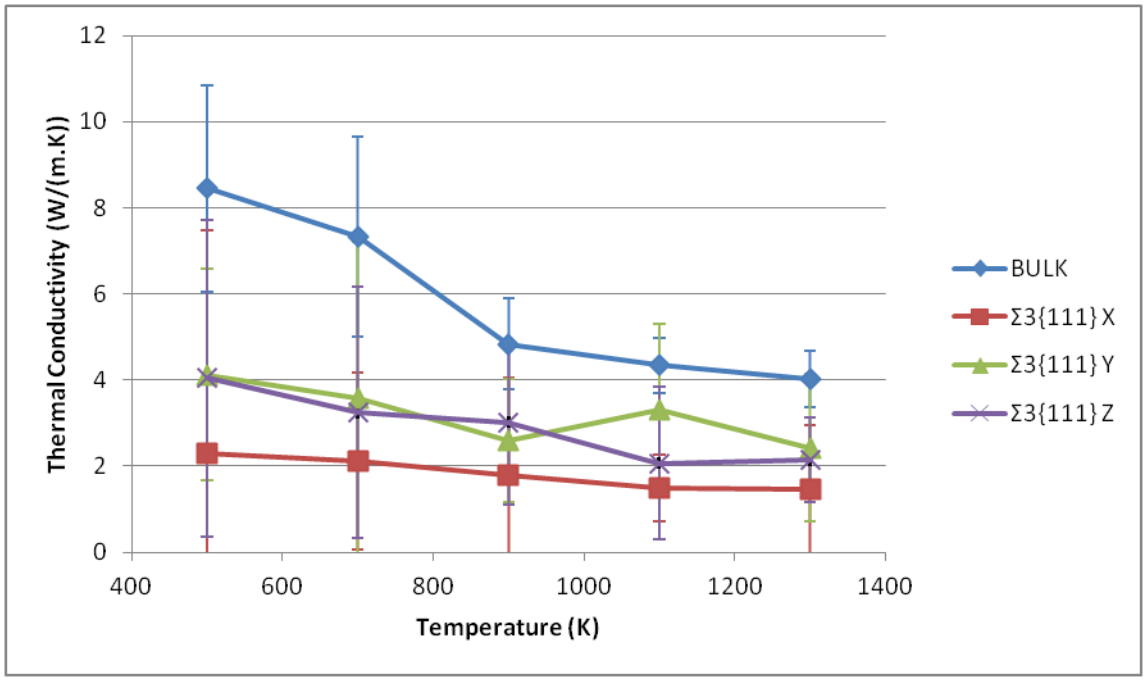

Figure 6.12 Directional thermal conductivity of the interacting Σ3{111} boundary.

The X direction is now lower than the Y and Z directions, a reverse of the behaviour seen in the isolated system. This is the expected behaviour as phonons travelling in the X direction will have a shorter mean free path before interacting with the boundary than phonons with a significant Y or Z component.

Thus, the origin of the increased X direction thermal conductivity in the isolated boundary system is still unclear, though it may stem from boundary-boundary interactions. Analysis of the Green-Kubo spectra for both the isolated and interacting system may give some idea as to how this effect arose.

6.3.1.2. Spectra of the Σ3{111} Boundary

The Green-Kubo spectra for the isolated Σ3{111} boundary at multiple temperatures are presented in Figure 6.13 and Figure 6.14.

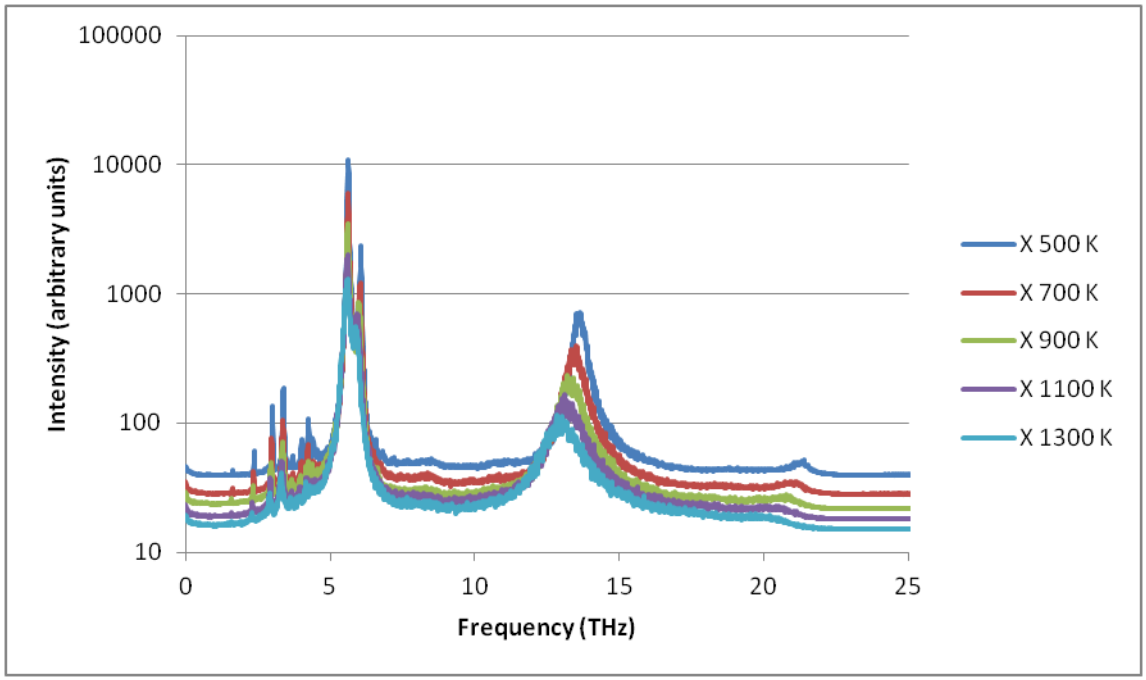

Figure 6.13 Green-Kubo spectra of the isolated Σ3{111} boundary in the X direction, Log_{10} scale.

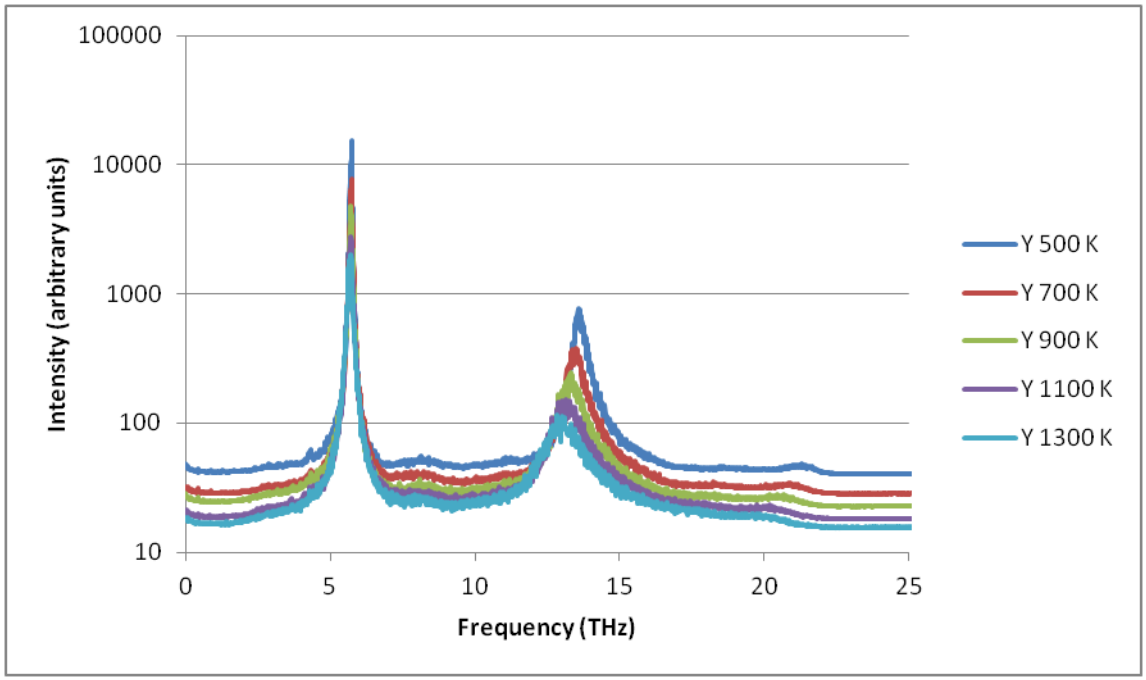

Figure 6.14 Green-Kubo spectra of the isolated Σ3{111} boundary in the Y direction, Log_{10} scale.

The Y and Z direction spectra are identical and so only the Y direction is presented. The Y/Z directions show almost no difference to the bulk spectra, whereas the X direction shows a new set of peaks at frequencies below 5 THz as well as a splitting of the peak at

~6 THz. It can be theorised that these changes are related to new vibrational modes introduced by the boundary and may be related to strontium based vibrations (as the new vibrational modes are in the region of the strontium peak) or to the vibration of the two grains with respect to each other in the X direction. A third option is the introduction of vibrational modes which are RUMs and hence low frequency.

The only possible source of the increased thermal conductivity may come from the slight splitting of the main strontium peak (5 THz), with the satellite at slightly higher frequency. The splitting and slightly shift to higher frequency means that the new peak will interact with fewer acoustic modes due to the Bose-Einstein distribution, leading to a larger thermal conductivity.

Further analysis of this system by lattice dynamics calculations is hampered by the large simulation cell. However, modes appearing in both the isolated Green-Kubo spectra and the interacting Green-Kubo spectra are likely to originate from the new boundary environments and so information about the new peaks in the X direction of the isolated system may still be obtainable from the spectra of the interacting system.

The Green-Kubo spectra for the interacting Σ3{111} boundary at multiple temperatures are presented in Figure 6.15 and Figure 6.16.

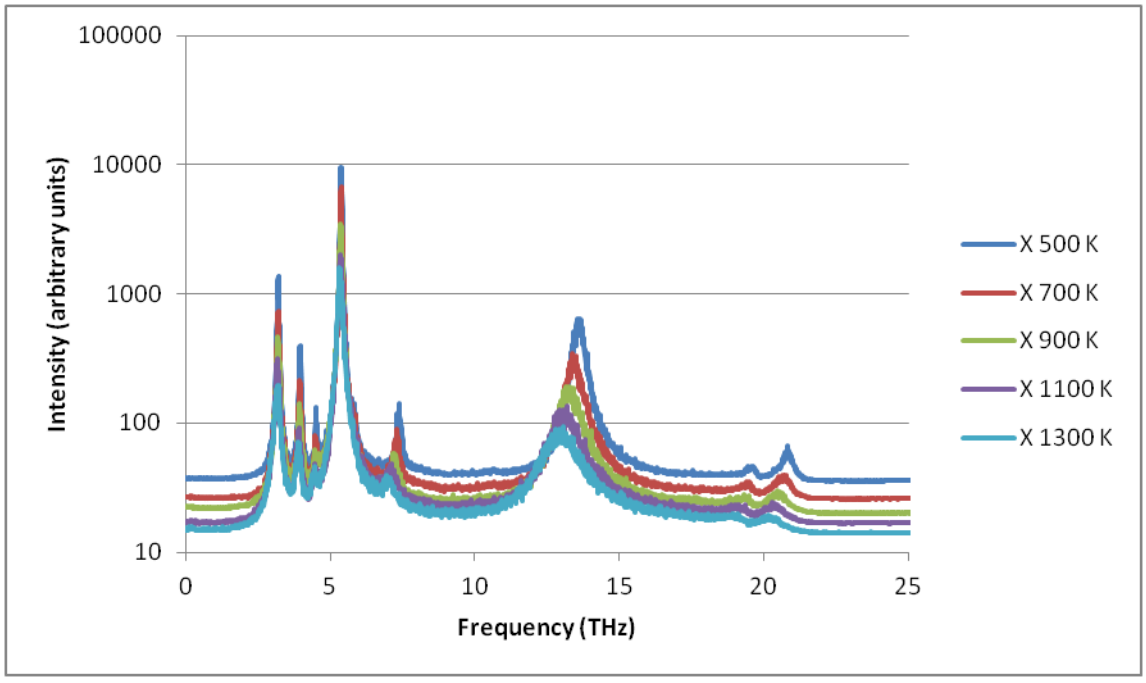

Figure 6.15 Green-Kubo spectra of the interacting Σ3{111} boundary in the X direction, Log_{10} scale.

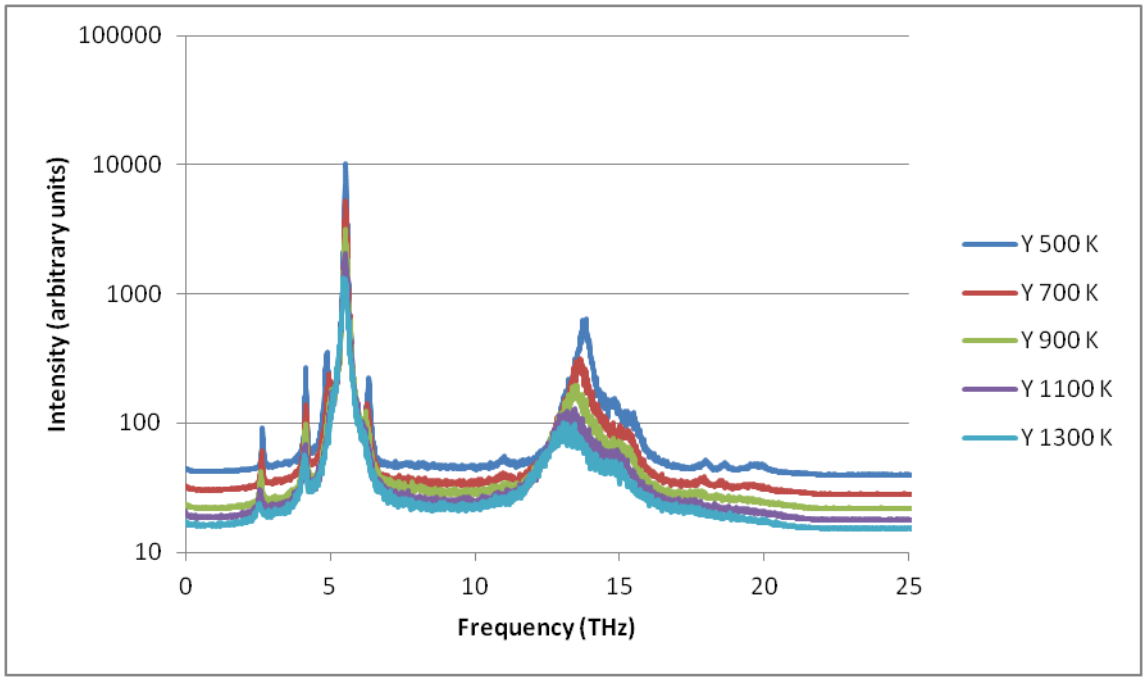

Figure 6.16 Green-Kubo spectra of the interacting Σ3{111} boundary in the Y direction, Log_{10} scale.

Once again the Y and Z directions are identical and so only the Y direction is displayed. The Green-Kubo spectra of the interacting Σ3{111} grain boundary have many more vibrational modes than the isolated version in all directions. Most of the new modes appear around the strontium peak (~6 THz). The strongest new vibrational modes appear perpendicular to the grain boundary in the X direction around the strontium peak. A couple of small intensity peaks appear in the oxygen region (~20 THz) of the X direction as well. An additional feature of the Y/Z direction is a significant broadening of the peak in the titanium region (~14 THz).

There do not appear to be many matching peaks compared to the isolated system. The discrepancy is probably due to the peaks being shifted in the interacting system because of boundary-boundary interactions.

The interacting system has a small enough unit cell that the phonon DOS can be calculated directly by lattice dynamics. The orthorhombic cell used contained 120 atoms with lattice vectors a=27.20 Å, b=5.52 Å and c=9.56 Å. By treating the phonon DOS in the same way as previously, the exact origins of the new peaks may be made clear. The same process has been used as previously to remove symmetric modes and split the

spectra into dimensional components. Once again broadening of the Gaussian peaks is arbitrary and is meant to serve only as a guide to the eye.

The phonon DOS for the interacting Σ3{111} boundary are presented in Figure 6.17 and Figure 6.18.

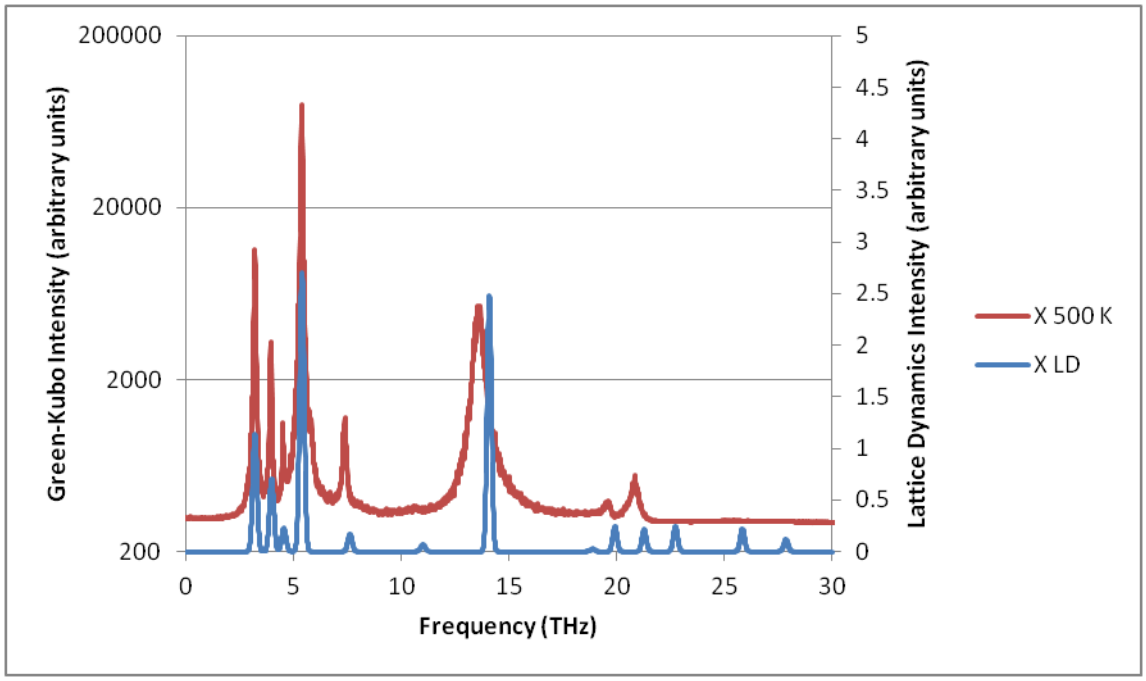

Figure 6.17 Lattice dynamics phonon DOS and 500 K Green-Kubo spectra of the interacting Σ3{111} boundary, X direction. Log_{10} scale on Green-Kubo intensity.

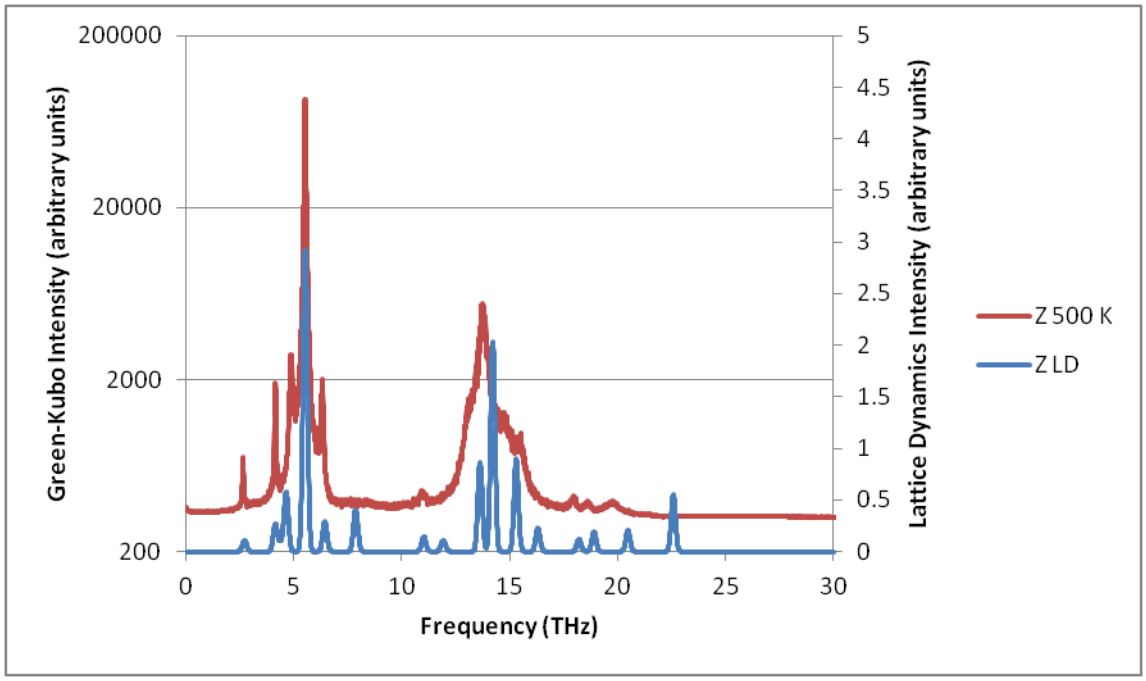

Figure 6.18 Lattice dynamics phonon DOS and 500 K Green-Kubo spectra of the interacting Σ3{111} boundary, Y direction. Log_{10} scale on Green-Kubo intensity.

As expected, the Y and Z directions are identical and so only the Y direction is presented. The number and position of peaks found by the lattice dynamics calculations matches almost exactly with those found in the Green-Kubo spectra. A few additional peaks appear in the phonon DOS calculation, but it may be a case of these peaks having very low intensity in the Green-Kubo spectra. Many of the additional peaks appear at very high frequencies where the population of acoustic phonons is negligible and thus do not interact significantly with the heat-flux of the system.

Several of the low frequency modes have some RUM character, but due to the boundary plane not all Ti-O octahedra are capable of the rigid unit motion. Furthermore, the modes cannot be conclusively related to the modes in the isolated system.

A secondary feature to note is that in the region of the titanium peak (~14 THz), there are relatively few modes whereas in the Green-Kubo spectra the peaks is quite broad. This suggests that there are many titanium based modes with slight asymmetry, which are not being detected by the lattice dynamics analysis using the chosen cutoff value.

The X direction of the interacting Σ3{111} boundary contains few enough modes to manually visualise the eigenvectors and assign the relative motion of each mode present. The 500 K X direction Green-Kubo spectrum of the interacting Σ3{111}

boundary is displayed again in Figure 6.19. The calculated lattice dynamics phonon DOS frequencies and a description of each mode are presented in Table 6.3. A diagram of the different strontium environments in the Σ3{111} boundary are presented in Figure 6.20.

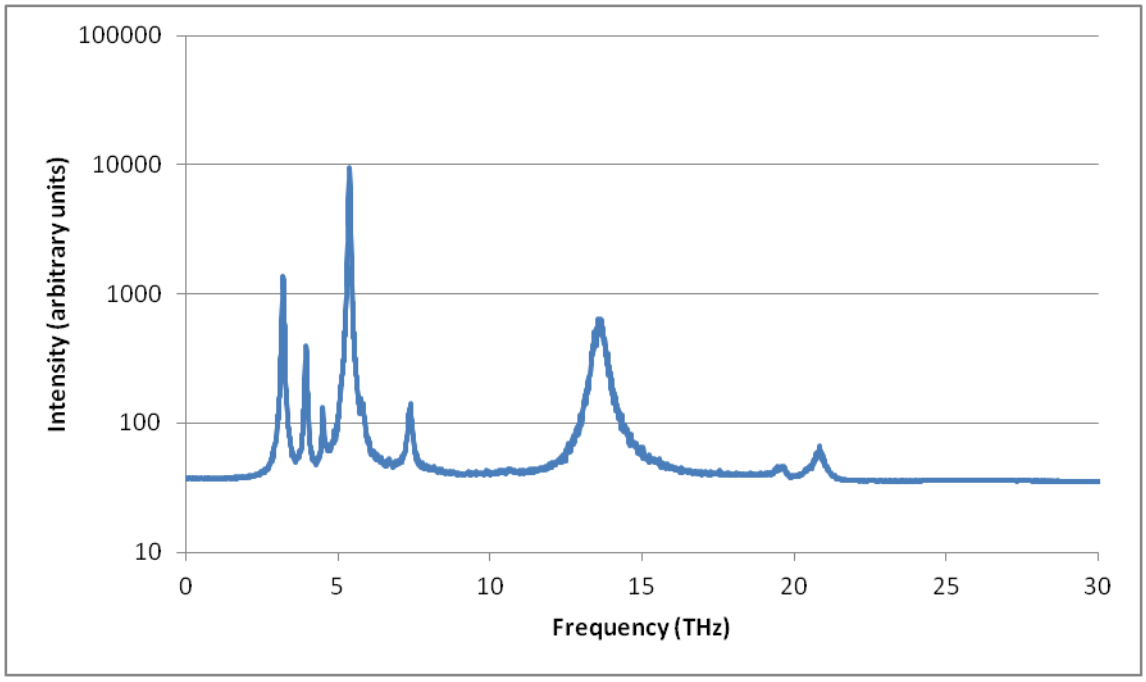

Figure 6.19 500 K Green-Kubo spectrum of the interacting Σ3{111} boundary in the X direction, Log_{10} scale.

Frequency (THz)	**Motion**
3.21	Outer-Boundary Sr rattling
3.99	Core-Boundary Sr rattling
4.55	Bulk-Only Sr rattling
5.39	All Sr rattling
7.62	Bulk-Ti and Boundary-Ti split mode
14.09	All Ti rattling
19.92	Alternating-Layers O rattling perpendicular to boundary
21.28	All O rattling

Table 6.3 Assigned modes of the interacting Σ3{111} boundary.

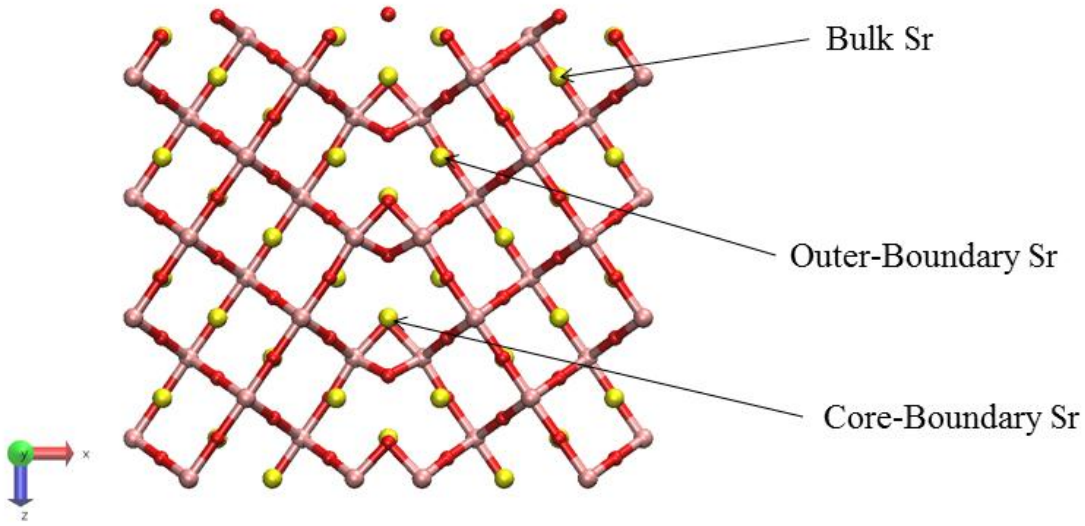

Figure 6.20 Strontium environments in the Σ3{111} STO boundary.

The assigned modes prove conclusively that the additional low frequency peaks are indeed due to strontium motion. In particular, the modes stem from the subtly different strontium environments present at the grain boundary.

At ~4.0 THz the strontium atoms present at the core of the boundary are rattling, at ~3.2 THz the strontium atoms either side of the core of the boundary are rattling and at ~4.6 THz only the bulk strontium atoms are rattling while all the boundary strontium atoms remain fixed. The mode at ~5.4 THz is the usual strontium mode of bulk STO where all strontium atoms in the system are vibrating, the shift in frequency is attributed to the increased number of strontium atoms in a different environment to bulk.

The mode present at ~7.6 THz is related to titanium motion rather than strontium motion and is due to the bulk titanium and boundary titanium rattling in opposite directions.

The final additional mode at ~19.9 THz is an additional oxygen mode where alternating layers of oxygen atoms rattle in opposite directions. The asymmetry here is thus dependent on the number of bulk layers between boundaries and so this mode may not be significant at different inter-boundary distances.

6.3.2. The Σ3{112} Boundary

The Σ3{112} grain boundary structure system again has the grain boundary perpendicular to the X direction. The boundary itself contains Ti-O bridges across the

boundary and little else. The environments adjacent to the boundary contain square-based pyramidal Ti-O groups and 8-fold coordinate strontium at the boundary. Due to the relatively empty grain boundary structure there are a small series of pipes running through the boundary in the Y direction which are expected to have an effect on the thermal conductivity.

6.3.2.1. Thermal Conductivity of the Σ3{112} Boundary

The isolated Σ3{112} boundary system is orthorhombic and approximately 193 Å x 22 Å x 20 Å and contains 7,200 atoms. The grain boundaries have a formation energy of 1.52 J/m^2 which is higher than either of the Σ3{111} boundary systems. The excess length of the isolated Σ3{112} boundary was also higher than the previous Σ3{111} boundary systems at 0.544 Å instead of ~0.27 Å.

The thermal conductivity of the isolated Σ3{112} boundary was calculated in the usual way. The average thermal conductivity compared to bulk is displayed in Figure 6.21.

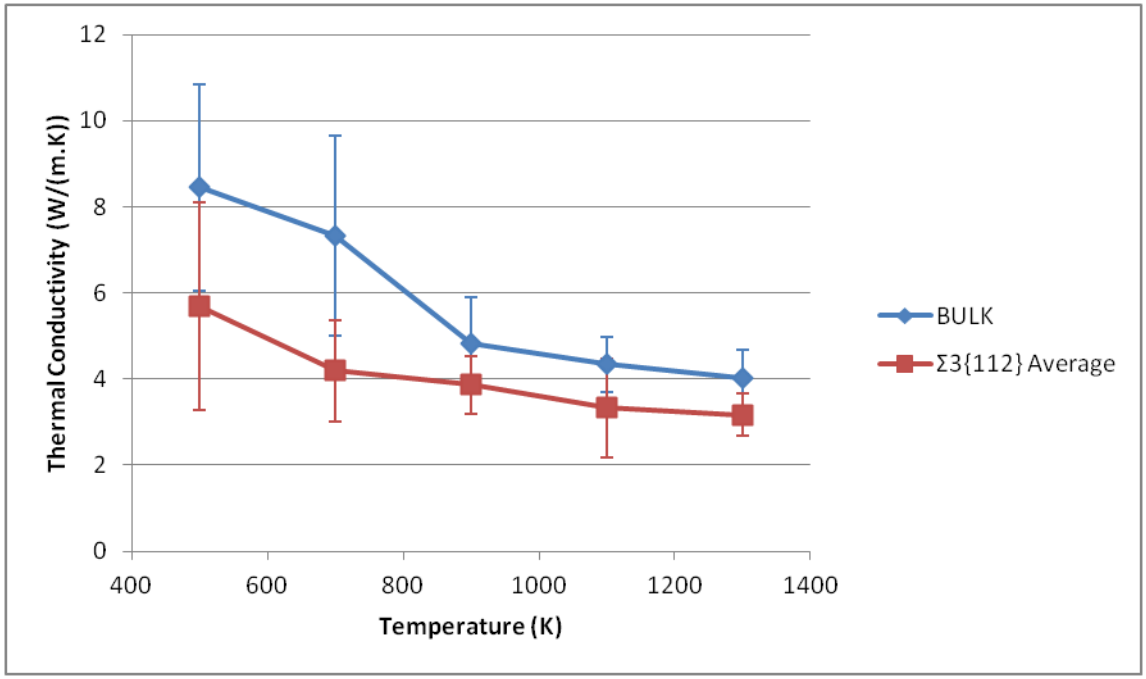

Figure 6.21 Average thermal conductivity of the isolated Σ3{112} boundary.

The thermal conductivity of the isolated Σ3{112} boundary system is lower than that of bulk across all temperatures. This is a change from the behaviour of the isolated Σ3{111} boundary system where the thermal conductivities converged to a similar value at high temperatures.

The X direction is again perpendicular to the grain boundary while the Y and Z directions are parallel. As the Σ3{112} boundary system is distinct in the Y and Z directions, the thermal conductivities are now expected to be different. The directional components to the thermal conductivity are presented in Figure 6.22.

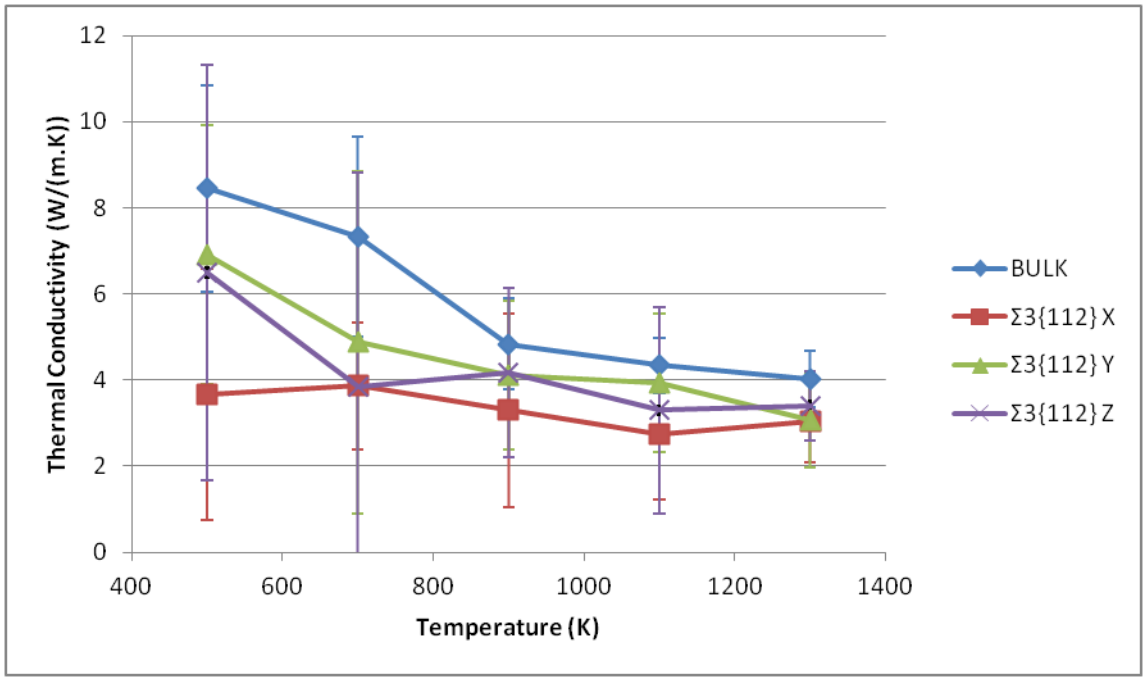

Figure 6.22 Directional thermal conductivity of the isolated Σ3{112} boundary.

The thermal conductivity of the isolated Σ3{112} boundary is lower than that of the bulk value in all directions. Additionally, the temperature dependence through the boundary (X direction) is greatly reduced and shows almost no dependence on temperature, indicating increased defect scattering and thus decreased phonon-phonon scattering.

The fluctuations in the autocorrelations appear much smaller for the isolated Σ3{112} boundary than for the isolated Σ3{111} boundary, indicating less long-lived optical component to the autocorrelation. This may be confirmed later by examining the Green-Kubo spectra.

The interacting Σ3{112} boundary system is again orthorhombic and approximately 39 Å x 22 Å x 20 Å and contains 1,440 atoms. The formation energy is 1.50 J/m^2, which is slightly lower than the isolated system at 1.52 J/m^2, a trend which was also observed for the Σ3{111} boundary systems. Likewise, the excess length has increased (as seen previously) to 0.551 Å from 0.544 Å.

The results for the average thermal conductivity of the interacting Σ3{112} boundary conductivity are displayed in Figure 6.23.

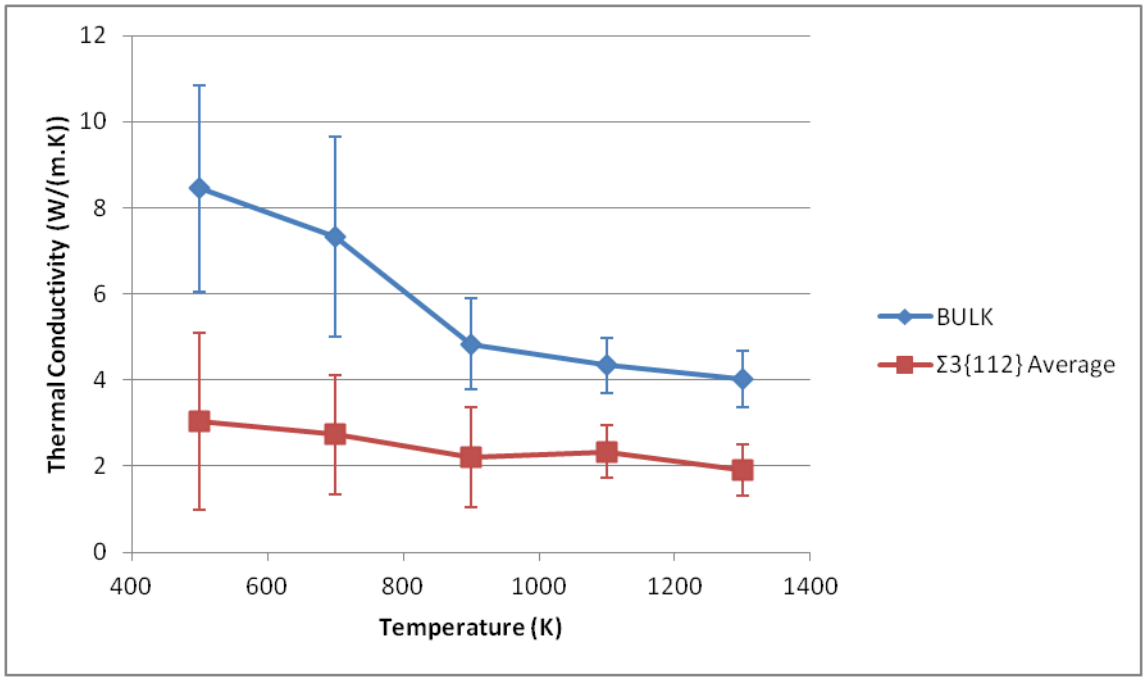

Figure 6.23 Average thermal conductivity of the interacting Σ3{112} boundary.

Figure 6.23 shows thermal conductivity values very similar to the Σ3{111} interacting boundary. All values are again around ~2.5 W/(m.K) and show only slight temperature dependence. The directional contributions are presented in Figure 6.24.

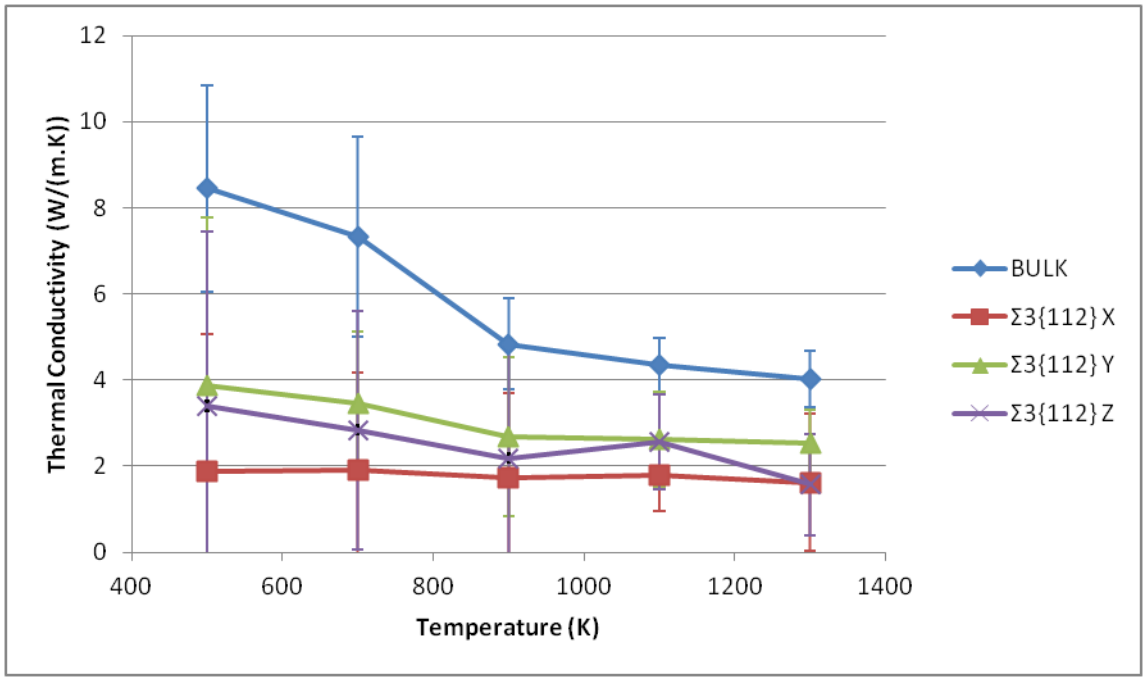

Figure 6.24 Directional thermal conductivity of the interacting Σ3{112} boundary.

The thermal conductivity of all three directions appear very similar, although the X direction has a slightly lower value. The X direction also displays no temperature dependence at all while the Y and Z directions have only slight temperature dependence.

6.3.2.2. Spectra of the Σ3{112} Boundary

The Green-Kubo spectra for all temperatures have been calculated and show the usual variation with temperature (i.e. flattening, broadening and shift to lower frequencies for the titanium related peaks). For clarity, only the lowest temperature Green-Kubo spectrum will be presented from now on. The lattice dynamics phonon DOS spectra have also been calculated for the smaller interacting systems and will be presented where available.

The spectra for the isolated Σ3{112} boundary are displayed in Figure 6.25.

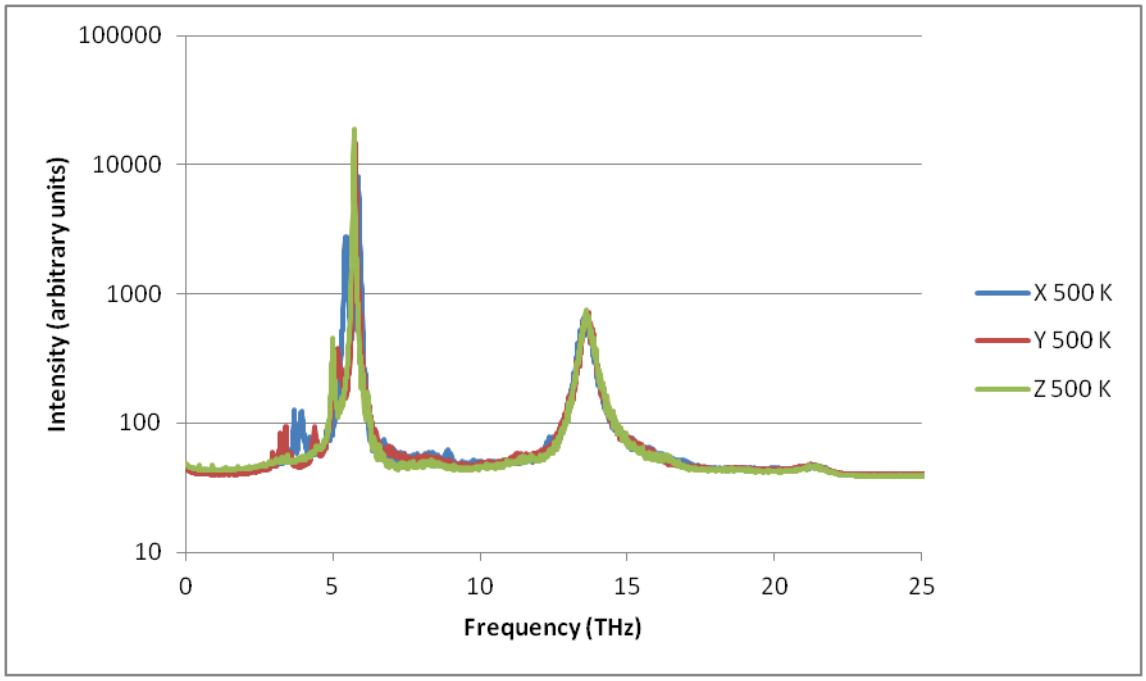

Figure 6.25 Green-Kubo spectra at 500 K of the isolated Σ3{112} boundary, Log_{10} scale.

All three directions display splitting of peaks and/or additional peaks. The peaks are also wider in these spectra than in the isolated Σ3{111} boundary, meaning that the lifetimes are shorter and leading to the smaller fluctuations seen when integrating the autocorrelation to obtain the thermal conductivity.

The additional peaks in Y and Z seem to be split from the strontium bulk peak. As these new peaks must arise from the introduction of the boundary, they are having a disproportionately large effect for such a small fraction of the number of strontium environments.

As the spectra for the isolated Σ3{112} boundary is more complex than the isolated Σ3{111} boundary, the spectra for the interacting Σ3{112} boundary is expected to be particularly complex. Again, the interacting Σ3{112} boundary contains 120 atoms with an orthorhombic cell with lattice vectors a=39.10 Å, b=5.46 Å and c=6.78 Å. This system is small enough to have its lattice dynamics phonon DOS calculated and is displayed alongside the Green-Kubo spectra in Figure 6.26, Figure 6.27 and Figure 6.28.

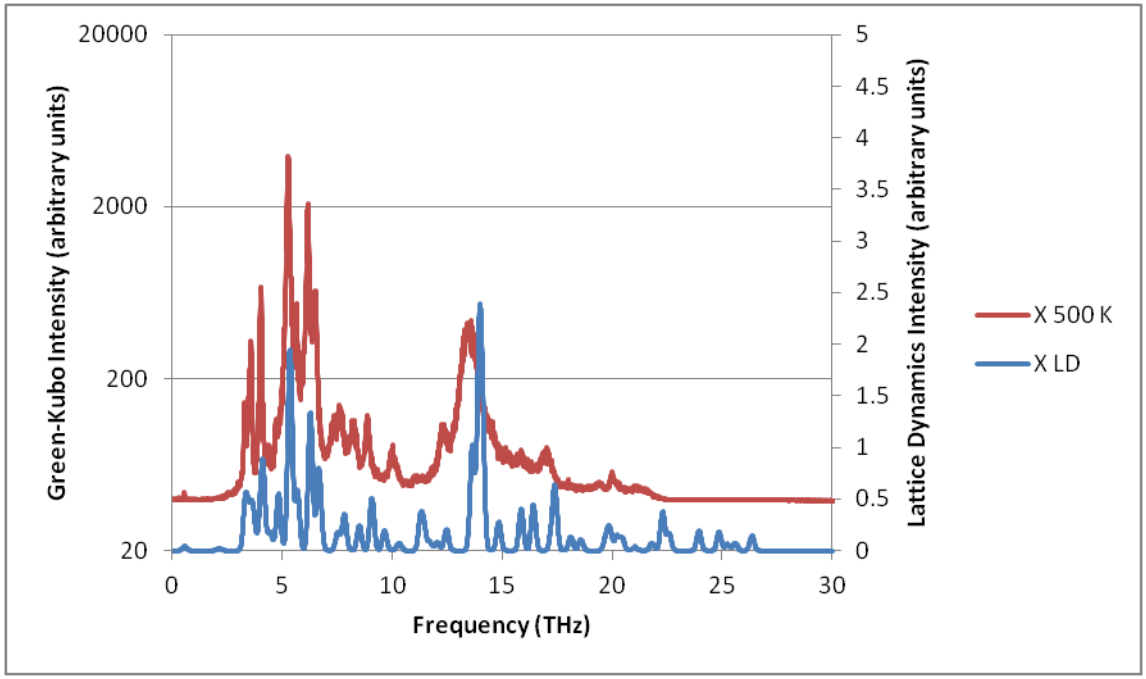

Figure 6.26 Lattice dynamics phonon DOS and 500 K Green-Kubo spectra of the interacting Σ3{112} boundary, X direction. Log_{10} scale on Green-Kubo intensity.

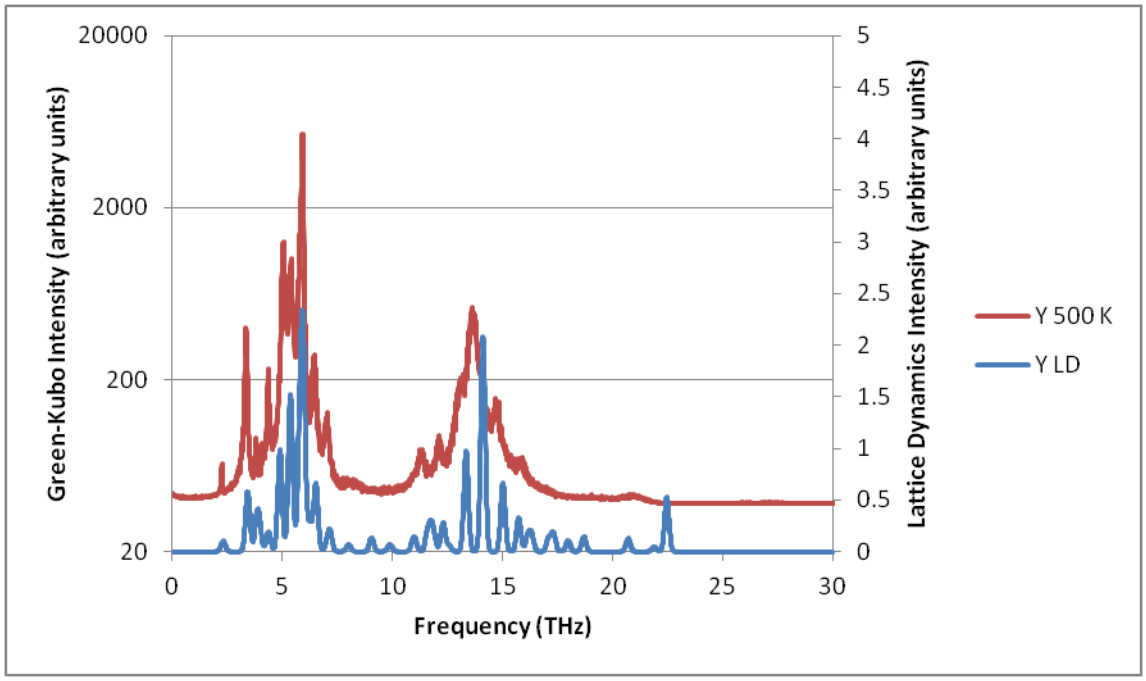

Figure 6.27 Lattice dynamics phonon DOS and 500 K Green-Kubo spectra of the interacting Σ3{112} boundary, Y direction. Log_{10} scale on Green-Kubo intensity.

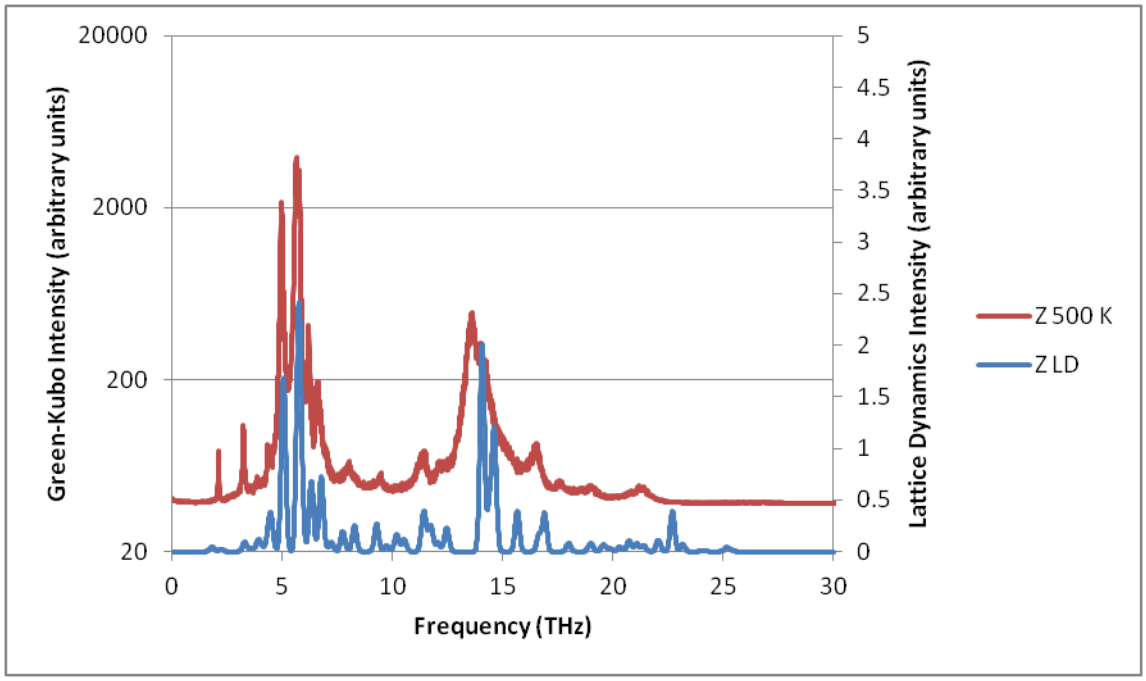

Figure 6.28 Lattice dynamics phonon DOS and 500 K Green-Kubo spectra of the interacting Σ3{112} boundary, Z direction. Log_{10} scale on Green-Kubo intensity.

All three spectra show a large number of additional vibrational modes introduced by the boundary. A number of vibrational modes have appeared in the regions between the

strontium peak (~6 THz) and the titanium peak (~14 THz) which are of uncertain character.

The Σ3{112} boundary phonon DOS calculation also matches well with the Green-Kubo calculation. Many additional modes are seen in the region between the strontium peak (~6 THz) and the titanium peak (~14 THz), as was observed in the Green-Kubo spectra.

A few low frequency modes appear to be missing from the phonon DOS calculation in the Z direction. Their absence is attributed to having a sum of non-mass-weighted eigenvectors below the cutoff used; their relatively large height in the Green-Kubo spectra being due to low frequency and relatively high probability of interacting with an acoustic phonon.

6.3.3. The Σ5{310} Boundary

The structure of the Σ5{310} grain boundary has the boundary perpendicular to the X direction and has many different environments at the boundary, which is further complicated by dynamical disorder. In the Y direction, there are several large pipes, which accommodate strontium atoms. However, the pipes may accommodate the strontium atoms in one of two positions and the strontium atom can be seen to transition between these positions at high temperature in molecular dynamics.

6.3.3.1. Thermal Conductivity of the Σ5{310} Boundary

The isolated Σ5{310} grain boundary system is approximately 199 Å x 20 Å x 37 Å and contains 12,000 atoms. The formation energy is 2.00 J/m^2, which is the highest of any of the studied grain boundaries. Additionally, the excess length caused by the boundary is 0.754 Å, again larger than the values observed for previous boundaries.

The thermal conductivity of the isolated Σ5{310} boundary was calculated in the same way as the Σ3{111} and Σ3{112} boundaries. The results for the average thermal conductivity compared to bulk are displayed in Figure 6.29.

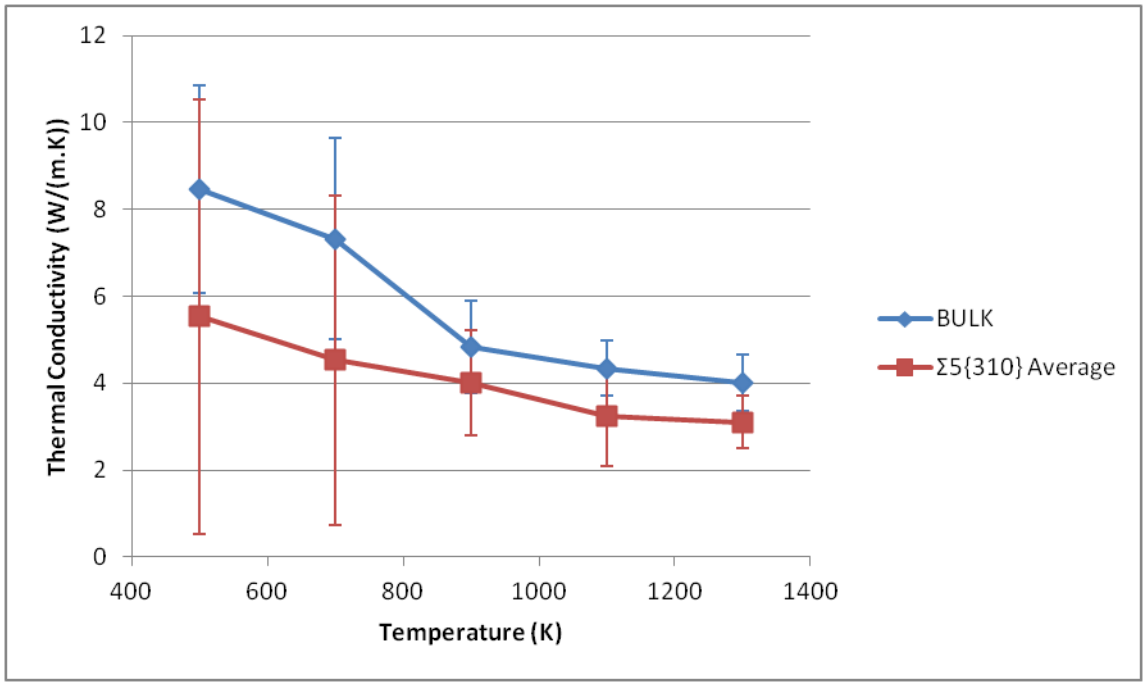

Figure 6.29 Average thermal conductivity of the isolated Σ5{310} boundary.

The thermal conductivity of the isolated Σ5{310} boundary shows temperature dependence and has a remarkably similar thermal conductivity values to the isolated Σ3{112} system, indicating a possible minimum thermal conductivity for these isolated systems (~100 Å).

The Σ5{310} boundary is once again perpendicular to the X direction. The pipes in the Y direction are expected to have a large effect on the thermal conductivity due to the disorder within them. The directional thermal conductivities of the isolated Σ5{310} boundary system are presented in Figure 6.30.

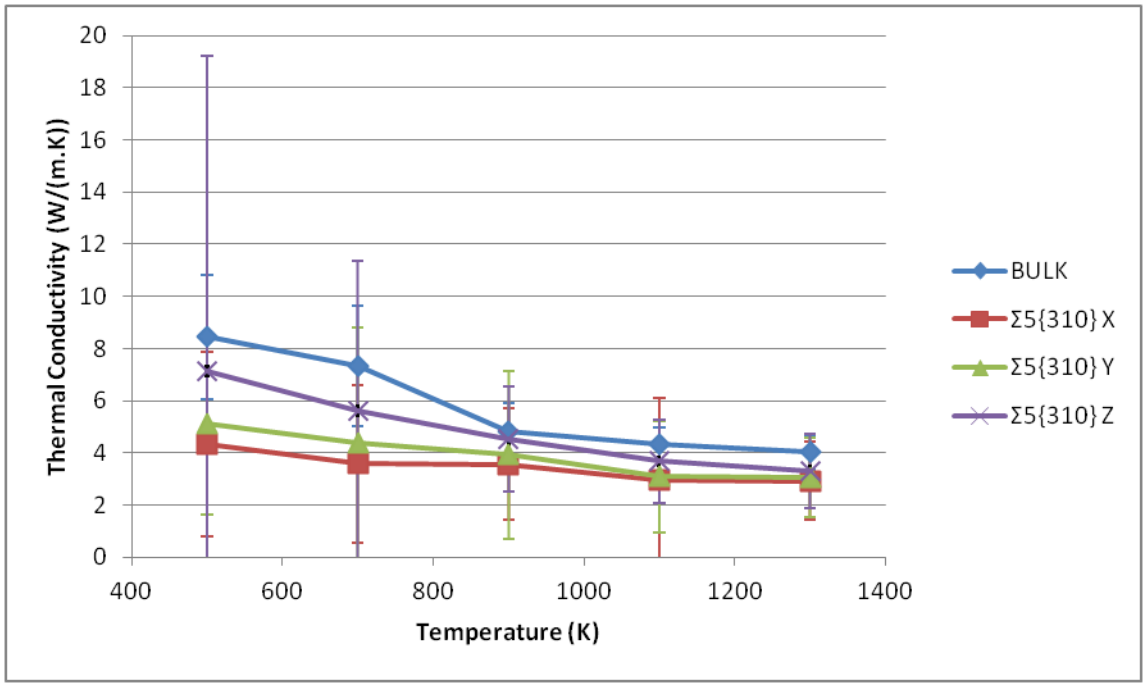

Figure 6.30 Directional thermal conductivity of the isolated Σ5{310} boundary.

Figure 6.30 shows the thermal conductivity for the Σ5{310} boundary. The Σ5{310} boundary has the lowest thermal conductivity in the X direction as was seen for the Σ3{112} boundary. The trend of thermal conductivity across temperature is more gradual than the Σ3{112} boundary and indicates strong phonon-phonon scattering is still important. Extremely large fluctuations are seen in the Z direction, which likely stem from the strontium disorder in the boundary pipes.

The interacting Σ5{310} grain boundary is orthorhombic and approximately 26 Å x 19 Å x 37 Å and contains 1,500 atoms. The formation energy is 2.00 J/m^2, which is the same as the isolated boundary, indicating that this boundary system is not especially stabilised by being in proximity to another boundary. However, the excess length still conforms to the usual trend and has increased in length to 0.765 Å (from 0.754 Å in the isolated case).

The thermal conductivity of the interacting Σ5{310} boundary has also been calculated. The results for the average thermal conductivity are displayed in Figure 6.31.

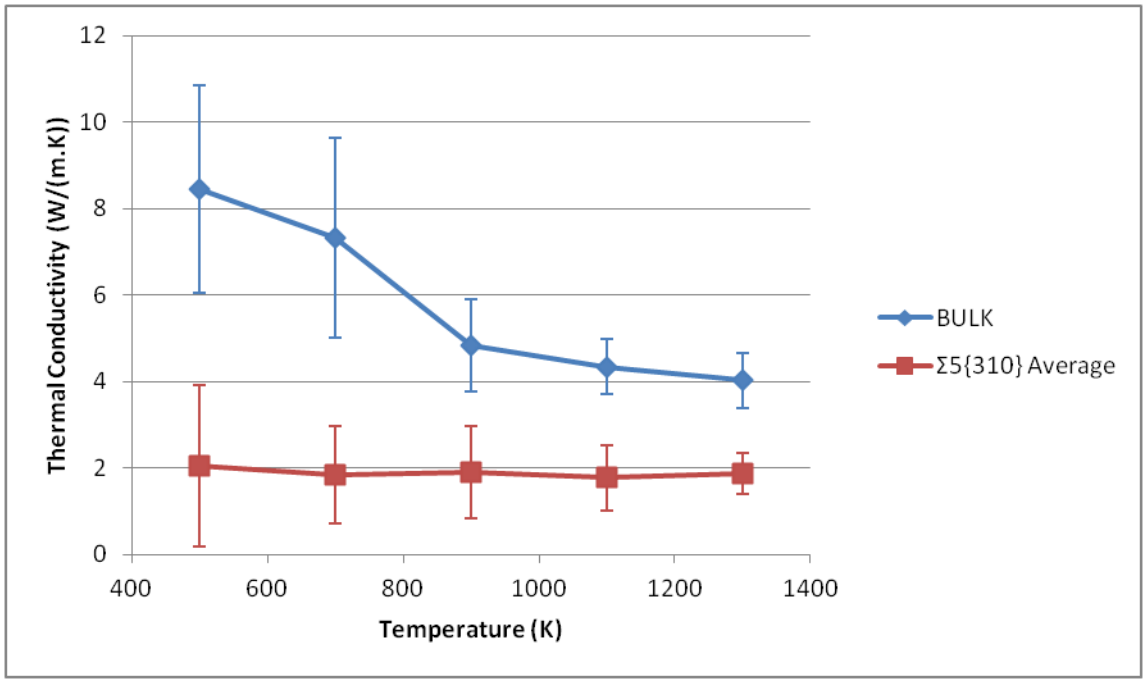

Figure 6.31 Average thermal conductivity of the interacting Σ5{310} boundary.

Figure 6.31 shows the thermal conductivity of the interacting Σ5{310} boundary. The behaviour is very similar to the interacting Σ3{111} and interacting Σ3{112} boundaries but the magnitude of the values are lower still. The directional thermal conductivities are presented in Figure 6.32.

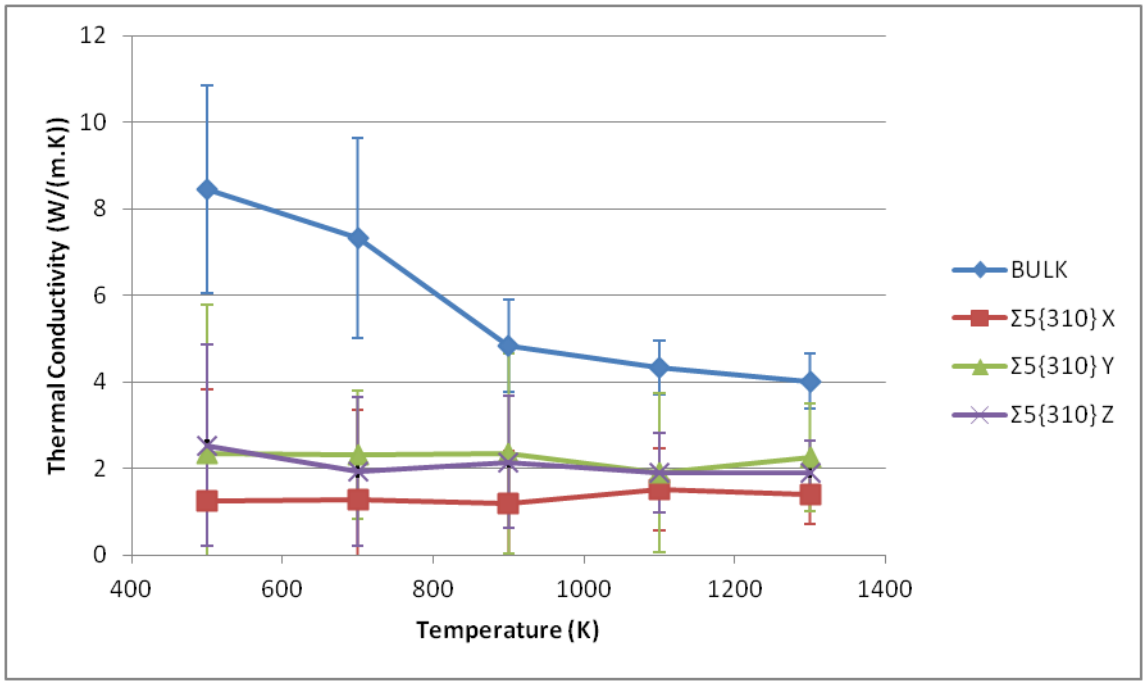

Figure 6.32 Directional thermal conductivity of the interacting Σ5{310} boundary.

The reduction in thermal conductivity likely reflects the low density and relatively large width of the Σ5{310} boundary, resulting in a very small region of bulk between the two boundaries. The thermal conductivity in the X direction is ~1.5 W/(m.K) at all temperatures. Furthermore, the thermal conductivities in the Y and Z directions are now also insensitive to temperature, although their values are very similar at ~2 W/(m.K).

6.3.3.2. Spectra of the Σ5{310} Boundary

The Green-Kubo spectra for the isolated Σ5{310} boundary were calculated by averaging the autocorrelations of the separate runs before applying the Fourier transform. The spectra for the different directions at 500 K are presented in Figure 6.33.

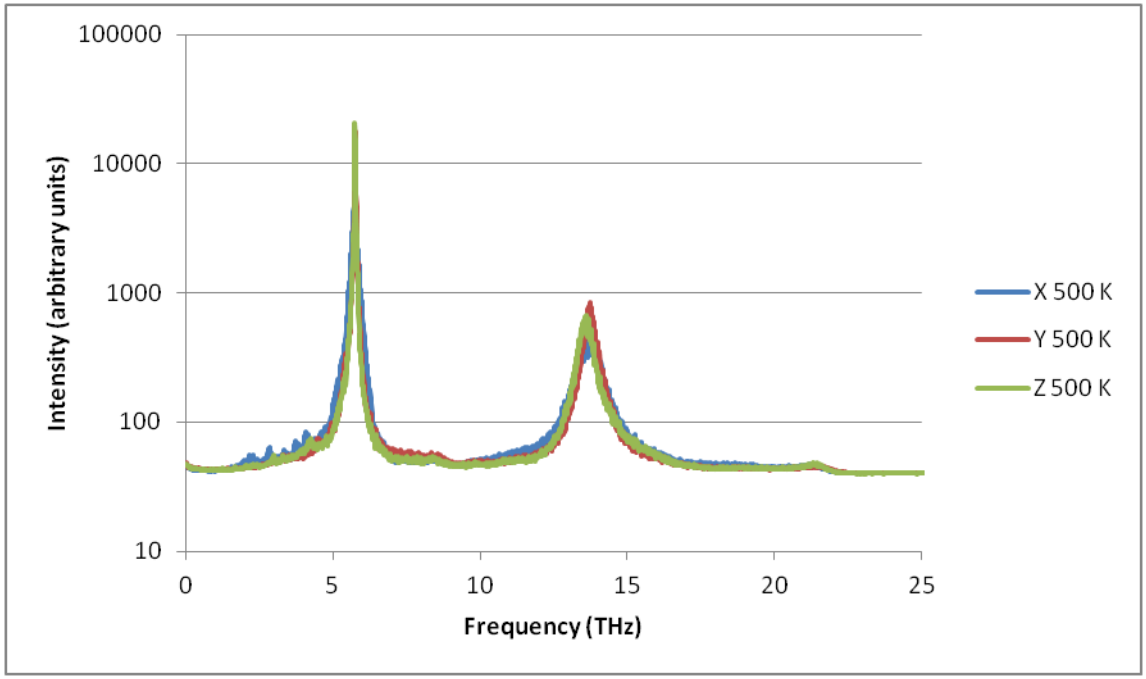

Figure 6.33 Green-Kubo spectra at 500 K of the isolated Σ5{310} boundary, Log_{10} scale.

All three spectra are remarkably similar to the bulk spectra and do not show large additional peaks. Smaller peaks are however visible at lower frequencies in the X direction, indicating some effect from the strontium environments at the grain boundaries.

One further subtle difference is the reduction in height of the ~6 THz strontium peak and the ~14 THz titanium peak in the X direction; a behaviour not seen in the other boundaries. The reduced peak heights likely stem from the low density of the boundary

and in particular the dynamical disorder of strontium atoms, leading to a broader set of strontium vibrations. The reduction of the titanium peak may then be explained as an increase in environments of titanium atoms near the disorder strontium.

The spectra for the interacting Σ5{310} boundary system are expected to have many peaks due to the large number of environments found in the Σ5{310} grain boundary. The cell used for the lattice dynamics of the interacting Σ5{310} boundary system is orthorhombic and contains 100 atoms. The lattice vectors are a=26.15 Å, b=3.86 Å and c=12.34 Å.

The Green-Kubo and lattice dynamics phonon DOS spectra are displayed together in Figure 6.34, Figure 6.35 and Figure 6.36.

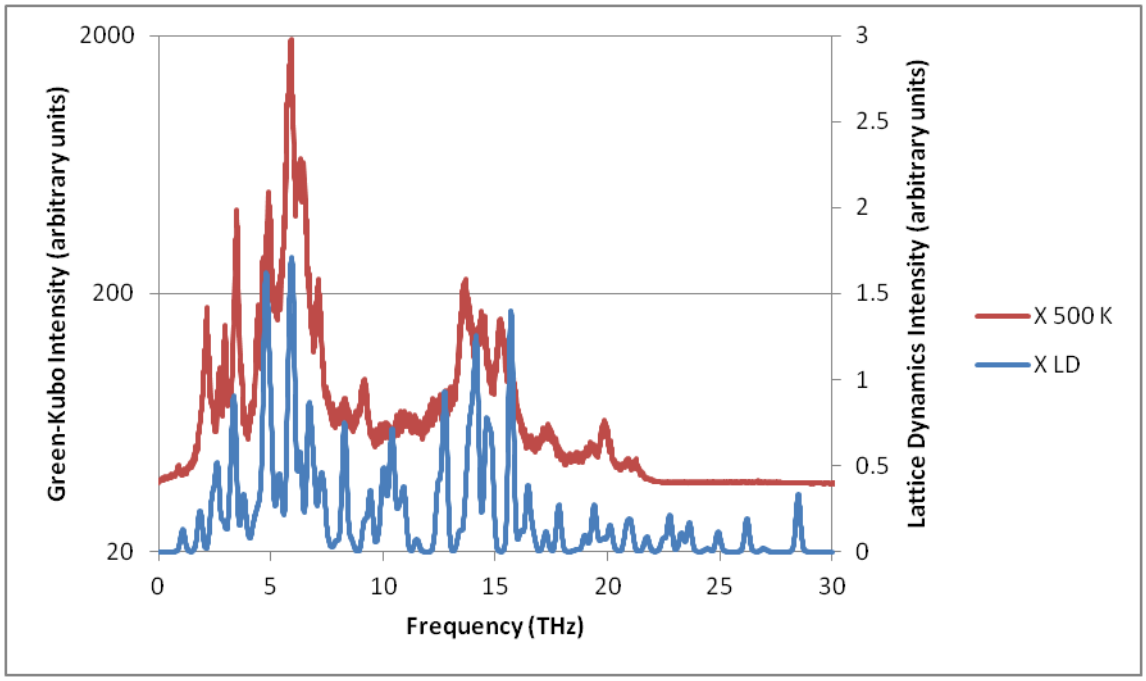

Figure 6.34 Lattice dynamics phonon DOS and 500 K Green-Kubo spectra of the interacting Σ5{310} boundary, X direction. Log_{10} scale on Green-Kubo intensity.

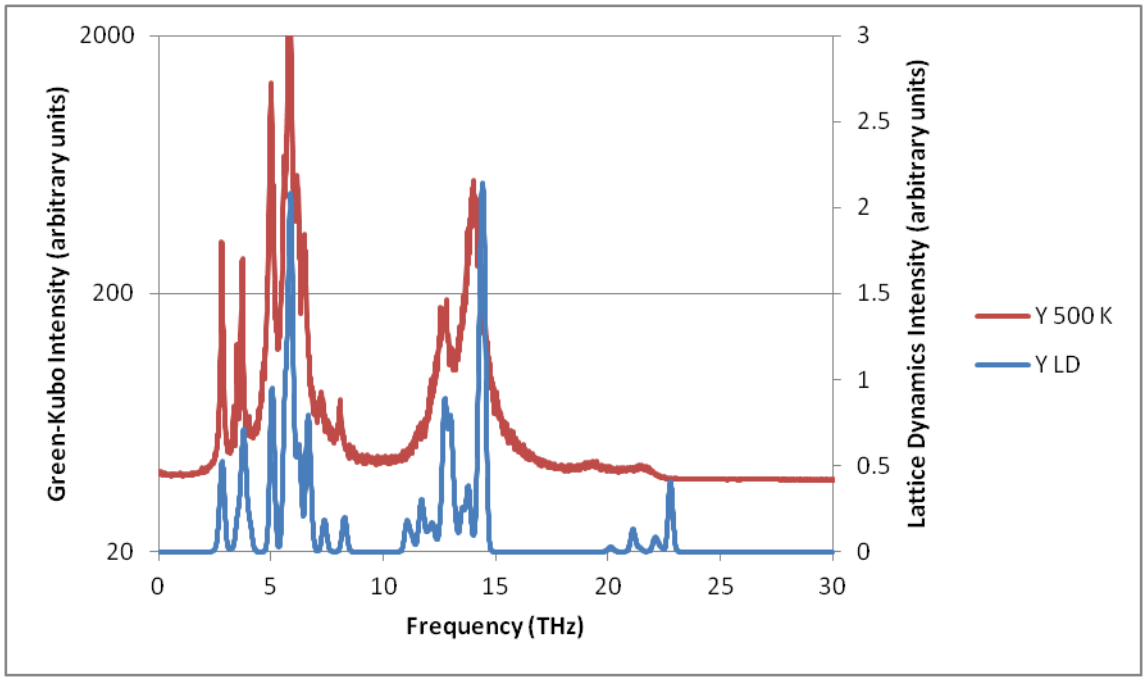

Figure 6.35 Lattice dynamics phonon DOS and 500 K Green-Kubo spectra of the interacting Σ5{310} boundary, Y direction. Log_{10} scale on Green-Kubo intensity.

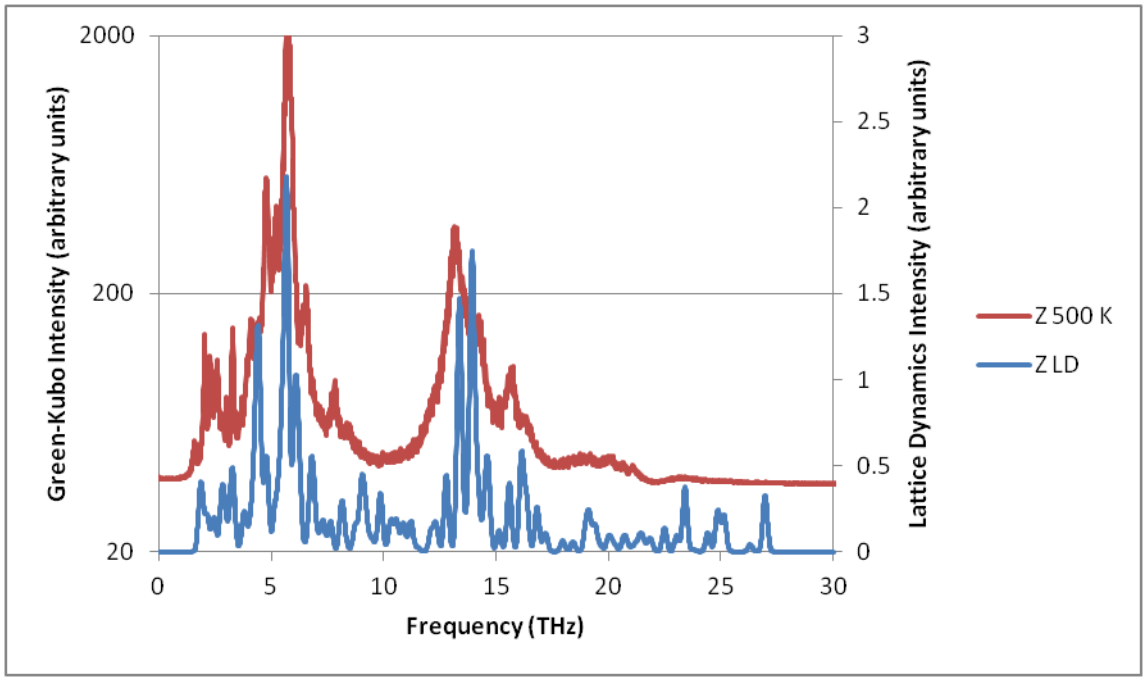

Figure 6.36 Lattice dynamics phonon DOS and 500 K Green-Kubo spectra of the interacting Σ5{310} boundary, Z direction. Log_{10} scale on Green-Kubo intensity.

The interacting Σ5{310} spectra do not show as many distinguishable peaks as expected; there are however very large broadenings on the original peaks and a few additional peaks indicating very short lifetime phonons. Additional peaks appear at low

frequency and are likely strontium based. The large number of modes in this region is a result of the dynamical disorder of strontium at the boundary. The broadening and flattening of the titanium peaks (~14 THz) is likely a result of the large number of titanium environments found at the boundary; in the X direction the intensity of the titanium peak is suppressed to near the level of the boundary peaks.

The phonon DOS for the interacting Σ5{310} boundary was slightly more challenging to calculate than the previous boundaries due to the dynamic disorder of strontium atoms at the boundary. The structure used for these calculations had strontium atoms in differing environments at each boundary, which was found to be the most energetically stable.

The Σ5{310} boundary has a very high number of peaks. Once again there are a few discrepancies between the phonon DOS calculation and the Green-Kubo calculations, but these can be explained by the intensity cutoff used on the phonon DOS, the high frequency of some modes, and the dynamic disorder found in the Σ5{310} boundary.

6.3.4. Isolated and Interacting Grain Boundary Discussion

Three different grain boundary systems have been studied, each having two different inter-boundary distances. The isolated boundary systems contain ~100 Å of bulk between the boundaries and the interacting boundary systems contain ~15-20 Å of bulk between the boundaries. The average thermal conductivities of all 6 systems are presented in Figure 6.37.

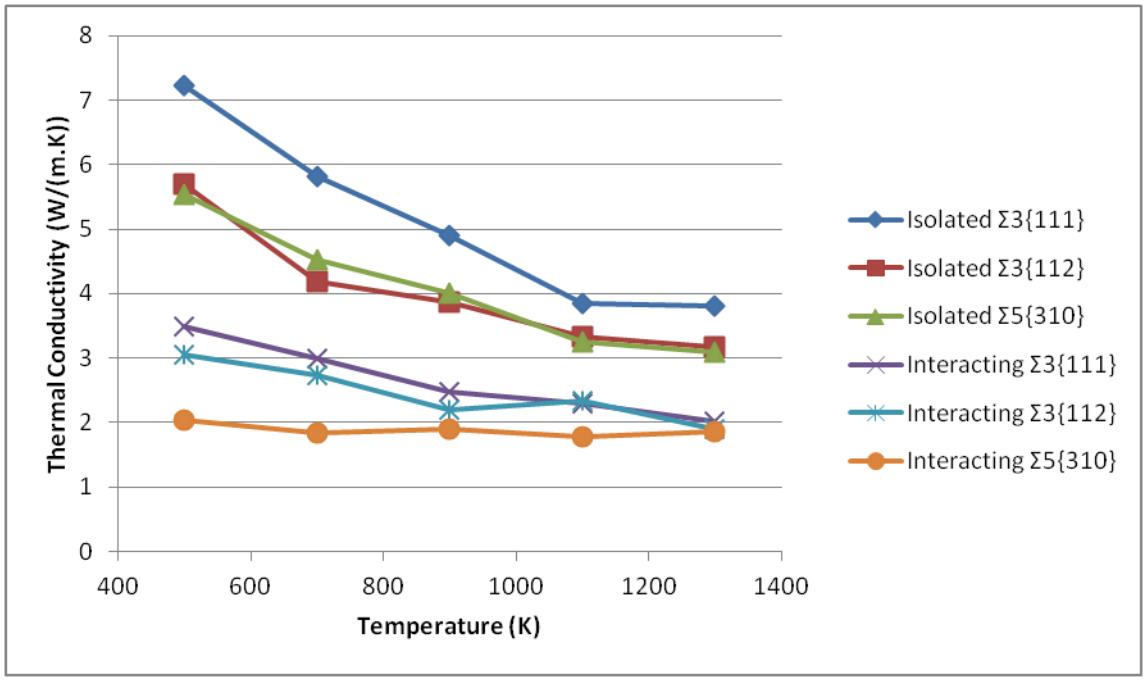

Figure 6.37 Average thermal conductivities for all grain boundary systems (without error bars for clarity).

The isolated grain boundaries do have a small effect on the thermal conductivity despite the large inter-boundary separations. Both the Σ3{112} and Σ5{310} boundaries have the lowest thermal conductivities for the isolated systems at all temperatures and are remarkably similar. The Σ3{111} boundary has a higher average thermal conductivity than the Σ3{112} and Σ5{310} boundaries which may be partially due to the unusual thermal conductivity in the X direction which was increased over the bulk value at nearly all temperatures.

The interacting boundaries have lower thermal conductivity in general than the isolated boundaries (Figure 6.37), which is found experimentally (i.e. smaller grain size) [339-341]. The reasons for this reduction are the greatly reduced amount of bulk material and therefore the relative increase in the number of scattering environments compared to bulk environments. Additionally the smaller bulk region reduces allowed long wavelength phonons, further reducing thermal conductivity.

The thermal conductivities of the STO grain boundaries follow some general trends, as presented in Table 6.4.

Structure	Average Thermal Conductivity at 500 K (W/(m.K))	Formation Energy (J/m^2)	Excess Length (Å)
Isolated Σ3{111}	7.23	0.894	0.265
Isolated Σ3{112}	5.69	1.52	0.544
Isolated Σ5{310}	5.53	2.00	0.754
Interacting Σ3{111}	3.49	0.875	0.270
Interacting Σ3{112}	3.05	1.50	0.551
Interacting Σ5{310}	2.04	2.00	0.765

Table 6.4 Calculated properties of STO grain boundaries.

Table 6.4 shows that the thermal conductivities of the interacting systems are generally lower than those of the isolated systems, stemming from the reduction in allowed wavelength and higher density of scattering centres. All systems show a reduction over the bulk thermal conductivity at 500 K, which was ~8.5 W/(m.K). Table 6.4 also shows that grain boundaries with higher formation energy have a lower thermal conductivity along with a larger excess length (defined as the additional length of the simulation cell due to the boundary structure).

The link between formation energy and thermal conductivity can be understood via the symmetry of the grain boundaries. Grain boundaries with lower symmetry (and thus a higher number of distinct environments) have higher formation energy. The greater variety of environments means a larger number of optical vibrational modes are present at the boundary with which the acoustic phonons may couple and scatter, reducing thermal conductivity. However, the exact frequency of these modes and the probability of scattering acoustic phonons are unknown and so quantitative predictions are challenging.

An additional contribution stems from the inter-boundary distance. At higher temperatures the thermal conductivities at any particular inter-boundary length tend to a single value (with the exception of the isolated Σ3{111} system). The mechanism for

this change is unclear but may be related to increased acoustic-acoustic phonon scattering at higher temperatures.

To obtain a better understanding of the importance of inter-boundary distance future work may concentrate on calculating the thermal conductivities at a wider variety of inter-boundary distances in order to calculate the interfacial thermal resistance (also known as Kapitza resistance) [331, 342, 343]. This approach allows derivation of the Kaptiza length, which is the amount of bulk a boundary represents in terms of thermal resistance. Such calculations require many more simulations of varying inter-boundary distance and are currently prohibitively expensive.

The systems studied so far have contained infinite bulk in the Y and Z directions, yet still have reduced thermal conductivity in those directions due to a grain boundary lying parallel. Systems where the bulk region is entirely contained may show exceptional reduction in thermal conductivity as compared to the bulk as long wavelength phonons are severely disrupted in all directions. The thermal conductivity measured here is likely nearing the limit of thermal conductivity reduction possible using a single type of defect.

In the next section (Chapter 6.4) several different STO nanocube systems are studied to determine whether different stacking orders have any effect on the thermal conductivity of the system.

6.4. STO Nanocubes

Assembled nanocube systems of STO are a promising thermoelectric material [316] due to the high density of interfaces. Each nanocube expresses the {001} surfaces but the surfaces may express different stoichiometries and may be further altered by appropriate doping. Indeed, although beyond the scope of this work, the work by Dang et al. suggested that doping with La would enhance the properties [318]. One of the proposed benefits is that if assembled together the boundaries between cubes may improve the electrical properties via formation of 2DEG [321] systems or energy filtering [95]. Simultaneously, the thermal transport via phonons is inhibited via increased scattering and confinement in sufficiently small systems. Therefore assembled nanocubes may make an excellent thermoelectric material if the size, composition and arrangement of nanocubes can be properly engineered [316].

6.4.1. Surface Termination

To study the effect the different surface terminations have on the thermal conductivity two different systems have been constructed. Both systems contain terminations on the {001} set of Miller planes, both have sides of ~70 Å but differ in that they terminate either in Sr-O or O-Ti-O; these are referred to as SrO rich and TiO_2 rich respectively. The cubes are then assembled in a simple geometry. A 3 x 3 x 3 example is displayed in Figure 6.38.

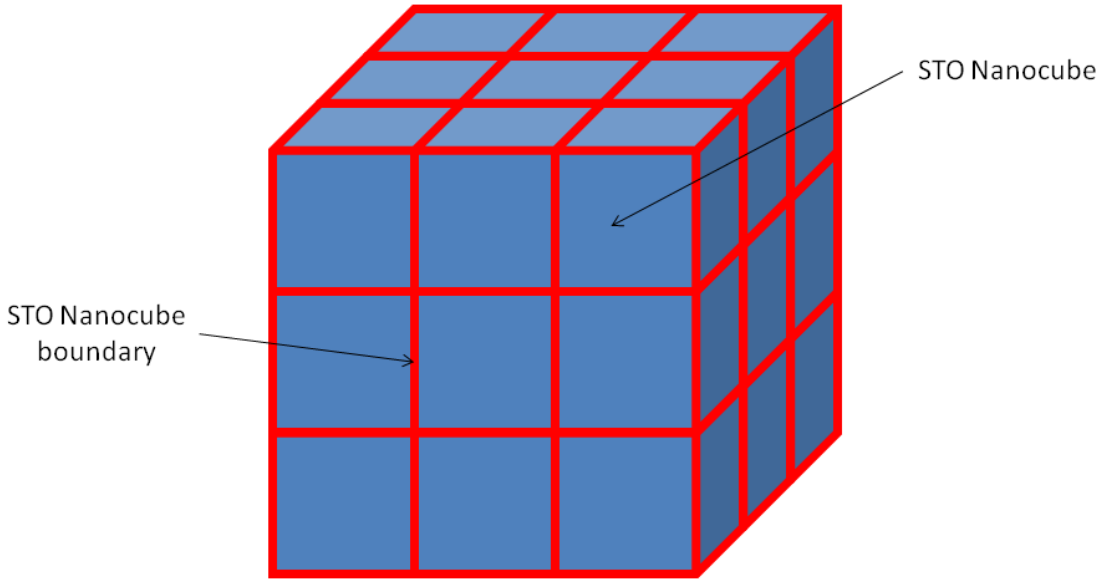

Figure 6.38 Schematic of the perfect cubic stacking of STO nanocubes, 3 x 3 x 3 expansion.

The simulation cells contain one complete nanocube in formation with its periodic images. The single cube in the simulation cell is not expected to cause any issues with convergence due to the large bulk region between the cube interfaces. The interfaces are partially disordered after annealing in molecular dynamics, especially at edges and corners. The disorder in the SrO rich nanocube system is primarily where 6-fold coordinated Ti has become 4-fold coordinated. Figure 6.39 shows a section of the SrO rich nanocube system, in particular the quadruple grain boundary structure.

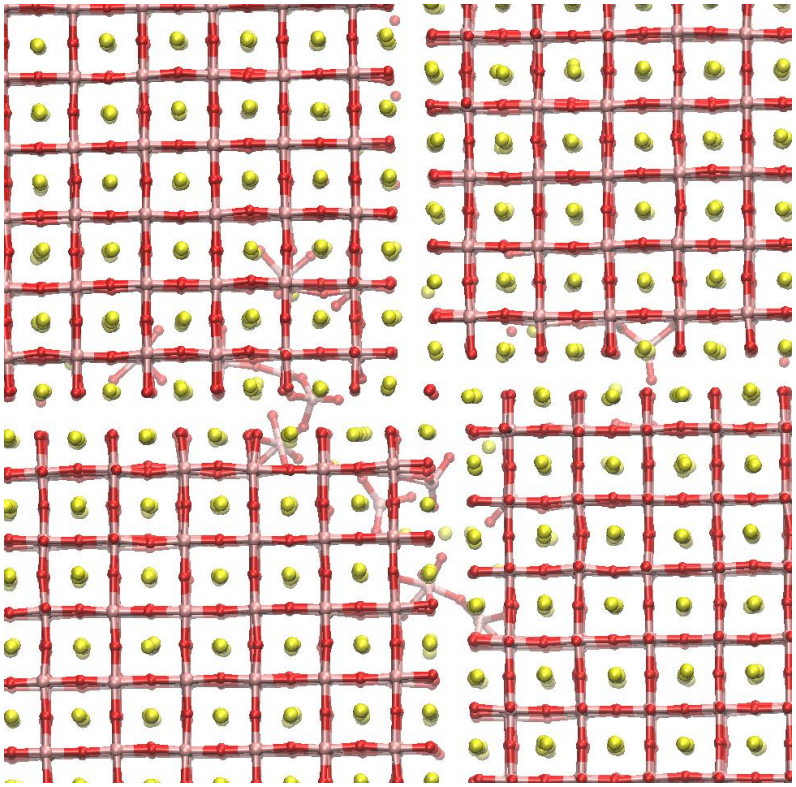

Figure 6.39 Disorder found at the quadruple grain boundary found in the SrO rich STO nanocube system.

6.4.1.1. SrO Rich Nanocube

The SrO rich nanocube system is approximately 70 Å x 70 Å x 70 Å, contains 26,288 atoms and has the approximate formula $Sr_{1.18}TiO_{3.18}$. Each of the five temperatures were equilibrated for 50,000 steps (50 ps) using an NPT isotropic ensemble. The averaged lattice vectors are then applied for the data collection. Heat-flux data was collected for 20 ns (20,000,000 fs steps) and the flux sampled every 10 fs. The heat-flux data collection here was sequential. The thermal conductivities are presented in Figure 6.40.

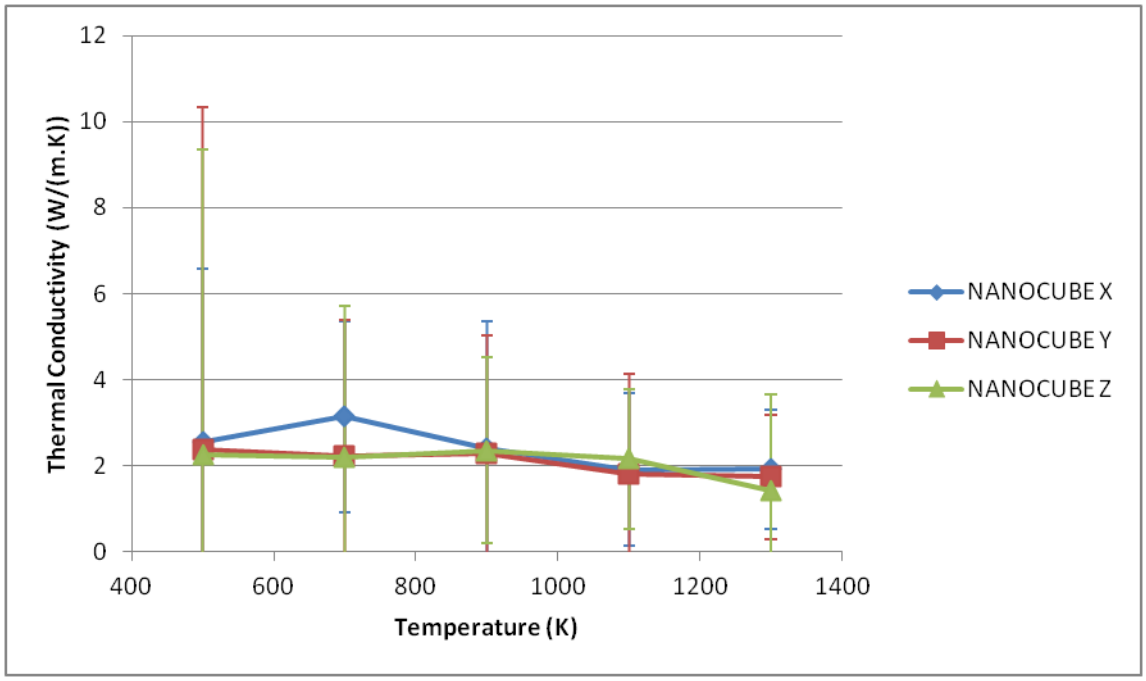

Figure 6.40 Thermal conductivity of the SrO rich nanocube system.

The SrO rich nanocube system has thermal conductivities that are almost entirely insensitive to temperature, all being approximately 2 W/(m.K).

The larger fluctuations at lower temperatures are very apparent. However, the general isotropy of the system is still reflected in the thermal conductivity as all three directions give almost identical values and thus the real error is likely much lower.

The Green-Kubo spectra for these systems are also available. However, they are too large to have their lattice dynamics phonon DOS spectra calculated and thus vibrational modes cannot be conclusively assigned. The Green-Kubo spectrum for the SrO rich nanocube system is presented in Figure 6.41.

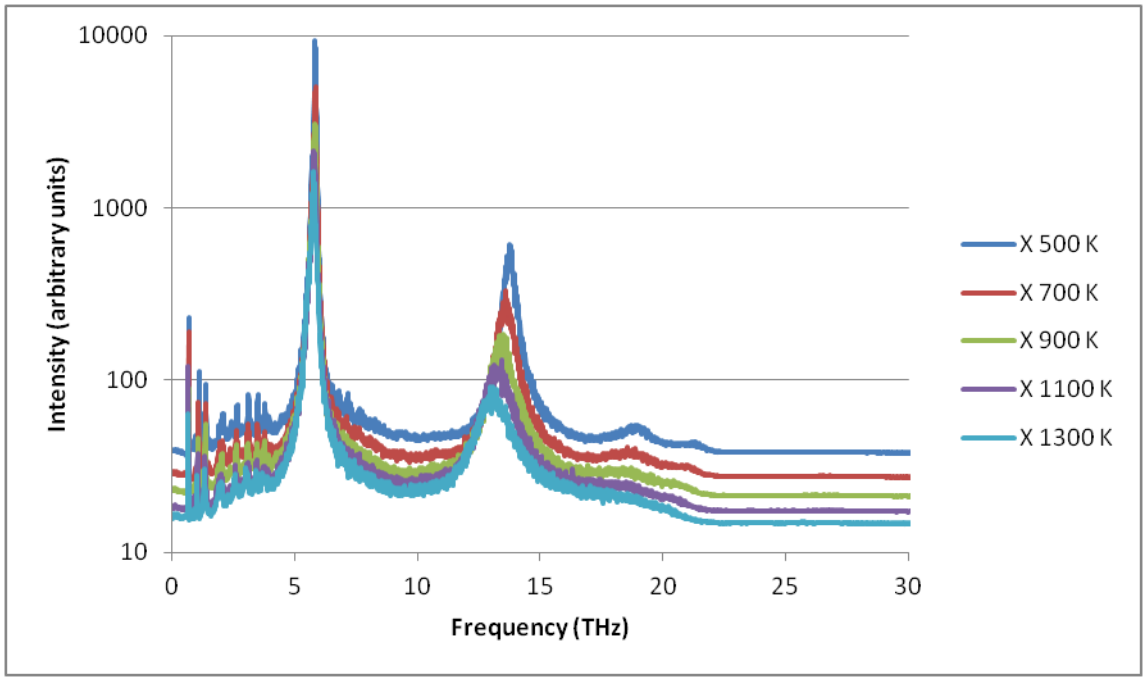

Figure 6.41 Green-Kubo spectra of the SrO rich nanocube system in the X direction, Log_{10} scale.

The X, Y and Z directions of the SrO rich STO nanocube have essentially the same Green-Kubo spectra and so only the X direction is presented for brevity. The Green-Kubo spectra for the SrO rich nanocube system shows many new peaks at very low frequencies, below even those seen for the grain boundary systems. These new peaks (below ~5 THz) are possibly RUMs due to being such low frequency.

6.4.1.2. TiO_2 Rich Nanocube

The TiO_2 rich nanocube system is very similar to the SrO rich system, differing only in the surfaces terminations. The system remains approximately 70 Å x 70 Å x 70 Å, contains 27,224 atoms and has an approximate formula of $SrTi_{1.18}O_{3.36}$. As was the case for the SrO rich system each of the five temperatures were equilibrated for 50,000 steps (50 ps) using an NPT isotropic ensemble. The averaged lattice vectors are then applied for the data collection. Heat-flux data was collected for 20 ns and was sampled every 10 fs. The heat-flux data collected here was sequential. The thermal conductivities are presented in Figure 6.42.

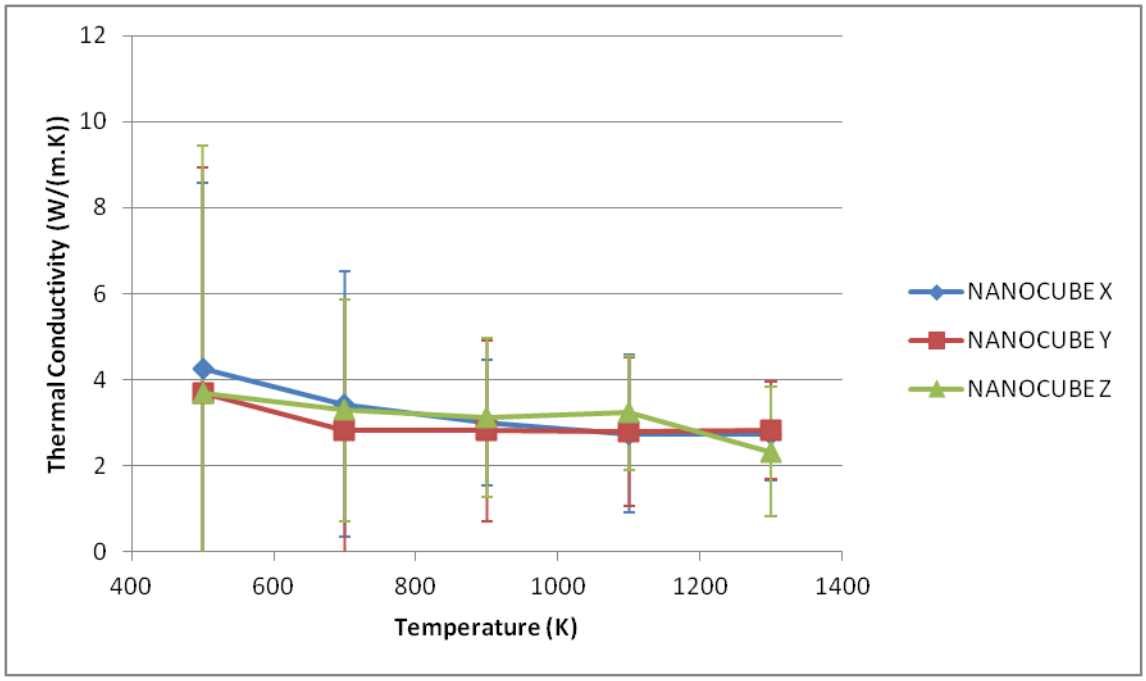

Figure 6.42 Thermal conductivity of the TiO_2 rich nanocube system.

The thermal conductivity of the TiO_2 rich nanocube system is slightly higher than the SrO rich system at around ~3 W/(m.K). There remains some sensitivity to temperature below 600 K but is effectively flat thereafter. Again no directional dependence is seen, which may be expected, although the TiO_2 rich boundaries are not necessarily identical.

The reason why the thermal conductivity is higher in the SrO rich nanocube system is likely due to the large degree of Ti-O cross-linking. Higher thermal conductivity was seen in the X direction of the Σ3{111} boundary, which also contained significant Ti-O cross-linking.

The Green-Kubo spectra for the TiO_2 rich nanocube system are presented in Figure 6.43, Figure 6.44 and Figure 6.45.

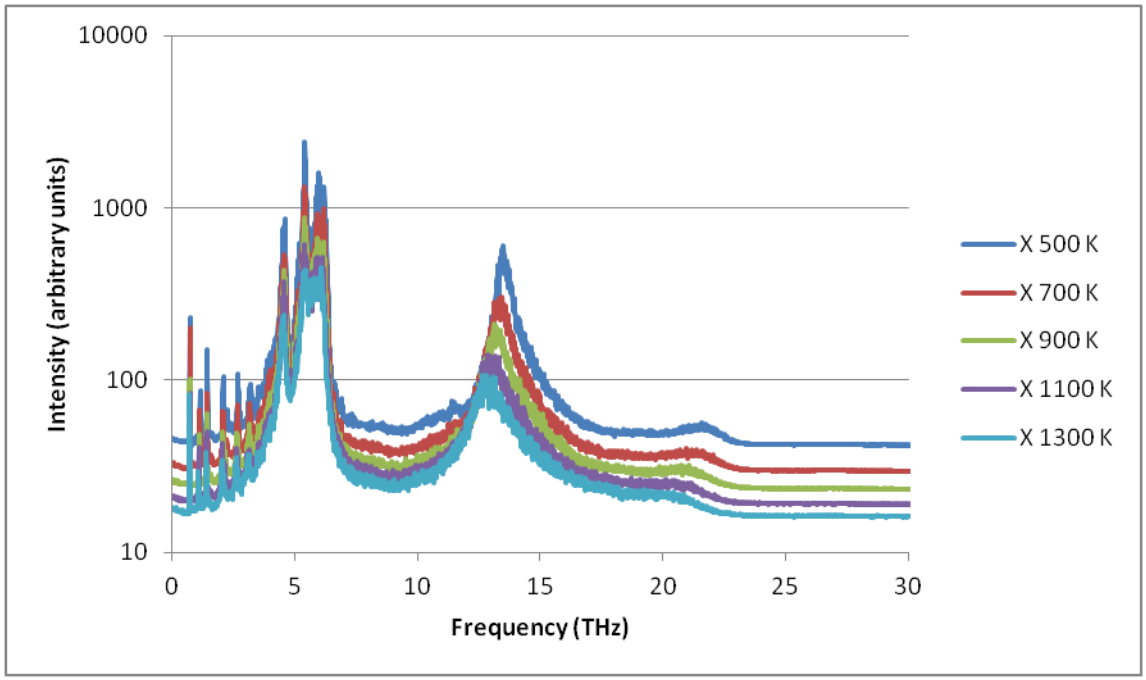

Figure 6.43 Green-Kubo spectra of the TiO_2 rich nanocube system in the X direction, Log_{10} scale.

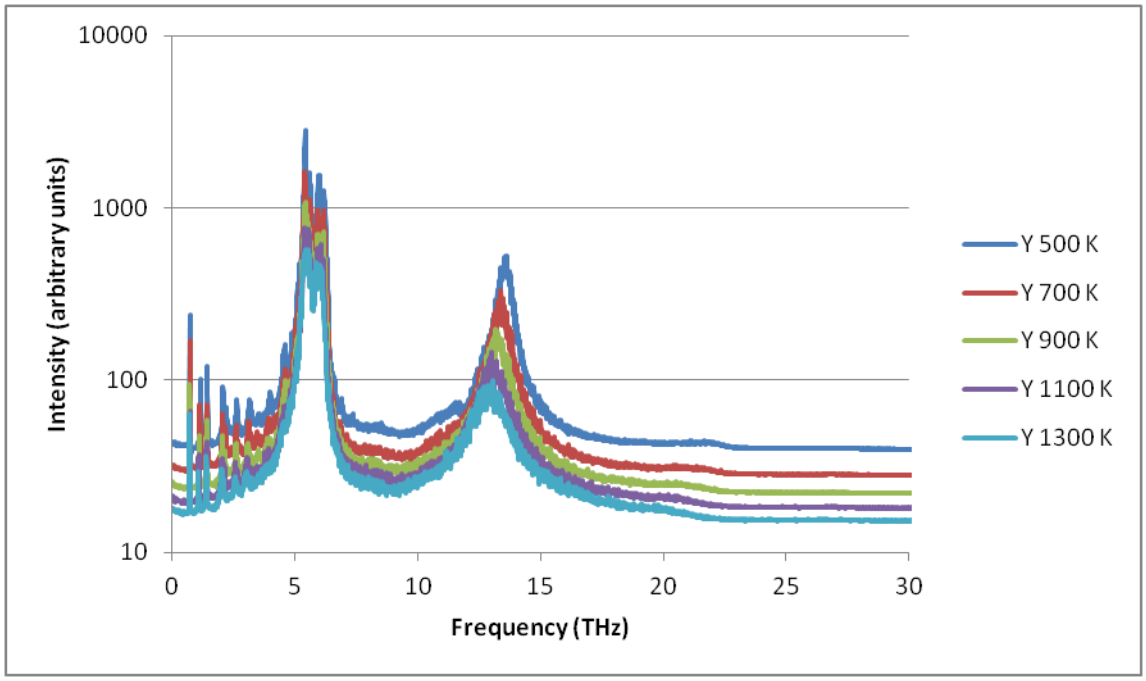

Figure 6.44 Green-Kubo spectra of the TiO_2 rich nanocube system in the Y direction, Log_{10} scale.

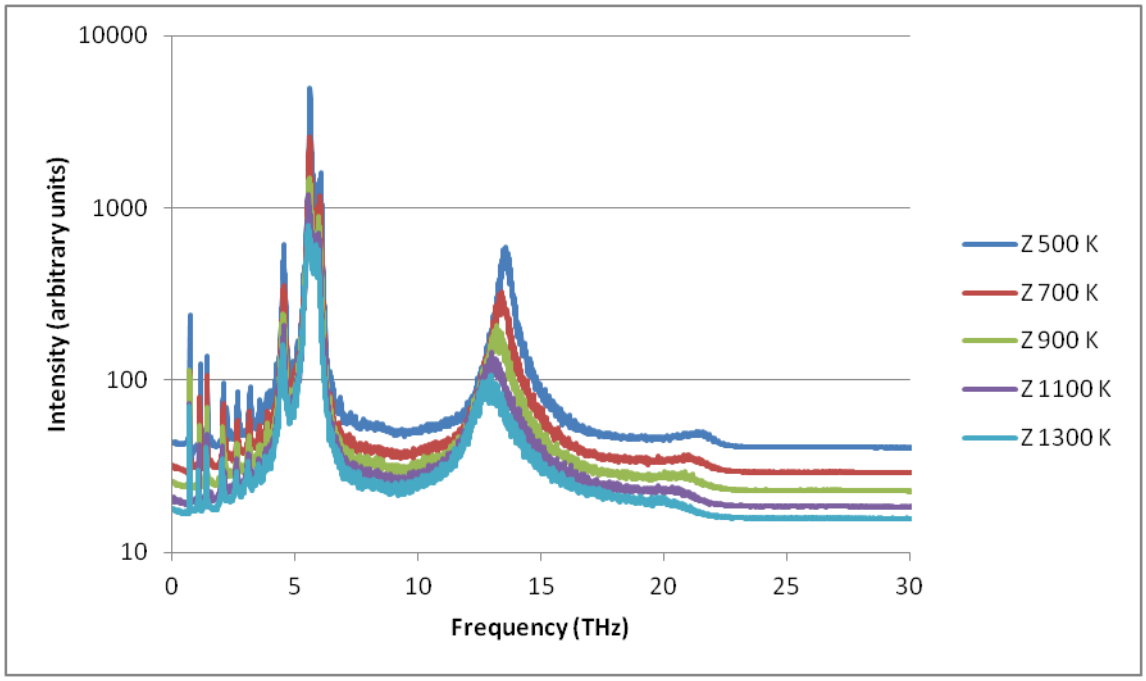

Figure 6.45 Green-Kubo spectra of the TiO_2 rich nanocube system in the Z direction, Log_{10} scale.

The spectra for the TiO_2 rich nanocube system also displays an abundance of very low frequency peaks. An unusual feature of the spectra is the apparent splitting of the strontium peak (~6 THz) however the additional peak is not necessarily a strontium peak but a hugely shifted titanium peak. One explanation may be due to TiO_2 like nature of the cube interfaces, which may have a significant peak at this position.

Another feature of the spectra is the clear difference between each direction in the additional peaks around 6 THz, stemming from the different covalent bonding arrangements of Ti-O at each interface. The very low frequency peaks (less than 3 THz) however are identical in each direction.

STO nanocubes may also be packed in other arrangements than the one outlined in Figure 6.38. The next section investigates two more possible stacking arrangements and evaluates their thermal conductivity. Due to the similarity of behaviour seen in the SrO rich and TiO_2 rich nanocube systems and the slightly lower thermal conductivities seen in the SrO rich system, only the SrO rich system is used in the following study.

6.4.2. Displaced Nanocubes

The STO nanocubes may assemble in other geometries than those presented above. By altering the stacking arrangement different systems may be formed which have a more complex boundary system. To study the effect different stacking orders have on the thermal conductivity two additional systems have been constructed.

The new systems are based on the SrO rich nanocube, which displayed lower thermal conductivity than the TiO_2 rich nanocube. The first system contains a single displacement in the Y direction of half a cube width relative to its neighbour; a schematic of the system is show in Figure 6.46. The shape of the system corresponds to lattice vectors of approximately 78 Å x 70 Å x 70 Å and an αβγ of 90° x 90° x 65°.

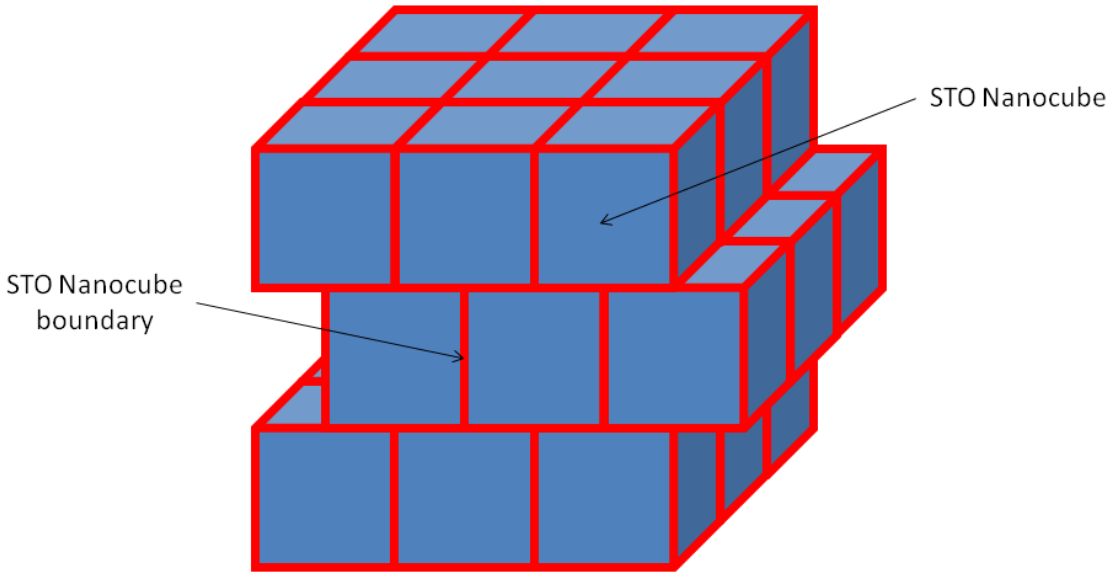

Figure 6.46 Schematic of the singly displaced cubic stacking of STO nanocubes.

The next new system is also based on the strontium rich system but contains a double displacement along the X and Y directions. A schematic of this system is shown in Figure 6.47. The system contains 26,288 atoms and has lattice vectors of 78 Å x 70 Å x 78 Å and an αβγ of 90° x 65° x 65°.

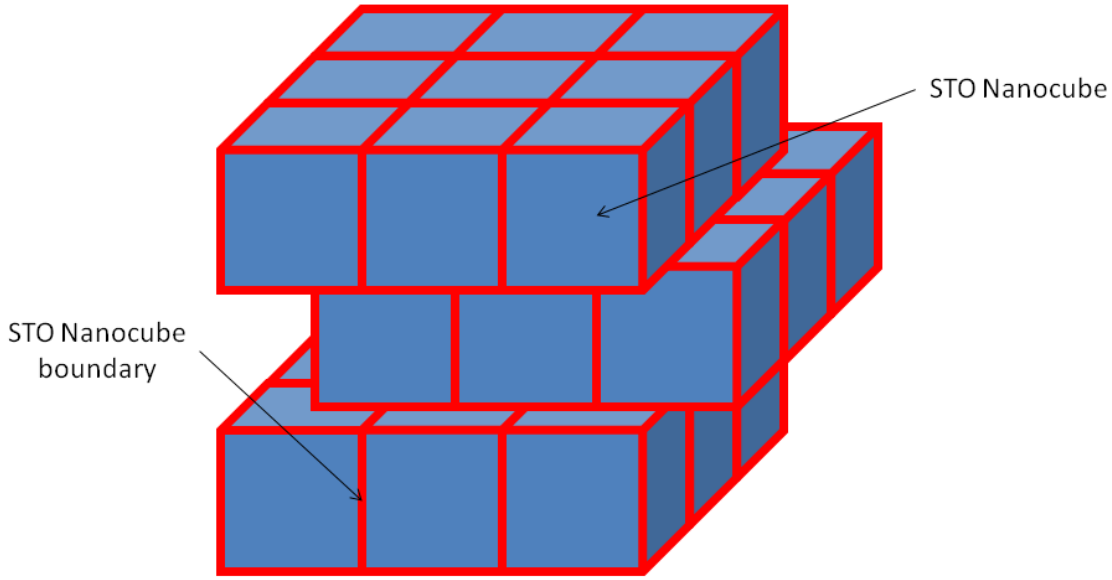

Figure 6.47 Schematic of the doubly displaced cubic stacking of STO nanocubes.

6.4.2.1. Single Displacement SrO Rich Nanocube

The data collection for the displaced nanocubes was the same as for the non-displaced nanocube with the exception that data was collected in parallel, using four separate runs of 5 ns each at each temperature. The results are displayed in Figure 6.48.

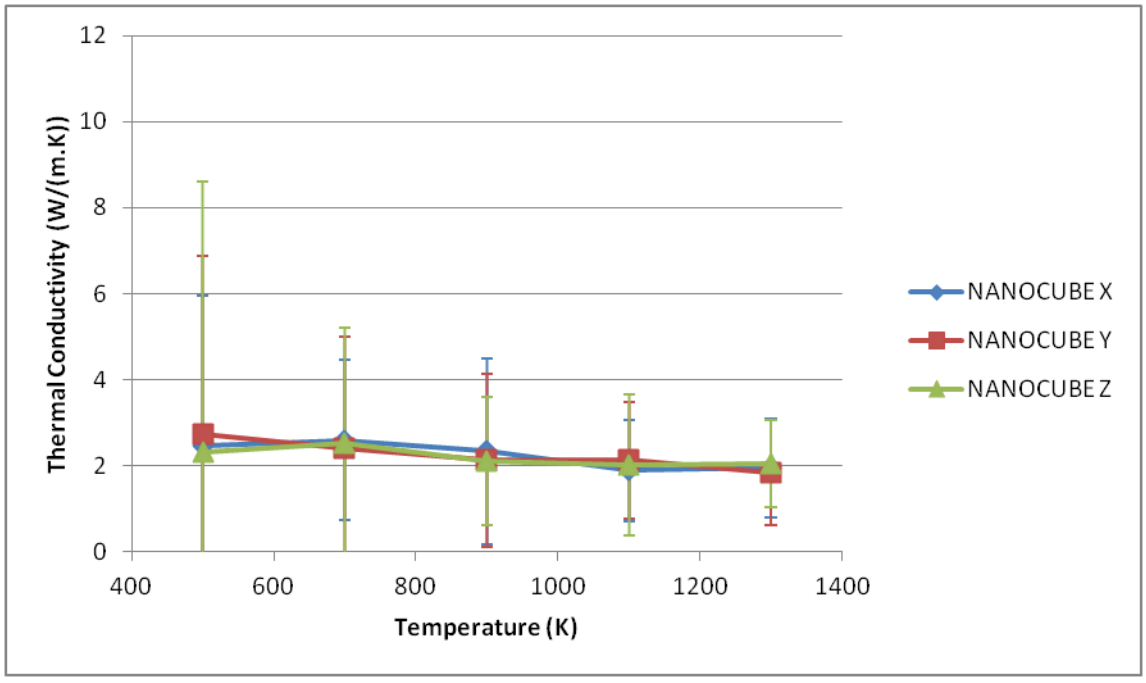

Figure 6.48 Thermal conductivity of the single displacement nanocube system.

The thermal conductivity of the single displacement system is remarkably similar to that of the non-displaced system with no sensitivity to temperature and all values at ~2 W/(m.K). The similarity of the two systems indicates that the arrangement of nanocubes may not be significant and it is only the existence of the boundaries themselves that are impacting the thermal conductivity. The Green-Kubo spectra can now be generated and any difference to the non-displaced system can be noted, the spectra are presented in Figure 6.49, Figure 6.50 and Figure 6.51.

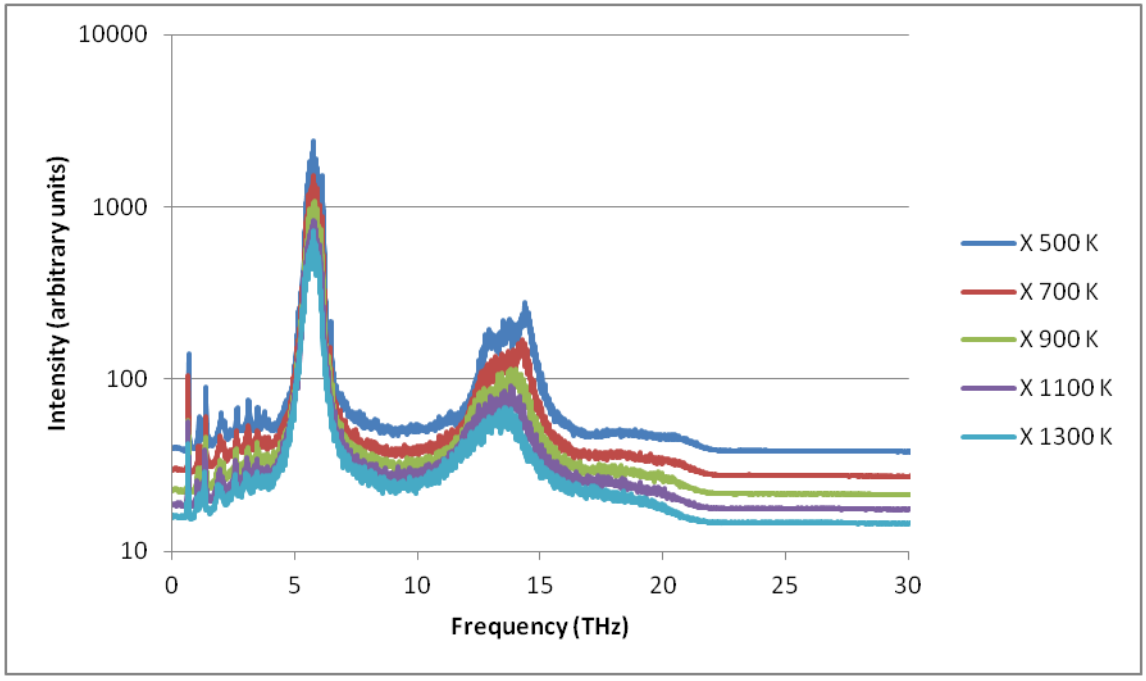

Figure 6.49 Green-Kubo spectra of the single displacement nanocube system in the X direction, Log_{10} scale.

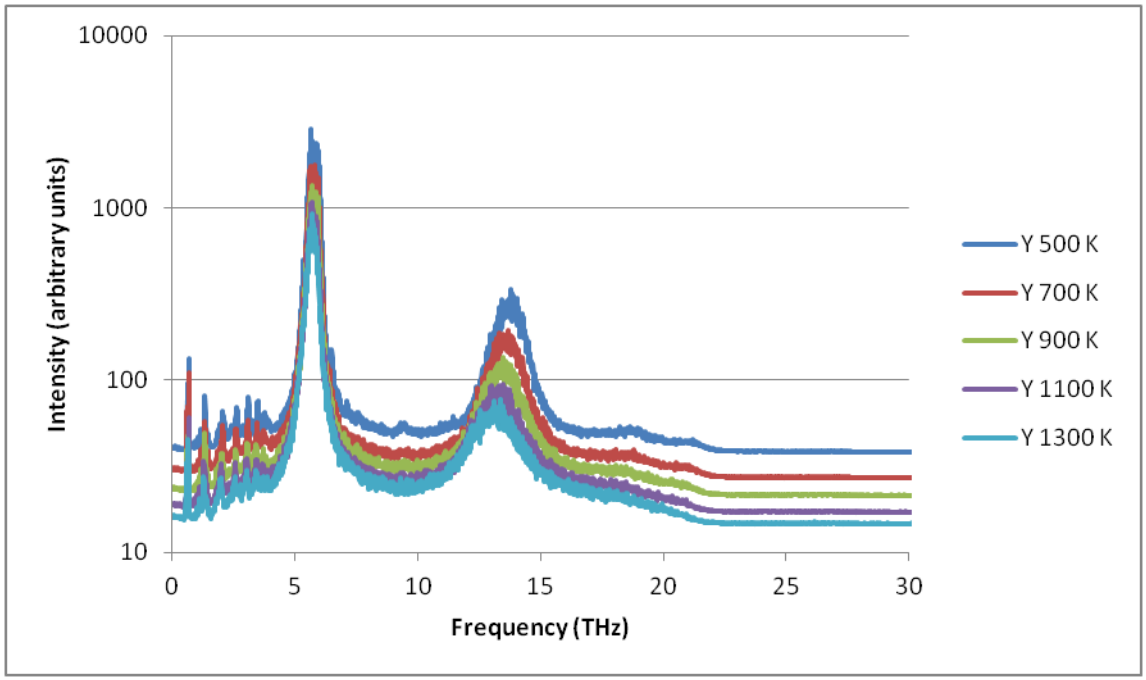

Figure 6.50 Green-Kubo spectra of the single displacement nanocube system in the Y direction, Log_{10} scale.

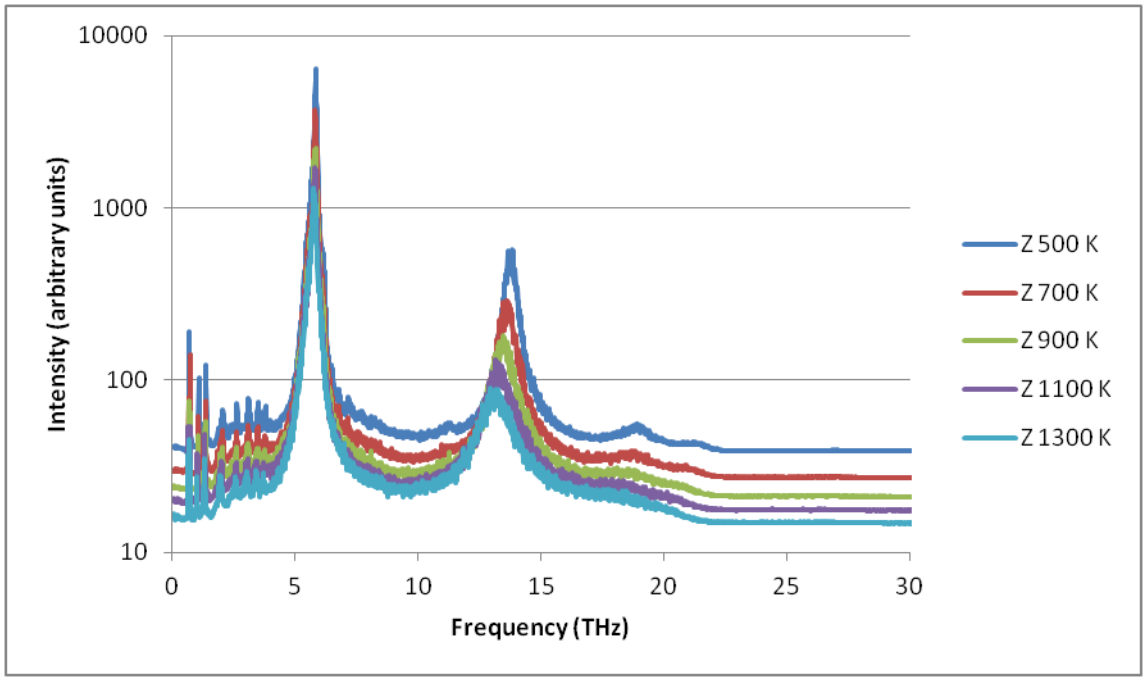

Figure 6.51 Green-Kubo spectra of the single displacement nanocube system in the Z direction, Log_{10} scale.

The Green-Kubo spectra of the single displacement system are very similar to those of the non-displaced system. The very low frequency peak pattern is almost identical between the two systems, as well as within the three directions. The similarities support

the idea that it is the existence of the boundaries themselves, rather than the arrangement of the cubes, which is the significant factor in reducing the thermal conductivity.

The only significant difference between the non-displaced system and the single displacement system is an additional splitting of the titanium peak (~14 THz) in the X and Y directions. While this may seem unusual given the strontium rich nature of the system, it can be explained as stemming from the titanium atoms near the double interface. The SrO-like interface itself is likely represented by some of the peaks between ~3 THz and ~5 THz near the bulk Sr peak, but at low magnitude due to the relatively low concentration of species in this environment.

6.4.2.2. Double Displacement SrO Rich Nanocube

The double displacement system was equilibrated in the same manner as the single displacement system and data collection was performed in the same way. The results are displayed in Figure 6.52.

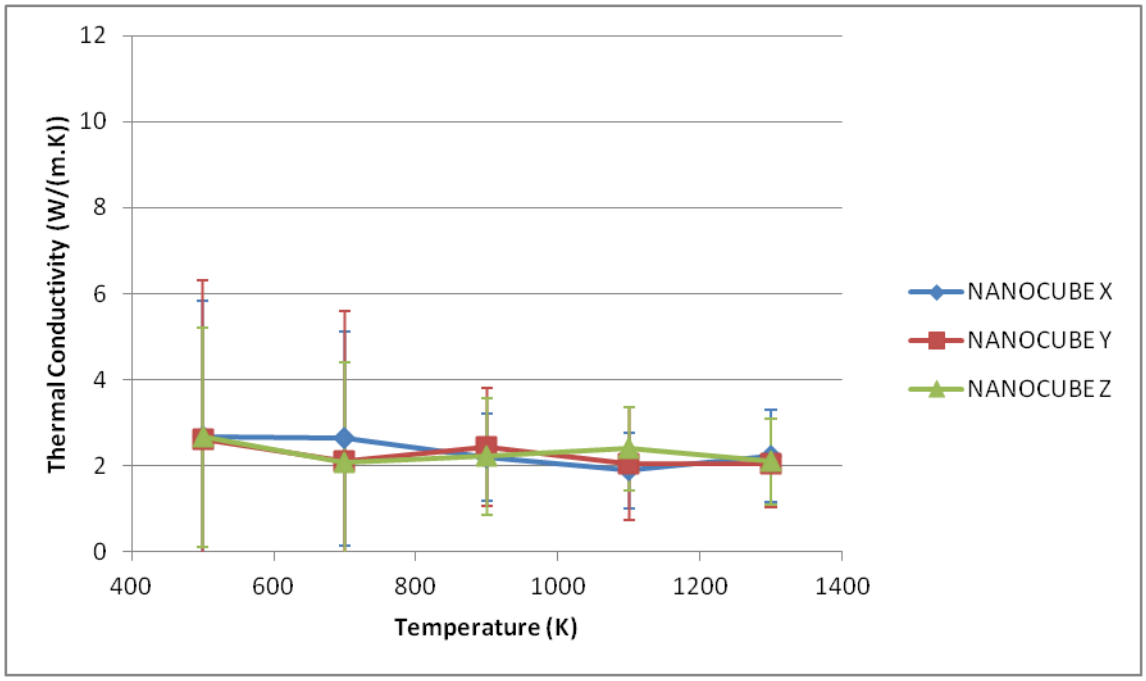

Figure 6.52 Thermal conductivity of the double displacement nanocube system.

Once again the thermal conductivity is flat with respect to temperature and has an average value of ~2 W/(m.K) and is significantly similar to the previous nanocube

thermal conductivity profiles. The Green-Kubo spectra are presented in Figure 6.53, Figure 6.54 and Figure 6.55.

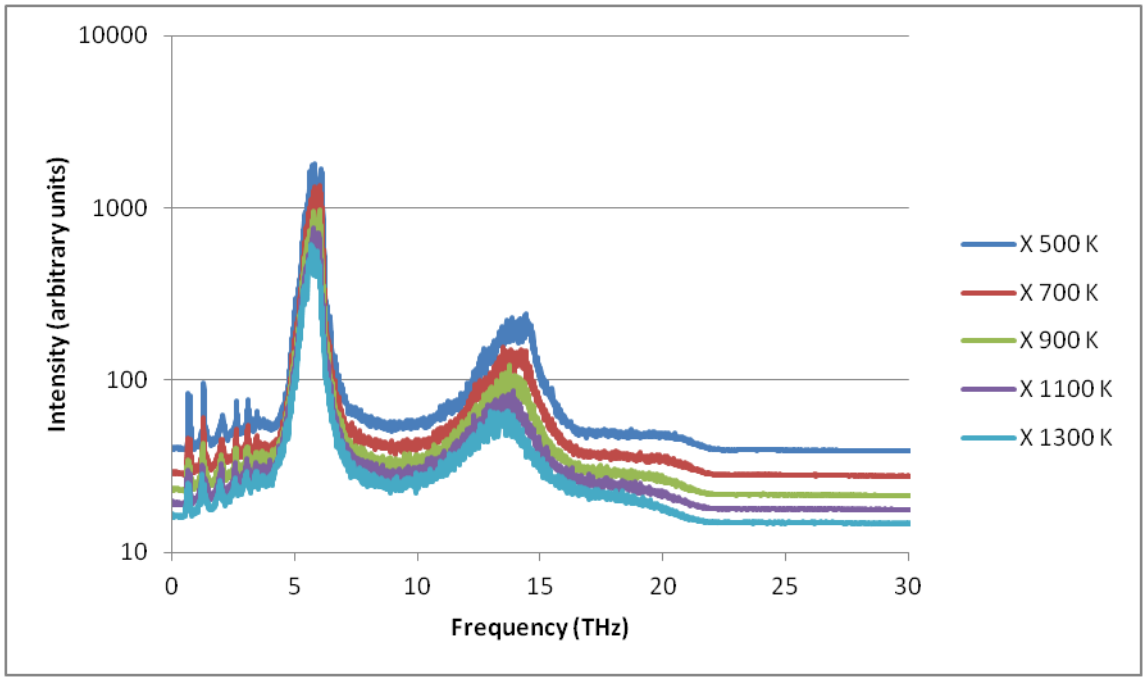

Figure 6.53 Green-Kubo spectra of the double displacement nanocube system in the X direction, Log_{10} scale.

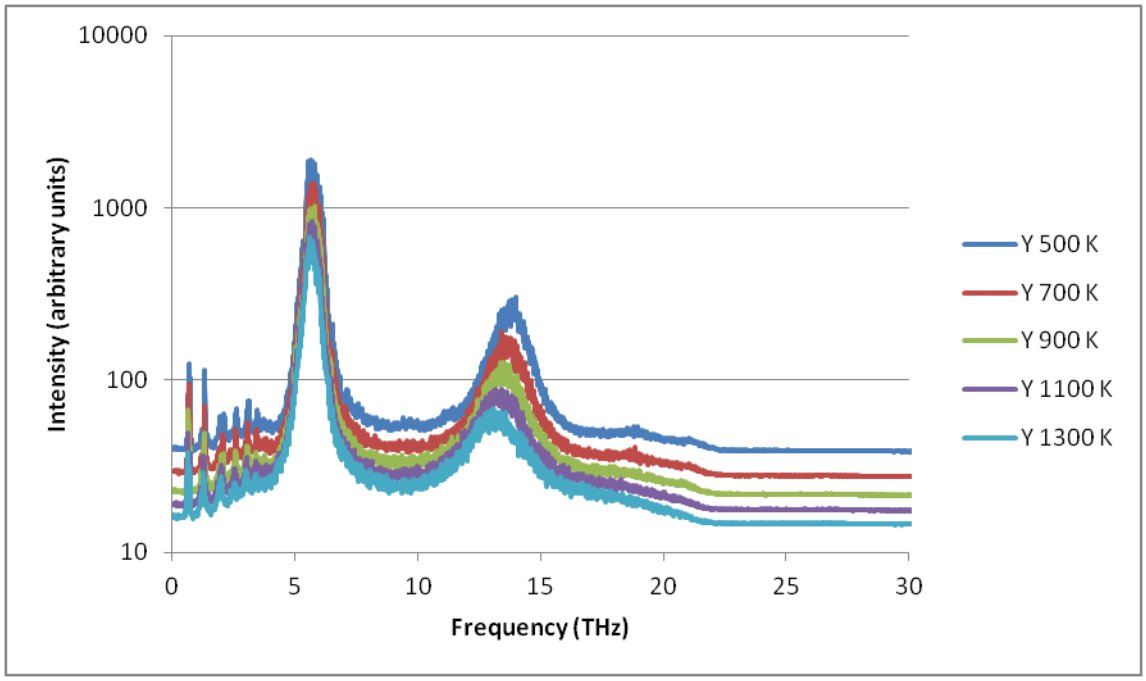

Figure 6.54 Green-Kubo spectra of the double displacement nanocube system in the Y direction, Log_{10} scale.

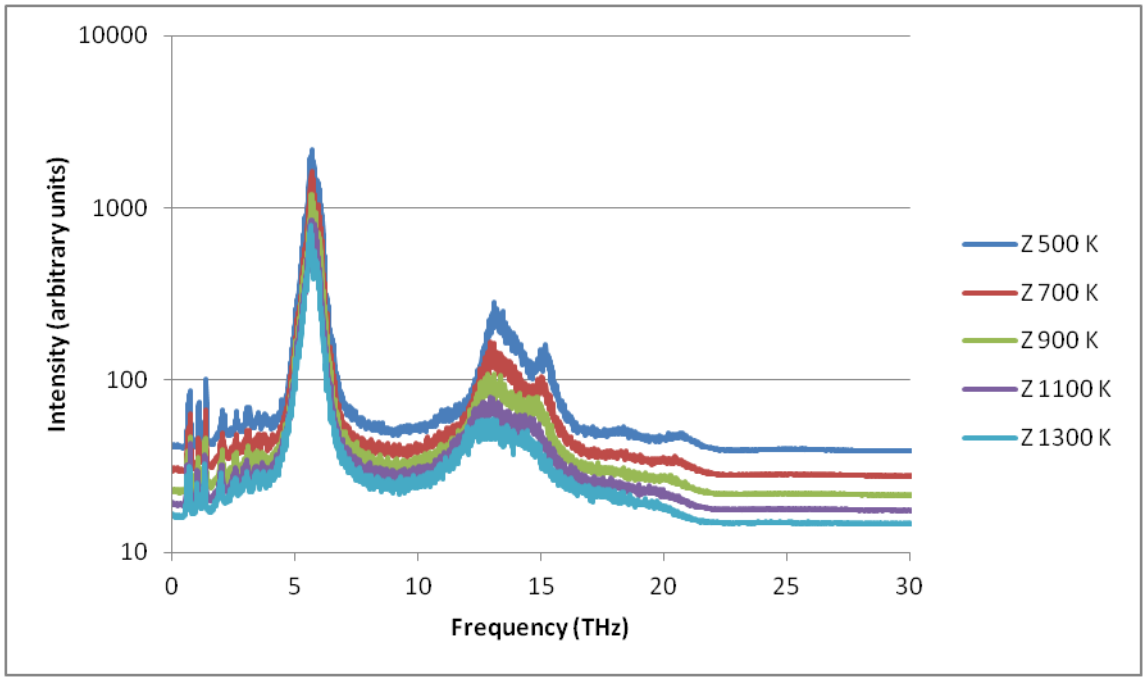

Figure 6.55 Green-Kubo spectra of the double displacement nanocube system in the Y direction, Log_{10} scale.

The three spectra are very similar to those seen previously. However, there are minor deviations in the low frequency peaks which may stem from the more complex cube ordering. While the relative positions and heights of the low frequency peaks have changed slightly it does not have a significant effect on the thermal conductivity.

Additional changes to the spectra are seen in the titanium peak (~14 THz) where there is splitting/broadening in the X and Z directions. These changes are expected and are likely to stem from titanium near the double/triple boundary environments.

6.4.3. Nanocube Discussion

The thermal conductivity values obtained from simulations on STO nanocubes have displayed thermal conductivities even lower than in the interacting grain boundary systems; even though the nanocube systems have a larger inter-boundary distance. The reason for this change in behaviour is that the nanocube system contains boundaries in all three dimensions, instead of just one. This means that phonons which would travel for a long distance in the Y and Z directions (yet retain some small X direction component) in the grain boundary system are scattered much earlier in the nanocube system. Therefore the grain boundary and nanocube systems are not directly comparable

as it cannot be said for certain if the grain boundaries studied individually scatter phonons more effectively than those used for the boundaries in the nanocube system.

Additionally the thermal conductivities for all nanocube systems have almost complete insensitivity to temperature, remaining at an almost constant value. This is converse to the behaviour seen in the grain-boundary system where a dependency to temperature could be observed across much of the range. This is again attributed to the boundaries found in all three dimensions in the nanocube systems which make boundary-acoustic phonon scattering processes the primary mechanism even at high temperature, instead of switching to an acoustic-acoustic phonon scattering regime.

The absolute value of thermal conductivity is higher in the TiO_2 rich system at ~3 W/(m.K) rather than ~2 W/(m.K) for the SrO rich system. Therefore it can be concluded that the type of boundary impacts the magnitude of the thermal conductivity, while the inter-boundary distance likely impacts the response to temperature and magnitude.

The thermal conductivities of all three displaced SrO rich nanocube systems are essentially identical in both magnitude and response to temperature. Furthermore, the thermal conductivity of the displaced systems is remarkably similar to that of the non-displaced system, further supporting the supposition that boundary-acoustic phonon scattering is highly dominant in a system of bulk surrounded by grain boundaries.

The dominance of the 3D grain boundary arrangement is further supported by the Green-Kubo spectra which show almost identical peaks for all SrO rich systems, particularly at low frequencies. It is these low frequency peaks which are likely to have a disproportionate effect on the thermal conductivity due to the Bose-Einstein distribution.

6.5. STO Summary

The work presented on STO systems has shown that systems with large mass discrepancies in the atoms will have optical modes with significant asymmetry and thus are more likely to effectively scatter acoustic phonons.

By introducing grain boundaries the number of optical modes increases, due to new atomic environments being created. These modes tend to be localised around the boundary and provide a mechanism for the thermal conductivity reduction seen by

introducing grain boundaries. Furthermore the effectiveness of a particular grain boundary at reducing thermal conductivity is related to the formation energy; higher formation energy tends to have more distinct boundary environments and thus more scattering centres.

Lattice dynamics phonon DOS calculations provide a key way to understand the motions of atoms at the boundary. Many of the additional vibrational modes introduced by grain boundaries arise from the different environments around the extended defect. Thus it can be seen that the different environments at the boundary play a prominent role in scattering phonons and reducing thermal conductivity. Lattice dynamics may then provide a useful tool for quickly analysing structures to try and predict whether they will have a significantly low thermal conductivity without the need to perform expensive thermal conductivity calculations.

By extending the grain boundary work into nanocube systems, where the interface can be considered a very thin separate phase, the thermal conductivity was lowered significantly and showed no response to temperature. The existence of separate phases has been known to be beneficial to thermoelectric materials and such systems are known as superlattice systems [344]. The actual arrangement of nanocubes in the superlattice system is of less importance. While there is some effect on the Green-Kubo spectra, the thermal conductivity is dominated by a few low frequency modes arising out of the two materials of different density and atomic arrangements.

All SrO rich nanocube simulations displayed a minimum thermal conductivity of ~2 W/(m.K) while the TiO_2 rich nanocube system had a thermal conductivity of ~3 W/(m.K). Both systems displayed no dependence on temperature. Compared with the bulk thermal conductivity of 7.5 W/(m.K) at 500 K, it is feasible that the bulk ZT of 0.24 could be increased to around 0.8 as suggested by Koumoto [316].

Future work on STO should concentrate on other defect types. Substitution of the A site cation (strontium) is the most obvious approach, further lowering the lowest frequency peak in the bulk spectra (~5 THz). Further doping of grain boundary systems may also be of benefit if the new low frequency peaks could be shifted to lower frequencies or higher intensities; this approach would also require the dopant to segregate to the boundary.

The SrO rich nanocube interface is a Ruddlesden-Popper (RP) type phase [345], which may be used as a model system of the SrO rich nanocube interface. The RP phase has a unit cell small enough that a lattice dynamics calculation is possible and so the modes appearing in the molecular dynamics simulations could be conclusively assigned. Furthermore, the RP phases allow the study of more complex nanocube interfaces by varying the distance between the interfaces and the thickness of the interface (rocksalt layer).

7. Conclusions and Future Work

The work presented here has demonstrated that the Green-Kubo approach for calculating thermal conductivity can give well converged results for a number of very different materials of different bonding, isotropy and complexity. While the Green-Kubo method gives apparently good thermal conductivities, error analysis is still challenging due to the semi-arbitrary choice of integral cutoff.

Additional information may be derived from the Fourier transform of the heat-flux autocorrelation function, referred to as the Green-Kubo spectra in this work. The modes visible in the Green-Kubo spectrum correspond to the optical phonon modes which are asymmetric and capable of interacting with the heat-flux of the system.

The same phonon modes may also be obtained from lattice dynamics calculations allowing qualitative analysis of the thermal conductivity prior to a full long time-scale molecular dynamics (MD) simulation and application of the Green-Kubo method.

The Boltzmann transport equation (BTE) has also been used (via Phono3py [122] and METADISE [165]) to calculate the thermal conductivity of several of these systems. The application of the BTE within the simulations presented here gives good thermal conductivity values for bulk STO, a good trend with temperature for bulk MgO (absolute value was shifted upwards by ~10 W/(m.K)) and failed to converge for bulk quartz. Furthermore, this approach is not suitable at present for large systems due to rapidly increasing memory requirements.

The Green-Kubo method gave good thermal conductivity values for bulk MgO when compared with experiments [215-217]. The shift of thermal conductivities observed when using lattice dynamics to solve the BTE may be related to the choice of potential cutoff in the MD (8.5 Å rather than the 15.0 Å cutoff used in the lattice dynamics calculations); alternatively the shift may be due to the BTE neglecting fourth-order and higher force constants.

Both of the MgO grain boundaries reduce the thermal conductivity to between 10 W/(m.K) at 500 K and 5 W/(m.K) at 1300 K and overall show remarkably similar behaviour at all temperatures and a reduced thermal conductivity as compared to bulk by a factor of 2-3. The similarity may be attributed to the very small inter-boundary

distance (~16 Å) in these systems, which acts to limit the allowed phonon wavelengths. While the boundaries do display differing Green-Kubo spectra, the simulations suggest that the dominant feature in this case is the very frequent scattering of phonons due to the small inter-boundary distance, rather than any particular structure found at either grain boundary.

Having demonstrated that the introduction of grain boundaries reduced the thermal conductivity, the work was extended to model nanostructures comprised of different orientated grains and included internal pores. It was found the the thermal conductivity of the MgO nanostructures was reduced dramatically, i.e. to ~2 W/(m.K) at all temperatures in the hexagonal nanostructure and to ~1 W/(m.K) at all temperatures for the cubic nanostructure. Analysis of the data found that the significantly increased reduction in thermal conductivity due to surface scattering via the use of a model system studied through lattice dynamics which demonstrated the origin of the strong additional peak appearing at ~25 THz.

Green-Kubo calculations on quartz resulted in a thermal conductivity which overlaid experimental results, however the minimum in thermal conductivity observed experimentally at the α-quartz to β-quartz phase transition (~846 K) was not reproduced. One possible explanation was that formation of domains of Dauphiné twins may be the cause of the minimum in thermal conductivity as they should occur spontaneously around the transition temperature from α-quartz to β-quartz. Although Dauphiné twins were stabilised at low temperatures the calculation of the thermal conductivity proved inconclusive due annealing of the twin.

The simulation results also suggest that in quartz a rigid unit mode (RUM) participated in scattering acoustic phonons while the material was in the α-quartz form, but its effect diminished as the material approached β-quartz. Upon analysis of the phonon DOS it was found that the mode was asymmetric in the Z direction due to the tilt of the SiO_4 tetrahedra at low temperatures but became symmetric at higher temperatures as the tilt of the tetrahedral is removed.

Extension of the quartz work to the siliceous zeolite, silicalite, showed exceptionally low thermal conductivity values of ~2.5 W/(m.K) at all temperatures. This result is interesting as this value is similar to preliminary values obtained from SiO_2 glass (Appendix B), indicating it is not the density of the system which is important but the

number of environments and the maximum phonon mean free path. Furthermore, the observed negative thermal expansion at high temperatures may lead to an expectation that the thermal conductivity may also increase at higher temperatures as was seen in experiments for quartz. However, this trend was not found but instead the thermal conductivity was virtually independent of temperature.

When applied to strontium titanate (STO), both the Green-Kubo method and BTE compared well with experiments, particularly at higher temperatures. Interestingly, the Green-Kubo method and BTE gave almost identical results, indicating that in STO the fourth-order force constants are not important for an accurate thermal conductivity in STO.

The grain boundaries of STO demonstrated that for a given inter-boundary distance, the formation energies correlated with the order of thermal conductivity. This relationship arises as higher formation energies tend to relate to greater deviation from the preferred coordination of atoms at the boundary; thus the number of scattering sites increases.

Given the recent interest orientated nanoparticles, the thermal conductivity of several STO assembled nanocube systems were also studied. STO nanocubes demonstrated an average thermal conductivity of 2 W/(m.K) when SrO rich and an average thermal conductivity of 3 W/(m.K) when TiO_2 rich. These values did not change with temperature. Furthermore, it was found that the exact stacking arrangement of the SrO rich cubes did not have an impact on the thermal conductivity, indicating significant boundary scattering in the enclosed nanocube.

In summary this work has found that the type of grain boundary plays a small role in the thermal conductivity through inclusion of new scattering environments. However, the underlying system geometry tends to dominate and results in very low thermal conductivities which are insensitive to temperature. Therefore nanostructuring is a promising approach to improving thermoelectric materials, provided the electronic contributions can be maintained.

7.1. Future Work

To extend this work further more Green-Kubo simulations should be run on the grain boundary systems allowing calculation of the Kapitza length [197, 331, 343]. This value

represents the amount of bulk a given grain boundary represents in terms of phonon scattering. However, such simulations rapidly become difficult due to the large system sizes and long simulation times required to achieve a converged thermal conductivity with the Green-Kubo method.

In the quartz system the RUMs provide a route to very low frequency modes which are sometimes capable of interacting significantly with acoustic phonons and thus the heat-flux. At present only one RUM was observed to interact with the heat-flux, but if it were possible to modify the system with dopants such that more RUMs interacted with the heat-flux then a significant reduction in thermal conductivity may be expected. Furthermore the dopant need not be high mass as the nature of a RUM means the frequency is already very low.

More Green-Kubo calculations should also be conducted on the Dauphiné twin system. As was discussed in Chapter 5.2.2.2, the size of Dauphiné twin domain plays a role in the stability and therefore exceptionally large systems may be required. Additionally high accuracy must be achieved as the effect of the twin boundary maybe very small.

The silicate systems as a whole are very interesting due to the large number of structures which are possible. Completing the work on the glass thermal conductivity (Appendix B) along with more zeolite structures may further elucidate other promising mechanisms for reducing thermal conductivity.

An avenue of research untouched in this work is the effect of dopants on the thermal conductivity in STO. The defect chemistry of STO is particular diverse as the system may accept dopants on either the A or B site. Furthermore intrinsic defects are also possible as either Schottky defects or by reduction of Ti^{4+} to Ti^{3+} and loss of oxygen. All these defects, as well as defect orderings, will have some impact on the thermal conductivity.

Further development of the BTE approach is also another interesting avenue of research. The current approach uses the single mode relaxation time (SMRT) approximation, although other approaches are available [122, 346]. Additionally, extending the method to the fourth-order force constants may improve the bulk MgO results, but problems may be encountered concerning numerical accuracy. One final problem is that obtaining the thermal conductivity via this route is extremely

computationally memory intensive and may require specialised hardware for larger calculations.

Finally, complementary ab initio calculations on the electronic properties of some of the presented systems in STO may help elucidate whether any particular system geometry or grain boundary will produce a particularly high ZT material. The different systems presented have vastly different environments at the boundary and are expected to have different impacts on the electronic properties. Taken together with the thermal conductivity calculations it may be possible to target a system geometry which maximises ZT.

8. References

1. Humphrey, W., Dalke, A., and Schulten, K., *VMD: visual molecular dynamics.* Journal of Molecular Graphics, 1996. **14**(1): p. 33-38.
2. Fthenakis, V. and Kim, H.C., *Life-cycle uses of water in US electricity generation.* Renewable & Sustainable Energy Reviews, 2010. **14**(7): p. 2039-2048.
3. Wang, T., Zhang, Y., Peng, Z., and Shu, G., *A review of researches on thermal exhaust heat recovery with Rankine cycle.* Renewable & Sustainable Energy Reviews, 2011. **15**(6): p. 2862-2871.
4. Saidur, R., Rezaei, M., Muzammil, W.K., Hassan, M.H., Paria, S., and Hasanuzzaman, M., *Technologies to recover exhaust heat from internal combustion engines.* Renewable & Sustainable Energy Reviews, 2012. **16**(8): p. 5649-5659.
5. Martin-Gonzalez, M., Caballero-Calero, O., and Diaz-Chao, P., *Nanoengineering thermoelectrics for 21st century: Energy harvesting and other trends in the field.* Renewable & Sustainable Energy Reviews, 2013. **24**: p. 288-305.
6. Niu, X., Yu, J., and Wang, S., *Experimental study on low-temperature waste heat thermoelectric generator.* Journal of Power Sources, 2009. **188**(2): p. 621-626.
7. Riffat, S.B. and Ma, X.L., *Thermoelectrics: a review of present and potential applications.* Applied Thermal Engineering, 2003. **23**(8): p. 913-935.
8. Tie, S.F. and Tan, C.W., *A review of energy sources and energy management system in electric vehicles.* Renewable & Sustainable Energy Reviews, 2013. **20**: p. 82-102.
9. Ullah, K.R., Saidur, R., Ping, H.W., Akikur, R.K., and Shuvo, N.H., *A review of solar thermal refrigeration and cooling methods.* Renewable & Sustainable Energy Reviews, 2013. **24**: p. 499-513.
10. Pichanusakorn, P. and Bandaru, P., *Nanostructured thermoelectrics.* Materials Science & Engineering R-Reports, 2010. **67**(2-4): p. 19-63.
11. Zhan, G.D., Kuntz, J.D., Mukherjee, A.K., Zhu, P.X., and Koumoto, K., *Thermoelectric properties of carbon nanotube/ceramic nanocomposites.* Scripta Materialia, 2006. **54**(1): p. 77-82.

12. Bell, L.E., *Cooling, heating, generating power, and recovering waste heat with thermoelectric systems.* Science, 2008. **321**(5895): p. 1457-1461.
13. Liu, S., Wang, J., Jia, J., Hu, X., and Liu, S., *Synthesis and thermoelectric performance of Li-doped NiO ceramics.* Ceramics International, 2012. **38**(6): p. 5023-5026.
14. Wang, Y.F., Lee, K.H., Ohta, H., and Kournoto, K., *Fabrication and thermoelectric properties of heavily rare-earth metal-doped SrO(SrTiO3)(n) (n=1, 2) ceramics.* Ceramics International, 2008. **34**(4): p. 849-852.
15. Balint, T.S. and Jordan, J.F., *RPS strategies to enable NASA's next decade robotic Mars missions.* Acta Astronautica, 2007. **60**(12): p. 992-1001.
16. Elsheikh, M.H., Shnawah, D.A., Sabri, M.F.M., Said, S.B.M., Hassan, M.H., Bashir, M.B.A., and Mohamad, M., *A review on thermoelectric renewable energy: Principle parameters that affect their performance.* Renewable & Sustainable Energy Reviews, 2014. **30**: p. 337-355.
17. Minnich, A.J., Dresselhaus, M.S., Ren, Z.F., and Chen, G., *Bulk nanostructured thermoelectric materials: current research and future prospects.* Energy & Environmental Science, 2009. **2**(5): p. 466-479.
18. Snyder, G.J. and Toberer, E.S., *Complex thermoelectric materials.* Nature Materials, 2008. **7**(2): p. 105-114.
19. Lan, Y., Minnich, A.J., Chen, G., and Ren, Z., *Enhancement of Thermoelectric Figure-of-Merit by a Bulk Nanostructuring Approach.* Advanced Functional Materials, 2010. **20**(3): p. 357-376.
20. Li, J.-F., Liu, W.-S., Zhao, L.-D., and Zhou, M., *High-performance nanostructured thermoelectric materials.* Npg Asia Materials, 2010. **2**(4): p. 152-158.
21. Vineis, C.J., Shakouri, A., Majumdar, A., and Kanatzidis, M.G., *Nanostructured Thermoelectrics: Big Efficiency Gains from Small Features.* Advanced Materials, 2010. **22**(36): p. 3970-3980.
22. Kanatzidis, M.G., *Nanostructured Thermoelectrics: The New Paradigm?* Chemistry of Materials, 2010. **22**(3): p. 648-659.
23. He, W., Zhang, G., Zhang, X., Ji, J., Li, G., and Zhao, X., *Recent development and application of thermoelectric generator and cooler.* Applied Energy, 2015. **143**: p. 1-25.

24. Zebarjadi, M., Esfarjani, K., Dresselhaus, M.S., Ren, Z.F., and Chen, G., *Perspectives on thermoelectrics: from fundamentals to device applications.* Energy & Environmental Science, 2012. **5**(1): p. 5147-5162.
25. Heremans, J.P., Wiendlocha, B., and Chamoire, A.M., *Resonant levels in bulk thermoelectric semiconductors.* Energy & Environmental Science, 2012. **5**(2): p. 5510-5530.
26. Liu, W., Yan, X., Chen, G., and Ren, Z., *Recent advances in thermoelectric nanocomposites.* Nano Energy, 2012. **1**(1): p. 42-56.
27. Pei, Y., Wang, H., and Snyder, G.J., *Band Engineering of Thermoelectric Materials.* Advanced Materials, 2012. **24**(46): p. 6125-6135.
28. Fergus, J.W., *Oxide materials for high temperature thermoelectric energy conversion.* Journal of the European Ceramic Society, 2012. **32**(3): p. 525-540.
29. Brazier, K. *Thermoelectric Generator Diagram*. 2008 [cited 2015 01/09/2015]; A diagram of a thermoelectric generator.]. Available from: http://commons.wikimedia.org/wiki/File:Thermoelectric_Generator_Diagram.svg.
30. Carnot, S., Thurston, R.H., Carnot, H., and Kelvin, W.T.B., *Reflections on the Motive Power of Heat and on Machines Fitted to Develop that Power*1890: J. Wiley.
31. Carcasci, C. and Facchini, B., *Comparison between two gas turbine solutions to increase combined power plant efficiency.* Energy Conversion and Management, 2000. **41**(8): p. 757-773.
32. Reitz, R.D., *Directions in internal combustion engine research.* Combustion and Flame, 2013. **160**(1): p. 1-8.
33. Yu, C. and Chau, K.T., *Thermoelectric automotive waste heat energy recovery using maximum power point tracking.* Energy Conversion and Management, 2009. **50**(6): p. 1506-1512.
34. Hsu, C.-T., Huang, G.-Y., Chu, H.-S., Yu, B., and Yao, D.-J., *Experiments and simulations on low-temperature waste heat harvesting system by thermoelectric power generators.* Applied Energy, 2011. **88**(4): p. 1291-1297.
35. Matsubara, K. and Ieee, I., *Development of a high efficient thermoelectric stack for a waste exhaust heat recovery of vehicles*. Xxi International Conference on Thermoelectrics, Proceedings Ict '022002. 418-423.

36. Vullers, R.J.M., van Schaijk, R., Doms, I., Van Hoof, C., and Mertens, R., *Micropower energy harvesting.* Solid-State Electronics, 2009. **53**(7): p. 684-693.
37. Kishi, M., Nemoto, H., Hamao, T., Yamamoto, M., Sudou, S., Mandai, M., and Yamamoto, S. *Micro thermoelectric modules and their application to wristwatches as an energy source*. in *Thermoelectrics, 1999. Eighteenth International Conference on*. 1999.
38. Kim, S.J., We, J.H., and Cho, B.J., *A wearable thermoelectric generator fabricated on a glass fabric.* Energy & Environmental Science, 2014. **7**(6): p. 1959-1965.
39. Harman, T.C., Cahn, J.H., and Logan, M.J., *Measurement of thermal conductivity by utilization of the Peltier effect.* Journal of Applied Physics, 1959. **30**(9): p. 1351-1359.
40. DiSalvo, F.J., *Thermoelectric cooling and power generation.* Science, 1999. **285**(5428): p. 703-706.
41. Brazier, K. *Thermoelectric Cooler Diagram*. 2008 [cited 2015 01/09/2015]; A diagram of a thermoelectric cooler.]. Available from: http://commons.wikimedia.org/wiki/File:Thermoelectric_Cooler_Diagram.svg.
42. Cai, K.F., Mueller, E., Drasar, C., and Stiewe, C., *The effect of titanium diboride addition on the thermoelectric properties of β-FeSi2 semiconductors.* Solid State Communications, 2004. **131**(5): p. 325-329.
43. Zide, J.M.O., Vashaee, D., Bian, Z.X., Zeng, G., Bowers, J.E., Shakouri, A., and Gossard, A.C., *Demonstration of electron filtering to increase the Seebeck coefficient in In(0.53)Ga(0.47)As/In(0.53)Ga(0.28)Al(0.19)As superlattices.* Physical Review B, 2006. **74**(20).
44. Rowe, D.M., *CRC Handbook of Thermoelectrics*1995: Taylor & Francis.
45. Seebeck, T.J., *Ueber die magnetische Polarisation der Metalle und Erze durch Temperaturdifferenz.* Annalen der Physik, 1826. **82**(3): p. 253-286.
46. Song, F., Wu, L., and Liang, S., *Giant Seebeck coefficient thermoelectric device of MnO2 powder.* Nanotechnology, 2012. **23**(8).
47. Hohn, C., Galffy, M., Dascoulidou, A., Freimuth, A., Soltner, H., and Poppe, U., *Seebeck-effect in the mixed state of Y-Ba-Cu-O.* Zeitschrift Fur Physik B-Condensed Matter, 1991. **85**(2): p. 161-168.
48. Snyder, G.J. and Ursell, T.S., *Thermoelectric efficiency and compatibility.* Physical Review Letters, 2003. **91**(14): p. 148301.

49. Kanamori, H., Fujii, N., and Mizutani, H., *Thermal diffusivity measurement of rock-forming minerals from 300° to 1100°K.* Journal of Geophysical Research, 1968. **73**(2): p. 595-605.
50. Lu, K., *Materials in Energy Conversion, Harvesting, and Storage*2014: Wiley.
51. Bulusu, A. and Walker, D.G., *Review of electronic transport models for thermoelectric materials.* Superlattices and Microstructures, 2008. **44**(1).
52. Goncalves, A.P., Lopes, E.B., Delaizir, G., Vaney, J.B., Lenoir, B., Piarristeguy, A., Pradel, A., Monnier, J., Ochin, P., and Godart, C., *Semiconducting glasses: A new class of thermoelectric materials?* Journal of Solid State Chemistry, 2012. **193**: p. 26-30.
53. Tan, G., Wang, S., Yan, Y., Li, H., and Tang, X., *Enhanced thermoelectric performance in p-type Ca0.5Ce0.5Fe4-xNixSb12 skutterudites by adjusting the carrier concentration.* Journal of Alloys and Compounds, 2012. **513**: p. 328-333.
54. Dmitriev, A.V. and Zvyagin, I.P., *Current trends in the physics of thermoelectric materials.* Physics-Uspekhi, 2010. **53**(8): p. 789-803.
55. Wang, S., Fu, F., She, X., Zheng, G., Li, H., and Tang, X., *Optimizing thermoelectric performance of Cd-doped beta-Zn4Sb3 through self-adjusting carrier concentration.* Intermetallics, 2011. **19**(12): p. 1823-1830.
56. Sootsman, J.R., Chung, D.Y., and Kanatzidis, M.G., *New and Old Concepts in Thermoelectric Materials.* Angewandte Chemie-International Edition, 2009. **48**(46): p. 8616-8639.
57. Poudel, B., Hao, Q., Ma, Y., Lan, Y., Minnich, A., Yu, B., Yan, X., Wang, D., Muto, A., Vashaee, D., Chen, X., Liu, J., Dresselhaus, M.S., Chen, G., and Ren, Z., *High-thermoelectric performance of nanostructured bismuth antimony telluride bulk alloys.* Science, 2008. **320**(5876): p. 634-638.
58. Goldsmid, H.J., *The thermal conductivity of bismuth telluride.* Proceedings of the Physical Society of London Section B, 1956. **69**(2): p. 203-209.
59. Mishra, S.K., Satpathy, S., and Jepsen, O., *Electronic structure and thermoelectric properties of bismuth telluride and bismuth selenide.* Journal of Physics-Condensed Matter, 1997. **9**(2): p. 461-470.
60. Huang, B.-L. and Kaviany, M., *Ab initio and molecular dynamics predictions for electron and phonon transport in bismuth telluride.* Physical Review B, 2008. **77**(12).

61. Madsen, G.K.H. and Singh, D.J., *BoltzTraP. A code for calculating band-structure dependent quantities.* Computer Physics Communications, 2006. **175**(1): p. 67-71.
62. Kusano, D., Hori, Y., and Ieee, I., *Effects of PbTe doping on the thermoelectric properties of (Bi2Te3)(0.2)(Sb2Te3)(0.8)*. Xxi International Conference on Thermoelectrics, Proceedings Ict '022002. 13-16.
63. Poudeu, P.F.P., D'Angelo, J., Kong, H., Downey, A., Short, J.L., Pcionek, R., Hogan, T.P., Uher, C., and Kanatzidis, M.G., *Nanostructures versus solid solutions: Low lattice thermal conductivity and enhanced thermoelectric figure of merit in Pb9.6Sb0.2Te10-xSex bulk materials.* Journal of the American Chemical Society, 2006. **128**(44): p. 14347-14355.
64. Shelimova, L.E., Konstantinov, P.P., Karpinskii, O.G., Avilov, E.S., Kretova, M.A., and Zemskov, V.S., *Thermoelectric properties of PbBi4Te7-Based anion-substituted layered solid solutions.* Inorganic Materials, 2004. **40**(11): p. 1146-1152.
65. Wright, D.A., *Thermoelectric properties of bismuth telluride and its alloys.* Nature, 1958. **181**(4612): p. 834-834.
66. Christensen, M., Abrahamsen, A.B., Christensen, N.B., Juranyi, F., Andersen, N.H., Lefmann, K., Andreasson, J., Bahl, C.R.H., and Iversen, B.B., *Avoided crossing of rattler modes in thermoelectric materials.* Nature Materials, 2008. **7**(10): p. 811-815.
67. Zhang, J., Xu, B., Wang, L.-M., Yu, D., Yang, J., Yu, F., Liu, Z., He, J., Wen, B., and Tian, Y., *High-pressure synthesis of phonon-glass electron-crystal featured thermoelectric LixCo4Sb12.* Acta Materialia, 2012. **60**(3): p. 1246-1251.
68. Wiebcke, M., *Structural links between zeolite-type and clathrate hydrate-type materials.* Journal of the Chemical Society-Chemical Communications, 1991(21): p. 1507-1508.
69. Kleinke, H., *New bulk Materials for Thermoelectric Power Generation: Clathrates and Complex Antimonides.* Chemistry of Materials, 2010. **22**(3): p. 604-611.
70. Christensen, M., Juranyi, F., and Iversen, B.B., *The rattler effect in thermoelectric clathrates studied by inelastic neutron scattering.* Physica B-Condensed Matter, 2006. **385**: p. 505-507.

71. Alboni, P.N., Ji, X., He, J., Gothard, N., Hubbard, J., and Tritt, T.M., *Synthesis and thermoelectric properties of "nano-engineered" CoSb3 skutterudite materials.* Journal of Electronic Materials, 2007. **36**(7): p. 711-715.

72. Wang, S.-H., Cheng, H.-M., Wu, R.-J., and Chao, W.-H., *Structural and thermoelectric properties of HfNiSn half-Heusler thin films.* Thin Solid Films, 2010. **518**(21): p. 5901-5904.

73. Zou, M., Li, J.-F., and Kita, T., *Thermoelectric properties of fine-grained FeVSb half-Heusler alloys tuned to p-type by substituting vanadium with titanium.* Journal of Solid State Chemistry, 2013. **198**: p. 125-130.

74. Wang, H.C., Wang, C.L., Su, W.B., Liu, J., Zhao, Y., Peng, H., Zhang, J.L., Zhao, M.L., Li, J.C., Yin, N., and Mei, L.M., *Enhancement of thermoelectric figure of merit by doping Dy in La0.1Sr0.9TiO3 ceramic.* Materials Research Bulletin, 2010. **45**(7): p. 809-812.

75. Terasaki, I., *Transport properties and electronic states of the thermoelectric oxide NaCo2O4.* Physica B-Condensed Matter, 2003. **328**(1-2): p. 63-67.

76. Tsubota, T., Ohtaki, M., Eguchi, K., and Arai, H., *Transport properties and thermoelectric performance of (Zn1-yMgy)(1-x)AlxO.* Journal of Materials Chemistry, 1998. **8**(2): p. 409-412.

77. Kenfaui, D., Chateigner, D., Gomina, M., and Noudem, J.G., *Texture, mechanical and thermoelectric properties of Ca3Co4O9 ceramics.* Journal of Alloys and Compounds, 2010. **490**(1-2): p. 472-479.

78. Tajima, S., Tani, T., Isobe, S., and Koumoto, K., *Thermoelectric properties of highly textured NaCo2O4 ceramics processed by the reactive templated grain growth (RTGG) method.* Materials Science and Engineering B-Solid State Materials for Advanced Technology, 2001. **86**(1): p. 20-25.

79. Yasukawa, M., Kono, T., Ueda, K., Yanagi, H., and Hosono, H., *High-temperature thermoelectric properties of La-doped BaSnO3 ceramics.* Materials Science and Engineering B-Advanced Functional Solid-State Materials, 2010. **173**(1-3): p. 29-32.

80. Yasukawa, M. and Kono, T., *Preparation of dense BaPbO3-based ceramics by a coprecipitation and their thermoelectric properties.* Journal of Alloys and Compounds, 2006. **426**(1-2): p. 420-425.

81. Liu, J., Wang, C.L., Su, W.B., Wang, H.C., Li, J.C., Zhang, J.L., and Mei, L.M., *Thermoelectric properties of Sr1-xNdxTiO3 ceramics.* Journal of Alloys and Compounds, 2010. **492**(1-2): p. L54-L56.
82. Balandin, A.A., *Thermal properties of graphene and nanostructured carbon materials.* Nature Materials, 2011. **10**(8): p. 569-581.
83. Terazawa, Y., Mikami, M., Itoh, T., and Takeuchi, T., *Effects of Heavy Element Substitution on Electronic Structure and Lattice Thermal Conductivity of Fe(2)VA1 Thermoelectric Material.* Journal of the Japan Institute of Metals, 2012. **76**(3): p. 216-221.
84. Takeuchi, T., Nagasako, N., Asahi, R., and Mizutani, U., *Extremely small thermal conductivity of the Al-based Mackay-type 1/1-cubic approximants.* Physical Review B, 2006. **74**(5).
85. Klemens, P.G., *The scattering of low-frequency lattice waves by static imperfections.* Proceedings of the Physical Society of London Section A, 1955. **68**(12): p. 1113-1128.
86. Onoda, M. and Tsukahara, S., *The upper limit of thermoelectric power factors in the metal-band-insulator crossover of the perovskite-type oxygen deficient system SrTiO3-(delta/2).* Journal of Physics-Condensed Matter, 2011. **23**(4).
87. Mi, Y., Geneste, G., Rault, J.E., Mathieu, C., Pancotti, A., and Barrett, N., *Polarization dependent chemistry of ferroelectric BaTiO3(001) domains.* Journal of Physics-Condensed Matter, 2012. **24**(27).
88. Lim, J., Hippalgaonkar, K., Andrews, S.C., Majumdar, A., and Yang, P., *Quantifying Surface Roughness Effects on Phonon Transport in Silicon Nanowires.* Nano Letters, 2012. **12**(5): p. 2475-2482.
89. Deng, Y., Zhang, Z., Wang, Y., and Xu, Y., *Preferential growth of Bi2Te3 films with a nanolayer structure: enhancement of thermoelectric properties induced by nanocrystal boundaries.* Journal of Nanoparticle Research, 2012. **14**(4).
90. Lan, J., Lin, Y.-H., Fang, H., Mei, A., Nan, C.-W., Liu, Y., Xu, S., and Peters, M., *High-Temperature Thermoelectric Behaviors of Fine-Grained Gd-Doped CaMnO3 Ceramics.* Journal of the American Ceramic Society, 2010. **93**(8): p. 2121-2124.
91. Cao, Y.Q., Zhu, T.J., and Zhao, X.B., *Low thermal conductivity and improved figure of merit in fine-grained binary PbTe thermoelectric alloys.* Journal of Physics D-Applied Physics, 2009. **42**(1).

92. Bertini, L., Billquist, K., Christensen, M., Gatti, C., Holmgren, L., Iversen, B., Mueller, E., Muhammed, M., Noriega, G., Palmqvist, A., Platzek, D., Rowe, D.M., Saramat, A., Stiewe, C., Toprak, M., Williams, S.G., Zhang, Y., and Ieee, *Thermoelectric properties of nano-grained CoSb3 skutterudites doped with Ni and Te*. Twenty-Second International Conference on Thermoelectrics, Proceedings Ict '032003. 48-51.

93. Wang, H., Dong, X., Peng, S., Dong, L., and Wang, Y., *Improvement of thermoelectric properties of WO3 ceramics by ZnO addition.* Journal of Alloys and Compounds, 2012. **527**: p. 204-209.

94. Yang, J.-Y., Wu, J., Li, G., Zhang, J.-S., and Peng, J., *Preparation and Thermoelectric Properties of Polycrystalline In4Sn3-x by Mechanical Alloying and Hot Pressing.* Journal of Electronic Materials, 2012. **41**(6): p. 1077-1080.

95. Dresselhaus, M.S., Chen, G., Tang, M.Y., Yang, R., Lee, H., Wang, D., Ren, Z., Fleurial, J.-P., and Gogna, P., *New directions for low-dimensional thermoelectric materials.* Advanced Materials, 2007. **19**(8): p. 1043-1053.

96. Hochbaum, A.I., Chen, R., Delgado, R.D., Liang, W., Garnett, E.C., Najarian, M., Majumdar, A., and Yang, P., *Enhanced thermoelectric performance of rough silicon nanowires.* Nature, 2008. **451**(7175): p. 163-U5.

97. Abutaha, A.I., Kumar, S.R.S., Li, K., Dehkordi, A.M., Tritt, T.M., and Ashareef, H.N., *Enhanced Thermoelectric Figure-of-Merit in Thermally Robust, Nanostructured Super lattices Based on SrTiO3.* Chemistry of Materials, 2015. **27**(6): p. 2165-2171.

98. Hicks, L.D. and Dresselhaus, M.S., *Effect of quantum-well structures on the thermoelectric figure of merit.* Physical Review B, 1993. **47**(19): p. 12727-12731.

99. Venkatasubramanian, R., Siivola, E., Colpitts, T., and O'Quinn, B., *Thin-film thermoelectric devices with high room-temperature figures of merit.* Nature, 2001. **413**(6856): p. 597-602.

100. Chiritescu, C., Cahill, D.G., Nguyen, N., Johnson, D., Bodapati, A., Keblinski, P., and Zschack, P., *Ultralow thermal conductivity in disordered, layered WSe2 crystals.* Science, 2007. **315**(5810): p. 351-353.

101. Harman, T.C., Taylor, P.J., Walsh, M.P., and LaForge, B.E., *Quantum dot superlattice thermoelectric materials and devices.* Science, 2002. **297**(5590): p. 2229-2232.

102. Hsu, K.F., Loo, S., Guo, F., Chen, W., Dyck, J.S., Uher, C., Hogan, T., Polychroniadis, E.K., and Kanatzidis, M.G., *Cubic AgPbmSbTe2+m: Bulk thermoelectric materials with high figure of merit.* Science, 2004. **303**(5659): p. 818-821.

103. Bao, Y., Liu, W.L., Shamsa, M., Alim, K., Balandin, A.A., and Liu, J.L., *Electrical and thermal conductivity of Ge/Si quantum dot superlattices.* Journal of the Electrochemical Society, 2005. **152**(6): p. G432-G435.

104. Wang, H., Li, J.F., Nan, C.W., Zhou, M., Liu, W.S., Zhang, B.P., and Kita, T., *High-performance Ag0.8Pb18+xSbTe20 thermoelectric bulk materials fabricated by mechanical alloying and spark plasma sintering.* Applied Physics Letters, 2006. **88**(9).

105. Wu, L., Zheng, J.-C., Zhou, J., Li, Q., Yang, J., and Zhu, Y., *Nanostructures and defects in thermoelectric AgPb18SbTe20 single crystal.* Journal of Applied Physics, 2009. **105**(9).

106. Poudeu, P.F.R., D'Angelo, J., Downey, A.D., Short, J.L., Hogan, T.P., and Kanatzidis, M.G., *High thermoelectric figure of merit and nanostructuring in bulk p-type Na1-xPbmSbyTem+2.* Angewandte Chemie-International Edition, 2006. **45**(23): p. 3835-3839.

107. Androulakis, J., Lin, C.-H., Kong, H.-J., Uher, C., Wu, C.-I., Hogan, T., Cook, B.A., Caillat, T., Paraskevopoulos, K.M., and Kanatzidis, M.G., *Spinodal decomposition and nucleation and growth as a means to bulk nanostructured thermoelectrics: Enhanced performance in Pb1-xSnxTe-PbS.* Journal of the American Chemical Society, 2007. **129**(31): p. 9780-9788.

108. Kim, W., Singer, S.L., Majumdar, A., Vashaee, D., Bian, Z., Shakouri, A., Zeng, G., Bowers, J.E., Zide, J.M.O., and Gossard, A.C., *Cross-plane lattice and electronic thermal conductivities of ErAs : InGaAs/InGaAlAs superlattices.* Applied Physics Letters, 2006. **88**(24).

109. Walker, C.T. and Pohl, R.O., *Phonon scattering by point defects.* Physical Review, 1963. **131**(4): p. 1433-&.

110. Kim, W., Zide, J., Gossard, A., Klenov, D., Stemmer, S., Shakouri, A., and Majumdar, A., *Thermal conductivity reduction and thermoelectric figure of merit increase by embedding nanoparticles in crystalline semiconductors.* Physical Review Letters, 2006. **96**(4).

111. Boukai, A.I., Bunimovich, Y., Tahir-Kheli, J., Yu, J.-K., Goddard, W.A., III, and Heath, J.R., *Silicon nanowires as efficient thermoelectric materials.* Nature, 2008. **451**(7175): p. 168-171.

112. Zhang, G., Yu, Q., Wang, W., and Li, X., *Nanostructures for Thermoelectric Applications: Synthesis, Growth Mechanism, and Property Studies.* Advanced Materials, 2010. **22**(17): p. 1959-1962.

113. Hicks, L.D. and Dresselhaus, M.S., *Thermoelectric figure of merit of a one-dimensional conductor.* Physical Review B, 1993. **47**(24): p. 16631-16634.

114. Oh, T.-S., *Thermoelectric Characteristics of p-Type (Bi,Sb)(2)Te-3/(Pb,Sn)Te Functional Gradient Materials with Variation of the Segment Ratio.* Journal of Electronic Materials, 2009. **38**(7): p. 1041-1047.

115. Landry, E.S., Hussein, M.I., and McGaughey, A.J.H., *Complex superlattice unit cell designs for reduced thermal conductivity.* Physical Review B, 2008. **77**(18).

116. Molinari, M., Tompsett, D.A., Parker, S.C., Azough, F., and Freer, R., *Structural, electronic and thermoelectric behaviour of CaMnO3 and CaMnO(3-delta).* Journal of Materials Chemistry A, 2014. **2**(34): p. 14109-14117.

117. Yang, J., Li, H., Wu, T., Zhang, W., Chen, L., and Yang, J., *Evaluation of Half-Heusler Compounds as Thermoelectric Materials Based on the Calculated Electrical Transport Properties.* Advanced Functional Materials, 2008. **18**(19): p. 2880-2888.

118. Balout, H., Boulet, P., and Record, M.-C., *Computational Investigation of the Electronic and Thermoelectric Properties of Strained Bulk Mg2Si.* Journal of Electronic Materials, 2014. **43**(10): p. 3801-3807.

119. Carbogno, C. *Thermal conductivity at high temperatures from first principles*. in *Seminar, Theoretische Chemie, Technische Universität*. 2012.

120. Turney, J.E., Landry, E.S., McGaughey, A.J.H., and Amon, C.H., *Predicting phonon properties and thermal conductivity from anharmonic lattice dynamics calculations and molecular dynamics simulations.* Physical Review B, 2009. **79**(6).

121. Togo, A., Oba, F., and Tanaka, I., *First-principles calculations of the ferroelastic transition between rutile-type and CaCl(2)-type SiO(2) at high pressures.* Physical Review B, 2008. **78**(13).

122. Togo, A., Chaput, L., and Tanaka, I., *Distributions of phonon lifetimes in Brillouin zones.* Physical Review B, 2015. **91**(9).

123. Schelling, P.K., Phillpot, S.R., and Keblinski, P., *Comparison of atomic-level simulation methods for computing thermal conductivity.* Physical Review B, 2002. **65**(14).

124. Green, M.S., *Markoff Random Processes and the Statistical Mechanics of Time-Dependent Phenomena. II. Irreversible Processes in Fluids.* Journal of Chemical Physics, 1954. **22**(3): p. 398-413.

125. Kubo, R., *Statistical-mechanical theory of irreversible processes. I. General theory and simple applications to magnetic and conduction problems.* Journal of the Physical Society of Japan, 1957. **12**(6): p. 570-586.

126. Muller-Plathe, F., *A simple nonequilibrium molecular dynamics method for calculating the thermal conductivity.* Journal of Chemical Physics, 1997. **106**(14): p. 6082-6085.

127. Shukla, P., Watanabe, T., Nino, J.C., Tulenko, J.S., and Phillpot, S.R., *Thermal transport properties of MgO and Nd2Zr2O7 pyrochlore by molecular dynamics simulation.* Journal of Nuclear Materials, 2008. **380**(1-3): p. 1-7.

128. Goh, W.F., Yoon, T.L., and Khan, S.A., *Molecular dynamics simulation of thermodynamic and thermal transport properties of strontium titanate with improved potential parameters.* Computational Materials Science, 2012. **60**: p. 123-129.

129. Schelling, P.K., Phillpot, S.R., and Keblinski, P., *Phonon wave-packet dynamics at semiconductor interfaces by molecular-dynamics simulation.* Applied Physics Letters, 2002. **80**(14): p. 2484-2486.

130. Jeng, M.-S., Yang, R., Song, D., and Chen, G., *Modeling the thermal conductivity and phonon transport in nanoparticle composites using Monte Carlo simulation.* Journal of Heat Transfer-Transactions of the Asme, 2008. **130**(4).

131. Pattamatta, A. and Madnia, C.K., *Modeling heat transfer in Bi2Te3-Sb2Te3 nanostructures.* International Journal of Heat and Mass Transfer, 2009. **52**(3-4): p. 860-869.

132. Born, M. and Huang, K., *Dynamical Theory of Crystal Lattices*, ed. O.U. Press1954, Oxford.

133. Ewald, P.P., *Die Berechnung optischer und elektrostatischer Gitterpotentiale.* Annalen der Physik, 1921. **369**(3): p. 253-287.

134. Leach, A., *Molecular Modelling: Principles and Applications (2nd Edition)*2001: Prentice Hall.
135. Kittel, C., *Introduction to Solid State Physics*2004: Wiley.
136. Aguado, A. and Madden, P.A., *Ewald summation of electrostatic multipole interactions up to the quadrupolar level.* Journal of Chemical Physics, 2003. **119**(14): p. 7471-7483.
137. Toukmaji, A.Y. and Board, J.A., *Ewald summation techniques in perspective: A survey.* Computer Physics Communications, 1996. **95**(2-3): p. 73-92.
138. Eastwood, J.W., Hockney, R.W., and Lawrence, D.N., *P3M3DP—The three-dimensional periodic particle-particle/particle-mesh program.* Computer Physics Communications, 1980. **19**(2): p. 215-261.
139. Hockney, R.W. and Eastwood, J.W., *Computer simulations using particles*1981, New York: McGraw-Hill.
140. Darden, T., York, D., and Pedersen, L., *Particle mesh Ewald: An N. log (N) method for Ewald sums in large systems.* Journal of Chemical Physics, 1993. **98**(12): p. 10089-10092.
141. Essmann, U., Perera, L., Berkowitz, M.L., Darden, T., Lee, H., and Pedersen, L.G., *A smooth particle mesh Ewald method.* Journal of Chemical Physics, 1995. **103**(19): p. 8577-8593.
142. Parry, D.E., *The electrostatic potential in the surface region of an ionic crystal.* Surface Science, 1975. **49**(2): p. 433-440.
143. Parry, D.E., *Correction.* Surface Science, 1976. **54**(1): p. 195-195.
144. Heyes, D.M., Barber, M., and Clarke, J.H.R., *Molecular dynamics computer simulation of surface properties of crystalline potassium chloride.* Journal of the Chemical Society-Faraday Transactions Ii, 1977. **73**: p. 1485-1496.
145. Lewis, G.V. and Catlow, C.R.A., *Potential models for ionic oxides.* Journal of Physics C-Solid State Physics, 1985. **18**(6): p. 1149-1161.
146. Jones, J.E., *On the Determination of Molecular Fields. I. From the Variation of the Viscosity of a Gas with Temperature.* Proceedings of the Royal Society of London. Series A, 1924. **106**(738): p. 441-462.
147. Jones, J.E., *On the Determination of Molecular Fields. II. From the Equation of State of a Gas.* Proceedings of the Royal Society of London. Series A, 1924. **106**(738): p. 463-477.

148. Kaplan, I.G., *Intermolecular interactions: physical picture, computational methods and model potentials*2006: Wiley.
149. Rahman, A., *Correlations in the Motion of Atoms in Liquid Argon.* Physical Review, 1964. **136**(2A): p. A405-A411.
150. Barker, J.A., Fisher, R.A., and Watts, R.O., *Liquid argon: Monte Carlo and molecular dynamics calculations.* Molecular Physics, 1971. **21**(4): p. 657-&.
151. Rowley, L.A., Nicholson, D., and Parsonage, N.G., *Monte Carlo grand canonical ensemble calculation in a gas-liquid transition region for 12-6 argon.* Journal of Computational Physics, 1975. **17**(4): p. 401-414.
152. White, J.A., *Lennard-Jones as a model for argon and test of extended renormalization group calculations.* Journal of Chemical Physics, 1999. **111**(20): p. 9352-9356.
153. Mie, G., *Zur kinetischen Theorie der einatomigen Körper.* Annalen der Physik, 1903. **316**(8): p. 657-697.
154. Buckingham, R.A., *The Classical Equation of State of Gaseous Helium, Neon and Argon*. Vol. 168. 1938. 264-283.
155. Morse, P.M., *Diatomic Molecules According to the Wave Mechanics. II. Vibrational Levels.* Physical Review, 1929. **34**(1): p. 57-64.
156. Pedone, A., Malavasi, G., Menziani, M.C., Cormack, A.N., and Segre, U., *A new self-consistent empirical interatomic potential model for oxides, silicates, and silica-based glasses.* Journal of Physical Chemistry B, 2006. **110**(24): p. 11780-11795.
157. Dick, B.G. and Overhauser, A.W., *Theory of the Dielectric Constants of Alkali Halide Crystals.* Physical Review, 1958. **112**(1): p. 90.
158. Lindan, P.J.D. and Gillan, M.J., *Shell-model molecular dynamics simulation of superionic conduction in CaF2.* Journal of Physics-Condensed Matter, 1993. **5**(8): p. 1019-1030.
159. Ferneyhough, R. and et al., *The melting of MgO studied by molecular dynamics simulation.* Modelling and Simulation in Materials Science and Engineering, 1994. **2**(6): p. 1101.
160. Mitchell, P.J. and Fincham, D., *Shell model simulations by adiabatic dynamics.* Journal of Physics-Condensed Matter, 1993. **5**(8): p. 1031-1038.

161. van Beest, B.W.H., Kramer, G.J., and van Santen, R.A., *Force fields for silicas and aluminophosphates based on ab initio calculations.* Physical Review Letters, 1990. **64**(16): p. 1955-1958.
162. Kramer, G.J., Farragher, N.P., van Beest, B.W.H., and van Santen, R.A., *Interatomic force fields for silicas, aluminophosphates, and zeolites: Derivation based on ab initio calculations.* Physical Review B, 1991. **43**(6): p. 5068-5080.
163. Canepa, P., *New Insights on Iron and Lead-based Materials Beyond Density Functional Theory*, 2012, University of Kent.
164. Toxvaerd, S. and Dyre, J.C., *Communication: Shifted forces in molecular dynamics.* Journal of Chemical Physics, 2011. **134**(8).
165. Watson, G.W., Kelsey, E.T., deLeeuw, N.H., Harris, D.J., and Parker, S.C., *Atomistic simulation of dislocations, surfaces and interfaces in MgO.* Journal of the Chemical Society-Faraday Transactions, 1996. **92**(3): p. 433-438.
166. Plimpton, S., *Fast parallel algorithms for short-range molecular dynamics.* Journal of Computational Physics, 1995. **117**(1): p. 1-19.
167. Fletcher, R. and Reeves, C.M., *Function minimization by conjugate gradients.* The Computer Journal, 1964. **7**(2): p. 149-154.
168. Norgett, M.J. and Fletcher, R., *Fast matrix methods for calculating the relaxation about defects in crystals.* Journal of Physics Part C Solid State Physics, 1970. **3**(11): p. L190-&.
169. Polak, E., *Computational Methods in Optimization: A Unified Approach. XA-GB*1971: Acad. Press.
170. Fletcher, R. and Powell, M.J.D., *A rapidly convergent descent method for minimization.* Computer Journal, 1963. **6**(2): p. 163-&.
171. Broyden, C.G., *The Convergence of a Class of Double-rank Minimization Algorithms 1. General Considerations.* IMA Journal of Applied Mathematics, 1970. **6**(1): p. 76-90.
172. Fletcher, R., *A new approach to variable metric algorithms.* Computer Journal, 1970. **13**(3): p. 317-&.
173. Goldfarb, D., *A family of variable-metric methods derived by variational means.* Mathematics of Computation, 1970. **24**(109): p. 23-&.
174. Shanno, D.F., *Conditioning of quasi-Newton methods for function minimization.* Mathematics of Computation, 1970. **24**(111): p. 647-&.

175. Bitzek, E., Koskinen, P., Gaehler, F., Moseler, M., and Gumbsch, P., *Structural relaxation made simple.* Physical Review Letters, 2006. **97**(17).
176. Toxvaerd, S., Heilmann, O.J., and Dyre, J.C., *Energy conservation in molecular dynamics simulations of classical systems.* Journal of Chemical Physics, 2012. **136**(22).
177. Verlet, L., *Computer" experiments" on classical fluids. I. Thermodynamical properties of Lennard-Jones molecules.* Physical Review, 1967. **159**(1): p. 98-&.
178. Swope, W.C., Andersen, H.C., Berens, P.H., and Wilson, K.R., *A computer simulation method for the calculation of equilibrium constants for the formation of physical clusters of molecules: Application to small water clusters.* Journal of Chemical Physics, 1982. **76**(1): p. 637-649.
179. Kroes, G.J., *The royal road to an energy-conserving predictor-corrector method.* Computer Physics Communications, 1992. **70**(1): p. 41-52.
180. Nose, S., *A Unified Formulation of the Constant Temperature Molecular-Dynamics Methods.* Journal of Chemical Physics, 1984. **81**(1): p. 511-519.
181. Nose, S., *A molecular dynamics method for simulations in the canonical ensemble.* Molecular Physics, 1984. **52**(2): p. 255-268.
182. Hoover, W.G., *Canonical dynamics: equilibrium phase-space distributions.* Physical Review A, 1985. **31**(3): p. 1695-1697.
183. Bertaut, F., *Le terme electrostatique de l'energie de surface.* Compte Rendus Hebdomadaire des Séances de l'Académie des Sciences, 1958. **246**: p. 3447-3450.
184. Tasker, P.W., *Stability of Ionic-Crystal Surfaces.* Journal of Physics C-Solid State Physics, 1979. **12**(22): p. 4977-4984.
185. Oliver, P., Parker, S., and Mackrodt, W., *Computer simulation of the crystal morphology of NiO.* Modelling and Simulation in Materials Science and Engineering, 1993. **1**(5): p. 755.
186. Gibbs, J.W., *The Collected Works*1928, New York: Longmans, Green and Co.
187. Wulff, G., *Zur Frage der Geschwindigkeit des Wachstums und der auflösung der Krystallflächen.* Zeitschrift fur Krystallographie und Mineralogie, 1901. **34**: p. 449-530.
188. Duffy, D.M., *Grain boundaries in ionic crystals.* Journal of Physics C-Solid State Physics, 1986. **19**(23): p. 4393-4412.

189. Lejcek, P., *Grain Boundary Segregation in Metals*, in *Grain Boundary Segregation in Metals*2010. p. 1-239.
190. Hsueh, H., Warren, M., Vass, H., Ackland, G., Clark, S., and Crain, J., *Vibrational properties of the layered semiconductor germanium sulfide under hydrostatic pressure: Theory and experiment.* Physical Review B, 1996. **53**(22): p. 14806.
191. Ackland, G., Warren, M., and Clark, S., *Practical methods in ab initio lattice dynamics.* Journal of Physics: Condensed Matter, 1997. **9**(37): p. 7861.
192. Dove, M.T., *Structure and Dynamics: An Atomic View of Materials*2003: OUP Oxford.
193. Schwen, D. *Phonon nu Process*. 2005 [cited 2015 01/09/2015]; Normal- and Umklapp scattering for phonons.]. Available from: http://commons.wikimedia.org/wiki/File:Phonon_nu_process.png.
194. Maznev, A. and Wright, O., *Demystifying umklapp vs normal scattering in lattice thermal conductivity.* American journal of physics, 2014. **82**(11): p. 1062-1066.
195. Trozzi, C. and Ciccotti, G., *Stationary nonequilibrium states by molecular dynamics. II. Newton's law.* Physical Review A, 1984. **29**(2): p. 916-925.
196. Baranyai, A., *Heat flow studies for large temperature gradients by molecular dynamics simulation.* Physical Review E, 1996. **54**(6): p. 6911-6917.
197. Maiti, A., Mahan, G.D., and Pantelides, S.T., *Dynamical simulations of nonequilibrium processes - Heat flow and the Kapitza resistance across grain boundaries.* Solid State Communications, 1997. **102**(7): p. 517-521.
198. Oligschleger, C. and Schon, J.C., *Simulation of thermal conductivity and heat transport in solids.* Physical Review B, 1999. **59**(6): p. 4125-4133.
199. Cao, B.-Y. and Li, Y.-W., *A uniform source-and-sink scheme for calculating thermal conductivity by nonequilibrium molecular dynamics.* Journal of Chemical Physics, 2010. **133**(2).
200. McGaughey, A. and Kaviany, M., *Molecular dynamics calculations of the thermal conductivity of silica based crystals.* Ann Arbor, 2002. **1001**: p. 48109-2125.
201. McGaughey, A.J. and Larkin, J.M., *Predicting phonon properties from equilibrium molecular dynamics simulations.* Ann. Rev. Heat Transfer, 2014. **17**: p. 49-87.

202. McGaughey, A.J.H. and Kaviany, M., *Thermal conductivity decomposition and analysis using molecular dynamics simulations - Part II. Complex silica structures.* International Journal of Heat and Mass Transfer, 2004. **47**(8-9): p. 1799-1816.

203. Zhou, X.W., Aubry, S., Jones, R.E., Greenstein, A., and Schelling, P.K., *Towards more accurate molecular dynamics calculation of thermal conductivity: Case study of GaN bulk crystals.* Physical Review B, 2009. **79**(11).

204. McGaughey, A.J. and Larkin, J.M., *Predicting phonon properties from equilibrium molecular dynamics simulations.*

205. McGaughey, A., Hussein, M., Landry, E., Kaviany, M., and Hulbert, G., *Phonon band structure and thermal transport correlation in a layered diatomic crystal.* Physical Review B, 2006. **74**(10): p. 104304.

206. Li, J., Porter, L., and Yip, S., *Atomistic modeling of finite-temperature properties of crystalline β-SiC: II. Thermal conductivity and effects of point defects.* Journal of Nuclear Materials, 1998. **255**(2): p. 139-152.

207. Dubrovinsky, L., Dubrovinskaia, N., Saxena, S., Annersten, H., Hålenius, E., Harryson, H., Tutti, F., Rekhi, S., and Le Bihan, T., *Stability of ferropericlase in the lower mantle.* Science, 2000. **289**(5478): p. 430-432.

208. Katsura, T., *Thermal diffusivity of periclase at high temperatures and high pressures.* Physics of the earth and planetary interiors, 1997. **101**(1): p. 73-77.

209. Sadowski, T., *Modelling of semi-brittle MgO ceramic behaviour under compression.* Mechanics of materials, 1994. **18**(1): p. 1-16.

210. Kvachadze, V., Dekanozishvili, G., Kalabegishvili, T., Vylet, V., Galustashvili, M., Akhvlediani, Z., Keratishvili, N., and Zardiashvili, D., *Thermally stimulated luminescence of MgO ceramic and single crystal samples irradiated in reactor.* Radiation Effects & Defects in Solids, 2007. **162**(1): p. 17-24.

211. Wereszczak, A., Kirkland, T., and Curtis, W., *Creep of CaO/SiO2-Containing MgO Refractories.* Journal of Materials Science, 1999. **34**(2): p. 215-227.

212. Medvedev, P., Frank, S., O'Holleran, T., and Meyer, M., *Dual phase MgO–ZrO 2 ceramics for use in LWR inert matrix fuel.* Journal of Nuclear Materials, 2005. **342**(1): p. 48-62.

213. Yates, S., Xu, P., Wang, J., Tulenko, J., and Nino, J., *Processing of magnesia–pyrochlore composites for inert matrix materials.* Journal of Nuclear Materials, 2007. **362**(2): p. 336-342.

214. Shin, W. and Murayama, N., *High performance p-type thermoelectric oxide based on NiO.* Materials Letters, 2000. **45**(6): p. 302-306.

215. Touloukian, Y.S., Powell, R.W., Ho, C.Y., and Klemens, P.G., *Thermophysical Properties of Matter - The TPRC Data Series. Volume 2. Thermal Conductivity - Nonmetallic Solids*1971: Defense Technical Information Center.

216. Slifka, A., Filla, B., and Phelps, J., *Thermal conductivity of magnesium oxide from absolute, steady-state measurements.* Journal of research of the National Institute of Standards and Technology, 1998. **103**(4): p. 357-363.

217. Hofmeister, A.M., *Thermal diffusivity and thermal conductivity of single-crystal MgO and Al2O3 and related compounds as a function of temperature.* Physics and Chemistry of Minerals, 2014. **41**(5): p. 361-371.

218. Skelton, J.M., Parker, S.C., Togo, A., Tanaka, I., and Walsh, A., *Thermal physics of the lead chalcogenides PbS, PbSe, and PbTe from first principles.* Physical Review B, 2014. **89**(20).

219. Stackhouse, S., Stixrude, L., and Karki, B.B., *Thermal conductivity of periclase (MgO) from first principles.* Physical Review Letters, 2010. **104**(20): p. 208501.

220. de Koker, N., *Thermal conductivity of MgO periclase from equilibrium first principles molecular dynamics.* Physical Review Letters, 2009. **103**(12): p. 125902.

221. Sangster, M. and Stoneham, A., *Calculation of absolute diffusion rates in oxides.* Journal of Physics C: Solid State Physics, 1984. **17**(34): p. 6093.

222. Landuzzi, F., Pasquini, L., Giusepponi, S., Celino, M., Montone, A., Palla, P., and Cleri, F., *Molecular dynamics of ionic self-diffusion at an MgO grain boundary.* Journal of Materials Science, 2015. **50**(6): p. 2502-2509.

223. Harding, J., Harris, D., and Parker, S., *Atomistic simulation of steps on the MgO (100) surface.* Surface Science, 1999. **422**(1): p. L183-L187.

224. Sayle, D.C., Seal, S., Wang, Z., Mangili, B.C., Price, D.W., Karakoti, A.S., Kuchibhatla, S.V., Hao, Q., Mobus, G., and Xu, X., *Mapping nanostructure: a systematic enumeration of nanomaterials by assembling nanobuilding blocks at crystallographic positions.* Acs Nano, 2008. **2**(6): p. 1237-1251.

225. Wyckoff, R.W.G. and Wyckoff, R.W., *Crystal structures*. Vol. 1. 1960: Interscience New York.

226. Isaak, D.G., Anderson, O.L., and Goto, T., *Measured elastic moduli of single-crystal MgO up to 1800 K.* Physics and Chemistry of Minerals, 1989. **16**(7): p. 704-713.

227. Srolovitz, D.J. and Vitek, V., *Atomistic simulation of materials: Beyond pair potentials*2012: Springer Science & Business Media.

228. Watanabe, T., Sinnott, S.B., Tulenko, J.S., Grimes, R.W., Schelling, P.K., and Phillpot, S.R., *Thermal transport properties of uranium dioxide by molecular dynamics simulations.* Journal of Nuclear Materials, 2008. **375**(3): p. 388-396.

229. Dubrovinsky, L. and Saxena, S., *Thermal expansion of periclase (MgO) and tungsten (W) to melting temperatures.* Physics and Chemistry of Minerals, 1997. **24**(8): p. 547-550.

230. Fiquet, G., Richet, P., and Montagnac, G., *High-temperature thermal expansion of lime, periclase, corundum and spinel.* Physics and Chemistry of Minerals, 1999. **27**(2): p. 103-111.

231. Tritt, T.M., *Thermal conductivity: theory, properties, and applications*2004: Springer Science & Business Media.

232. Voneshen, D., Refson, K., Borissenko, E., Krisch, M., Bosak, A., Piovano, A., Cemal, E., Enderle, M., Gutmann, M., and Hoesch, M., *Suppression of thermal conductivity by rattling modes in thermoelectric sodium cobaltate.* Nature Materials, 2013. **12**(11): p. 1028-1032.

233. Abascal, J.L.F., Sanz, E., Fernandez, R.G., and Vega, C., *A potential model for the study of ices and amorphous water: TIP4P/Ice.* Journal of Chemical Physics, 2005. **122**(23).

234. Chaudhari, P.t. and Matthews, J., *Coincidence twist boundaries between crystals of MgO smoke.* Applied Physics Letters, 1970. **17**(3): p. 115-117.

235. Nowak, J.D. and Carter, C.B., *Forming contacts and grain boundaries between MgO nanoparticles.* Journal of Materials Science, 2009. **44**(9): p. 2408-2418.

236. Ohta, H., Kim, S., Mune, Y., Mizoguchi, T., Nomura, K., Ohta, S., Nomura, T., Nakanishi, Y., Ikuhara, Y., Hirano, M., Hosono, H., and Koumoto, K., *Giant thermoelectric Seebeck coefficient of two-dimensional electron gas in SrTiO3.* Nature Materials, 2007. **6**(2): p. 129-134.

237. Wang, N., Han, L., He, H., Ba, Y., and Koumoto, K., *Effects of mesoporous silica addition on thermoelectric properties of Nb-doped SrTiO 3.* Journal of Alloys and Compounds, 2010. **497**(1): p. 308-311.

238. Höche, T., Neumann, W., Esmaeilzadeh, S., Uecker, R., Lentzen, M., and Rüssel, C., *The crystal structure of Sr 2 TiSi 2 O 8.* Journal of Solid State Chemistry, 2002. **166**(1): p. 15-23.

239. Dove, M.T., Heine, V., and Hammonds, K.D., *Rigid unit modes in framework silicates.* Mineralogical Magazine, 1995. **59**(397): p. 629-640.

240. El Goresy, A., Dera, P., Sharp, T.G., Prewitt, C.T., Chen, M., Dubrovinsky, L., Wopenka, B., Boctor, N.Z., and Hemley, R.J., *Seifertite, a dense orthorhombic polymorph of silica from the Martian meteorites Shergotty and Zagami.* European Journal of Mineralogy, 2008. **20**(4): p. 523-528.

241. Lakshtanov, D.L., Sinogeikin, S.V., and Bass, J.D., *High-temperature phase transitions and elasticity of silica polymorphs.* Physics and Chemistry of Minerals, 2007. **34**(1): p. 11-22.

242. Jung, J.S., Park, J.W., and Seo, G., *Catalytic cracking of n-octane over alkali-treated MFI zeolites.* Applied Catalysis A: General, 2005. **288**(1): p. 149-157.

243. Vessal, B., Amini, M., and Catlow, C., *Computer simulation of the structure of silica glass.* Journal of Non-Crystalline Solids, 1993. **159**(1): p. 184-186.

244. Tsuneyuki, S., Matsui, Y., Aoki, H., and Tsukada, M., *New pressure-induced structural transformations in silica obtained by computer simulation.* Nature, 1989. **339**(6221): p. 209-211.

245. Nicholas, J.B., Hopfinger, A.J., Trouw, F.R., and Iton, L.E., *Molecular modeling of zeolite structure. 2. Structure and dynamics of silica sodalite and silicate force field.* Journal of the American Chemical Society, 1991. **113**(13): p. 4792-4800.

246. Tautz, F.S., Heine, V., Dove, M.T., and Chen, X., *Rigid unit modes in the molecular dynamics simulation of quartz and the incommensurate phase transition.* Physics and Chemistry of Minerals, 1991. **18**(5): p. 326-336.

247. Wells, S.A., Dove, M.T., Tucker, M.G., and Trachenko, K., *Real-space rigid-unit-mode analysis of dynamic disorder in quartz, cristobalite and amorphous silica.* Journal of Physics: Condensed Matter, 2002. **14**(18): p. 4645.

248. Barrera, G.D., Bruno, J.A.O., Barron, T.H.K., and Allan, N.L., *Negative thermal expansion.* Journal of Physics: Condensed Matter, 2005. **17**(4): p. R217.

249. Welche, P.R.L., Heine, V., and Dove, M.T., *Negative thermal expansion in beta-quartz.* Physics and Chemistry of Minerals, 1998. **26**(1): p. 63-77.

250. Herzbach, D., Binder, K., and Müser, M.H., *Comparison of model potentials for molecular-dynamics simulations of silica.* The Journal of Chemical Physics, 2005. **123**(12): p. 124711.

251. Van Duin, A.C., Strachan, A., Stewman, S., Zhang, Q., Xu, X., and Goddard, W.A., *ReaxFFSiO reactive force field for silicon and silicon oxide systems.* The Journal of Physical Chemistry A, 2003. **107**(19): p. 3803-3811.

252. Müser, M. and Binder, K., *Molecular dynamics study of the α–β transition in quartz: elastic properties, finite size effects, and hysteresis in the local structure.* Physics and Chemistry of Minerals, 2001. **28**(10): p. 746-755.

253. Tse, J.S. and Klug, D.D., *Mechanical instability of α-quartz: A molecular dynamics study.* Physical Review Letters, 1991. **67**(25): p. 3559-3562.

254. Benoit, M. and Kob, W., *The vibrational dynamics of vitreous silica: Classical force fields vs. first principles.* EPL (Europhysics Letters), 2002. **60**(2): p. 269.

255. Farrow, M.R. and Probert, M.I., *Atomistic molecular dynamics simulations of shock compressed quartz.* The Journal of Chemical Physics, 2011. **135**(4): p. 044508.

256. Watson, G.W. and Parker, S.C., *Dynamical instabilities in α-quartz and α-berlinite: A mechanism for amorphization.* Physical Review B, 1995. **52**(18): p. 13306-13309.

257. Watson, G.W. and Parker, S.C., *Quartz amorphization: a dynamical instability.* Philosophical Magazine Letters, 1995. **71**(1): p. 59-64.

258. Vollmayr, K., Kob, W., and Binder, K., *Cooling-rate effects in amorphous silica: A computer-simulation study.* Physical Review B, 1996. **54**(22): p. 15808.

259. Benoit, M., Ispas, S., Jund, P., and Jullien, R., *Model of silica glass from combined classical and ab initio molecular-dynamics simulations.* The European Physical Journal B-Condensed Matter and Complex Systems, 2000. **13**(4): p. 631-636.

260. Van Ginhoven, R.M., Jónsson, H., and Corrales, L.R., *Silica glass structure generation for ab initio calculations using small samples of amorphous silica.* Physical Review B, 2005. **71**(2): p. 024208.

261. Kimizuka, H., Kaburaki, H., and Kogure, Y., *Molecular-dynamics study of the high-temperature elasticity of quartz above the α-β phase transition.* Physical Review B, 2003. **67**(2): p. 024105.

262. Saika-Voivod, I., Sciortino, F., Grande, T., and Poole, P.H., *Phase diagram of silica from computer simulation.* Physical Review E, 2004. **70**(6): p. 061507.

263. Vashishta, P., Kalia, R.K., Rino, J.P., and Ebbsjö, I., *Interaction potential for SiO 2: a molecular-dynamics study of structural correlations.* Physical Review B, 1990. **41**(17): p. 12197.

264. Ma, Y. and Garofalini, S., *Lattice dynamics and molecular-dynamics study of quartz using a many-body variable potential.* Physical Review B, 2006. **73**(17): p. 174109.

265. de Boer, K., Jansen, A.P.J., van Santen, R.A., Watson, G.W., and Parker, S.C., *Free-energy calculations of thermodynamic, vibrational, elastic, and structural properties of α-quartz at variable pressures and temperatures.* Physical Review B, 1996. **54**(2): p. 826-835.

266. McLaren, A. and Pitkethly, D., *The twinning microstructure and growth of amethyst quartz.* Physics and Chemistry of Minerals, 1982. **8**(3): p. 128-135.

267. Alderson, A. and Evans, K., *Deformation mechanisms leading to auxetic behaviour in the α-cristobalite and α-quartz structures of both silica and germania.* Journal of Physics: Condensed Matter, 2009. **21**(2): p. 025401.

268. Heaney, P.J. and Veblen, D.R., *Observations of the alpha-beta phase transition in quartz; a review of imaging and diffraction studies and some new results.* American Mineralogist, 1991. **76**(5-6): p. 1018-1032.

269. Barron, T.H.K., Huang, C.C., and Pasternak, A., *Interatomic forces and lattice dynamics of α-quartz.* Journal of Physics C: Solid State Physics, 1976. **9**(21): p. 3925.

270. Barron, T.H.K., Collins, J.F., Smith, T.W., and White, G.K., *Thermal expansion, Gruneisen functions and static lattice properties of quartz.* Journal of Physics C: Solid State Physics, 1982. **15**(20): p. 4311.

271. Barron, T.H.K. and Pasternak, A., *Internal strain and thermal expansion of alpha-quartz below room temperature: a lattice dynamical model.* Journal of Physics C: Solid State Physics, 1987. **20**(2): p. 215.

272. Yoon, Y.-G., Car, R., Srolovitz, D.J., and Scandolo, S., *Thermal conductivity of crystalline quartz from classical simulations.* Physical Review B, 2004. **70**(1): p. 012302.

273. Wolf, D., Keblinski, P., Phillpot, S.R., and Eggebrecht, J., *Exact method for the simulation of Coulombic systems by spherically truncated, pairwise r− 1 summation.* The Journal of Chemical Physics, 1999. **110**(17): p. 8254-8282.

274. Nikitin, A., Markova, G., Balagurov, A., Vasin, R., and Alekseeva, O., *Investigation of the structure and properties of quartz in the α-β transition range by neutron diffraction and mechanical spectroscopy.* Crystallography Reports, 2007. **52**(3): p. 428-435.

275. Wright, A. and Lehmann, M., *The structure of quartz at 25 and 590 C determined by neutron diffraction.* Journal of Solid State Chemistry, 1981. **36**(3): p. 371-380.

276. Levien, L., Prewitt, C.T., and Weidner, D.J., *Structure and elastic properties of quartz at pressure.* American Mineralogist, 1980. **65**(9-10): p. 920-930.

277. McSkimin, H., Andreatch Jr, P., and Thurston, R., *Elastic moduli of quartz versus hydrostatic pressure at 25 and− 195.8 C.* Journal of Applied Physics, 1965. **36**(5): p. 1624-1632.

278. John, S.T. and Klug, D.D., *The structure and dynamics of silica polymorphs using a two-body effective potential model.* The Journal of Chemical Physics, 1991. **95**(12): p. 9176-9185.

279. Taylor, D., *The thermal expansion behaviour of the framework silicates.* Mineral. Mag, 1972. **38**(297): p. 593-604.

280. Jay, A., *The thermal expansion of quartz by X-ray measurements.* Proceedings of the Royal Society of London. Series A, Containing Papers of a Mathematical and Physical Character, 1933: p. 237-247.

281. Khadem, M.H. and Wemhoff, A.P., *Comparison of Green–Kubo and NEMD heat flux formulations for thermal conductivity prediction using the Tersoff potential.* Computational Materials Science, 2013. **69**: p. 428-434.

282. Van Landuyt, J., Van Tendeloo, G., Amelinckx, S., and Walker, M., *Interpretation of Dauphiné-twin-domain configurations resulting from the α-β phase transition in quartz and aluminum phosphate.* Physical Review B, 1985. **31**(5): p. 2986.

283. Bart, F. and Gautier, M., *A LEED study of the (0001) a-quartz surface reconstruction.* Surface Science, 1994. **311**(1): p. L671-L676.

284. Eder, S., Fladischer, K., Yeandel, S., Lelarge, A., Parker, S., Søndergård, E., and Holst, B., *A Giant Reconstruction of α-quartz (0001) Interpreted as Three Domains of Nano Dauphine Twins.* Scientific Reports, 2015. **5**.

285. Baerlocher, C. and McCusker, L.B. *Database of Zeolite Structures*. [cited 2015 10/08/2015]; Available from: http://www.iza-structure.org/databases/.

286. Weitkamp, J., *Zeolites and catalysis.* Solid State Ionics, 2000. **131**(1): p. 175-188.

287. Ackley, M.W., Rege, S.U., and Saxena, H., *Application of natural zeolites in the purification and separation of gases.* Microporous and Mesoporous Materials, 2003. **61**(1): p. 25-42.

288. De Baerdemaeker, T. and De Vos, D., *Gas separation: Trapdoors in zeolites.* Nature chemistry, 2013. **5**(2): p. 89-90.

289. Newsam, J., *The zeolite cage structure.* Science, 1986. **231**(4742): p. 1093-1099.

290. Davis, M.E., *Ordered porous materials for emerging applications.* Nature, 2002. **417**(6891): p. 813-821.

291. El-Kamash, A.M., El-Naggar, M.R., and El-Dessouky, M.I., *Immobilization of cesium and strontium radionuclides in zeolite-cement blends.* Journal of Hazardous Materials, 2006. **136**(2): p. 310-316.

292. Chatterjee, A. and Mizukami, F., *Location and role of exchangeable cations in zeolite catalysis: a first principle study.* Chemical Physics Letters, 2004. **385**(1): p. 20-24.

293. Schnell, S.K. and Vlugt, T.J., *Thermal Conductivity in Zeolites Studied by Non-equilibrium Molecular Dynamics Simulations.* International Journal of Thermophysics, 2013. **34**(7): p. 1197-1213.

294. Demontis, P., Suffritti, G., Quartieri, S., Fois, E., and Gamba, A., *Molecular dynamics studies on zeolites. 3. Dehydrated zeolite A.* The Journal of physical chemistry, 1988. **92**(4): p. 867-871.

295. Vlugt, T.J. and Schenk, M., *Influence of framework flexibility on the adsorption properties of hydrocarbons in the zeolite silicalite.* The Journal of Physical Chemistry B, 2002. **106**(49): p. 12757-12763.

296. Hudiono, Y., Greenstein, A., Saha-Kuete, C., Olson, B., Graham, S., and Nair, S., *Effects of composition and phonon scattering mechanisms on thermal transport in MFI zeolite films.* Journal of Applied Physics, 2007. **102**(5): p. 053523.

297. Sanders, M.J., Leslie, M., and Catlow, C.R.A., *Interatomic potentials for SiO2.* Journal of the Chemical Society, Chemical Communications, 1984(19): p. 1271-1273.

298. Sanchez-Valle, C., Lethbridge, Z.A., Sinogeikin, S.V., Williams, J.J., Walton, R.I., Evans, K.E., and Bass, J.D., *Negative Poisson's ratios in siliceous zeolite MFI-silicalite.* Journal of Chemical Physics, 2008. **128**(18): p. 184503-184503.

299. Bhange, D. and Ramaswamy, V., *Negative thermal expansion in silicalite-1 and zirconium silicalite-1 having MFI structure.* Materials Research Bulletin, 2006. **41**(7): p. 1392-1402.

300. Fang, J., Huang, Y., Lew, C.M., Yan, Y., and Pilon, L., *Temperature dependent thermal conductivity of pure silica MEL and MFI zeolite thin films.* Journal of Applied Physics, 2012. **111**(5): p. 054910.

301. Greenstein, A., *Analysis of thermal conductivity models with an extension to complex crystalline materials*2008: ProQuest.

302. Hayward, S. and Salje, E., *Cubic-tetragonal phase transition in SrTiO3 revisited: Landau theory and transition mechanism.* Phase Transitions: A Multinational Journal, 1999. **68**(3): p. 501-522.

303. Piskunov, S., Heifets, E., Eglitis, R., and Borstel, G., *Bulk properties and electronic structure of SrTiO 3, BaTiO 3, PbTiO 3 perovskites: an ab initio HF/DFT study.* Computational Materials Science, 2004. **29**(2): p. 165-178.

304. Evarestov, R.A., *Quantum chemistry of solids: the LCAO first principles treatment of crystals*. Vol. 153. 2007: Springer Science & Business Media.

305. Jalan, B., Engel-Herbert, R., Mates, T.E., and Stemmer, S., *Effects of hydrogen anneals on oxygen deficient SrTio3-x single crystals.* Applied Physics Letters, 2008. **93**(052907).

306. Cai, H., Wu, X., and Gao, J., *Effect of oxygen content on structural and transport properties in SrTiO 3− x thin films.* Chemical Physics Letters, 2009. **467**(4): p. 313-317.

307. Catlow, C.R.A., *Computer simulation studies of strontium titanate.* J. Am. Ceram. Soc, 1995. **78**(I2): p. 421-28.

308. Kikuchi, A., Okinaka, N., and Akiyama, T., *A large thermoelectric figure of merit of La-doped SrTiO 3 prepared by combustion synthesis with post-spark plasma sintering.* Scripta Materialia, 2010. **63**(4): p. 407-410.

309. Li, L., Liu, Y., Qin, X., Li, D., Zhang, J., Song, C., and Wang, L., *Enhanced thermoelectric performance of highly dense and fine-grained (Sr 1− xGdx) TiO 3− δ ceramics synthesized by sol–gel process and spark plasma sintering.* Journal of Alloys and Compounds, 2014. **588**: p. 562-567.

310. Kovalevsky, A., Yaremchenko, A., Populoh, S., Weidenkaff, A., and Frade, J., *Enhancement of thermoelectric performance in strontium titanate by praseodymium substitution.* Journal of Applied Physics, 2013. **113**(5): p. 053704.

311. Kumar, S.S., Barasheed, A.Z., and Alshareef, H., *High Temperature Thermoelectric Properties of Strontium Titanate Thin Films with Oxygen Vacancy and Niobium Doping.* ACS applied materials & interfaces, 2013. **5**(15): p. 7268-7273.

312. Moos, R. and Härdtl, K.H., *Electronic transport properties of Sr1− xLaxTiO3 ceramics.* Journal of Applied Physics, 1996. **80**(1): p. 393-400.

313. Zhang, L., Tosho, T., Okinaka, N., and Akiyama, T., *Thermoelectric properties of combustion-synthesized lanthanum-doped strontium titanate.* Materials transactions, 2007. **48**(5): p. 1079-1083.

314. Yu, C., Scullin, M.L., Huijben, M., Ramesh, R., and Majumdar, A., *Thermal conductivity reduction in oxygen-deficient strontium titanates.* Applied Physics Letters, 2008. **92**(19): p. 191911-191911.

315. Ohta, S., Nomura, T., Ohta, H., and Koumoto, K., *High-temperature carrier transport and thermoelectric properties of heavily La-or Nb-doped SrTiO3 single crystals.* Journal of Applied Physics, 2005. **97**(3): p. 034106.

316. Koumoto, K., Wang, Y.F., Zhang, R.Z., Kosuga, A., and Funahashi, R., *Oxide Thermoelectric Materials: A Nanostructuring Approach*, in *Annual Review of Materials Research, Vol 40*, D.R. Clarke, M. Ruhle, and F. Zok, Editors. 2010, Annual Reviews: Palo Alto. p. 363-394.

317. Wang, N., He, H., Li, X., Han, L., and Zhang, C., *Enhanced thermoelectric properties of Nb-doped SrTiO 3 polycrystalline ceramic by titanate nanotube addition.* Journal of Alloys and Compounds, 2010. **506**(1): p. 293-296.

318. Dang, F., Wan, C., Park, N.-H., Tsuruta, K., Seo, W.-S., and Koumoto, K., *Thermoelectric Performance of SrTiO3 Enhanced by Nanostructuring・Self-*

Assembled Particulate Film of Nanocubes. ACS applied materials & interfaces, 2013. **5**(21): p. 10933-10937.

319. Wang, Y., Fujinami, K., Zhang, R., Wan, C., Wang, N., Ba, Y., and Koumoto, K., *Interfacial thermal resistance and thermal conductivity in nanograined SrTiO3.* Applied physics express, 2010. **3**(3): p. 031101.
320. Ohta, H., *Thermoelectrics based on strontium titanate.* Materials Today, 2007. **10**(10): p. 44-49.
321. Zhang, R.z., Wang, C.l., Li, J.c., and Koumoto, K., *Simulation of Thermoelectric Performance of Bulk SrTiO3 with Two-Dimensional Electron Gas Grain Boundaries.* Journal of the American Ceramic Society, 2010. **93**(6): p. 1677-1681.
322. Benedek, N.A., Chua, A.L.-S., Elsässer, C., Sutton, A.P., and Finnis, M.W., *Interatomic potentials for strontium titanate: An assessment of their transferability and comparison with density functional theory.* Physical Review B, 2008. **78**(6): p. 064110.
323. Tosawat, S., Chanchana, T., and Vittaya, A., *Molecular dynamics simulation of strontium titanate.* Chinese Physics Letters, 2010. **27**(2): p. 026501.
324. Schmidbauer, M., Kwasniewski, A., and Schwarzkopf, J., *High-precision absolute lattice parameter determination of SrTiO3, DyScO3 and NdGaO3 single crystals.* Acta Crystallographica Section B: Structural Science, 2012. **68**(1): p. 8-14.
325. Bell, R. and Rupprecht, G., *Elastic constants of strontium titanate.* Physical Review, 1963. **129**(1): p. 90.
326. de Ligny, D. and Richet, P., *High-temperature heat capacity and thermal expansion of SrTiO~ 3 and SrZrO~ 3 perovskites.* Physical Review B, 1996. **53**(6): p. 3013-3022.
327. Muta, H., Kurosaki, K., and Yamanaka, S., *Thermoelectric properties of reduced and La-doped single-crystalline SrTiO 3.* Journal of Alloys and Compounds, 2005. **392**(1): p. 306-309.
328. Yamanaka, S., Kurosaki, K., Maekawa, T., Matsuda, T., Kobayashi, S.-i., and Uno, M., *Thermochemical and thermophysical properties of alkaline-earth perovskites.* Journal of Nuclear Materials, 2005. **344**(1): p. 61-66.
329. Nolas, G., Cohn, J., and Slack, G., *Effect of partial void filling on the lattice thermal conductivity of skutterudites.* Physical Review B, 1998. **58**(1): p. 164.

330. Phillpot, S.R., Schelling, P.K., and Keblinski, P., *Interfacial thermal conductivity: Insights from atomic level simulation.* Journal of Materials Science, 2005. **40**(12): p. 3143-3148.

331. Schelling, P.K., Phillpot, S.R., and Keblinski, P., *Kapitza conductance and phonon scattering at grain boundaries by simulation.* Journal of Applied Physics, 2004. **95**(11): p. 6082-6091.

332. Kienzle, O., Exner, M., and Ernst, F., *Atomistic structure of Σ= 3,(111) grain boundaries in strontium titanate.* physica status solidi (a), 1998. **166**(1): p. 57-71.

333. Hutt, S., Köstlmeier, S., and Elsässer, C., *Density functional study of the Σ3 (111)[10] symmetrical tilt grain boundary in SrTiO3.* Journal of Physics: Condensed Matter, 2001. **13**(18): p. 3949.

334. Kienzle, O. and Ernst, F., *Effect of shear stress on the atomistic structure of a grain boundary in strontium titanate.* Journal of the American Ceramic Society, 1997. **80**(7): p. 1639-1644.

335. Dudeck, K.J., Benedek, N.A., Finnis, M.W., and Cockayne, D.J.H., *Atomic-scale characterization of the SrTiO 3 Σ 3 (112)[1¯10] grain boundary.* Physical Review B, 2010. **81**(13): p. 134109.

336. Imaeda, M., Mizoguchi, T., Sato, Y., Lee, H.-S., Findlay, S., Shibata, N., Yamamoto, T., and Ikuhara, Y., *Atomic structure, electronic structure, and defect energetics in [001](310) Σ 5 grain boundaries of SrTiO 3 and BaTiO 3.* Physical Review B, 2008. **78**(24): p. 245320.

337. Lee, S.B., Sigle, W., Kurtz, W., and Rühle, M., *Temperature dependence of faceting in Σ5 (310)[001] grain boundary of SrTiO 3.* Acta Materialia, 2003. **51**(4): p. 975-981.

338. Ravikumar, V., Dravid, V., and Wolf, D., *Atomic structure and properties of the (310) symmetrical tilt grain boundary (STGB) in SrTiO3. Part I: Atomistic simulations.* Interface Science, 2000. **8**(2-3): p. 157-175.

339. Lee, Y.-J., Park, Y.-H., and Hinoki, T. *Influence of grain size on thermal conductivity of SiC ceramics*. in *IOP Conference Series: Materials Science and Engineering*. 2011. IOP Publishing.

340. Fayette, S., Smith, D.S., Smith, A., and Martin, C., *Influence of grain size on the thermal conductivity of tin oxide ceramics.* Journal of the European Ceramic Society, 2000. **20**(3): p. 297-302.

341. Soyez, G., Eastman, J.A., Thompson, L.J., Bai, G.-R., Baldo, P.M., McCormick, A.W., DiMelfi, R.J., Elmustafa, A.A., Tambwe, M.F., and Stone, D.S., *Grain-size-dependent thermal conductivity of nanocrystalline yttria-stabilized zirconia films grown by metal-organic chemical vapor deposition.* Applied Physics Letters, 2000. **77**(8): p. 1155-1157.

342. Shenogin, S., Xue, L., Ozisik, R., Keblinski, P., and Cahill, D.G., *Role of thermal boundary resistance on the heat flow in carbon-nanotube composites.* Journal of Applied Physics, 2004. **95**(12): p. 8136-8144.

343. Pham, A.T., Barisik, M., and Kim, B., *Molecular dynamics simulations of Kapitza length for argon-silicon and water-silicon interfaces.* International journal of precision engineering and manufacturing, 2014. **15**(2): p. 323-329.

344. Böttner, H., Chen, G., and Venkatasubramanian, R., *Aspects of thin-film superlattice thermoelectric materials, devices, and applications.* Mrs Bulletin, 2006. **31**(03): p. 211-217.

345. McCoy, M.A., Grimes, R.W., and Lee, W.E., *Phase stability and interfacial structures in the SrO-SrTiO3 system.* Philosophical Magazine a-Physics of Condensed Matter Structure Defects and Mechanical Properties, 1997. **75**(3): p. 833-846.

346. Chaput, L., *Direct Solution to the Linearized Phonon Boltzmann Equation.* Physical Review Letters, 2013. **110**(26): p. 265506.

Appendix A. Preliminary Quartz Lattice Dynamics Thermal Conductivity

The thermal conductivity of quartz as calculated via lattice dynamics and the BTE failed to give a converged result with respect to supercell size and q-point sampling mesh. Some results are presented in Figure A.1 and A.2 (X and Z directions correspond to crystallographic a and c directions respectively) showing a large variation in obtained thermal conductivity values.

Furthermore the thermal conductivities obtained via this method will be suspect as the structure used is that of α-quartz which is the most stable form at 0 K. Ideally the structure used at each temperature would be the time averaged molecular dynamics structure, however this introduces imaginary phonon modes which must be dealt with.

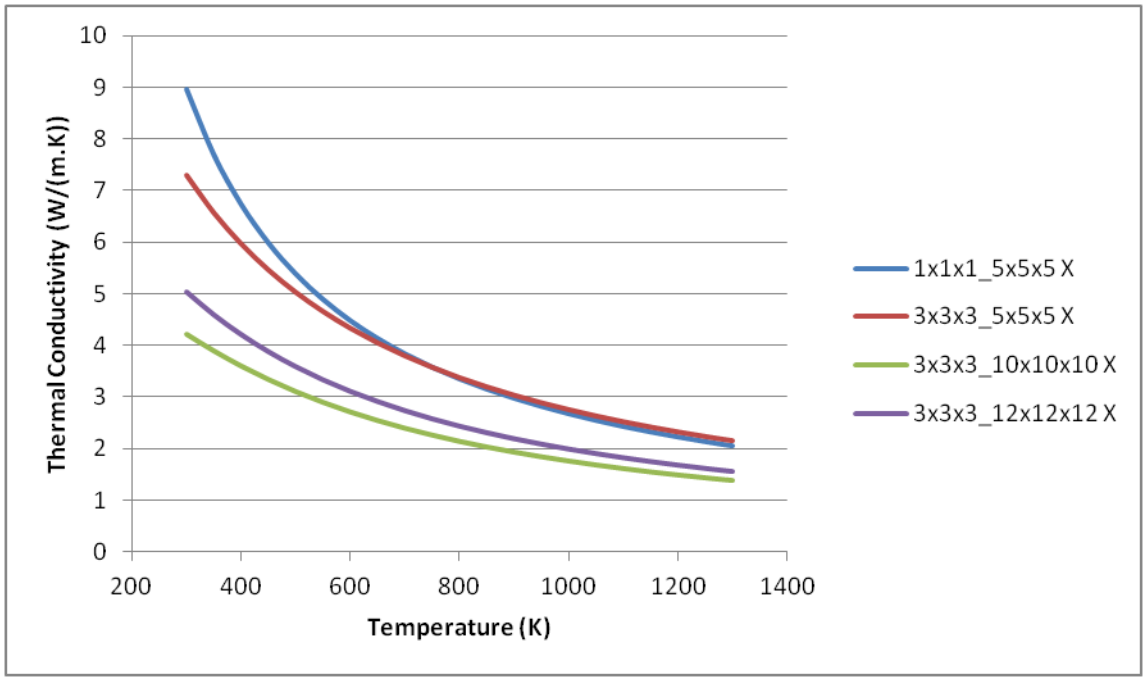

Figure A.1 Thermal conductivity of quartz, X/Y direction. Left most set of numbers give supercell size and right most set of numbers give the q-point mesh.

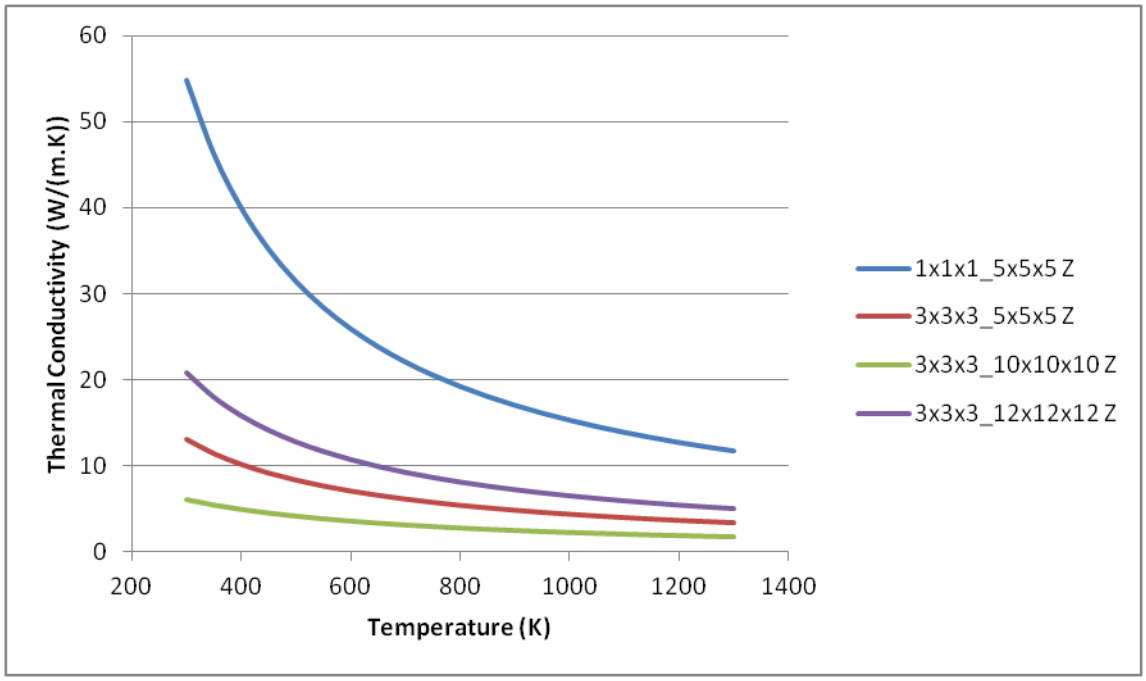

Figure A.2 Thermal conductivity of quartz, Z direction.

Appendix B. Preliminary Glass Green-Kubo Thermal Conductivity

The glass unit cell of approximately 22 Å x 22 Å x 22 Å and containing 648 atoms was run for 10 ns at 8 temperatures. The system is considered too small to draw conclusive results. The thermal conductivities are presented in Figure B.1.

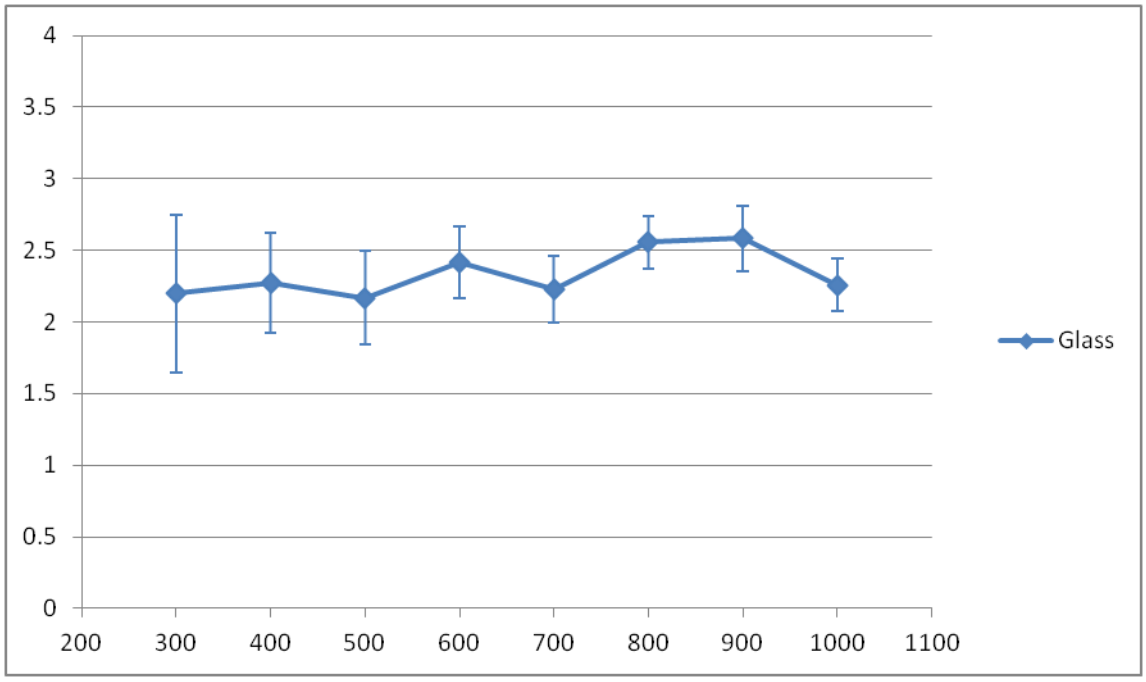

Figure B.1 Preliminary glass thermal conductivity.

The lattice dynamics phonon DOS has also been calculated and analysed to remove optical phonon modes which do not contribute to scattering, Figure B.2.

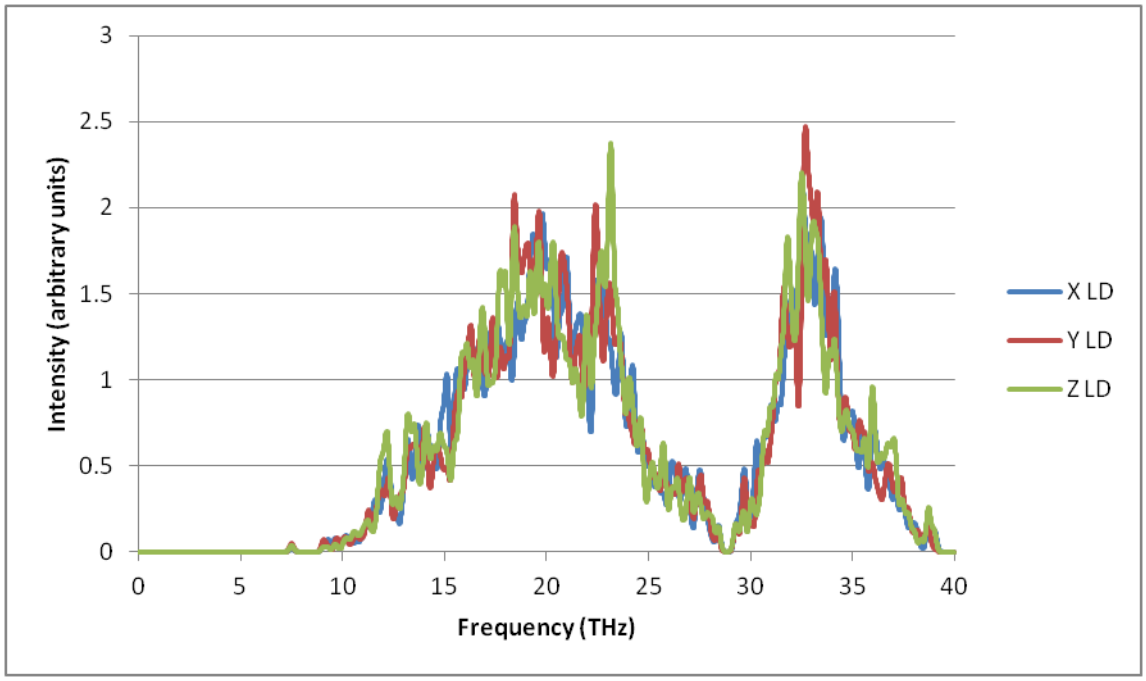

Figure B.2 Analysed Lattice dynamics phonon DOS of the glass system.

Appendix C. LAMMPS Thermal Conductivity Script

The following input script is designed to be run with an accompanying data file of the structure of interest, with modifications to "pair_coeff" to give the correct potential parameters. The units are LMMPS "real" units:

- mass = grams/mole
- distance = Angstroms
- time = femtoseconds
- energy = kcal/mole
- temperature = Kelvin
- pressure = atmospheres

This script was designed to function with the LAMMPS program circa February 2014 and may require some small modification as commands are updated within LAMMPS.

```
#thermal conductivity script

###########################################################################
###########################################################################

units real

variable T equal      1100     # temperature
variable Q equal     94275     # random number seed
variable dt equal      1.0     # timestep in fs
variable s equal       500     # screen output frequency
variable trop equal      3     # system isotropy, 1 = isotropic, 2 = anisotropic, 3 = triclinic

variable Ep equal    50000     # npt equilibriation steps
variable Ev equal    50000     # nvt equilibriation steps

variable NT equal        2     # data collection ensemble, 1 = NVE, 2 = NVT, 3 = NPT

variable N equal   5000000     # number of steps
variable d equal        10     # calculation frequency (equilibration lattice vectors and production heat-flux)

variable rep equal       0     # 0 = do not replicate cell, 1 = replicate cell
variable repx equal     12     # replication factor for x
variable repy equal     12     # replication factor for y
variable repz equal     12     # replication factor for z

variable xyz equal       0     # 1 = print xyz file during production phase

###########################################################################
###########################################################################
#system settings

atom_style      full
pair_style      buck/coul/long 8.5

processors * * * grid numa
```

```
read_data       data.lmp
if "${rep} == 1" then "replicate ${repx} ${repy} ${repz}"
balance 1.0 shift xyz 20 1.0

#kcal/mol for unit style "real"
pair_coeff    *    *         0.000000  1.000000      0.000000
pair_coeff    1    3    335921.2159    0.245015   1885.767153
pair_coeff    2    3    546728.0894    0.18558    334.684293
pair_coeff    3    3     42541.68289   0.343645   4441.08738

kspace_style    pppm 1.0e-5

#########################################################################
#########################################################################
#general settings
timestep        ${dt}
thermo          $s
thermo_style    custom step temp etotal press vol lx ly lz xy xz yz
thermo_modify flush no
run_style       verlet

#########################################################################
#########################################################################
#npt equi skipping

if "${Ep} == 0" then "jump input.lmp NVT"

#########################################################################
#########################################################################
#npt equi

variable myLx equal lx
variable myLy equal ly
variable myLz equal lz
variable myxy equal xy
variable myxz equal xz
variable myyz equal yz
variable repeat equal v_Ep/v_d

velocity all create $T $Q mom yes rot yes dist gaussian

fix             A all momentum 100 linear 1 1 1

if "${trop} == 1" then "fix B all npt temp $T $T 100.0 iso 0.0 0.0 1000.0"
if "${trop} == 2" then "fix B all npt temp $T $T 100.0 aniso 0.0 0.0 1000.0"
if "${trop} == 3" then "fix B all npt temp $T $T 100.0 tri 0.0 0.0 1000.0"

fix             C all ave/time $d ${repeat} ${Ep} v_myLx v_myLy v_myLz v_myxy v_myxz v_myyz mode
scalar ave one

run ${Ep}

variable newX equal f_C[1]
variable newY equal f_C[2]
variable newZ equal f_C[3]
variable newxy equal f_C[4]
variable newxz equal f_C[5]
variable newyz equal f_C[6]
```

```
if "${trop} == 1" then "change_box all x final 0.0 ${newX} y final 0.0 ${newY} z final 0.0 ${newZ} remap units box"
if "${trop} == 2" then "change_box all x final 0.0 ${newX} y final 0.0 ${newY} z final 0.0 ${newZ} remap units box"
if "${trop} == 3" then "change_box all x final 0.0 ${newX} y final 0.0 ${newY} z final 0.0 ${newZ} xy final ${newxy} xz final ${newxz} yz final ${newyz} remap units box"

unfix A
unfix B
unfix C

write_data equi_vol.lmp

################################################################################
################################################################################
#nvt equi skipping

label NVT
if "${Ev} == 0" then "jump input.lmp RUN"

################################################################################
################################################################################
#nvt equi

velocity all create $T $Q mom yes rot yes dist gaussian

fix         A all momentum 100 linear 1 1 1
fix         B all nvt temp $T $T 100.0

run ${Ev}

unfix A
unfix B

################################################################################
################################################################################
#choose data collection type

label RUN
if "$N == 0" then "jump input.lmp END"

if "${NT} == 1" then "fix B all nve"
if "${NT} == 2" then "fix B all nvt temp $T $T 100.0"
if "${NT} == 3 && ${trop} == 1" then "fix B all npt temp $T $T 100.0 iso 0.0 0.0 1000.0"
if "${NT} == 3 && ${trop} == 2" then "fix B all npt temp $T $T 100.0 aniso 0.0 0.0 1000.0"
if "${NT} == 3 && ${trop} == 3" then "fix B all npt temp $T $T 100.0 tri 0.0 0.0 1000.0"

################################################################################
################################################################################
#output variables

variable V equal vol

shell echo $T >> variables.txt
shell echo $V >> variables.txt
shell echo ${dt} >> variables.txt
shell echo $d >> variables.txt

################################################################################
################################################################################
```

```
#heat-flux output

reset_timestep 0

compute myKE all ke/atom
compute myPE all pe/atom
compute myStress all stress/atom NULL virial
compute flux all heat/flux myKE myPE myStress

thermo_style    custom step temp press pe ke etotal
thermo_modify flush no                  #flush output

#########################################################################
#########################################################################
#running output

variable timestep equal step
variable Xflux equal c_flux[1]
variable Yflux equal c_flux[2]
variable Zflux equal c_flux[3]

fix C all print $d "${timestep} ${Xflux} ${Yflux} ${Zflux}" append flux.txt screen no

if "${xyz} == 1" then &
"dump           1 all xyz $s structure.xyz" &
"dump_modify    1 element Sr Ti O"

#########################################################################
#########################################################################
#data collection

run $N

#########################################################################
#########################################################################
#new data generation

label END

write_data new_data.lmp

#########################################################################
#########################################################################
```

Appendix D. Source Code for Analysis Programs

The programs outlined in this chapter are designed to be run with the input script given in Appendix C and so use the same units. Use of these programs with other unit systems will require modification of the source code.

Thermal Conductivity

The following source code was compiled with gfortran-4.7.3 using the command "gfortran –O2 source.f90". The program is run on the heat-flux data produced by the script presented in Appendix C with the first (header) line removed and also the variables.txt file produced by the same script. The program produces an autocorrelation file and a running integration file.

```
PROGRAM HEATFLUX
IMPLICIT NONE
REAL*8 :: DUMMY,TEMP,VOL,CONV,STEP
REAL*8, DIMENSION(:,:), ALLOCATABLE :: INARRAY,OUTARRAY
REAL*8, DIMENSION(:), ALLOCATABLE :: SUMARRAY
INTEGER :: I,IA,IB,IC,IE,COL,FINALSTEP,INTERVAL,N,LENGTH
CHARACTER*20 :: FILENAME1,FILENAME2

!READ IN FILENAMES
PRINT*,'INPUT FLUX FILENAME'
READ'(A20)',FILENAME1
OPEN(8,FILE=FILENAME1,STATUS='OLD')
PRINT*,'INPUT VARIABLES FILE'
READ'(A20)',FILENAME2
OPEN(9,FILE=FILENAME2,STATUS='OLD')

!READ IN VARIABLES SETTINGS
READ(9,*),TEMP
READ(9,*),VOL
READ(9,*),STEP
READ(9,*),INTERVAL

!READ IN ADDITIONAL SETINGS
PRINT*,'INPUT FINAL TIMESTEP'
READ*,FINALSTEP
PRINT*,'INPUT MAXIMUM AUTOCORRELATION LENGTH IN TIMESTEPS'
READ*,LENGTH
LENGTH=(LENGTH/INTERVAL)+1

!SETUP ARRAYS ETC.
N=(FINALSTEP/INTERVAL)
ALLOCATE(INARRAY(9,N))
ALLOCATE(OUTARRAY(10,LENGTH))
ALLOCATE(SUMARRAY(9))
OUTARRAY=0D0
SUMARRAY=0D0
!SET WORKING COLUMN
```

```
COL=1

!READ IN FLUX DATA
DO I=1,N
        READ(8,*),DUMMY,INARRAY(1,I),INARRAY(2,I),INARRAY(3,I)
ENDDO

!FILL FIRST COLUMN WITH INTERVALS
DO I=1,LENGTH
        OUTARRAY(COL,I)=(I-1)*STEP*INTERVAL
ENDDO

!DO THE AUTOCORRELATION
DO IA=1,3                                       !LOOP OVER FIRST DIMENSION
        DO IE=1,3                               !LOOP OVER SECOND DIMENSION
                COL=COL+1                       !SHIFT TO COLUMN 2
                DO IB=1,LENGTH                  !LOOP OVER CORRELATION LENGTHS
                        DO IC=1,(N-(IB-1))      !LOOP OVER ALL VALUES
                                OUTARRAY(COL,IB)=OUTARRAY(COL,IB)+&
                                ((INARRAY(IA,IC)*INARRAY(IE,((IC+(IB-1)))))/&
                                (N-(IB-1)))
                        ENDDO
                ENDDO
        ENDDO
ENDDO

!OUTPUT AUTOCORR TO FILE
OPEN(9,FILE='autocorr.txt')
WRITE(9,*),'TIME   XX       XY       XZ       YX       YY       YZ       ZX
        ZY       ZZ'
DO I=1,LENGTH
WRITE(9,*),OUTARRAY(1,I),' ',OUTARRAY(2,I),'   ',&
OUTARRAY(3,I),'    ',OUTARRAY(4,I),'   ',OUTARRAY(5,I),'   ',&
OUTARRAY(6,I),'    ',OUTARRAY(7,I),'   ',OUTARRAY(8,I),'   ',&
OUTARRAY(9,I),'    ',OUTARRAY(10,I)
ENDDO
CLOSE(9)

!INTEGRATE SECTION

!CONVERSION CONSTANT FOR REAL UNITS
CONV=34995566.6257005D0/TEMP/TEMP/VOL*INTERVAL*STEP

!SETUP OUTPUT FILE
OPEN(9,FILE='therm.txt',STATUS='NEW')
WRITE(9,*),'TIME   XX       XY       XZ       YX       YY       YZ       ZX
        ZY       ZZ'

!CONVERT ARRAYS TO CORRECT UNITS
DO IA=2,10
        DO IB=1,LENGTH
                OUTARRAY(IA,IB)=OUTARRAY(IA,IB)*CONV
        ENDDO
ENDDO

!DO SHIFTING INTEGRATION
DO IB=1,(LENGTH-1)
        !INTEGRATE
        DO IA=1,9
                SUMARRAY(IA)=SUMARRAY(IA)+(OUTARRAY((IA+1),IB)/2)&
```

```
                +(OUTARRAY((IA+1),(IB+1))/2)
        ENDDO
        !WRITE OUT
        WRITE(9,*),(IB*STEP*INTERVAL),'       ',SUMARRAY(1),&
        '             ',SUMARRAY(2),'     ',SUMARRAY(3),'     ',&
        SUMARRAY(4),'       ',SUMARRAY(5),'     ',SUMARRAY(6),&
        '             ',SUMARRAY(7),'     ',SUMARRAY(8),'     ',&
        SUMARRAY(9)
ENDDO

!CLOSE FILE
CLOSE(9)

STOP
END
```

Green-Kubo Spectra

The following source code was also compiled with gfortran-4.7.3 using the command "gfortran source.f90 –lfftw3" and includes the FFTW3 library. The program is then run on the autocorr.txt file produced by the program in Appendix C and the variables.txt file produced by the script in Chapter 0. The spec.txt file produced gives the Green-Kubo spectra with respect to frequency in THz.

```
PROGRAM SPEC
IMPLICIT NONE
INCLUDE 'fftw3.f'
REAL*8 :: DUMMY,INTERVAL,VEL,TIMESTEP,TEMP,VOL,CONV
REAL*8, DIMENSION(:), ALLOCATABLE :: FFTIN
COMPLEX*16, DIMENSION(:), ALLOCATABLE :: FFTOUT
REAL*8, DIMENSION(:,:), ALLOCATABLE :: INPUT,OUTPUT
INTEGER*8 :: N,I,IA,FFTPLAN,STEP
CHARACTER*20 :: FILENAME

!INPUT FILENAMES
PRINT*,'INPUT AUTOCORRELATION FILE'
READ'(A20)',FILENAME
OPEN(7,FILE=FILENAME,STATUS='OLD')

PRINT*,'INPUT VARIABLES FILE'
READ'(A20)',FILENAME
OPEN(9,FILE=FILENAME,STATUS='OLD')

!READ IN VARIABLES SETTINGS
READ(9,*),TEMP
READ(9,*),VOL
READ(9,*),TIMESTEP
READ(9,*),STEP

!READ IN USER VARIABLES
PRINT*,'INPUT LENGTH OF AUTOCORRELATION (fs)'
READ*,N
N=N/STEP

!ASSIGN ARRAY SIZES
```

```
ALLOCATE(INPUT(4,N))
ALLOCATE(OUTPUT(4,N/2))
ALLOCATE(FFTIN(N))
ALLOCATE(FFTOUT((N/2)+1))

!IGNORE FIRST LINE, READ DATA INTO ARRAY, CALCULATE SOME VALUES, CLOSE FILE
READ(7,*)
DO I=1,N
        READ(7,*),INPUT(1,I),INPUT(2,I),DUMMY,DUMMY,DUMMY,INPUT(3,I),&
        DUMMY,DUMMY,DUMMY,INPUT(4,I)
ENDDO
CLOSE(7)

!CONVERT VALUES TO CORRECT UNITS
CONV=34995566.6257005D0/TEMP/TEMP/VOL*TIMESTEP*STEP
DO I=2,4
        DO IA=1,N
                INPUT(I,IA)=INPUT(I,IA)*CONV
        ENDDO
ENDDO

!TIMESTEP CONVERSION TO SECONDS,
!DIVIDE BY MEASUREMENT INTERVAL, DIVIDE BY NUMBER OF SAMPLES
INTERVAL=((1E15/TIMESTEP)/STEP)/N
DO I=1,N/2
        OUTPUT(1,I)=((I-1)*INTERVAL)/1E12
ENDDO

!LOOP OVER THREE DIMENSIONS
DO IA=2,4

        !COPY DATA INTO INPUT ARRAY
        DO I=1,N
                FFTIN(I)=INPUT(IA,I)
        ENDDO

        !CALL FFT ROUTINE
        CALL DFFTW_PLAN_DFT_R2C_1D(FFTPLAN,N,FFTIN,FFTOUT,FFTW_ESTIMATE)
        CALL DFFTW_EXECUTE_DFT_R2C(FFTPLAN,FFTIN,FFTOUT)
        CALL DFFTW_DESTROY_PLAN(FFTPLAN)

        !COPY INTO OUTPUT ARRAY
        DO I=1,N/2
                OUTPUT(IA,I)=REALPART(FFTOUT(I))
        ENDDO

ENDDO

!OUTPUT TO A FILE
OPEN(7,FILE='spec.txt',STATUS='REPLACE')
WRITE(7,*),'FREQUENCY(THz)          X          Y          Z'
DO I=1,N/2
        WRITE(7,*),OUTPUT(1,I),'       ',OUTPUT(2,I),'       ',OUTPUT(3,I),'
        ',OUTPUT(4,I)
ENDDO
CLOSE(7)

STOP
END
```